NASA/CR–2012-217331

Quantitative Global Heat Transfer in a Mach-6 Quiet Tunnel

John P. Sullivan and Steven P. Schneider
Purdue University, West Lafayette, Indiana

Tianshu Liu
Western Michigan University, Kalamazoo, Michigan

Justin Rubal, Chris Ward, Joseph Dussling, Cody Rice, and Ryan Foley
Purdue University, West Lafayette, Indiana

Zeimin Cai, Bo Wang, and Sudesh Woodiga
Western Michigan University, Kalamazoo, Michigan

February 2012

NASA STI Program . . . in Profile

Since its founding, NASA has been dedicated to the advancement of aeronautics and space science. The NASA scientific and technical information (STI) program plays a key part in helping NASA maintain this important role.

The NASA STI program operates under the auspices of the Agency Chief Information Officer. It collects, organizes, provides for archiving, and disseminates NASA's STI. The NASA STI program provides access to the NASA Aeronautics and Space Database and its public interface, the NASA Technical Report Server, thus providing one of the largest collections of aeronautical and space science STI in the world. Results are published in both non-NASA channels and by NASA in the NASA STI Report Series, which includes the following report types:

- TECHNICAL PUBLICATION. Reports of completed research or a major significant phase of research that present the results of NASA programs and include extensive data or theoretical analysis. Includes compilations of significant scientific and technical data and information deemed to be of continuing reference value. NASA counterpart of peer-reviewed formal professional papers, but having less stringent limitations on manuscript length and extent of graphic presentations.

- TECHNICAL MEMORANDUM. Scientific and technical findings that are preliminary or of specialized interest, e.g., quick release reports, working papers, and bibliographies that contain minimal annotation. Does not contain extensive analysis.

- CONTRACTOR REPORT. Scientific and technical findings by NASA-sponsored contractors and grantees.

- CONFERENCE PUBLICATION. Collected papers from scientific and technical conferences, symposia, seminars, or other meetings sponsored or co-sponsored by NASA.

- SPECIAL PUBLICATION. Scientific, technical, or historical information from NASA programs, projects, and missions, often concerned with subjects having substantial public interest.

- TECHNICAL TRANSLATION. English-language translations of foreign scientific and technical material pertinent to NASA's mission.

Specialized services also include creating custom thesauri, building customized databases, and organizing and publishing research results.

For more information about the NASA STI program, see the following:

- Access the NASA STI program home page at *http://www.sti.nasa.gov*

- E-mail your question via the Internet to help@sti.nasa.gov

- Fax your question to the NASA STI Help Desk at 443-757-5803

- Phone the NASA STI Help Desk at 443-757-5802

- Write to:
  NASA STI Help Desk
  NASA Center for AeroSpace Information
  7115 Standard Drive
  Hanover, MD 21076-1320

NASA/CR–2012-217331

Quantitative Global Heat Transfer in a Mach-6 Quiet Tunnel

John P. Sullivan and Steven P. Schneider
Purdue University, West Lafayette, Indiana

Tianshu Liu
Western Michigan University, Kalamazoo, Michigan

Justin Rubal, Chris Ward, Joseph Dussling, Cody Rice, and Ryan Foley
Purdue University, West Lafayette, Indiana

Zeimin Cai, Bo Wang, and Sudesh Woodiga
Western Michigan University, Kalamazoo, Michigan

National Aeronautics and
Space Administration

Langley Research Center
Hampton, Virginia 23681-2199

Prepared for Langley Research Center
under Cooperative Agreement NNX08AC97A

February 2012

Available from:

NASA Center for AeroSpace Information
7115 Standard Drive
Hanover, MD 21076-1320
443-757-5802

Final Technical Report for Cooperative Agreement NNX08AC97A
1 Jan. 2008 to 31 August 2011

Quantitative Global Heat Transfer in a Mach-6 Quiet Tunnel

John P. Sullivan, Steven P. Schneider
Purdue University, West Lafayette, IN 47907

Tianshu Liu
Western Michigan University, Kalamazoo, MI 490008

Students
Justin Rubal, Chris Ward, Joseph Dussling, Cody Rice, Ryan Foley (Purdue U.)
Zeimin Cai, Bo Wang, Sudesh Woodiga (Western Michigan U.)

Abstract

This project developed quantitative methods for obtaining heat transfer from temperature-sensitive paint (TSP) measurements in the Mach-6 quiet tunnel at Purdue, which is a Ludwieg tube with a downstream valve, moderately-short flow duration and low levels of heat transfer. The measurements are used to obtain critical information on important physical phenomena like laminar-turbulent transition and near-surface stationary vortices. The heat-transfer data-reduction methods might later prove useful in other hypersonic facilities at NASA, Sandia National Laboratories, the Arnold Engineering Development Center, and other institutions.

Previous difficulties with inferring heat transfer from TSP in the Mach-6 quiet tunnel were traced to (1) the large transient heat transfer that occurs during the unusually long tunnel startup and shutdown, (2) the non-uniform thickness of the insulating coating, (3) inconsistencies and imperfections in the painting process and (4) the low levels of heat transfer observed on slender models at typical stagnation temperatures near 430K. Repeated measurements were conducted on 7^{o}-half-angle sharp circular cones at zero angle of attack (AoA) in order to evaluate the techniques, isolate the problems and identify solutions. A small number of Schmidt-Boelter heat-transfer gauges are now installed in every model, to get accurate single-point results that can be used for in-situ TSP calibrations on every tunnel run. The models are now made of aluminum covered with insulating paint, since it was found that the startup heat-transfer pulse diffuses rapidly into the aluminum, so that it can be neglected during the run. New kinds of paint are used to insulate the model and bind the TSP, improving uniformity, repeatability, ease of use and adherence. These factors in combination have resulted in a simple and practical method that has yielded promising results for simple geometries, as described in Appendix I.

En route to this promising simple method, sophisticated analytical and numerical inverse methods were developed for calculating heat flux from TSP data, and the image deconvolution method was developed for correcting the lateral heat conduction effect. These developments and their validation are described in Appendix II. An attempt at developing a two-color TSP method is also summarized below; this attempt was partially successful but has not yet become practical for regular use.

Summary

Development of Current Procedure

Measurements have been conducted on a 7°-half-angle aluminum circular cone at Mach 6 in the Purdue Ludwieg tube to evaluate the accuracy of calculating heat flux from a time sequence of TSP images. Low heat fluxes of less than 6 kW/m^2 and small surface temperature changes of a few degrees C pose challenges to quantitative global heat flux measurements. These challenges increase due to the relatively large heat transfer that is observed during the startup and shutdown of the quiet Ludwieg tube, which is necessarily initiated by a valve that is downstream of the nozzle. A sharp 7°-half-angle cone at zero angle of attack with a laminar boundary layer was used as a well-known canonical flow field, in order to develop improved TSP processes.

The boundary-layer similarity solution and the reference temperature method for hypersonic laminar boundary layers on sharp circular cones were examined by comparing them with numerical Navier-Stokes solutions. It was shown that these approximate solutions are accurate enough to serve as a reference for comparison with the TSP-derived heat flux distributions.

Theoretical analysis indicates that for a thin polymer layer on a highly-conductive metal model the discrete linear Fourier law is approximately valid. However, since the error sources could not be successfully corrected, the TSP is now calibrated in-situ using heat flux measurements obtained by Schmidt-Boelter (SB) gauges. The SB data are compared to the TSP data to determine the slope and intercept of the linear Fourier approximation. Experiments have been performed on a 7°-half-angle sharp cone equipped with 6 SB heat-transfer gauges to validate this linear in-situ calibration method. The linear heat-transfer reduction procedure agrees well with the similarity solution for the hypersonic laminar boundary layer, when the SB gauges are accurate. It has not been trivial to get accurate SB results at the very low heat-transfer levels typically measured near the aft end of slender models. Thus, this method of anchoring the calibration requires two or more SB gauges to produce reliable results.

Related Developments

Early in the development process, four tests were conducted sequentially under different total pressures and temperatures in the Ludwieg tube. It was found that the TSP-derived heat flux distribution increasingly deviated from the theoretical solutions as the pre-run surface temperature of the cone increased during sequential runs. This non-physical shift is caused by a slow increase in the temperature of the aluminum cone over the course of several tunnel runs. The effect of this increase on the analytical inverse method is estimated as a linear term that depends on the difference between the pre-run near-surface temperature and the ambient temperature, where the effect of the non-uniformity of the coating thickness is included. The unknown coefficient in this term is determined in situ by using the data given by a single-point heat flux sensor amounted on the cone surface. The accuracy of TSP heat flux measurements in the Ludwieg tube is improved when the analytical inverse method is coupled with (1) an in-situ correction scheme for this slow warming effect and (2) corrections for the coating non-uniformity. In addition, the thickness distribution of the insulating coating can be determined by utilizing the decay of the coating surface temperature immediately after the rapid heating in the start-up process of the Ludwieg tube. However, these methods have not been accurate enough to

replace the current procedure described above. They do seem promising and may be useful for other experimentalists.

The exact inverse solution of the one-dimensional (1D) time-dependent heat conduction equation is obtained by using the Laplace transform for a thin polymer (TSP or TSP/insulator layer) on a semi-infinite base. This solution leads to the analytical method for determining heat flux from a time history of the surface temperature, as is measured by TSP in hypersonic tunnels. Simulations indicate that the analytical method is able to determine a complicated transient heat flux history as long as the intrinsic response time of the TSP is sufficiently small. The heat flux recovered by the analytical method is independent of a complicated tunnel-starting process after a transient process. Therefore, the analytical method can be used for various hypersonic tunnels with different starting characteristics. The uncertainty of the heat flux calculation is composed of elemental errors such as those in the polymer thickness, thermal conductivity, thermal diffusivity, and the ratio of the thermal properties between the polymer and base. The sensitivity of the calculated heat flux to the elemental errors is much weaker for a low thermal-conductive base than for a metal base. Data interpolation from a small sample group can improve the accuracy of the heat flux calculation. An iterative scheme for obtaining the polymer surface temperature from the TSP-measured temperature could improve the accuracy of heat flux measurements, particularly when heat flux is very large. To examine the analytical method, TSP images on a sharp $25^{o}/45^{o}$ indented metal cone model at Mach 11 were reprocessed, and the recovered heat flux results are in good agreement with those measured by thin-film heat flux gauges. Furthermore, the analytical method is applied to TSP measurements on a nylon cone at Mach 6, and the recovered heat flux field indicates a turbulent wedge triggered by a roughness element on the cone surface. The results for infrared laser heating in a bench test are also presented.

The numerical inverse method was developed to determine heat flux from TSP images obtained in short-duration hypersonic tunnels. This method is an iterative algorithm based on a numerical solution for the positive heat transfer problem and an optimization scheme to minimize the error between the calculated and measured surface temperatures. Simulations indicate that the numerical and analytical inverse methods yield the same heat flux for a simulated tunnel run when the thermal properties of the TSP and base materials are constant. Nevertheless, the numerical inverse method has the substantial advantage that it can take into effect the temperature dependencies of the thermal properties. The numerical inverse method is applied to TSP measurements on a sharp stainless steel $25^{o}/45^{o}$ indented model at Mach 10, and a sharp 7^{o}-half-angle Nylon-6 cone model with a roughness element, at Mach 6. The extracted heat-flux distributions compare favorably with those given by thin-film heat transfer gauges and the laminar boundary-layer solution.

The accuracy of image-based surface heat flux measurements on high-curvature models can be improved by correcting for lateral heat conduction effects. A convolution-type integral equation with a Gaussian filter (kernel) is given as a model, which physically interprets a heat flux field obtained by using the 1D inverse method as a Gaussian-filtered (spatially-averaged or spatially-diffused) heat flux field in a 3D case. Therefore, the problem for correcting the lateral heat conduction effect becomes the classical image deconvolution problem, and the total variation regularization method can be used for image deconvolution. The two-step method is developed to calculate a heat flux field from a time sequence of surface temperature images, where the 1D inverse method as a time-integral processing is used in tandem with the image deconvolution method as a field processing. In simulations, by utilizing a uniformly distributed

heat flux source suddenly applied onto a surface in a square region, the accuracy of the two-step method for correcting the lateral heat conduction effect is evaluated. In particular, the linear relations between the empirical standard deviation in the Gaussian filter and the thermal diffusion length scale are determined by optimization for different materials. In temperature-sensitive-paint measurements on a 7^{o}-half-angle circular cone in the Purdue Mach-6 wind tunnel, improved heat flux images are obtained by using the two-step method to correct the lateral heat conduction effect and remove the random noise. The two-step method is not only computationally efficient and robust, but also easy to implement in applications. Furthermore, to deal with a projection problem related to the use of the image deconvolution method for a highly curved surface, a simple method is proposed and examined for a developable surface (e.g. the conical surface).

Towards Two-Color Temperature-Sensitive Paints for the Mach-6 Quiet Tunnel

A two-color temperature sensitive paint (TSP) system was developed for the Boeing/AFOSR Mach-6 Quiet Tunnel (BAM6QT). TSP has previously been used in the BAM6QT for feature detection and quantitative heat transfer measurements. This new system, however, improves sensitivity and reduces noise. The sensitivity was increased by using Europium (III) Thenoyltrifluoroacetonate (EuTTA). EuTTA is favorable in this application due to its high temperature sensitivity, bright emission and pressure insensitivity. Noise was reduced through the use of a second (reference) color. Coumarin 540a was selected as the second luminophore. Calibrations were obtained using a single, color camera with a Bayer filtered CCD array. This is beneficial in that errors can be reduced from model motion, illumination instability, and temporal variation. Furthermore both color channels are obtained at a single location. Calibrations on the two-color paint were found to be repeatable. The paint had a maximum sensitivity of 1.68%/ deg. C (an improvement of 60% over the current system). Simple impinging jet experiments were performed showing well defined temperature wake profiles. Using similar spatial resolution as the traditional system, the two-color paint showed a 22% reduction in noise compared with the traditional system. However, experiments that were performed in the BAM6QT yielded results that were unacceptable. These limitations are most likely attributed to the limited spectral transmittance of the thick plexiglas windows at the shorter wavelengths needed to excite EuTTA, and the increased noise level of the Nikon D200 camera in comparison with the thermoelectrically cooled pco.1600 camera. The details of this work are reported by Joseph Dussling in his M.S. thesis entitled "Development of an Improved Temperature Sensitive Paint System for the Boeing/AFOSR Mach-6 Quiet Tunnel", School of Aeronautics and Astronautics, Purdue University, Dec. 2011.

Appendices

I. *Testing an Improved Method for Determining Heat Transfer from Temperature-Sensitive Paint*, Christopher A.C. Ward and Steven P. Schneider, 33 pages.

II. *Analytical and Numerical Inverse Methods for Temperature Sensitive Paint Heat Flux Measurements in Hypersonic Tunnels,* Tianshu Liu et al., 111 pages.

Appendix I: Testing an Improved Method for Determining Heat Transfer From Temperature-Sensitive Paint

Christopher A. C. Ward
Steven P. Schneider

Abstract

A linear method of determining heat transfer from TSP data was tested in the Boeing/AFOSR Mach-6 Quiet Tunnel. A 7-deg half-angle sharp cone was tested at 0-deg angle of attack with temperature-sensitive paint and 6 Schmidt-Boelter heat transfer gauges. The linear reduction method agrees well with the theoretical heat transfer, if the heat transfer gauge used to reduce the TSP data is accurate. After resolving many of the issues involved with utilizing the Schmidt-Boelter gauges, accurate readings could be obtained from five of six gauges at once.

An alternate method of obtaining heat transfer from the TSP using measurements of the paint thickness, model temperature and an estimate of the thermal conductivity of the insulating paint did not produce the desired results. In order to obtain accurate heat transfer from the TSP, at least one Schmidt-Boelter gauge needs to be installed in the model.

1 Hypersonic Boundary-Layer Transition

Hypersonic laminar-to-turbulent transition is important for predictions of heat transfer, skin friction, separation, and other boundary-layer properties [1]. Therefore, to obtain an accurate prediction of these properties, an accurate prediction of the boundary-layer transition location is crucial. The uncertainty in predicting boundary-layer transition affects the design of hypersonic vehicles. A conservative approach for a vehicle would mean designing a thermal protection system (TPS) that would be able to withstand high turbulent boundary-layer heating, even though the boundary layer may be laminar. Figure 1 is a plot of heat transfer against non-dimensional distance along a 13-foot beryllium cone during atmospheric re-entry. The computations can match the experimental results well if the transition location is known. Since a turbulent boundary layer has roughly 3–8 times higher heating than its laminar counterpart, the computations can produce substantial errors if the transition location is not known.

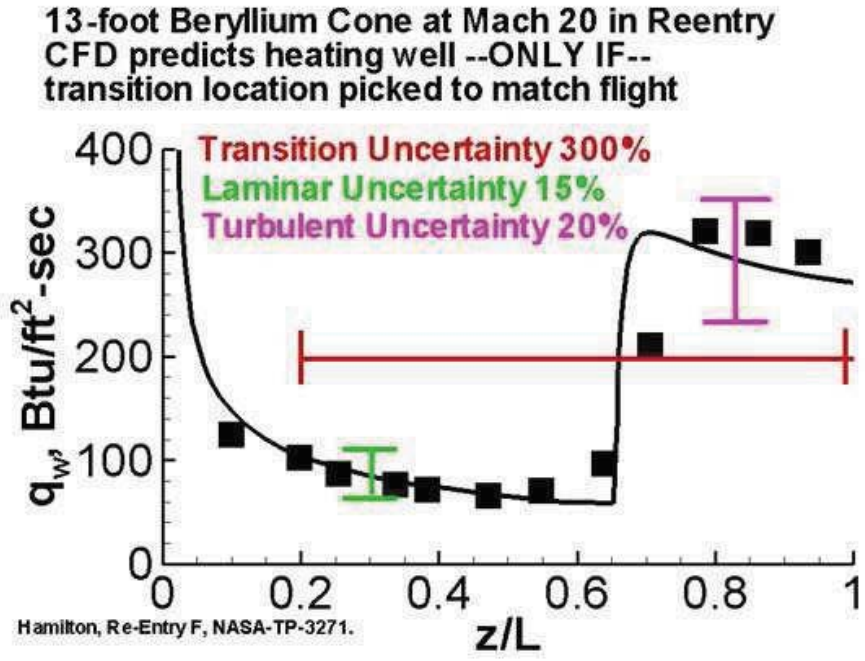

Figure 1: Comparison of computationally and experimentally obtained heat-transfer rates from Reference [2]. Error bars are approximate.

Boundary-layer transition is a complicated and poorly understood process. Disturbances can be created in the freestream (acoustic radiation or vorticity) or by the vehicle surface (surface roughness or waviness) [3]. The disturbances enter the boundary layer through the process of receptivity. Receptivity can be affected by roughness, bluntness, Mach number and other factors [4]. These disturbances grow and may lead to turbulence, depending on the instabilities present in the boundary layer. Empirical and semi-empirical methods (such as the e^N method [5]) can be used to predict the growth of these instabilities and predict transition [6], but these empirical methods are not reliable for a wide range of cases. Empirical methods are based solely on observation or exper-

imentation, while semi-empirical methods attempt to incorporate physical attributes or scientific law along with experimental results. Empirical methods also do not work well when a 3-D instability is present. A more basic understanding of the flow physics that causes transition is needed, thereby reducing empiricism.

2 Facility, Models and Equipment

2.1 Boeing/AFOSR Mach 6 Quiet Tunnel

All the experiments were performed in the Boeing/AFOSR Mach-6 Quiet Tunnel, pictured in Figure 2. The BAM6QT is the largest hypersonic quiet tunnel in the world. The BAM6QT is a Ludwieg tube, comprising of a long driver tube with a converging-diverging nozzle at the end. A Ludwieg tube design helps minimize costs and provides relatively high Reynolds numbers.

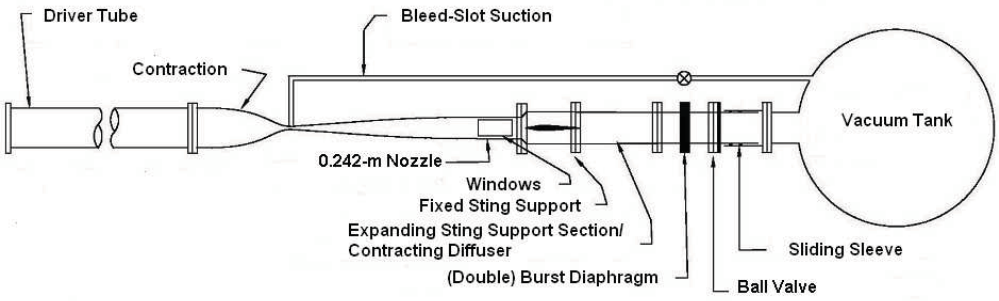

Figure 2: Schematic of the Boeing/AFOSR Mach-6 Quiet Tunnel

To operate the tunnel, the upstream end of the tunnel is brought to the desired stagnation pressure and the downstream end is brought to near vacuum, separated by a set of double burst diaphragms. To start the tunnel, the air is evacuated from between the two diaphragms, causing them to burst. An expansion fan then travels upstream and a shock wave travels downstream. Mach-6 flow is initiated when the expansion fan passes through the throat. The expansion fan reflects between the upstream end of the driver tube and the contraction, taking on the order of 200 ms. The stagnation pressure drops with each reflection. For each 200 ms time segment, the flow conditions are quasi-static. A typical run lasts between 5 and 10 seconds, therefore for any given run a range of Reynolds numbers can be tested.

The BAM6QT is capable of producing low noise levels on the order of 0.05% and employs several features to maintain a laminar nozzle wall boundary layer and achieve this low noise. A suction slot is present upstream of the throat and removes the boundary layer on the contraction wall, allowing a new undisturbed laminar boundary layer to grow on the nozzle wall. This suction slot is connected to the vacuum tank through a fast valve. The fast valve can be closed to allow a turbulent nozzle-wall boundary layer to develop. The noise levels with the fast valve closed are on the order of 3%, similar to conventional hypersonic tunnels. The tunnel also features a long

nozzle designed to reduce the growth of Görtler vortices, a highly polished throat and nozzle, and high-quality air filters to reduce air-borne particulate in the tunnel.

2.2 Schmidt-Boelter Heat Transfer Gauges

Schmidt-Boelter gauges were used to obtain heat transfer on the surface of the models. The gauges have an outside diameter of 3.175 mm (0.125 inches). The gauges house a thermopile in a 2.79 mm (0.11 inch) diameter cavity. The thermopile is coated with a black epoxy, allowing the gauge to more effectively absorb heat (although radiation is likely not significant in the present experiments). The epoxied region has a diameter of 3.175 mm, therefore the sensing region has that same diameter. According to the Medtherm Corporation, the epoxy has a thickness on the order of 0.001–0.003 inches, but is typically closer to 0.001 inches [7].

Two different models of gauges bought from the Medtherm Corporation were used in the testing, the 8-2-0.25-48-2083TBS and 8-1-0.25-48-2083TBS models. Both gauges contain two type T thermocouples, one at the base and one at the surface of the thermopile. The former gauge has a calibration range of 0–2 Btu/ft^2/s (0–22 kW/m^2), and the latter has a range of 0–1 Btu/ft^2/s (0–11 kW/m^2).

2.3 Model

All the experiments were performed in the BAM6QT with a nominally sharp 7° half-angle cone at 0° angle of attack. The model is equipped with six sensor ports. The axial locations of the ports are shown in Table 1. For the tests presented in this paper, all the ports were filled with Schmidt-Boelter heat transfer gauges.

Position	Axial Distance from Nosetip [m]
1	0.15
2	0.19
3	0.23
4	0.28
5	0.32
6	0.36

Table 1: Axial location of each sensor port in the 7° half-angle cone.

3 Temperature-sensitive Paint Background

Temperature-sensitive paint is a luminescent paint that can be airbrushed onto a model to provide a global temperature distribution. The advantage of using TSP over discrete sensors, such as thermocouples, is the increased spatial resolution and the relatively low cost [8]. The temperature

distribution can help map important flow features such as shocks or vortices. Temperature-sensitive paint can also help quantify the region of boundary-layer transition, since there is a sharp increase in temperature at the onset of transition.

The temperature-sensitive paint is created by doping a polymer coating with luminescent molecules. The luminescent molecules are typically dissolved in a solvent first. The luminescent molecules used are 99.95% Tris(2,22-bipyridine) dichlororuthenium(II) Hexahydrate (Ru(bpy)) and the solvent is ethanol. The polymer coating is a BASF LIMCO LC4000 Urethane Clearcoat and a LIMCO LHM activator.

The temperature-sensitive paint measures temperature through the process of thermal quenching. When the luminophore molecules absorb a photon of radiation, the molecule moves to an excited electronic state [8]. Upon returning to a lower energy state, a longer wavelength photon is emitted by the molecule [9]. There are two mechanisms at work when the electron returns to its ground state, radiationless and radiative process [10].

If the radiative processes dominate the return to ground state, the intensity of the emitted photons will be high. Conversely, if the radiationless process dominates, the intensity will be low. One process will always dominate the electron's transition to ground state, and this has been shown to be temperature dependent [8]. At the experimental temperatures of the BAM6QT, radiationless processes dominate. Thermal quenching occurs when the radiationless process dominate (intensity is inversely proportional to temperature). Since the intensity of the emitted photons is dependent on the temperature of the paint, surface temperature can be determined by measuring the emitted light intensity.

Typically an insulating layer of paint is placed between the model and the TSP to thermally insulate the TSP layer from the model. This is done to increase the signal-to-noise ratio. This higher signal-to-noise ratio is important when trying to visualize low amplitude instability waves such as stationary crossflow waves [11].

Figure 3 shows a schematic of how TSP works. A short wave incident light source is used to excite the luminescent molecules. The emitted photons are then captured by a camera with a long-pass filter. The intensity of the emitted photons can be converted to temperature.

3.1 Temperature-Sensitive Paint Apparatus

Two blue light-emitting-diode arrays were used to excite the temperature-sensitive paint, an Innovative Scientific Solutions Inc. LMA LM4 array and an ISSI LM2xLZ-465 LED array. The two arrays emitted light with a 465 nm wavelength. Both LED arrays were used in order to illuminate the model as much as possible, therefore increasing the signal from the TSP.

A Cooke Corporation PCO.1600 14-bit CCD camera was used. It was controlled by a PC through the CamWare software. The CCD camera captures images with a resolution of 1600 $\times$ 1200 pixels. The pixels were averaged to reduce noise; therefore the presented images have a resolution of 800 $\times$ 600 pixels. Figure 4 shows the experimental setup with the CCD camera and the two LED arrays. The model can be seen through the porthole windows installed in the tunnel. There is a larger rectangular window also used in testing, but it can only be used for pressures up to 140 psig.

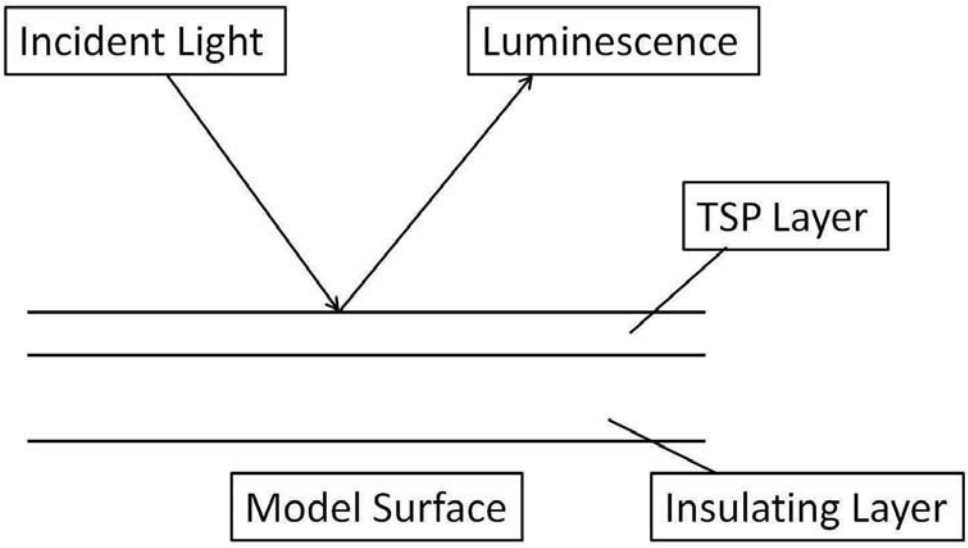

Figure 3: Schematic of the temperature-sensitive paint layer. Re-drawn from Figure 1 of Reference [12]

.

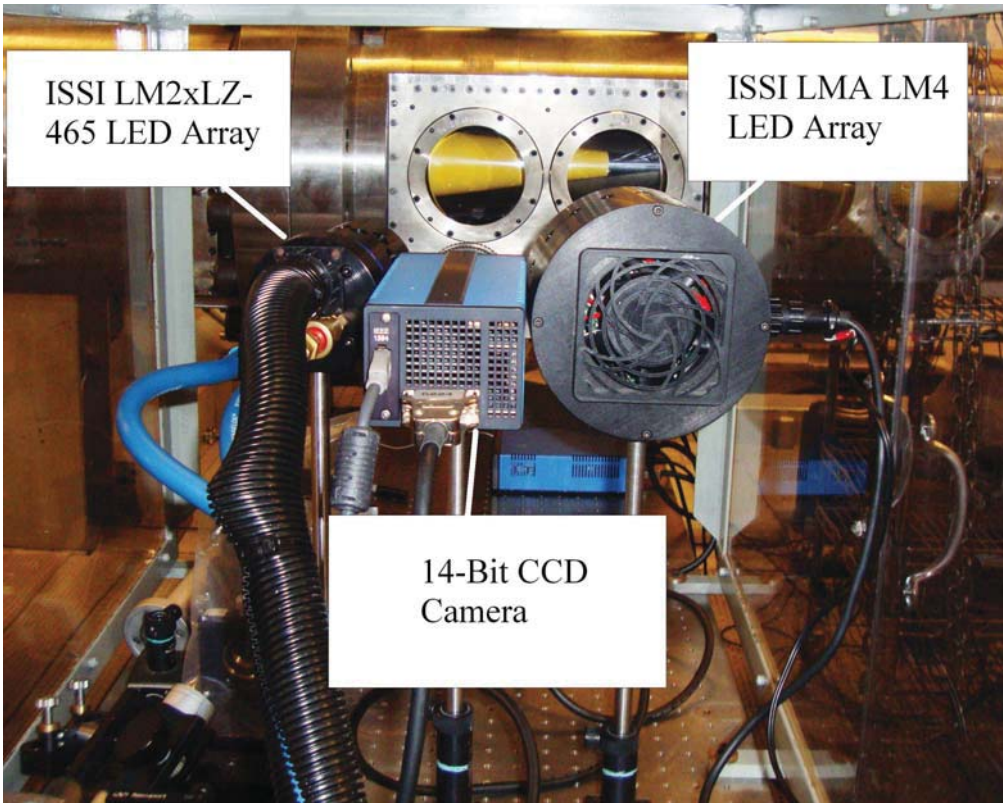

Figure 4: Experimental setup of the CCD camera and the 2 blue LED arrays.

.

3.2 Temperature-sensitive Paint Post-Processing

To convert the images from the CCD camera to temperature profiles, several steps are required. Three images of the model are captured. First, a dark image is taken with all the lights off. An "off" image is taken just before the run starts, with the LED lights on. Finally, an "on" image is taken during the run. In practice, many "on" images are taken during a run, up to 50 images per second. The three intensity images can then be converted to temperature with the following equation [8]:

$$\Delta T = f\left(\frac{I_{on} - I_{dark}}{I_{off} - I_{dark}}\right) \tag{1}$$

The function f can be any function (for example an exponential or polynomial) that fits the TSP calibration data over the desired working temperature range [8]. ΔT is the number of degrees Celsius the temperature is above the "off" or initial model temperature. The "off" temperature can be found several ways. One can go through the post-processing method, and compare an "off" image with an image taken when the model is at ambient temperature, and calculate how many degrees the "off" image is above the ambient image. Another method is to place a thermocouple somewhere on the model, preferable at the base in order to be non-intrusive. The latter method is preferred since the model temperature data during the run can also be collected. For all the cases presented, a thermocouple was present either at the base of the model or the base of the thermopile in the Schmidt-Boelter gauge.

By taking the ratio of the "on" and "off" images, this should theoretically remove any discrepancies in light uniformity since the same pixel is compared in the "on" and "off" images. In reality, when the BAM6QT starts, there is a slight shift in the model in the axial direction (on the order of 1–3 pixels). This means that a pixel will not necessarily have the same lighting conditions in the 'off" image compared to the "on" image. To reduce error caused by non-uniform lighting, the LED arrays are placed as far as possible from the tunnel window without sacrificing the TSP intensity.

The "off" and "on" images need to be aligned correctly due to the tunnel shift, and this was done through an image registration code provided by Dr. John Sullivan. This code uses the edges of the model to align the "on" and "off" images. Previous experiments in the BAM6QT used registration dots placed on the model to align the two images [13, 14, 15].

The TSP calibration was found using a linear fit to the data in Figure 3.13 of Reference [8]. The calibration curve is number 7 in the figure (Ru(bpy)) in Dupont ChromaClear). The details behind the calibration can be found in Reference [12]. After performing a linear fit and moving the reference temperature of -150°C to the initial model temperature, the following calibration was found:

$$\Delta T = (362 - T_{ref})\left(1 - \frac{I_{on} - I_{dark}}{I_{off} - I_{dark}}\right) \tag{2}$$

The calibration is good for temperatures between 15°C and 60°C (288-340 K).

4 Extracting Heat Transfer from Temperature-Sensitive Paint

Obtaining quantitative heat transfer from temperature-sensitive paints is the primary goal of the TSP project. A method was devised by Dr. John P. Sullivan of Purdue University to calibrate the TSP using data from Schmidt-Boelter (SB) heat transfer gauges [16]. A square patch of TSP is compared to the SB gauge. Ideally, the patch of TSP should be in a location where the heat transfer rate is the same as measured by the SB gauge. This is not always a trivial task especially when dealing with a three-dimensional flowfield. The local heat flux can be found using Fourier's law,

$$\dot{q} = -k\nabla T \tag{3}$$

where $\dot{q}$ is the local heat flux and k is the thermal conductivity of the insulating paint layer. Several assumptions need to be made to simplify Equation 3. It is assumed that the heat transfer is one-dimensional (in the wall-normal direction). It is also assumed that the temperature profile in the wall-normal direction across the insulating layer is linear. Finally, the temperature at the base of the insulator (model temperature, T_{model}) is assumed to be constant spatially and temporally during a run. This spatially uniform model temperature assumption was found to be accurate to within roughly 4% [11]. The temporally constant temperature over the course of a run (roughly 10 seconds) assumption was also shown to be valid in Figure 5.49 of Reference [11]. The first 10 seconds of a run showed negligible change in the model temperature. The only change in model temperature was roughly 10 seconds after tunnel unstart. Fourier's law can then be simplified to the following linear equation, incorporating the finite thickness of the insulating paint layer,

$$\dot{q} = \frac{k}{L}(T - T_{model}) \tag{4}$$

where L is the thickness of the insulating layer and T is the temperature of the surface during the run, obtained from the TSP. Finally, Equation 4 can be modified to include ΔT since all the TSP images can be calibrated to give ΔT,

$$\dot{q} = \frac{k}{L}(\Delta T + T_{ref} - T_{model}) \tag{5}$$

$$\Delta T = T - T_{ref} \tag{6}$$

where T_{ref} is the temperature of the model surface just before the run starts. The calibration method works by iterating T_{model} and k/L until good agreement is found between the TSP and a Schmidt-Boelter gauge on the model. A least-squares method was employed to find values for the two constants that produced the best fit between the calibrated TSP and the SB readings. According to the definitions of T_{model} and T_{ref} and the assumption of a constant model temperature during a run, these two temperatures should be nominally the same. However, T_{model} was chosen to best fit the data, regardless of how much it varied from T_{ref}.

In several plots, the non-dimensional heat transfer (Stanton Number) will be shown. The Stanton number is defined as

$$St = \frac{\dot{q}}{\rho_\infty u_\infty \left(H_0 - h_w\right)} \tag{7}$$

$$H_0 - h_w = \left(c_p T_\infty + \frac{u_\infty^2}{2}\right) - c_p T_w \tag{8}$$

where ρ is the density, u is the velocity, H is the total enthalpy, h is the enthalpy, T is the temperature and c_p is the specific heat. The subscript 0 is the total value, w is the model wall value and ∞ is the freestream value.

There are some inherent issues involved with obtaining quantitative heat transfer from the TSP in the BAM6QT. During tunnel startup, the model experiences significant heating. This large impulse of heating is thought to dissipate through the aluminium model before the run starts, but it is possible that the TSP might show some residual heating. The residual heating, if present, would cause problems in obtaining accurate heat transfer from the TSP. The low heat transfer in the BAM6QT also presents a problem. It may be difficult to obtain a good calibration if the range of heat transfer is low.

4.1 Theoretical Heat Transfer

The experimental heat transfer data obtained in the BAM6QT can be compared to a theoretical solution developed by Dr. John Sullivan of Purdue University, along with Dr. Tianshu Liu of Western Michigan University. The theoretical solution is only good for laminar flow. Dr. Sullivan developed a theoretical solution using both a similarity solution and a reference temperature method. The similarity equations for a compressible boundary layer can be found in Reference [17, 18]. The viscosity was modelled using the work of Lemmon and Jacobson [19]. The outer flow conditions were provided by solving the Taylor-Maccoll solution for conical flow [20]. For more information on the reference temperature method, refer to White [17]. One of the major uncertainties in determining the theoretical solution is deciding the initial wall (model) temperature. A constant and uniform wall temperature was assumed, and was taken as the measured model temperature before the run started. This is the same as T_{ref} in the TSP data reduction.

5 Paint Thickness Measurements

It is important to obtain an accurate measurement of the paint thickness to verify the assumption that the paint thickness is constant. A method to measure paint thickness on a curved surface was devised with an Elcometer 456 capacitance gauge. The raw numbers from the gauge are not necessarily accurate on a curved model surface since the capacitance gauge sensing surface is flat. As the curvature of the model surface increases, the error of the gauge increases. To test the accuracy of the gauge, a roll of 3M 471 vinyl tape was used, with a known thickness of 127 μm. The vinyl tape was first placed on a flat metallic surface. Placing the gauge at 10 random locations on the bare metallic surface gave an average reading of 0.6 μm. Thickness measurements were

then taken at 10 random locations on the vinyl tape, giving an average reading of 125 μm. The gauge appears to have a high accuracy when measurements are taken on a flat metallic surface.

The next test was done with the vinyl tape placed on a 7° half-angle cone. The tape was placed along the surface of the cone in the axial direction. Measurements of the tape thickness were taken at 4 inches to 15 inches from the nosetip, at 1 inch intervals. Measurements were then taken at the same axial positions on the bare surface of the cone. The results are shown in Figure 5. The red symbols are the thickness of the tape measured by the capacitance gauge. The green symbols are thickness measured by the gauge when it is placed on the bare aluminium surface of the cone. The gauge placed on the bare aluminium surface should theoretically give a thickness reading of zero, but error is introduced due to the curvature of the cone. Note that the error is greater the further upstream, since the curvature of the cone increases towards the nosetip. The non-zero thickness measured by the gauge when placed on a bare metallic surface will be referred to as the "thickness offset". The blue symbols are the offset thickness subtracted from the measured thickness. The black line is the actual thickness of the tape. The maximum error in the blue symbols from the actual thickness is about 6%. Note that the error in the offset subtraction method tends to gets larger near the nosetip due to the increase in the surface curvature.

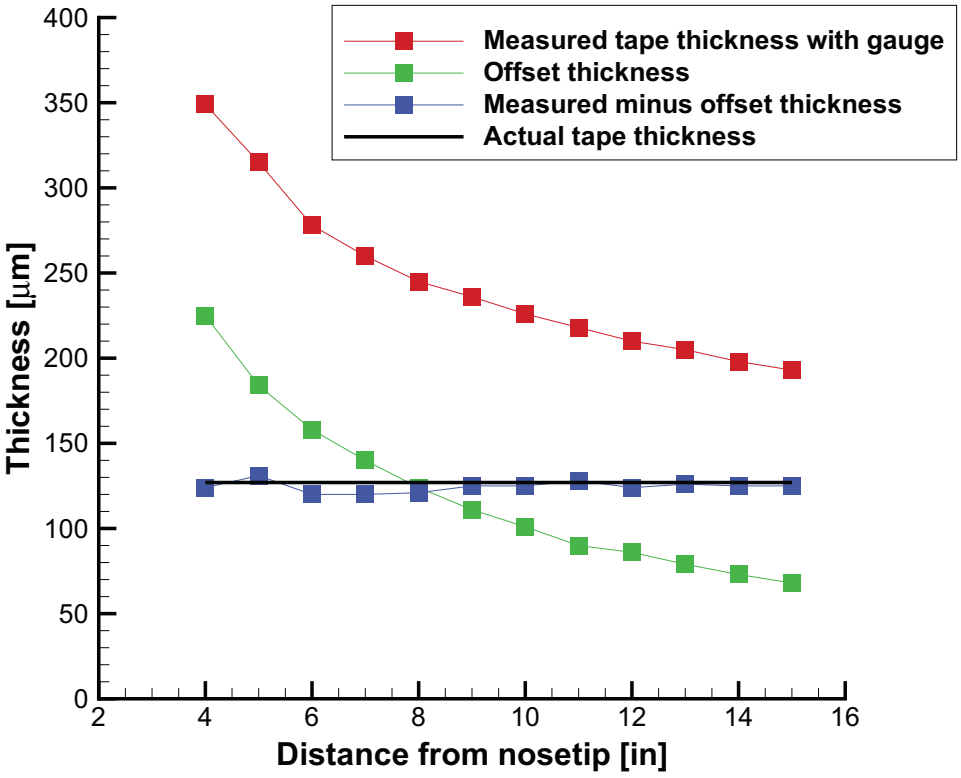

Figure 5: Measurements of tape thickness on the surface of a 7° half-angle cone.

.

6 Paint Feathering

In previous experiments [11, 21, 22], TSP was added to the frustum of the cone, with the nosetip removed. Therefore, when the nosetip was installed, there would be a forward facing step of about 200μm created by the addition of the TSP at the nosetip-frustum junction. The slope at this forward facing step was roughly 900–1200 μm/mm, utilizing a Mitutoyo surface roughness tester (Model number SJ-301) to obtain the measurements.

A new method of painting is used in the current set of experiments, where the paint is feathered at the leading edge. The nosetip is also left installed in the model during the painting process. The paint is sparingly added to the nosetip region, and then sanded down so there is a smooth gradual increase of paint thickness going from the bare upstream tip of the nose to the frustum. The slope measured with the surface roughness tester is typically near 5–10 μm/mm. This new paint feathering technique appears to have essentially eliminated the forward facing step created by the paint, but future tests need to be performed to confirm if in fact there is no residual effect created by this much reduced forward facing step.

7 Results

The first set of results to test the validity of the heat-transfer data-reduction method was measured in January 2011. The sensors used in this set of experiments are shown in Table 2.

Position	Gauge Name	Serial Number	Calibration Range
1	SB–A	168636	0–22 kW/m^2
2	SB–B	168635	0–22 kW/m^2
3	SB–C	167032	0–22 kW/m^2
4	SB–D	167034	0–22 kW/m^2
5	SB–E	168136	0–22 kW/m^2
6	SB–F	168633	0–22 kW/m^2

Table 2: Position and serial number of the Schmidt-Boelter heat transfer gauges for the January 2011 experiments.

Figure 6 shows the TSP image of an experiment performed under quiet flow at a stagnation pressure of 131 psia and a freestream Reynolds number of 9.9×10^6/m. The SB gauges can be seen along the model centerline as black dots. The TSP image shows a roughly uniform temperature distribution in the spanwise direction, which is to be expected. It also appears that the boundary layer is fully laminar since the TSP shows low, even heating. The higher heating near the nosetip is due to the thinner boundary layer.

A plot of the data collected from sensors SB–A and SB–F, along with the heat transfer calculated at the comparison patch of TSP is shown in Figure 7. The TSP and SB data were compared at roughly t = 0.2 s to t = 2 s. The fit is fairly good. Table 3 shows the values for k/L and T_{model} (from Equation 5) for sensors SB–A and SB–F. Note that the constants for the two sensors are different.

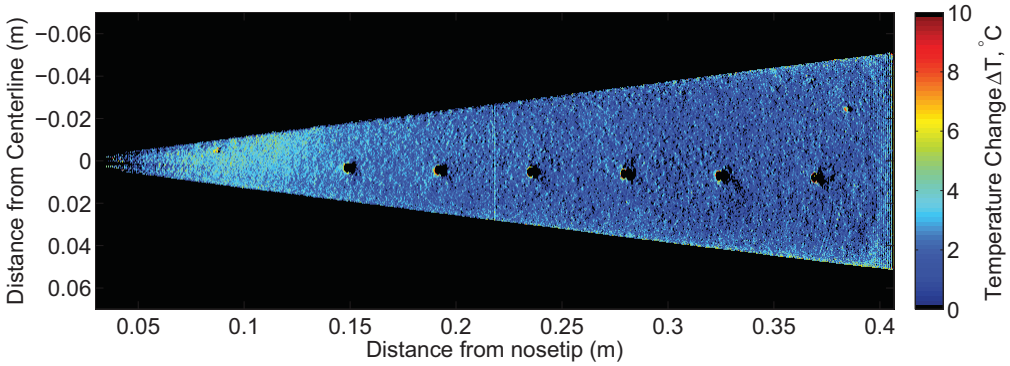

Figure 6: TSP image of the 7° half-angle cone at 0° angle of attack. p_0 = 131 psia, $\mathrm{Re}_\infty = 9.9 \times 10^6$/m. Quiet flow. January 2011 tests.

	k/L [W/K·m^2]	**T$_{model}$ [K]**
SB–A	1.16	300.9
SB–F	0.856	297.8

Table 3: Constants used in the linear fit converting the TSP temperature to heat transfer.

For each experiment the signal from three of the six SB gauges were amplified 100 times by three separate Stanford Research Systems SR560 low-noise voltage preamplifiers before being digitized by the oscilloscopes. The oscilloscopes were four channel Tektronix DPO7054 Digital Phosphor Oscilloscopes. For the January 2011 experiments, the SB gauges were sampled at 50 kHz. The scopes were operated in Hi-Res mode for all experiments. In Hi-Res mode, the scope samples 8-bit data at the maximum sampling rate and averages this data in real time to obtain 12-bit data at the desired sampling rate. Hi-Res mode decreases random noise and increases the vertical resolution.

Before each run, the tunnel is allowed to "settle" for 10-15 minutes after pressurizing the tunnel. Therefore the model should be in thermal equilibrium after this settling period, but the gauges typically gave a non-zero heat transfer. It was decided to shift the heat transfer data so that it would read 0.0 W/m^2 in the pre-run. The magnitude of this shift will be referred to as the "offset". The calibrated heat transfer is plotted along with the theoretical laminar heat transfer in Figure 8. In this figure, SB–D, SB–E and SB–F were amplified 100 times. The solid green and red lines represent the global heat transfer along the model centerline when calibrating the TSP using SB–A and SB–F respectively. Five pixels in the spanwise direction were averaged and a moving filter was utilized to produce the line plots. The `smooth` function in MATLAB was used, and the function is simply a moving average with a span of 10 pixels (in the streamwise direction). 1 pixel is approximately 0.15 mm. The solid squares in the figure are the heat transfer obtained from the SB gauges. The blue squares show the heat transfer with no offset subtracted, while the pink squares show the heat transfer with the pre-run offset subtracted.

Four of the six SB gauges (SB–A, SB–C, SB–D, and SB–E) are within 25% of the theoretical

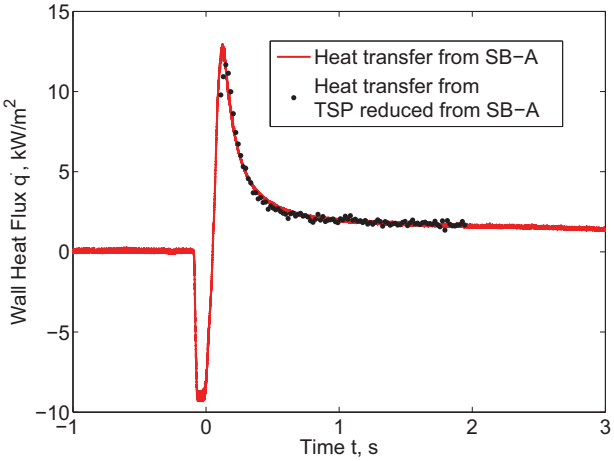

(a) SB–A

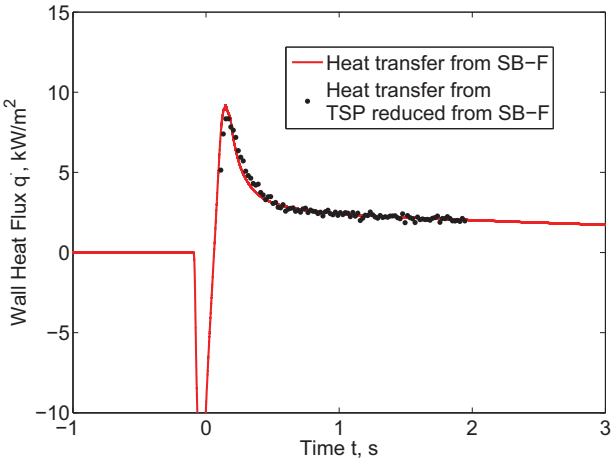

(b) SB–F

Figure 7: Plot of heat transfer from the SB gauge along with the heat transfer calculated at the comparison patch of TSP. p_0 = 131 psia, $\mathrm{Re}_\infty = 9.9 \times 10^6$/m. Quiet flow. January 2011 tests.

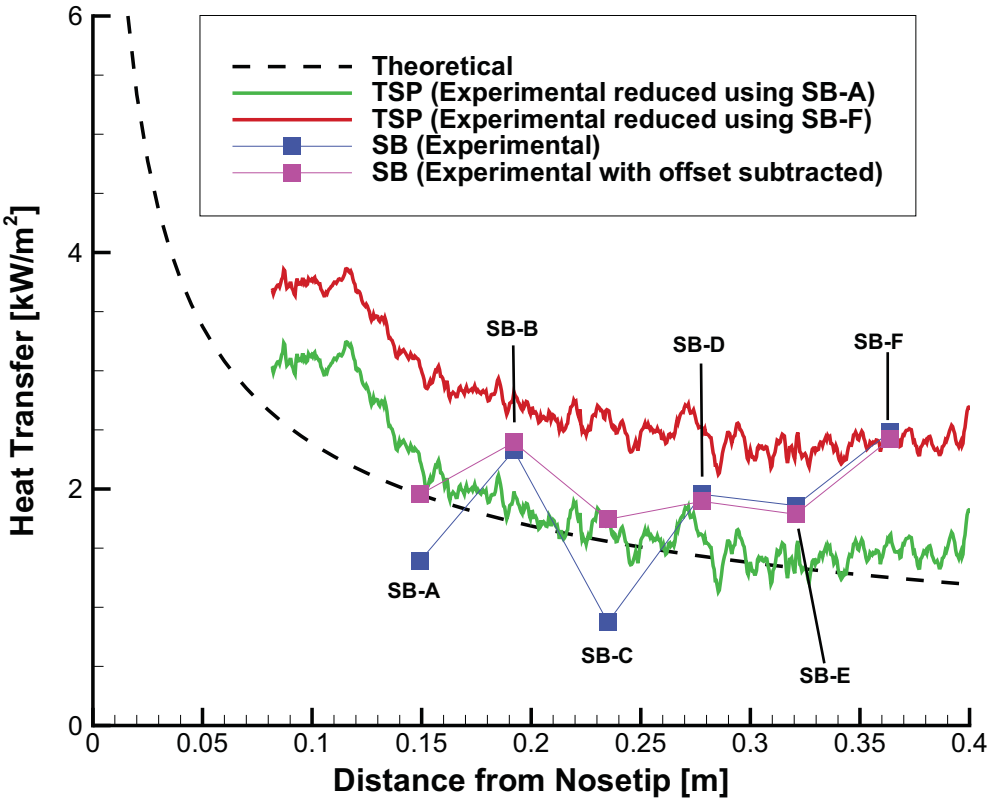

Figure 8: Heat transfer rates calculated from TSP with the reduction method and compared to theory. p_0 = 131 psia, $\mathrm{Re}_\infty = 9.9 \times 10^6$/m. Quiet flow. January 2011 tests.

.

heat transfer with the offset subtracted. SB–B is within 30% of the theory, and SB–F is within roughly 50% of the theory. Although this accuracy leaves much to be desired, it is difficult to make measurements of such low levels of heat transfer. The present measurements use only a small portion of the range of the most-sensitive SB gauges that are commercially available. For the three un-amplified SB gauges, the offset appears to have a significant impact on the calibrated heat transfer rates. If accurate data from the SB gauges are used to calibrate the TSP to heat transfer, the results are in good agreement with theory. However if the inaccurate data from the last SB gauge is used, the red curve shows poor agreement with theory.

The discrepancy between the reduced and theoretical data also tends to increase upstream of the first sensor. This may be due to the breakdown of the assumptions made to reduce Fourier's law to a linear relationship. For example, it was assumed that the model temperature is spatially uniform, but this may not be true approaching the nosetip. But, most likely the reason for the discrepancy is the feathering of the paint near the nosetip. The TSP is thinner because of the sanding in this region near the nosetip, so this data should be ignored.

A set of tests were done at a lower Reynolds number (7.9×10^6 /m) to see if the linear reduction method and the heat transfer from the gauges would produce similar results. These tests were also performed in January 2011. Figure 9 shows the TSP image at a freestream Reynolds number of 7.9×10^6 /m and a stagnation pressure of 103 psia. Once again the boundary layer appears to be fully laminar since the TSP shows low even heating.

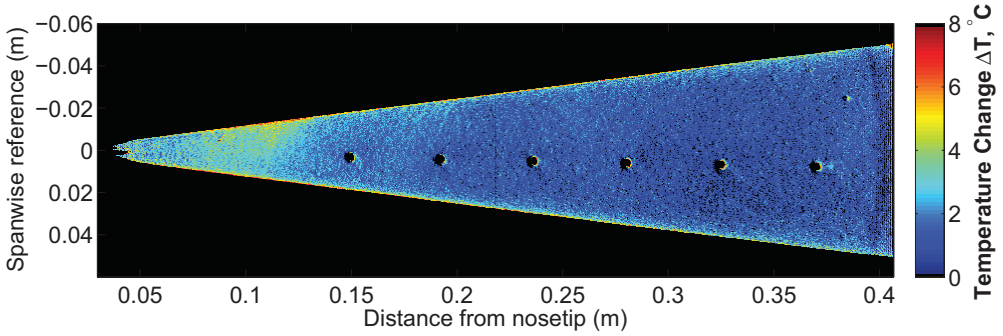

Figure 9: TSP image of the 7° half-angle cone at 0° angle of attack. p_0 = 103 psia, $\mathrm{Re}_\infty = 7.9 \times 10^6$/m. Quiet flow. January 2011 tests.

A plot of the data collected from the sensor SB–A at this lower Reynolds number, along with the heat transfer calculated at the comparison patch of TSP is shown in Figure 10. The TSP and SSB data were compared at roughly t = 0.2 s to t = 1.2 s. The entire heat transfer peak near t = 0.0 s is not used in the heat transfer reduction method, because the assumption of a spatially uniform model temperature is probably not valid right at tunnel start up. The data was also not used near t = 2.0 s, where an increase in heat transfer is seen. This is due to the nozzle-wall boundary layer

separating. It is unclear how the flow conditions change when this occurs. The curve fit algorithm creates good agreement between the reduced heat transfer and the heat transfer from the SB gauge.

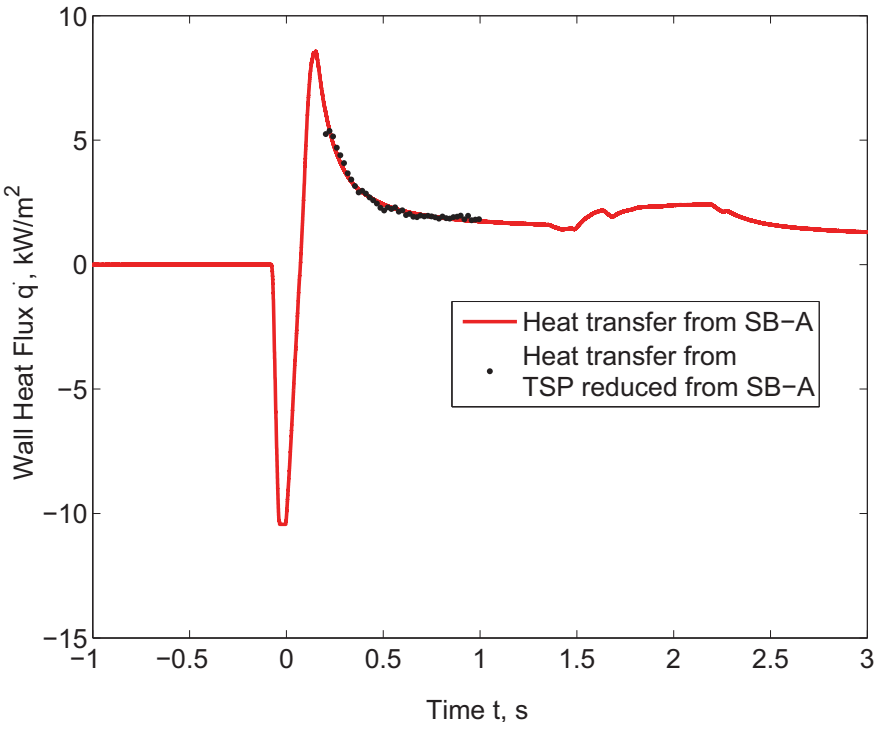

Figure 10: Plot of heat transfer from the SB gauge along with the heat transfer calculated at the comparison patch of TSP. p_0 = 103 psia, $\mathrm{Re}_\infty = 7.9 \times 10^6$/m. Quiet flow. January 2011 tests.

The calibrated heat transfer is plotted along with the theoretical laminar heat transfer in Figure 11. In this figure, SB–A, SB–B and SB–C were amplified 100 times. Once again, the solid green and red lines represent the global heat transfer along the model centerline when calibrating the TSP using SB–A and SB–F respectively. The same `smooth` function in MATLAB was used to filter the line plots. The solid squares in the figure are the heat transfer obtained from the SB gauges. The blue squares show the heat transfer with no offset subtracted, while the pink squares show the heat transfer with the pre-run offset subtracted. The results are similar to the results presented in Figure 8. If an inaccurate gauge is used to calibrate the TSP, the calibration is inaccurate (red curve). If an accurate gauge is used to calibrate the TSP, the calibration agrees well with the theory (green curve).

Another set of experiments were performed during the same January 2011 entry at roughly the same Reynolds number (9.9×10^6/m) to examine the effect of amplifying different SB gauges. Figure 12 shows the heat transfer from the SB gauges for four different tests, along with the theoretical heat transfer. Table 4 shows the specifics of each test.

When the SB gauge is not amplified, subtracting the offset seems to give good agreement with the amplified gauge. Therefore, if no amplifiers are available, simply subtracting this pre-run offset

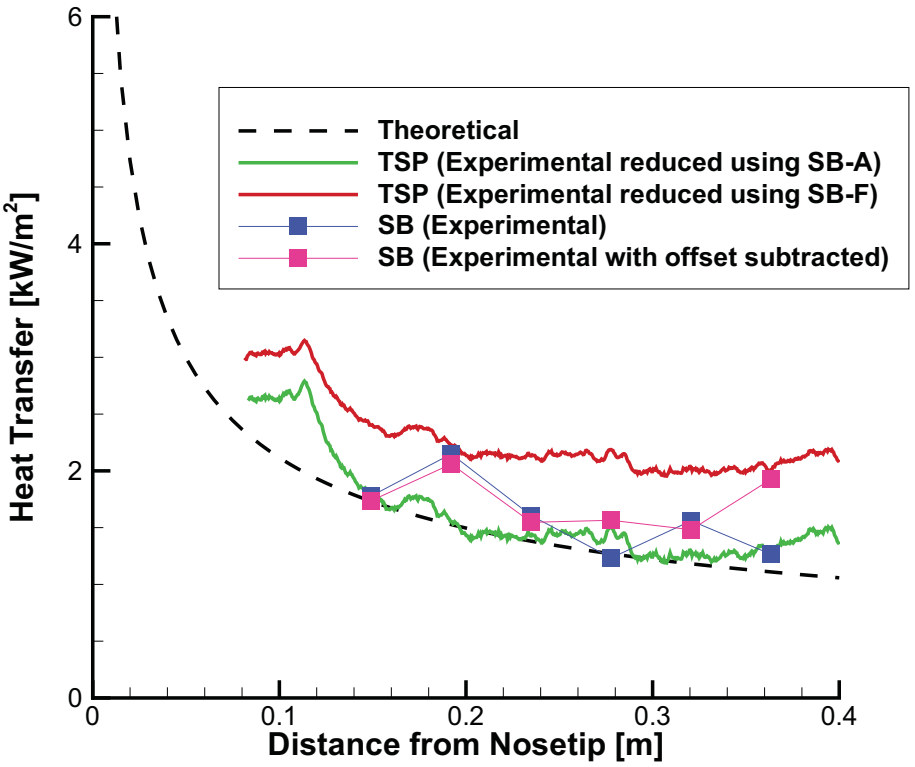

Figure 11: Heat transfer rates calculated from TSP with the reduction method and compared to theory. p_0 = 103 psia, $\mathrm{Re}_\infty = 7.9 \times 10^6$/m. Quiet flow. January 2011 tests.

seems to work well. Also note that SB–B and SB–F consistently read significantly higher heat transfer than the theory. This seems to suggest that there is some inherent error with the gauges, or that the calibration is not precise, since swapping the electronics still yields these inaccurate readings.

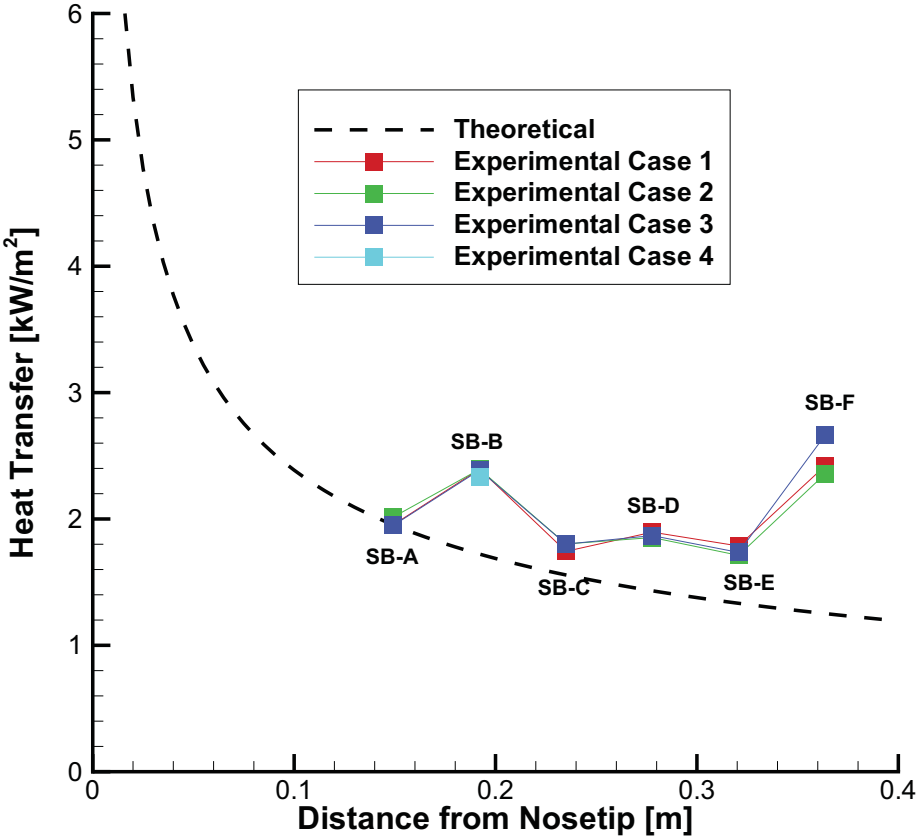

Figure 12: Heat transfer rates with different SB gauges amplified. p_0 = 131 psia, $\mathrm{Re}_\infty = 9.9 \times 10^6$/m. Quiet flow. All data shown with pre-run offset subtracted. January 2011 tests.

.

A second set of experiments were performed in April 2011 with some of the sensor positions swapped and some sensors replaced. This was done to see if SB–B in the previous tests would still produce inaccurate readings, and if SB–A and SB–E would still yield accurate readings. The gauges used in this set of experiments are shown in Table 5. Note that the gauges in positions 1, 2 and 5 from the January 2011 tests (Table 2) have been moved to positions 2, 5 and 6 respectively.

The April 2011 experiments were performed under quiet flow at a stagnation pressure of 131 psia, and a freestream unit Reynolds number of 9.9×10^6/m. The heat transfer from the SB gauges along with the theoretical heat transfer is shown in Figure 13. Three of the six sensors appear to give accurate readings. SB–B once again shows heat transfer higher than the theory. SB–E shows

Test	Notes
Case 1	SB–D, SB–E and SB–F amplified 100 times.
Case 2	SB–A, SB–B and SB–C amplified 100 times.
Case 3	no SB gauges amplified.
Case 4	only SB–B collecting data and not amplified.

Table 4: Specifics of each test looking at the effect of amplification on SB gauges. January 2011 tests.

fairly accurate heat transfer readings during both set of experiments. Finally, SB–A gave accurate readings in the January 2011 experiments, but was inaccurate in the April 2011 experiments. It is not clear why SB–A now provides inaccurate heat transfer data.

Position	Gauge Name	Serial Number	Calibration Range
1	SB–G	169256	0–11 kW/m^2
2	SB–A	168636	0–22 kW/m^2
3	SB–H	169251	0–11 kW/m^2
4	SB–I	169255	0–11 kW/m^2
5	SB–B	168635	0–22 kW/m^2
6	SB–E	168136	0–22 kW/m^2

Table 5: Position and serial number of the Schmidt-Boelter heat transfer gauges for the April 2011 experiments.

These two set of experiments show that the linear reduction of heat transfer from the TSP agrees well with the theory, if the SB gauge used in the reduction process is accurate. The experiments showed that roughly half the SB gauges were within 25% of the theoretical heat transfer. Since the linear reduction method is heavily dependent on the gauge used for the calibrations, it was decided that the factory calibrations should be verified. Several SB gauges were sent back to the Medtherm Corporation in August 2011 for recalibration, including SB–E and SB–F. The new calibrations only differed by 0.5%. Therefore, an error in the calibrations does not appear to be the reason for the higher than theoretical heat transfer readings from these gauges. Unfortunately, at the time of these tests, the step created by the sensor was not measured. It will be shown in Section 8 that this step can have a significant impact on the measured heat transfer.

8 Effect of Gauge Height and Sampling Rate on Measured Heat Transfer

It was suggested by Dan Lewis of the AEDC Tunnel 9 that the Schmidt-Boelter gauges should be sampled at a lower frequency [23]. Previously, the gauges were sampled at 50 kHz. The SB gauges do not have a very high frequency response, therefore sampling at such a high rate was not

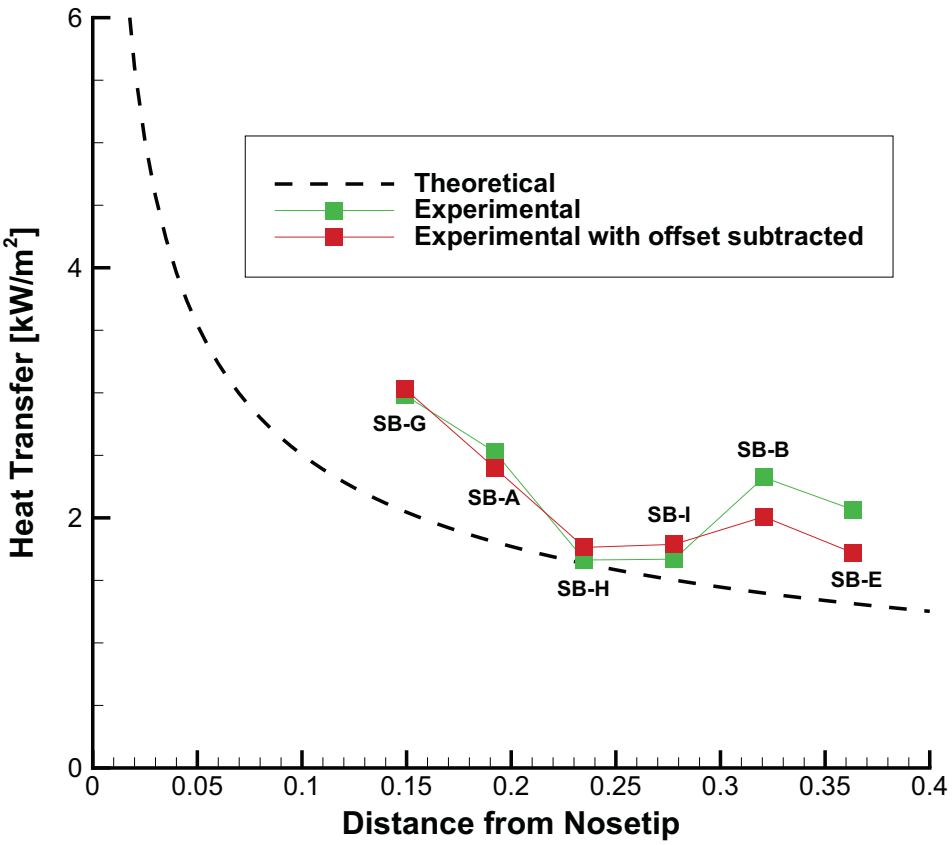

Figure 13: Heat transfer rates with SB gauges swapped. p_0 = 131 psia, $\mathrm{Re}_\infty = 9.9 \times 10^6$/m. Quiet flow. All data shown with pre-run offset subtracted.

necessary. The lower sampling rate also allows for more averaging thereby reducing random noise in the SB output signal. It was decided to sample at 50 Hz. In hindsight this might be too low of a sampling rate because the peak in heat transfer at tunnel start up is not fully captured. Capturing this peak may prove to be useful for future data processing.

Experiments were performed in August and September 2011, looking at the effect of lowering the sampling rate. Table 6 gives the gauge model numbers for these set of tests. The first set of tests did not produce good results, with many of the gauges showing heat transfer more than 20% above the theoretical heat transfer (Case 1 in Figure 14). Figure 14 shows the non-dimensional heat transfer plotted against axial distance along the cone. It was noticed that several of the gauges in Case 1 were not flush with the cone. The last gauge was protruding by roughly 300 μm. It was decided to remove the model from the tunnel, and fix the last gauge. The last gauge was pushed down, reducing the step to about 30μm. Case 2 in Figure 14 shows that the furthest downstream gauge is in better agreement with the theoretical heat transfer. This is an expected result, as a gauge protruding into the boundary layer would most likely measure a higher heat transfer than a gauge flush with the surface. Note that the first four gauges agree very well between Cases 1 and 2. Also note that the 5th gauge was broken during the second model installation, so no data was gathered from this gauge for Case 2.

It was then decided to reinstall all the Schmidt-Boelter gauges. Table 7 lists the steps created by the each gauge for each case. The steps were measured using a Mitutoyo surface roughness tester (Model number SJ–301) All the gauges were installed as flush as possible for Case 3, using a small ruler to push down the gauge until it was flush with the surface and the ruler was lying flat on the surface of the cone. The ruler was held in place for roughly 1 minute to allow the nail polished used to fix the gauge to dry slightly. Case 3 in Figure 14 shows the heat transfer obtained from this third test. Five of the six gauges are within 20% of the theoretical heat transfer. The Stanton number is plotted here because each case had a different model temperature, allowing for an easier comparison between the three cases. It is not clear what had a greater impact, the lower sampling rate allowing for more noise to be removed, or the gauges being as close to flush with the surface as possible. The author believes that having a flush gauge is more important, but regardless both measures should be taken in future tests. Only SB–E shows heat transfer more than 20% above the theoretical, even though in the January and April 2011 tests this gauge gave more accurate results. This gauge will be sent back to the Medtherm Corporation in October 2011 to check the calibration.

The TSP image for Case 3 is shown in Figure 15. The boundary layer is most likely laminar since the TSP shows a low even level of heating. Figure 16 shows the heat transfer reduced from the TSP using SB–C for Case 3, along with the heat transfer obtained from the six heat transfer gauges and the theoretical heat transfer. Once again, the linear heat transfer reduction method works well. The reduced heat transfer agrees well with the theoretical if the gauge also agrees with the theory. Figure 17 shows the heat transfer from SB–C over the course of a run, along with the calibrated TSP at the comparative patch. The curve fit algorithm does not seem to have issues when the gauge remains laminar. Issues tend to arise when the boundary layer transitions [11], and it is not yet clear how well the linear reduction method works in a case where transition is present.

Position	Gauge Name	Serial Number	Calibration Range
1	SB–C	167032	0–22 kW/m^2
2	SB–L	164576	0–11 kW/m^2
3	SB–I	169255	0–11 kW/m^2
4	SB–D	167034	0–22 kW/m^2
5	SB–E	167036	0–22 kW/m^2
6	SB–J	169254	0–11 kW/m^2

Table 6: Position and serial number of the Schmidt-Boelter heat transfer gauges for the August-September 2011 experiments.

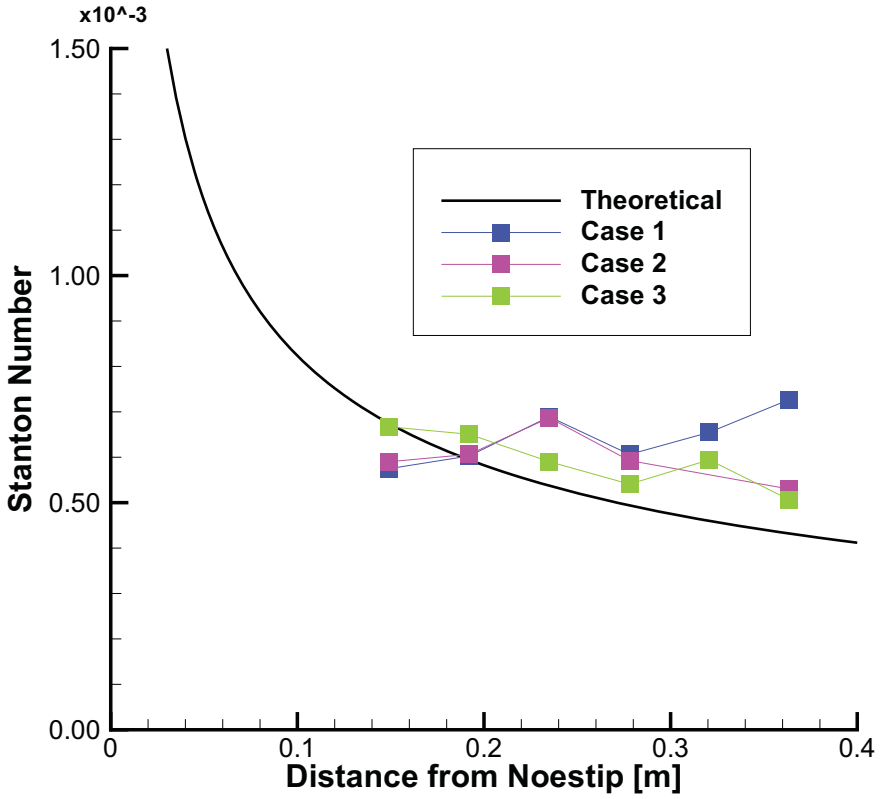

Figure 14: Heat transfer from SB gauges with varying protuberance heights into the boundary layer. $p_0 = 131$ psia, $\mathrm{Re}_\infty = 9.9 \times 10^6$/m. Quiet flow. All data shown with pre-run offset subtracted. August-September 2011 experiments.

Position	Gauge Number	Case 1 Step	Case 2 Step	Case 3 Step
1	SB–C	-10μm	-10μm	+8μm
2	SB–L	-26μm	-26μm	-10μm
3	SB–I	+40μm	+40μm	+5μm
4	SB–D	-26μm	-26μm	-19μm
5	SB–E	-10μm	-10μm	+10μm
6	SB–J	+300μm	-30μm	+5μm

Table 7: Step created by the heat transfer gauges for the August-September 2011 experiments.

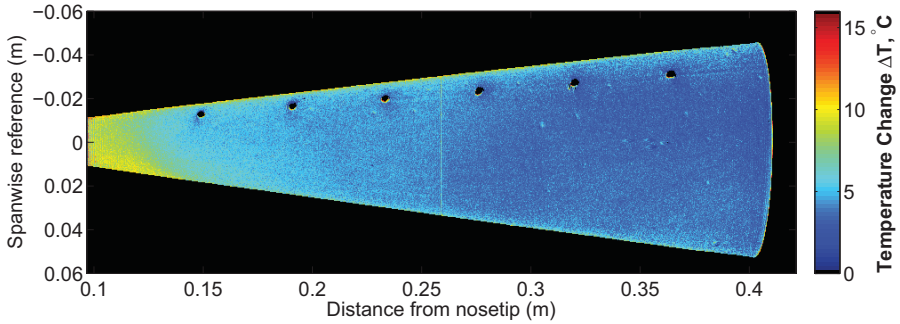

Figure 15: TSP image of the 7° half-angle cone at 0° angle of attack. Case 3 from Figure 14. p_0 = 131 psia, $\mathrm{Re}_\infty = 9.9 \times 10^6$/m. Quiet flow. August-September 2011 experiments.

.

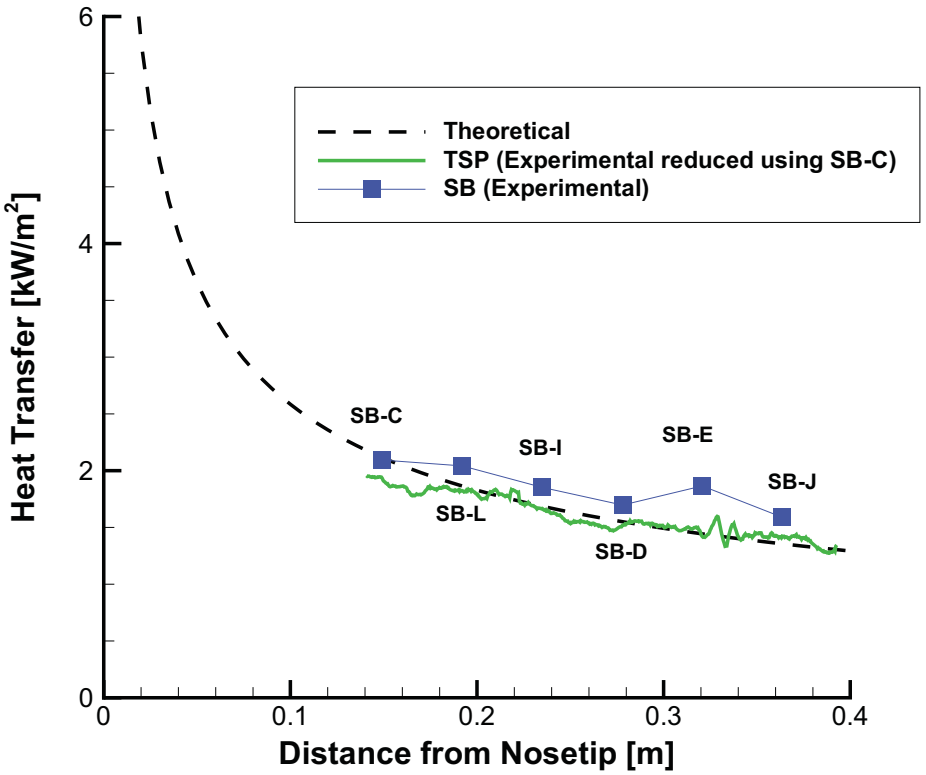

Figure 16: Heat transfer rates calculated from TSP with the reduction method and compared to theory. p_0 = 131 psia, $\mathrm{Re}_\infty = 9.9 \times 10^6$/m. Quiet flow. All data shown with pre-run offset subtracted. August-September 2011 experiments.

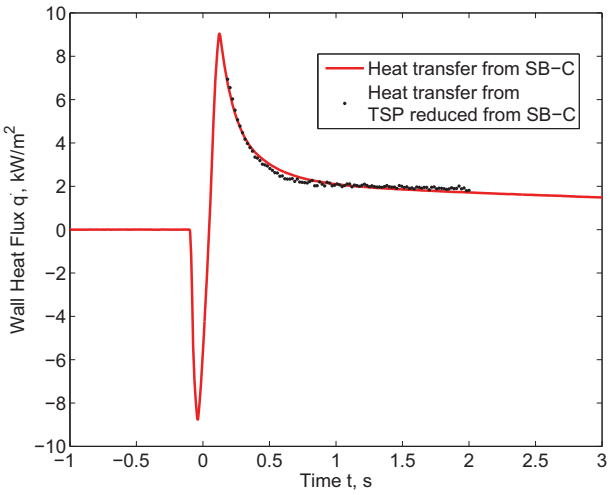

Figure 17: Plot of heat transfer from SB–C along with the heat transfer calculated at the comparison patch of TSP. Case 3 from Figure 14. p_0 = 130 psia, $\mathrm{Re}_\infty = 9.9 \times 10^6$/m. Quiet flow. August-September 2011 tests.

9 Reducing Heat Transfer Using Known Paint Thickness and Model Temperature

The final set of tests presented in this report examined the possibility of calibrating the TSP to heat transfer using the measured paint thickness and the measured model temperature. For this case, T_{model} and T_{ref} are assumed to be equal; therefore the heat transfer equation reduces to

$$\dot{q} = \frac{k}{L}\Delta T. \tag{9}$$

According to Dr. Tianshu Liu, the thermal conductivity (k) for the insulating paint is between 0.21 and 0.50 W/m-K, with a typical value being 0.25 W/m-K [24]. The paint thickness was measured using an Elcometer 456 capacitance gauge and the method discussed in Section 5. The average paint thickness in the June 2011 tests was 277μm, with a $\pm$15% variation from the average. The August-September tests had an average thickness of 201μm with a $\pm$5% variation from the mean.

Figure 18 shows data from the June 2011 tests, with the heat transfer calibrated from the TSP with the linear reduction method (green curve). This plot also shows the heat transfer calculated with the known paint thickness, thermal conductivity and model temperature (red and turquoise curve). The turquoise curve is the lower limit of the calculated heat transfer assuming the paint thickness is 15% below the mean, and the red curve is assuming the paint thickness is 15% above the mean. From this plot, it can be seen that the calibration method needs to be anchored with a SB gauge due to the larger error in the red and turquoise curves. It is not clear if the error is largest in the estimated thermal conductivity, the measured model temperature or the measured

paint thickness.

Figure 19 shows the results from the August–September 2011 tests. This plot shows the same results. The heat transfer calculated from the known paint thickness, model temperature and thermal conductivity yielded heat transfer levels 2–3 times higher than the theory. Once again, the calibration method needs to have a Schmidt-Boelter gauge to anchor it.

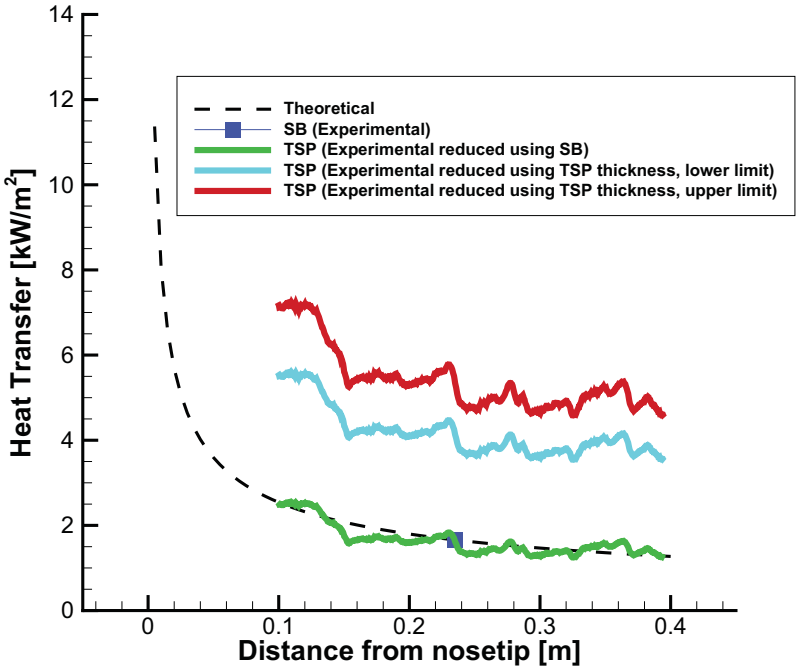

Figure 18: Heat transfer rates calibrated from TSP with the linear reduction method and known paint thickness and model temperature. p_0 = 131 psia, $\mathrm{Re}_\infty = 9.9 \times 10^6$/m. Quiet flow. June 2011 tests.

10 Issues with Schmidt-Boelter Heat Transfer Gauges

There have been many difficulties experienced by the author in the 8 months of testing. Obtaining accurate heat transfer data from the Schmidt-Boelter gauges proved to be difficult. This section will outline the measures taken by the author to obtain the most accurate heat transfer data from these gauges.

An offset in the Schmidt-Boelter output voltage was found before each run, when the heat transfer should have been zero. The offset only appears when the gauges are plugged into the oscilloscopes, and not a multimeter, suggesting there is some sort of feedback or ground loop causing this error. The magnitude of the offset was found to shift temporally, and depended on

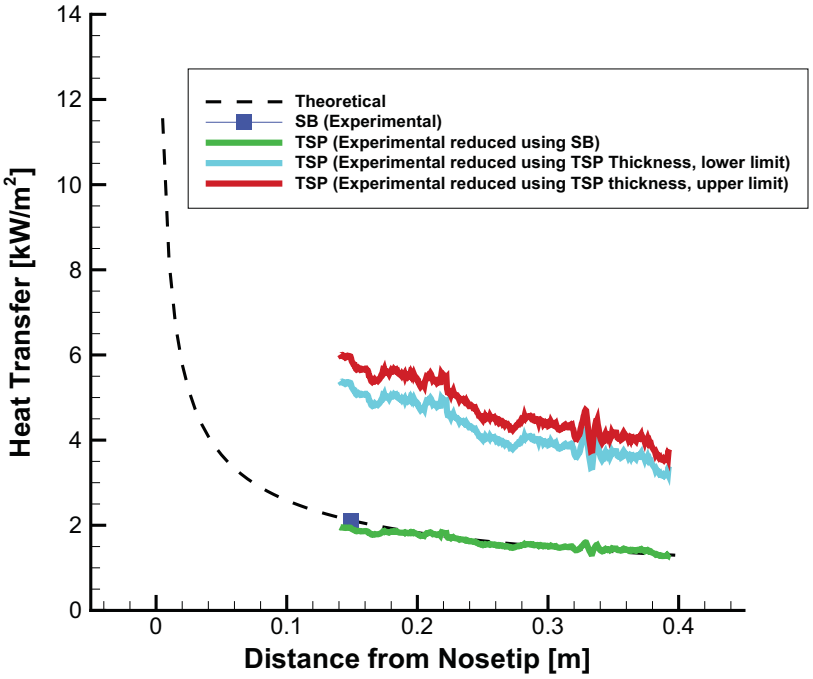

Figure 19: Heat transfer rates calculated from TSP with the reduction method and known paint thickness and model temperature. p_0 = 131 psia, $\mathrm{Re}_\infty = 9.9 \times 10^6$/m. Quiet flow. August-September 2011 tests.

how many amplifiers were being used. Over a period of roughly 60 seconds, the offset appeared to not shift, and therefore the offset could be taken as a constant over the course of a run. The offsets were found to be systematic errors, and could be subtracted from the output voltage. It is also advantageous to amplify the Schmidt-Boelter gauges. Not only does this help minimize the effect of the offset, it allows for a better resolution of the small voltage changes during a run. The SR560 amplifiers also included an analogue filter. It is suggested to set this filter to a 300-Hz low-pass filter. The filter would help remove any high frequency noise, but still allow for the peak heating during tunnel startup to be captured.

Upstream of the nozzle, the air is heated by a 2000-amp DC current running through the driver tube. This large current resulted in a significant offset in the DC voltage of the SB and thermocouple gauges when the model was in electrical contact with the tunnel. Gilbert designed a nylon sting adapter that separated the model electrically from the rest of the tunnel [25]. Since the author did not use a nylon sting adapter, the heaters were deactivated before the run, and reactivated after the run finishes. Deactivating the heaters allowed for the DC offset in the gauges to be minimized, but would not completely remove the offset.

It is extremely important to get the SB gauges as flush as possible with the model surface. If the gauge is protruding by as little as 30 μm or more, this can create an error of 20% or more in heat transfer. The author used a simple method of using a small ruler to push down the gauge until the gauge was flush with the model surface, and the ruler was lying flat on the surface. The ruler was left in place for roughly 1 minute, allowing the nail polish that holds the sensor in place to partially dry. If some nail polish slides up the side of the gauge onto the face of the gauge and the painted surface of the cone, it is possible to remove the nail polish with some acetone. Care is needed when removing this nail polish, since the acetone will also remove some of the paint, and may remove some of the black epoxy on the surface of the gauge.

In previous experiments, the SB gauges were sampled at 50 kHz by the oscilloscope. In future experiments, it is suggested that the gauges are sampled near 500 Hz. It is not necessary to sample the gauges at the 50 kHz frequency, since the gauges frequency response is not that high, and it would make sense to sample the gauges at the same rate as the CCD camera. The lower sampling rate also allows for more averaging of the signal, helping to remove random noise. Sampling at 500 Hz should also allow for the peak in heat transfer at tunnel start up to be captured.

11 Concluding Remarks

Experiments were done to validate a linear calibration method for obtaining quantitative heat transfer from temperature-sensitive paint. The experiments were performed with a 7° half-angle sharp cone at 0° angle of attack, where the theoretical heat transfer solution is known (under laminar flow). The model was equipped with 6 SB heat transfer gauges, and the linear heat-transfer reduction procedure agreed well with the theory if the SB gauges were accurate. After several measures were taken including removing random noise and amplifying the heat transfer gauges, five of six gauges agreed well with the theoretical heat transfer. It is not clear why the 6th gauge was inaccurate; a new calibration is currently being obtained.

Attempting to calibrate the TSP to heat transfer using measurements of the paint thickness,

model temperature and an estimate of the thermal conductivity of the insulating paint did not produce the desired results. Currently the method still requires a SB gauge to anchor the calibrations. Although the method only requires one SB gauge, the author would suggest installing at least two because it is not clear if every gauge can produce reliable and accurate results.

References

[1] Steven P. Schneider. Laminar-Turbulent Transition on Reentry Capsules and Planetary Probes. *Journal of Spacecraft and Rockets*, 43(6):1153–1173, November-December 2004.

[2] Steven P. Schneider. Hypersonic Laminar-Turbulent Transition on Circular Cones and Scramjet Forebodies. *Progress in Aerospace Sciences*, 40:1–50, 2004.

[3] Sandy C. Tirtey. *Characterization of a Transitional Hypersonic Boundary Layer in Wind Tunnel and Flight Conditions*. PhD thesis, Von Karman Institute for Fluid Dynamics, Brussels, Belgium, August 2006.

[4] M. Morkovin. Critical Evaluation of Transition from Laminar to Turbulent Shear Layers with Emphasis on Hypersonically Travelling Bodies. Air Force Flight Dynamics Laboratory Rep. AFFDL-TR-68-149, April 1969.

[5] Dennis C. Berridge. Measurements of Second-Mode Instability Waves in Hypersonic Boundary Layers with a High-Frequency Pressure Transducer. Master's thesis, Purdue University School of Aeronautics & Astronautics, West Lafayette, IN, December 2010.

[6] H. Reed, W. Saric, and D. Arnal. Linear Stability Theory Applied to Boundary Layers. *Annual Review of Fluid Mechanics*, 28:389–428, 1996.

[7] Medtherm Corporation. Personal Communication - Phone Call, October 2010.

[8] T. Liu and J. Sullivan. *Pressure and Temperature Sensitive Paints*. Springer, 1st edition, 2005.

[9] Di Peng, James W. Gregory, Jim Crafton, and Sergey Fonov. Development of a Two Layer Dual-Luminophore Pressure Sensitive Paint for Unsteady Pressure Measurements. AIAA Paper 2010-4918, June 2010.

[10] Matthew P. Borg. *Laminar Instability and Transition on the X-51A*. PhD thesis, Purdue University School of Aeronautics & Astronautics, West Lafayette, Indiana, August 2009.

[11] Christopher Ward. Hypersonic Crossflow Instability and Transition on a Circular Cone at Angle of Attack. Master's thesis, Purdue University School of Aeronautics & Astronautics, West Lafayette, IN, December 2010.

[12] Tianshu Liu, Bryan T. Campbell, Steven P. Burns, and John P. Sullivan. Temperature and Pressure-Sensitive Luminescent Paints in Aerodynamics. *Applied Mechanics Review*, 50(4):227–246, 1994.

[13] Bradley M. Wheaton. Roughness-Induced Instability in a Laminar Boundary Layer at Mach 6. Master's thesis, Purdue University School of Aeronautics & Astronautics, West Lafayette, IN, December 2009.

[14] Shin Matsumura. Streamwise Vortex Instability and Hypersonic Boundary-Layer Transition on the Hyper-2000. Master's thesis, Purdue University School of Aeronautics & Astronautics, West Lafayette, IN, August 2003.

[15] Thomas J. Juliano. *Instability and Transition on the HIFIRE-5 in a Mach-6 Quiet Tunnel*. PhD thesis, Purdue University School of Aeronautics & Astronautics, West Lafayette, Indiana, August 2010.

[16] John P. Sullivan. Extracting Heat Transfer from TSP. Personal Communication - Email, May 2010.

[17] Frank M. White. *Viscious Fluid Flow*. McGraw-Hill, 1st edition, 1974.

[18] Tianshu Liu. Comparison of Calculated and Measured Heat Transfer in Hypersonic Laminar Flows on Cones. Unpublished Report, April 2009.

[19] E. W. Lemmon and R. T. Jacobson. Viscosity and Thermal Conductivity Equations for Nitrogen, Oxygen, Argon and Air. *International Journal of Thermophysics*, 25(1):21–69, 2004.

[20] John D. Anderson. *Computational Fluid Mechanics and Heat Transfer*. McGraw-Hill Book Company, 1st edition, 1984.

[21] Dennis C. Berridge, Amanda Chou, Christopher A.C. Ward, Laura E. Steen, Peter L. Gilbert, Thomas J. Juliano, Steven P. Schneider, and Joel E. Gronvall. Hypersonic Boundary-Layer Transition Experiments in a Mach-6 Quiet Tunnel. AIAA Paper 2010-1061, January 2010.

[22] Christopher A.C. Ward, Bradley M. Wheaton, Amanda Chou, Peter L. Gilbert, Laura E. Steen, and Steven P. Schneider. Boundary-Layer Transition Measurements in a Mach-6 Quiet Tunnel. AIAA Paper 2010-4721, June 2010.

[23] AEDC Tunnel 9 Dan Lewis. Personal Communication, October 2010.

[24] Tianshu Liu. Personal Communication - Email, October 2011.

[25] Peter L. Gilbert. Effect of Tunnel Noise on Laminar Stagnation-Point Heating at Mach 6. Master's thesis, Purdue University School of Aeronautics & Astronautics, West Lafayette, IN, August 2010.

Appendix I–A: Painting and Data Acquisition Method

This appendix will lay out the method used by the author to paint the models and measure accurate heat transfer data with the Schmidt-Boelter (SB) heat transfer gauges.

- The model is first prepped for painting. The surface is cleaned with acetone and any sensor holes are plugged with cylindrical stainless steel dowels. The nosetip is left installed in the model.

- Four coats of the LustreKote White Primer spray paint are applied to the surface, waiting approximately 3 minutes between coats. Paint is added sparingly near the nosetip region, creating a smooth transition from the bare nosetip to the full thickness of the paint. The relative humidity should be maintained low in the room while painting, or the paint will not dry properly. The relative humidity was typically held around 40% in the summer, and 20% in the winter.

- Typically the paint is not sanded after the application of the White Primer unless the paint layer is significantly uneven. If sanding is needed, the paint should be allowed to dry for 24 hours. 700 grit sandpaper is used first and the dowel pins are removed. The sandpaper is fixed to a small piece of wood. The sandpaper is coated with water, and sanding is done in the streamwise direction.

- Four coats of the LustreKote Jet White spray paint is applied after allowing the White Primer to dry for 24 hours (if sanding the White Primer was needed, the Jet White can be added directly after sanding). Once again, paint is added sparingly in the nosetip region.

- The Jet White paint is allowed to dry for 24 hours, and at this point the paint is sanded. The paint is wet sanded first with 700 grit sandpaper fixed to small piece of wood. Sanding is done in the streamwise direction. The paint is then wet sanded with 1000 grit sandpaper, once again in the streamwise direction. If additional sanding is desired, 2000 or 3000 grit sandpaper can be used.

- Four coats of the temperature-sensitive paint is now applied. The luminophore molecules are 99.95% Tris(2,22-bipyridine) dichlororuthenium(II) Hexahydrate (Ru(bpy)), or Ru(bpy) for short. For every 12 mg of the Ru(bpy), 10 mL of ethanol is needed to dissolve the molecules. The Ru(bpy) dissolved in ethanol is then added to 20 mL of Urethane Clearcoat. The Urethane Clearcoat used is BASF LIMCO LC4000. Finally, the BASF LIMCO LHM activator is added. The bottle of the activator calls for a 4:1 ratio of Clearcoat to activator. The author adds approximately 10% more activator since the TSP will be slightly harder when fully dried. This is desirable when sanding the TSP.

- The author suggests waiting at least 24 hours before sanding the TSP, but it is better to wait 48 hours. The TSP is wet sanded with the same procedure as mentioned earlier.

- The sensors are installed using nail polish. The sensors are made flush with the model surface by slowing pushing down on them with a small ruler, until the ruler lies flat on the model surface. The ruler is left in place for approximately a minute, allowing the nail polish to partially dry.

- Proper setup of the oscilloscopes is necessary to remove a lot of random noise. The SB gauges should be sampled near 500 Hz. This sampling rate is low enough to remove random noise, but high enough to capture the initial peak in heat transfer at tunnel start up. The scopes should be set to acquire in hi-res mode, and the scopes should be grounded to the tunnel. The heaters used to heat the air in the driver tube should be deactivated before the run, and reactivated after the run.

- The SB gauges should be amplified before being digitized by the oscilloscopes. If available, the sensor output should also be filtered by a 30-Hz low-pass filter.

- The author captured TSP images at 50 images per second. This high frame rate is not required for the heat transfer reduction method. Tests have been performed with a frame rate of 25-30 Hz with good results.

Appendix II:

Analytical and Numerical Inverse Methods for Temperature Sensitive Paint Heat Flux Measurements in Hypersonic Tunnels

Abstract

This report documents the development of temperature sensitive paint (TSP) technique for global quantitative heat flux measurements in the Boeing/AFOSR Mach-6 Quiet Tunnel (the Ludwieg tube) at Purdue University. The general characteristics of the Ludwieg tube are described and the relevant issues in TSP measurements are identified. The one-dimensional (1D) analytical and numerical inverse heat transfer methods are developed, which particularly take the effect of a polymer layer (TSP/insulator) on heat flux calculation into account. The uncertainty analysis is given, and the accuracy of these methods in extracting heat flux from TSP images is critically evaluated through simulations and experiments in hypersonic wind tunnels.

Further, to correct the lateral heat conduction effect, the image deconvolution method is developed based on a convolution-type integral equation with a Gaussian filter (kernel) that relates a heat flux field obtained by using the 1D inverse heat transfer method on a surface to the true heat flux field. It is coupled with the 1D inverse heat transfer method to calculate more accurate heat flux fields by correcting the lateral heat conduction effect and removing a random noise in TSP measurements. The accuracy of the deconvolution method is evaluated and the standard deviation in the Gaussian filter is determined for different materials through simulations.

The data-processing procedure based on these methods is used to calculate heat flux distributions on a model from a time sequence of TSP images of a 7-deg-half-angle circular metal cone acquired in the Ludwieg tube. It is found that the historical effect of the warming-up process of a model in sequential runs becomes significant and it must be corrected by in-situ calibration to obtain accurate heat flux distributions. After this historical effect and the effect of the non-uniform coating thickness are corrected, the TSP-derived heat flux distributions on the cone are in good agreement with those given by the similarity solution and the reference temperature method. The simple methods to determine the coating thickness distribution from TSP measurements at the start-up process of the Ludwieg tube are developed. The error sources in TSP heat flux measurements in the Ludwieg tube are discussed. Although this work focuses on TSP heat flux measurements in the Ludwieg tube, the developed methods are generally applicable to other hypersonic wind tunnels.

Table of Contents

1. The Purdue Mach-6 Quiet Tunnel and Temperature Sensitive Paint Measurement

1.1. General Characteristics and Issues

Temperature sensitive paints (TSP) have been used effectively to obtain qualitative information, such as transition location and vortex features, in the Boeing/AFOSR Mach-6 Quiet Tunnel (the Mach 6 Ludwieg tube) at Purdue University (Schneider et al. 2003, Matsumura et al. 2003, 2005, Swanson 2008, Casper et al. 2008). The objective of the current work is to improve the quantitative heat transfer measurements and enhance the detection transition, vortices and separation. The Ludwieg tube is shown in Fig. 1.1. Construction of this tunnel was completed in 2001, and it has been running quiet flow since 2005.

To run the tunnel, high pressure air at an elevated temperature (about 433 K) is added from the left side of Fig. 1.1. The valve is located downstream of the contraction and nozzle, and the test area contains the model. The 113 m^3 vacuum tank is brought down to roughly 1-3 kPa before each run, depending on the stagnation pressure. For quiet runs, the boundary layer on the contraction wall is removed via the bleed slots. Typical characteristic properties of the tunnel can be found in Table 1.1. The low value of surface heat flux and the subsequent small changes in surface temperature make quantitative TSP heat flux measurements in the Ludwieg tube challenging.

Initiation of supersonic flow involves complex three dimensional, unsteady shocks and expansion waves. When the diaphragm breaks, an expansion wave travels upstream and then reflects between the end of the driver tube and the contraction. The pressure drops with each reflection, until it decreases to the point that the tunnel unstarts. Run times of three to five seconds are typical. The Ludwieg tube has an additional effect because of the differential heating along the tube. The contraction and driver tube, upstream of the nozzle, are heated but the test section and model are not. Therefore, the initial expansion wave during the start-up cools the test section and model, and this is followed by heating as the hot gas from upstream enters the test section. Such a large oscillating change in heat flux in the start-up is unusual in hypersonic tunnels, and it is the result of the downstream valve which is necessary but unusual. In addition, determining accurate heat flux usually requires that a model be in thermal equilibrium just prior to tunnel start and that the model temperature is accurately known. For the first run of the day, these conditions are satisfied, but at the end of the run transonic flow in the tube leads to high heat flux and the model warms up considerably. The model cools during preparation for the next run and also during the pump-up for the run. A good method for calculating heat flux from TSP measurements in the Ludwieg tube must cope with these issues.

During the course of the project, the following issues have been identified as contributing to errors in the heat flux measurement. The order of the following list represents our current opinion of the order or importance of the issues.

a. Start-up of the Ludwieg tube,
b. Unstable model boundary/initial conditions,
c. Pressure sensitivity of TSP,
d. Thickness non-uniformity of insulator/paint (multi-layer coatings),
e. Multiple scattering within stainless steel test section and filter leakage,
f. Variation in material properties,
g. Preconditioning of paint,

Qualitative information for TSP has been very valuable in the past and continues to be very useful, but accurate measurements of heat flux had not been made. This report explains efforts made by Purdue University and Western Michigan University to improve the quantitative measurement of heat flux. This report will present the contributions to all of the issues and results from tests of the 7^o-half-angle circular cone.

Table 1.1. Characteristics of the Mach 6 Ludwieg Tube

Total Pressure P_o	300 psia
Total Temperature T_o	160°C
Re/ft	3.0 E+06
Runtime	≈ 5 seconds
On a 7-deg Cone	
ΔT on Nylon Cone	~10° C
ΔT on Aluminum Cone	~2°C
Heat Flux	~1000 W/m^2
Stanton Number	~ 3.0 E-04
Recovery Temperature	104 C
Skin Friction Coefficient	4.730E-04
Skin Friction	11.042 Pa

1.2. Start-up of the Ludwieg Tube

The start-up of a Ludwieg tube, following diaphragm burst, involves complex three dimensional, unsteady shocks and expansion waves. The Purdue Ludwieg tube has an additional effect to the differential heating along the tube as depicted in Fig. 1.1. The main part of the tube, upstream of the nozzle, is heated but the test section and model are only slightly heated by convection and conduction. Thus, the initial expansion wave during the start-up cools the test section and model, which is followed by heating as the hot gas from upstream enters the test section.

A one-dimensional (1D) explicit finite difference numerical model of thin insulating layer on a semi-infinite material has been implemented in Matlab. The model can be used for analysis, given the surface heat flux, or data reduction, given the surface temperature from TSP. The model is used to simulate the Ludweig tube start-up effect on the temperature distribution in a single Mylar insulating layer on an aluminum model representing the Hyper 2000 tests. The input heat flux to the finite difference thermal model of the paint, insulating layer and aluminum wind tunnel model during the start up was matched to times from the previous Pitot probe measurements and the amplitudes chosen to match the temperature decrease and temperature increase during the start-up transient. The heat flux after the transient start is determined by a reference temperature method and includes the decrease in heat flux due to the decreasing total pressure P_o and total temperature T_o. In order to match the TSP measurements an initial negative heat flux 10 times the steady value for 0.07 seconds followed by a positive heat flux 16 times steady state value for 0.25 seconds is needed as shown in Fig. 1.2. The numerical model then matches the TSP very well as shown in Fig. 1.3. The temperature distribution in the insulating layer/TSP at various times is shown in Fig. 1.4. During the start-up transient there is significant variation in the temperature distribution. The estimated time constant for the layer is about

$\tau = l^2 \pi / 4\alpha \approx 1.9\ s$ The temperature in the layer at 5 seconds is monotonic as expected. The start-up of the Ludwieg tube gives a different initial condition than that in a typical hypersonic tunnel.

1.3. Unstable Model Boundary/Initial Conditions

Determining accurate heat flux requires that the model be in thermal equilibrium just prior to tunnel start and that the model temperature is accurately known. For the first run of the day these conditions are true but at the end of the run, transonic flow in the tube leads to high heat flux and the model warms up ~12°C. The model cools during preparation for the next run and also during the pump-up for the run. Figure 1.5 shows these temperature changes during the day of 10-19-2009. This should not be a problem if the model is thermally stable and temperatures are known but reduction of the TSP data to obtain heat flux shows the non-physical shifts in the data after the first run of the day. This issue will continue to be looked at and in the mean time an *in-situ* method described later is used to obtain quantitative data.

1.4. Pressure Sensitivity of TSP

The pressure sensitivity of TSP is relatively unknown. Ruthenium-based luminophores are susceptible to the effects of pressure through oxygen quenching. This is highly undesirable for TSP as pressure effects will reduce the quality of the data taken. A binder which is oxygen impermeable must be chosen. It had been presented by Matsumura et al. (2003) that TSP (specifically Ru(bpy) in a polyurethane binder) did show an effect due to an increase in pressure as seen in Fig. 1.6. Knowing the true variations of TSP intensity due to an increase in pressure is highly desirable.

A series of experiments have been performed in an effort to determine the pressure sensitivity of TSP. Up to this point, Ru(bpy) has been considered in an automotive clear coat. Future experiments will also analyze EuTTA in dope. In the first set of experiments, Ru(bpy) is exposed to pure oxygen. Ru(bpy) interacts with oxygen based on the partial pressure. In atmospheric conditions, the partial pressure of oxygen is around 20%. Pure oxygen would therefore register as 5 times as much pressure as that of normal air. This exposure to pure oxygen would be equivalent to that of a large pressure change. Clear coat (which is mostly oxygen impermeable) is typically used as the binder for Ru(bpy) for just this reason.

In the experiment, pressurized oxygen was run through 50 ft copper tubing placed in a room temperature water bath to bring the oxygen close to that of room temperature. A blue LED excited an aluminum sample treated with Ru(bpy) in clear coat and the data was recorded using a CCD camera. The results are displayed in Fig. 1.7. The small upward trend in change in temperature could result from a temperature difference in the ambient and the water. The results show virtually no sensitivity to oxygen.

Experiments have also been performed placing a sample in a viewing window of a pressure chamber, as seen in Fig. 1.8. The pressure chamber was connected to shop air through a gate valve. The chamber was then brought up to 95 psig and maintained at this pressure for at least five minutes in order for the system to return to an equilibrium state. The pressure chamber was returned to atmospheric pressure over the period of roughly 80 minutes. This slow drain resembled an isenthalpic process, in which the temperature showed relatively no change (see Fig. 1.9). The thermocouple indicated a change of less than 0.3°C during the duration of the test which could be attributed to changing conditions within the room. The sample was treated with Ru(bpy) and was excited by a UV light and the images were recorded using a CCD camera.

Each frame was divided by a control frame taken at ambient conditions to give a ratio of intensities. As the temperature remains mostly constant during this experiment, the ratio of the intensities should remain close to one. Figure 1.10 displays the results from this experiment. The data from the experiment indicates a change in intensity of roughly 7.5% which correlates to a change in temperature of the paint of about 2.5°C for a sample of Ru(bpy). This change in intensity of the paint is due to the pressure as the temperature is held almost entirely constant.

The results in the pressure chamber are different from the oxygen tests and if verified will need to be eliminated with a different binder or taken into account in the data reduction. It is very important to determine the effects of pressure on TSP. The experiments presented above indicate what is necessary to determine the true impact of pressure sensitivity on TSP.

1.5. Thickness Non-Uniformity of Insulator/Paint

In the case of an aluminum model with a thin TSP/insulating layer, the heat flux derived from TSP measurements is approximately proportional to the TSP/insulator thickness. The tests of 10-19-2009 used an aluminum cones with a LusterKote insulating layer and a Ru(bpy) in clearcote for the TSP. The paint thickness along a ray of the cone was measured by using a Capactec Model HPS-75 cylindrical probe with an amplifier. The cone was mounted on a milling machine table and scanned under the probe which was mounted in the tool holder. Results for are shown in Fig. 1.11. The paint distribution pattern shows a similarity to the heat flux distribution and the thickness data will be included heat flux calculations. Also, we will explore other methods of measuring the thickness distribution using optical and heat flux methods.

1.6. Multiple Scattering within Stainless Steel Test Section and Filter Leakage

The inside of the Ludwieg tube test section is polished stainless steel so multiple reflections of the emitted luminescence from the TSP are detected by the CCD camera. In addition the strong reflections of the incident LED light leak through the CCD camera filter. It is clear from many tests that both of these effects are contributing to errors but the extent and importance is not known yet but will be explored in the future.

1.7. Variation in Material Properties

The thermal properties of TSP/insulator are dependent of temperature, which should be taken into account in heat flux calculation when heat flux is large. Some possible methods of measuring the properties of the TSP and insulating layer will be explored.

1.8. Preconditioning of paint

Past results from Campbell et al. (1994) showed that the polymer in the TSP undergoes a change during the first time the paint is heated that changes the calibration. Subsequent heating and cooling cycles are stable and give the same calibration curve. In may be necessary to heat the model prior to the first Ludwieg tube run.

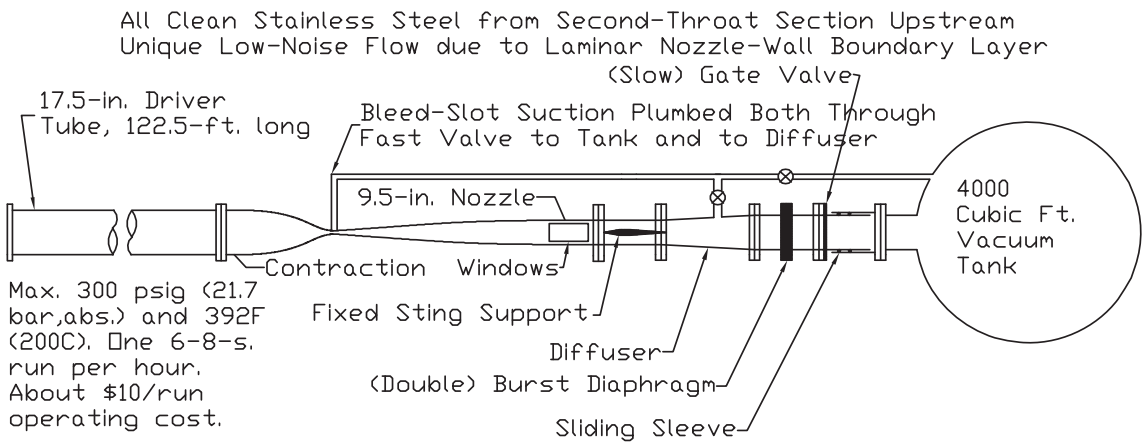

(a)

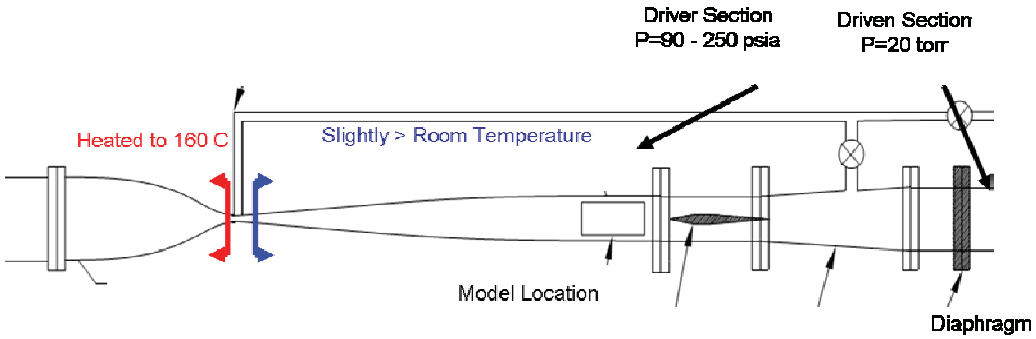

(b)

Figure 1.1. Schematic of the Purdue Ludwieg tube, (a) the overall view and (b) close view of the test section

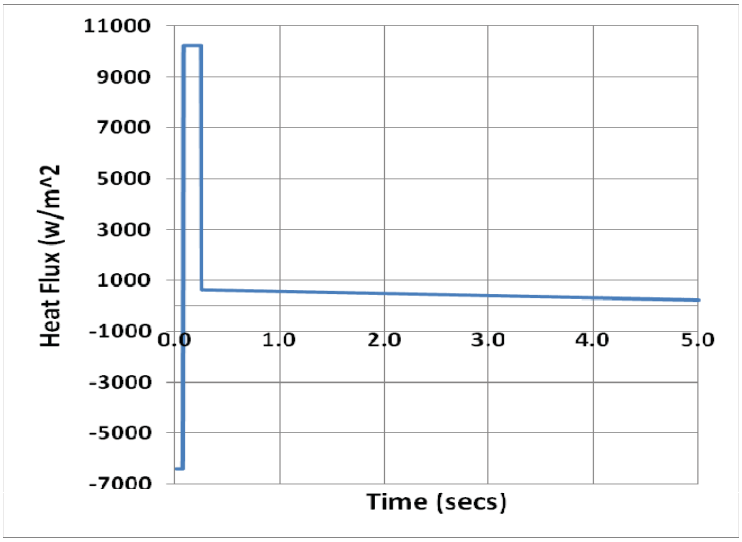

Figure 1.2. Input heat flux to the Hyper 2000 model during a Ludwieg tube run

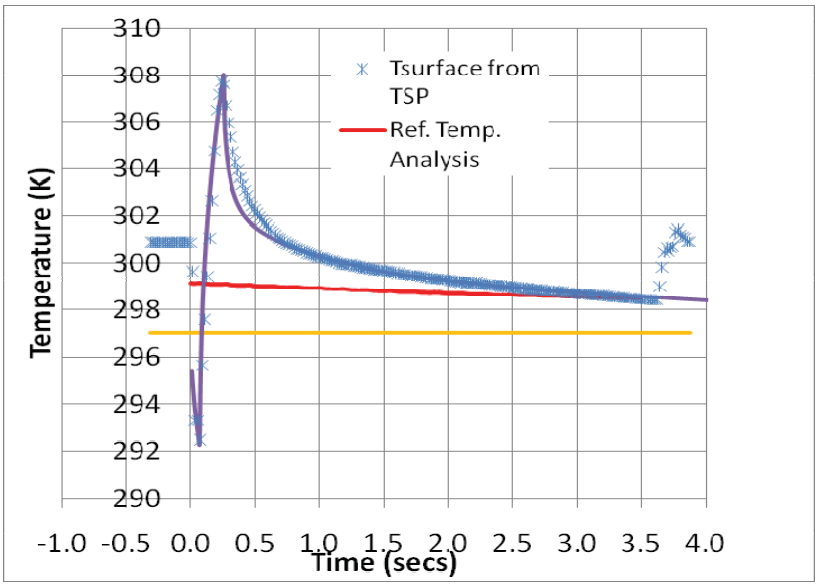

Figure 1.3. Comparison of the 1D explicit finite difference numerical model of surface temperatures and TSP measurements on the Hyper 2000 model at x/L= 0.5

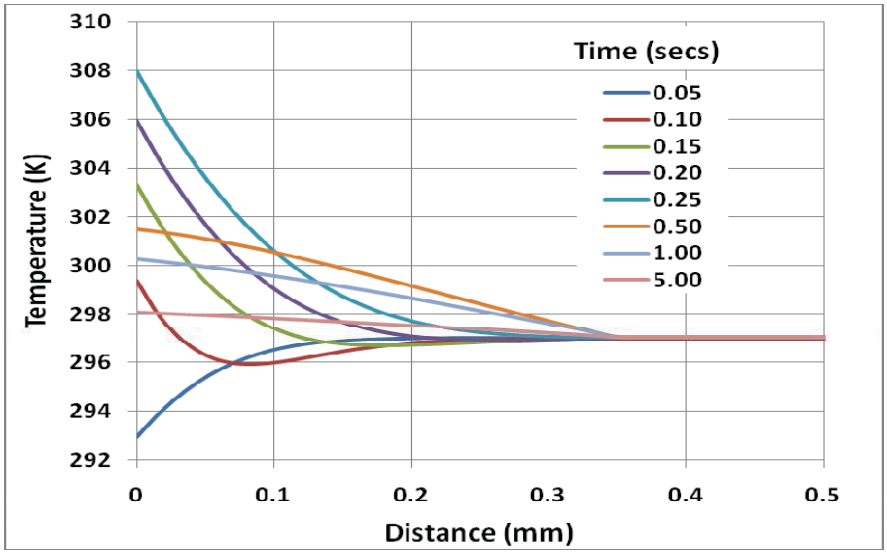

Figure 1.4. The effects of the Ludwieg tube start-up on the temperature distribution throught the thickness of the paint

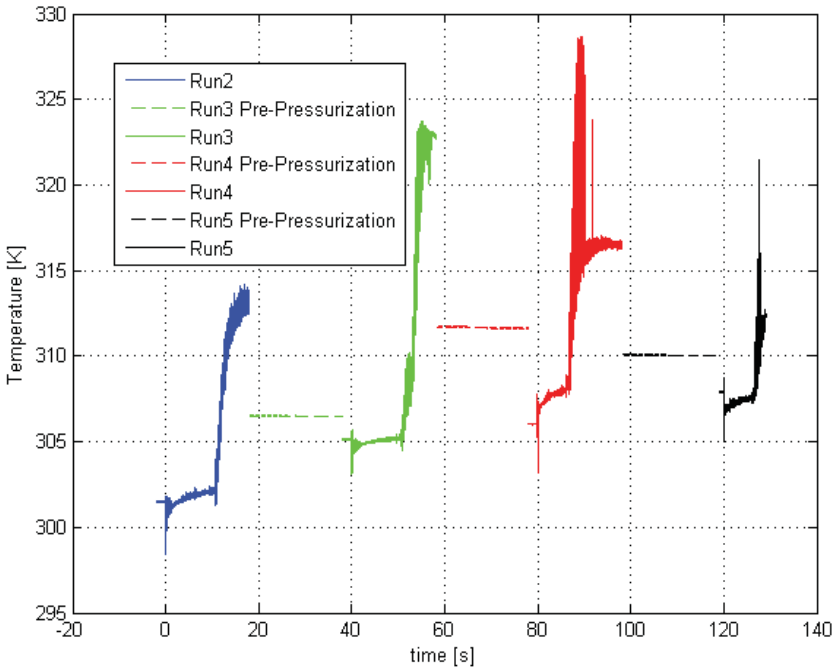

Figure 1.5. Model base temperature changes over several runs, where the times for these runs are listed in Table 5.1

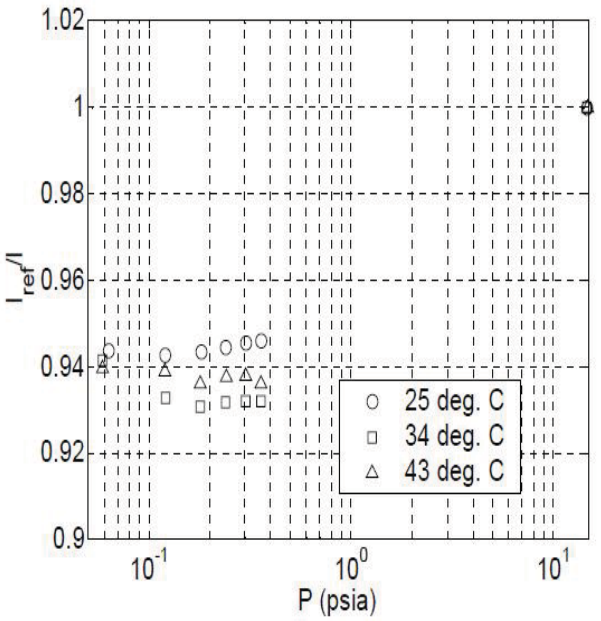

Figure 1.6. Sensitivity of Ru(bpy) in a polyurethane binder at varying temperatures and pressures (Matsumura et al. 2003)

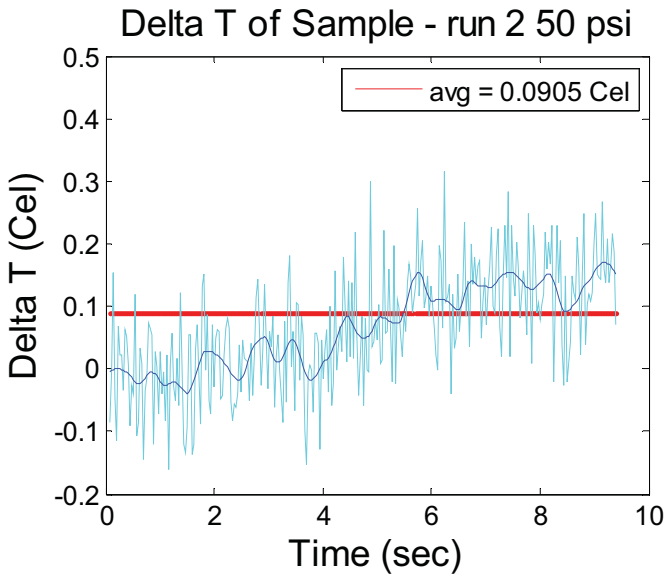

Figure 1.7. Oxygen exposure experiment

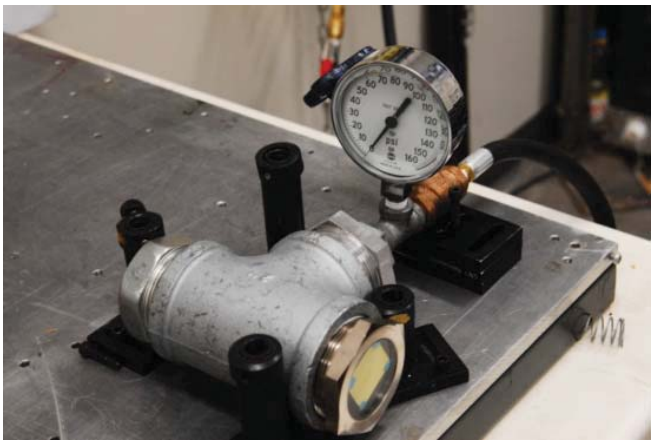

Figure 1.8. Pressure chamber

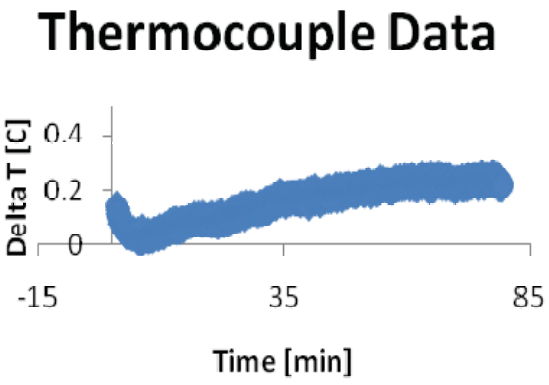

Figure 1.9. Data from thermocouple mounted on sample inside the pressure chamber

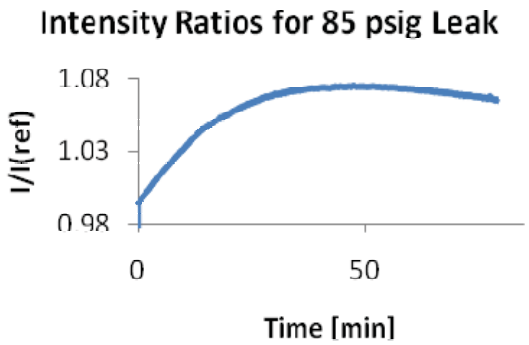

Figure 1.10. TSP intensity data recorded using a CCD camera during a leak of the pressure chamber starting at 95 psig

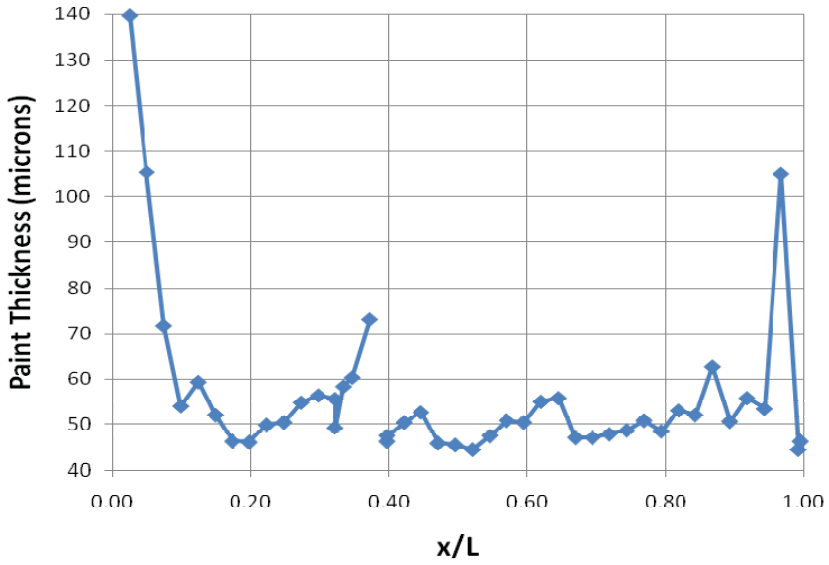

Figure 1.11. Paint thickness distribution along a conical ray corresponding to Runs 1-5 of tunnel entry 10-19-2009

2. 1D Analytical Inverse Heat Transfer Method

This chapter describes the analytical method used for temperature sensitive paint (TSP) measurements to obtain quantitative global heat flux diagnostics in hypersonic tunnels. An exact inverse solution of the one-dimensional unsteady heat conduction equation for a polymer layer (TSP or TSP/insulator layer) on a base of any material is obtained to calculate heat flux into the polymer surface as an explicit function of a time-dependent surface temperature change measured by TSP. In addition, an analytical solution of the three-dimensional unsteady heat conduction equation is given to consider the effect of the lateral heat conduction. Simulations and experiments are conducted to examine the analytical method and assess the relevant factors regarding the measurement uncertainty.

2.1. Introduction

Heat transfer to a hypersonic vehicle surface is one of the most important aerothermodynamic quantities, and one that often remains difficult to predict using modern computational fluid dynamics. Global heat transfer measurement is particularly critical to a deep understanding of relevant phenomena like transition, near-surface stationary vortices, and separation. Arrays of thermocouples have been used to measure heat transfer on a model. However, due to the limited spatial resolution of the array, critical effects are often difficult or impossible to capture. Temperature sensitive paint (TSP) provides a useful tool for quantitative global heat transfer diagnostics in hypersonic tunnels (Liu et al. 1995, Hubner et al. 2002, Norris et al. 2004, Kurits et al. 2007, Matsumura et al. 2003, 2005, Schneider et al. 2003). TSP is a thin polymer layer doped with certain luminescent molecules whose emission is sensitive to temperature. Therefore, once TSP coated on a surface is calibrated, surface temperature fields can be measured by detecting the luminescent emission from TSP (Liu and Sullivan 2004). TSP is usually air brushed directly on a model surface or a surface of an insulating layer used to coat a metal model. Illumination lights with a suitable wavelength are used to excite TSP. Digital cameras with optical filters are used to image TSP. After a time sequence of the surface temperature fields is obtained from TSP in a hypersonic tunnel, the main problem is how to accurately extract a heat flux field on a model surface. Heat transfer measurements using conventional local gauges like thin film thermocouples in hypersonic tunnels have been comprehensively described by Schultz and Jones (1973). In contrast, methods for calculation of heat flux from TSP measurements are not given in a systematical and general fashion. In particular, TSP as a polymer layer alters a history of the surface temperature, and therefore the effect of TSP itself on heat flux calculation should be addressed.

A simple method for calculating heat flux is the use of the discrete Fourier law, which has been used for heat transfer data reduction in TSP measurements in hypersonic tunnels since it is simple and reasonably accurate for high-conductive bases (Liu et al. 1995, Hubner et al. 2002). Another method is based on the transient solution of the one-dimensional (1D) time-dependent heat conduction equation. To process thermographic phosphor data, Merski (1998, 1999) has used an analytical solution of the 1D time dependent heat conduction equation to a step change of heat transfer on a semi-infinite body assuming that heat flux is proportional to the enthalpy difference between the adiabatic wall and real model wall. Since a model is injected to the tunnel, the model does not experience an ideal step function of time in heat transfer. Thus, an effective time is introduced. In addition, the thermal diffusivity depending on temperature and adiabatic wall enthalpy are estimated. The heat conduction equation can be directly solved using a finite difference or finite element method when the measured temperature fields are given as a

boundary condition. Thus, heat flux on the surface can be calculated. However, this forward numerical calculation of the temperature gradient is sensitive to the uncertainty of surface temperature measurement. In fact, the determination of heat flux from measured temperature fields is generally considered as an inverse heat transfer problem (Alifanov 1994, Beck et al. 1985). The inverse method has been compared with other methods by Walker and Scott (1998) for thermocouples. The inverse method has been used for IR cameras (Smith et al. 2001), TSP (Kojima et al. 2004) and general thermographic data (Estorf 2005).

This chapter gives a simple and robust analytical method for calculating heat flux from TSP measurements. Since a TSP layer is a polymer layer, a combination of a TSP layer and a thermal resistance layer is treated as a single polymer layer. The fundamental heat transfer problem for TSP measurements in hypersonic flow is to extract heat flux into a thin polymer layer on a large base from a time history of the surface temperature measured by TSP. The thin polymer could be TSP itself or TSP plus an insulator layer (for example Mylar sheet) with a suitable thickness. Compared with the polymer layer, the thickness of a base is much larger such that a semi-infinite base can be used as a good approximation. Figure 2.1 shows a thin polymer layer with a thickness covered on a semi-infinite base. A model in hypersonic testing is typically made of metals like stainless steel and aluminum that have much larger thermal conductivity than a polymer. Low thermal-conductive ceramic and nylon models are also used. First, an exact solution for the constant thermal properties is given by applying the inverse Laplace transform to the problem. The discrete form of the solution, which is a generalization of the Cook-Felderman method, can be used to calculate heat flux from a time history of the surface temperature. An analytical solution of the 3D heat conduction equation is also sought by using the Fourier transform and Laplace transform to consider the effect of the lateral heat conduction. The developed method is examined in simulations and experiments.

2.2. Analytical Method for Determination of Heat Flux from TSP Data

The transient solution of the 1D time-dependent heat conduction equation is sought for a thin polymer (TSP or TSP/insulator) on a semi-infinite base. An exact solution for a polymer on a base of an arbitrary material is derived by inverting the Laplace transform in Appendix A, and it is used as a general method for calculation of heat flux from TSP data. The heat flux at the polymer surface is given by

$$q_s(t) = \frac{k_p(1-\bar{\varepsilon}^2)}{\sqrt{\pi a_p}} \int_0^t \frac{\overline{W}(t-\tau, \bar{\varepsilon})}{\sqrt{t-\tau}} \frac{d\theta_{ps}(\tau)}{d\tau} d\tau \ , \tag{2.1}$$

where $\theta_{ps}(t) = T(t,L) - T_{in}$ is the temperature change at the polymer surface from the initial temperature T_{in}, L is the polymer layer thickness, and

$$\overline{W}(t, \bar{\varepsilon}) = \frac{2}{\sqrt{\pi}} \int_0^\infty \frac{exp(-\xi^2)\, d\xi}{1+\bar{\varepsilon}^2 - 2\bar{\varepsilon}\, cos(2L\xi / \sqrt{a_p\, t})} . \tag{2.2}$$

The parameter $\bar{\varepsilon}$ is defined as $\bar{\varepsilon} = (1-\varepsilon)/(1+\varepsilon)$, where $\varepsilon = \sqrt{k_p \rho_p c_p / k_b \rho_b c_b}$, k_p, c_p and ρ_p are the thermal conductivity, specific heat and density of the polymer, respectively, k_b, c_b and ρ_b are the thermal conductivity, specific heat and density of the base material, respectively, and $a_p = k_p / c_p \rho_p$ is the thermal diffusivity of the polymer. For $\bar{\varepsilon} = 0$, Eq. (2.1) recovers the classical solution for a semi-infinite base since $\overline{W}(t, 0) = 1$. This means that the function

$\overline{W}(t,\bar{\varepsilon})$ represents the effect of the polymer layer (or TSP itself) on the determination of heat flux, which depends on $\bar{\varepsilon}$, a_p and L.

The discrete form of Eq. (2.1) for actual calculation of heat flux is

$$q_s(t_n) \cong \frac{k_p(1-\bar{\varepsilon}^2)}{\sqrt{\pi a_p}} \sum_{i=1}^{n} \frac{\theta_{ps}(t_i)-\theta_{ps}(t_{i-1})}{\sqrt{t_n-t_i}+\sqrt{t_n-t_{i-1}}} \left[\overline{W}(t_n-t_i)+\overline{W}(t_n-t_{i-1}) \right]. \tag{2.3}$$

Eq. (2.3) can be considered as a generalization of the Cook-Felderman method for a combination of a polymer layer and a semi-infinite base of any material. Like the Cook-Felderman method (Cook and Feldeman 1970), the numerical scheme, Eq. (2.3), is easy to implement in applications.

2.3. Effect of Lateral Heat Conduction

The analysis based on the 1D heat conduction equation assumes that the lateral heat conduction can be neglected. To evaluate the effect of the lateral heat conduction, the 3D heat conduction equations for a polymer layer and a semi-infinite base are solved by using a combination of the Fourier transform and the Laplace transform (see Appendix). A similar treatment of the lateral heat conduction is given by Estorf (2005). In this case, we obtain the heat flux into the surface of the polymer layer

$$q_s(t) = \frac{k_p(1-\bar{\varepsilon}^2)}{\sqrt{\pi a_p}} \left[\int_0^t \frac{\overline{W}(t-\tau,\bar{\varepsilon})}{\sqrt{t-\tau}} \frac{d\langle\theta_{ps}\rangle_{g_1}(\tau)}{d\tau} d\tau + \int_0^t \frac{\overline{W}(t-\tau,\bar{\varepsilon})}{\sqrt{t-\tau}} \langle\theta_{ps}\rangle_{g_2}(\tau) d\tau \right], \tag{2.4}$$

where the spatially-filtered (averaged) temperature changes are

$$\langle\theta_{ps}\rangle_{g_1} = \int_{-\infty}^{\infty} \int_{-\infty}^{\infty} g_1(x-x', z-z', t-\tau)\theta_{ps}(\tau, x', z') dx' dz' , \tag{2.5}$$

$$\langle\theta_{ps}\rangle_{g_2} = \int_{-\infty}^{\infty} \int_{-\infty}^{\infty} g_2(x-x', z-z', t-\tau)\theta_{ps}(\tau, x', z') dx' dz' \tag{2.6}$$

The filter functions g_1 and g_2 are defined as

$$g_1(x,z,t) = \frac{1}{4\pi a_p t} exp\left(-\frac{x^2+z^2}{4a_p t} \right), \tag{2.7}$$

$$g_2(x,z,t) = \frac{1}{4\pi a_p t^2} \left(1+\frac{x^2+z^2}{4a_p t} \right) exp\left(-\frac{x^2+z^2}{4a_p t} \right). \tag{2.8}$$

The functions g_1 and g_2 are the Gaussian filter and modified Gaussian filter, respectively. Eq. (2.4) has a similar form to Eq. (2.1) for the 1D case except an additional integral term related to the filtered temperature change based on g_2. The lateral heat conduction is characterized by the size of the filter functions for the averaged temperature change, and the standard deviation $\sqrt{2a_p t}$ defines the affected region. For Mylar, $\sqrt{2a_p t} \approx 4.4\times10^{-4}\sqrt{t}$, and therefore $\sqrt{2a_p t} \approx 0.62\ mm$ at t = 2 s. When heat flux does not drastically change in a small circular region of 0.62 mm, the 1D solution Eq. (2.1) is sufficiently accurate. In the limit case, when

$\sqrt{2a_p t} \to 0$, g_1 approaches the Dirac delta function $\delta(x,z)$, and Eq. (2.4) is reduced to Eq. (2.1).

2.4. TSP Surface Temperature and TSP-Measured Temperature

In the above analysis, the temperature $T_{ps}(t)$ at a TSP surface is presumably known as a boundary condition. However, $T_{ps}(t)$ does not equal the TSP-measured temperature, and this difference has not been considered in previous measurements. Since a camera detects the integrated luminescent intensity across a thin TSP layer, the surface temperature measured by using TSP is an averaged temperature across the TSP layer, i.e.,

$$T_{TSP}(t) = L_{TSP}^{-1} \int_0^{L_{TSP}} T(t,y)dy, \tag{2.9}$$

where L_{TSP} is the thickness of the TSP layer. Using a Taylor expansion $T(t,y) \approx T_{ps} + (y - L_{TSP})\partial T / \partial y\big|_{y=L_{TSP}}$ at the TSP surface and $q_s = k_p \partial T / \partial y$ into the TSP layer, we have an iterative relation

$$T_{ps}^{(n+1)}(t) = T_{TSP}(t) + 0.5\, q_s^{(n)}(t) L_{TSP} / k_p. \tag{2.10}$$

Since the heat flux into the surface is considered to be positive here, $T_{ps}(t)$ is always larger than $T_{TSP}(t)$ depending on the heat flux and the thickness of the TSP layer. Eq. (2.10) is used as an iterative correction scheme. For an initial guess $T_{ps}^{(0)}(t) = T_{TSP}(t)$, an estimate of $q_s(t)$ can be obtained from the above analytical method. Then, a corrected $T_{ps}(t)$ is given by using Eq. (2.10) and an improved $q_s(t)$ is obtained. Usually, the temperature correction is required for high heat flux, and three iterations lead to a convergent result.

2.5. Simulations

2.5.1. Recovered Results for Modeled Starting Processes

To examine the general analytical solution, we consider a PVC layer on semi-infinite bases made of aluminum and Nylon 6. A step change followed by a sinusoidal variation in heat flux are used as a preliminary model of the transient starting process in the Boeing/AFOSR Mach 6 Quiet Tunnel at Purdue, as shown in Fig. 2.2. Table 2.1 lists the thermal properties of these materials commonly used for models and polymer layers in hypersonic testing. In simulations, aluminum and Nylon 6 are used as typical high- and low-conductive materials for models, respectively. Usually, TSP has the similar thermal properties to those of PVC. The time history of temperature on a 0.01 mm thick PVC surface on a semi-infinite aluminum base is generated by solving the unsteady 1D heat conduction equation using a forward time centered space finite difference scheme. Typically, the number of points selected in the polymer layer and base is 20 and 500, respectively. The number of points selected in the time domain varies from 501 to 4001, depending on the time interval and the properties of materials.

Figure 2.3 shows the resulting temperature histories responding to the simulated heat flux. Then, the heat flux history is recovered by using the general method Eq. (2.3), and the excellent agreement with the simulated one is achieved as shown in Fig. 2.4. The parallel simulations are conducted for a 0.01 mm thick PVC layer on a Nylon 6 base. Figures 2.5 and 2.6 show the corresponding results. The system of the PVC layer on the Nylon 6 base has a larger

characteristic timescale than that of the PVC with the aluminum base. In calculations, the numbers of points in the time domain for the PVC layer on the Al and Nylon 6 bases are 501 and 4001, respectively. A question is whether a different starting process alters the recovered heat flux using the general method since hypersonic facilities have different starting behaviors. The linear and the random starting processes have been also examined (Liu et al. 2009). It is found that they do not affect the recovered heat flux almost immediately after the transient process.

2.5.2. Error Analysis

The sensitivity analysis is given to assess the uncertainty of heat flux recovered by the general method, which depends on the elemental error sources in the parameters L, k_p, $\bar{\varepsilon}$, and a_p. For a simulated step heat flux ($q_s = 3000\,W/m^2$ for $t > 0$), the uncertainty $\Delta q_s / q_s$ is estimated as a function of the elemental errors $\Delta L / L$, $\Delta k_p / k_p$, $\Delta \bar{\varepsilon} / \bar{\varepsilon}$, and $\Delta a_p / a_p$ for a 0.05 mm thick PVC layer on a semi-infinite aluminum and Nylon 6 bases, as shown in Fig. 2.7. The sensitivity of $\Delta q_s / q_s$ to the elemental error $\Delta L / L$ in the polymer thickness is weak for the PVC layer on the Nylon 6 base. This consequence can be directly drawn from Eq. (2.2) in which the effect of L is limited in the term $\bar{\varepsilon}\, cos(2L\xi / \sqrt{a_p t})$. Clearly, for a low-conductive base like Nylon 6 where $\bar{\varepsilon}$ is small, a change of L will cause a relatively small effect on the calculated heat flux q_s. In contrast, for the PVC layer on the aluminum base, $\Delta q_s / q_s$ is sensitively dependent of $\Delta L / L$. In addition, $\Delta q_s / q_s$ is weakly dependent of $\Delta k_p / k_p$ and $\Delta \bar{\varepsilon} / \bar{\varepsilon}$ for the Nylon 6. The dependency of $\Delta q_s / q_s$ on $\Delta a_p / a_p$ is very weak for both aluminum and Nylon 6. According to the above sensitivity analysis, when the thermal properties of the materials and the polymer layer thickness cannot be measured accurately, a low-conductive base is a preferred choice. For the aluminum base, however, accurate measurements of the polymer layer thickness and the thermal properties are more critical to calculation of q_s.

The uncertainty in surface temperature measurements will lead to the uncertainty in calculation of heat transfer, which consists of a random error and a bias error of temperature. Although a random error in temperature propagates to the heat flux through the calculation, it is indicated that the random error in temperature does not produce a significant bias error in the time-averaged heat flux (Liu et al. 2009). In other words, time averaging or ensemble averaging will remove the effect of a random error. Further, the effect of a bias error of temperature on the determination of heat flux is examined. The linear dependence of the relative error in heat flux on the relative error in temperature is found in simulations.

In measurements in short-duration hypersonic tunnels, a small group of sample points in a temperature history is often obtained due to a limited rate of frames of a camera. In this case, heat flux calculation by using Eq. (2.3) has a greater numerical error since the time interval in the numerical integration is larger. For a simulated step heat flux ($q_s = 3000\,W/m^2$ for $t > 0$), 501 points in temperature in a time period of 5 s for a 0.1 mm thick PVC layer on a semi-infinite Nylon 6 are generated numerically. As shown in Fig. 2.8, a significant bias error in heat flux calculation is found for 21 sample points. To solve this problem, a third-order polynomial fit to 21 sample points is applied, and 501 interpolated points are used to calculate heat flux by using Eq. (2.3). As also shown in Fig. 2.8, the significantly improved result is obtained simply based on the suitable interpolation to the temperature data. A larger error in the transient process is due

to the fitting error. Furthermore, the recovered heat flux in the transient process is not accurate since the step change in heat flux cannot be truly recovered due to the intrinsic thermal inertia of a polymer layer and a base. For a 0.1 mm thick PVC layer on a semi-infinite aluminum, the recovered heat flux is very close to the true value even for 11 sample points after the transient starting process. In this case, the time evolution of the surface temperature is so gradual that a reasonable result can be obtained even though sample points are small.

2.6. Experiments

2.6.1. 48-inch Shock Tunnel

To examine the proposed analytical method, we reprocess raw TSP images on the sharp $25^o/45^o$ indented cone model obtained by Hubner et al. (2002) in Run # 46 at Mach 11 in the 48-inch Shock Tunnel at Calspan-University of Buffalo Research Center. The detailed description of the experiments is given by Hubner et al. (2002), and here only data relevant to heat flux calculation using the analytical method are given. Over sixty platinum thin-film heat transfer gauges were installed along a ray of the model, providing heat flux data for comparison with TSP. The reported measurement accuracy of the gauges is ±5%, and the measurement resolution is 5 kW/m^2. TSP was Ru-phen in a non-oxygen-permeable polyurethane binder. The TSP calibration data are fit by a polynomial

$$T / T_{ref} = \sum_{n=0}^{8} a_n \left[ln\left(I_{ref} / I \right) \right]^n ,$$

where $a_0 = 1.0$, $a_1 = 0.1167$, $a_2 = 0.0853$, $a_3 = -0.1404$, $a_4 = -0.2186$, $a_5 = 0.498$, $a_6 = -0.3386$, $a_7 = 0.0996$, and $a_8 = -0.0109$. The reference temperature T_{ref} was 295 K. The thickness of TSP was 10 μm, and the white polyurethane basecoat was 40 μm. Thus, the total thickness of the polymer layer was 50 μm. The measured thermal conductivity and diffusivity of the polyurethane layer were 0.48 W/K-m and 2.7×10^{-7} m^2/s, respectively. The model was made of stainless steel. In image processing, the raw flow-off and flow-on TSP images are corrected by subtracting the background intensity that is contributed by the ambient light and leakage of the optical filter before taking a ratio between the flow-off and flow-on images. Then, the ratio images are converted to the temperature images by using a priori calibration data. Figure 2.9 shows a typical surface temperature image selected from a total of 16 images in the run and the averaged heat flux image in an interval of 4-6 ms in which the flow was stabilized. The surface temperature is obtained by using the iterative relation Eq. (2.10) from the TSP-measured temperature. Figure 2.10 shows three iterations for correction of the surface temperature by Eq. (2.10) at the maximum heat flux location. The temperature correction for this case is significant due to a high heat transfer rate, and three iterations seem sufficient in this case. Figure 2.11 shows the heat flux distributions obtained by using the analytical method, Eq. (2.3), from 16 points and 100 points interpolated from 16 points in comparison with the data given by an array of thin-film heat flux gauges. The heat flux in Fig. 2.11 is the averaged value in an interval of 4-6 ms in which the flow was stabilized. The interpolation from 16 points gives an improved result, as indicated in the simulations. Note that the results from TSP are not in-situ-corrected.

2.6.2. Boeing/AFOSR Mach-6 Quiet Tunnel

TSP measurements on a Nylon cone were conducted in the Boeing/AFOSR Mach-6 Quiet Tunnel at Purdue University (Casper 2008). The TSP, Ru(bpy) in Chromaclear auto paint, was directly coated on the Nylon surface. The stagnation temperature and pressure were 160^{o}C and 255 psia, respectively. Figure 2.12(a) is a raw TSP image of the Nylon cone with a surface roughness element triggering boundary layer transition at Mach 6. Figure 2.12(b) shows the averaged heat flux image from t = 0.5 s to 4 s, which is downsampled over windows of 3×3 pixels to reduce the data processing time. A turbulent wedge triggered by the roughness element is visible due to the difference between the turbulent and laminar flow regimes. Figure 2.13 shows typical time histories of the surface temperature and heat flux at (x, y) = (25, 35) pixels in the turbulent wedge and (x, y) = (15, 25) pixels in the laminar boundary layer (reference Fig. 12(b) for the two positions). The transient starting process of the tunnel is observed in Fig. 2.13. By assuming that the TSP has the same thermal properties as Mylar and the TSP thickness is 40 microns, the heat flux is calculated by using Eq. (2.3) from 45 points and 300 points interpolated from 45 points. In this case, the interpolation does not show a significant improvement, and it indicates that 45 points are sufficient for heat flux calculation using Eq. (2.3).

2.6.3. Infrared Laser Heating

Infrared laser heating on a base provides a simple bench test in a laboratory to simulate the time-dependent heat flux in hypersonic tunnels. As illustrated in Fig. 2.14, the sample was made of substrate, and insulator, and a layer of TSP. Substrates used were nylon, aluminum, and PVC. Vinyl electrical tape and black Mylar were used as an insulating layer. The dark color decreases signal returned to the camera, but increases absorption of the IR laser. Before each run the laser was turned on and allowed to warm up while a shutter prevented the laser from reaching the sample. Then, the shutter was removed as the camera was recording images. The first test was step heating provided by an IR laser with a 0.3 OD filter of 0.2 cm thickness to reduce the power of the laser. Substrate was 0.5-inch-thick aluminum and insulator was 600-μm-thick electrical tape. The thermal conductivity and diffusivity of the insulating layer are 0.15 W/m-K and 9.7×10^{-8} m^2/s, respectively. The ambient temperature was 77 degrees F.

Figure 2.15 shows a typical time history of the surface temperature for step heating and the recovered heat flux at the center of the heated spot. The large temporal variation in the calculated heat flux in Fig. 2.15(b) indicates that the result is sensitive to a noise in the time derivative calculation in Eq. (2.1) or Eq. (2.3). This phenomenon is typical in inverse problems. Figure 2.16 shows the time-averaged heat flux distribution in the step laser heating. The recovered heat flux is not exactly a step function because the thick insulating layer has a large time constant. Periodically oscillating laser heating was also measured. The surface temperature increases gradually during the heating while it oscillates. The peaks and valleys of the recovered surface heat flux remain the same level, which is reasonable. Periodically oscillating laser heating was also measured. Figure 2.17 shows typical time histories of the surface temperature and the recovered heat flux at the center of the heated spot for oscillating laser heating. The surface temperature increases gradually during the heating while it oscillates. The peaks and valleys of the recovered surface heat flux remain the same level, which is reasonable.

2.7. Conclusions

The exact inverse solution of the 1D time-dependent heat conduction equation is obtained by using the Laplace transform for a thin polymer (TSP or TSP/insulator layer) on a semi-infinite

base. This solution leads to the analytical method for determining heat flux from a time history of the surface temperature measured by TSP in hypersonic tunnels. Simulations indicate that the analytical method is able to determine a complicated transient heat flux history as long as the intrinsic response time of TSP is sufficiently small. The heat flux recovered by the analytical method is independent of a complicated tunnel-starting process after a transient process. Therefore, the analytical method can be used for various hypersonic tunnels with different starting characteristics. The uncertainty of heat flux calculation is contributed by the elemental errors such as the polymer thickness, thermal conductivity, thermal diffusivity, and ratio of the thermal properties between the polymer and base. The sensitivity of calculated heat flux to the elemental sources for a low thermal-conductive base is much weaker than that for a metal base. Data interpolation from a small sample group can improve the accuracy of heat flux calculation. An iterative scheme for the polymer surface temperature from the TSP-measured temperature could improve the accuracy of heat flux measurement particularly when heat flux is very large. To examine the analytical method, TSP images on a sharp $25^o/45^o$ indented metal cone model at Mach 11 are reprocessed, and the recovered heat flux results are in good agreement with those measured by thin-film heat flux gauges. Furthermore, the analytical method is applied to TSP measurements on a nylon cone at Mach 6, and the recovered heat flux field indicates a turbulent wedge triggered by a roughness element on the cone surface. The results in IR laser heating as a bench test are also presented.

Table 2.1. Thermal Properties of Polymer and Base Materials

	Mylar	PVC	Al	Stainless Steel	Nylon 6	Macor
k (W/m-K)	0.15	0.16	204	16	0.25	1.5
ρ (kg/m^3)	1420	1300	2700	7900	1140	2520
c_p (J/kg-K)	1090	1500	904	500	878	790

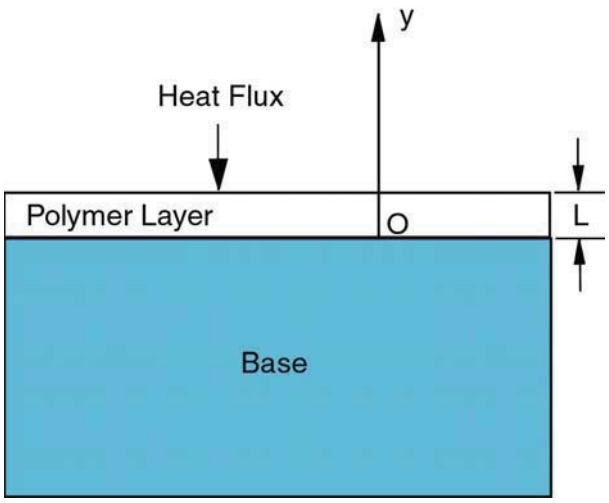

Figure 2.1. A thin polymer layer on a semi-infinite base and a coordinate system

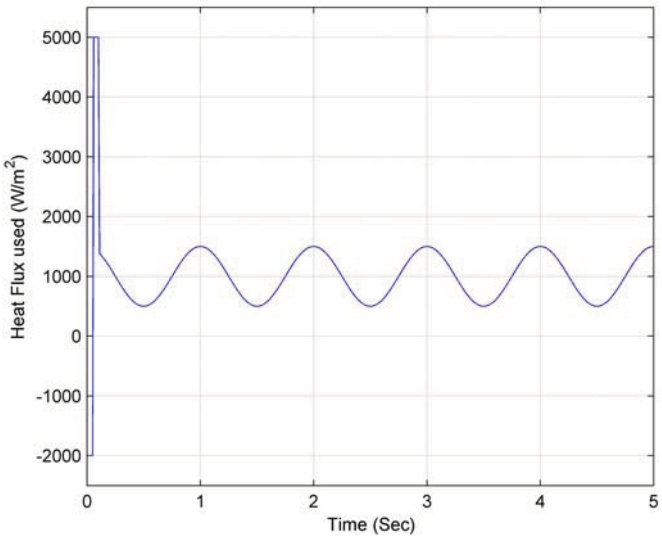

Figure 2.2. The simulated heat flux with starting step changes followed by a sinusoidal change

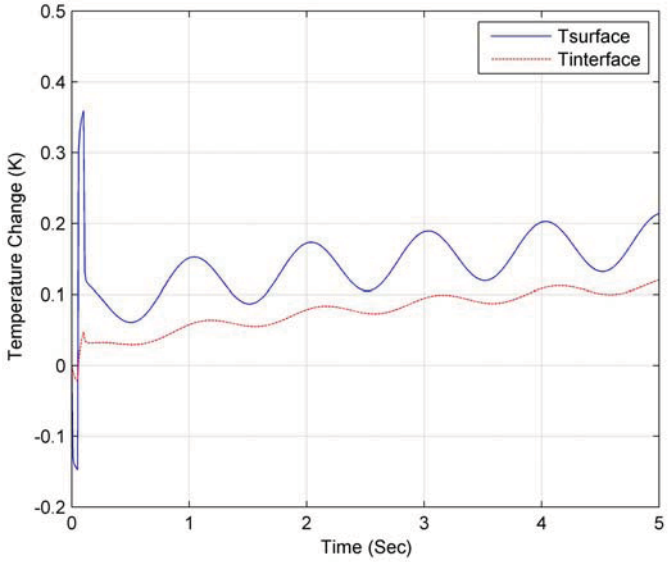

Figure 2.3. The temperature histories at the PVC surface and interface between the 0.01 mm thick PVC sheet and a semi-infinite aluminum base, responding to the simulated heat flux

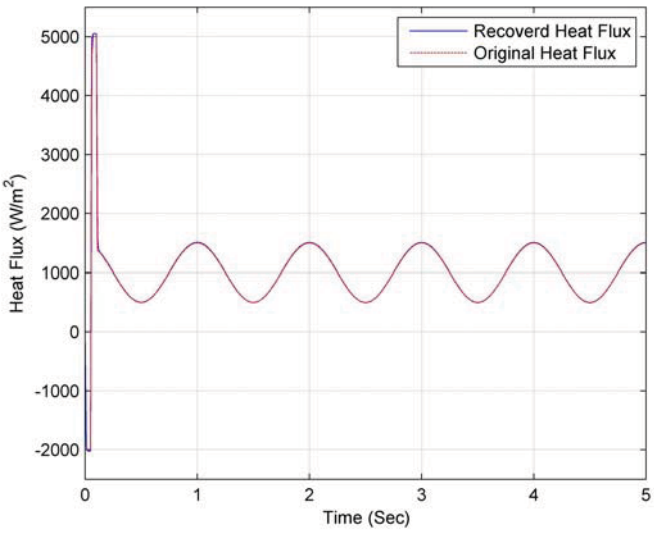

Figure 2.4. Comparison of the recovered heat flux using the general method with the given one for a 0.01 mm PVC layer on a semi-infinite aluminum base

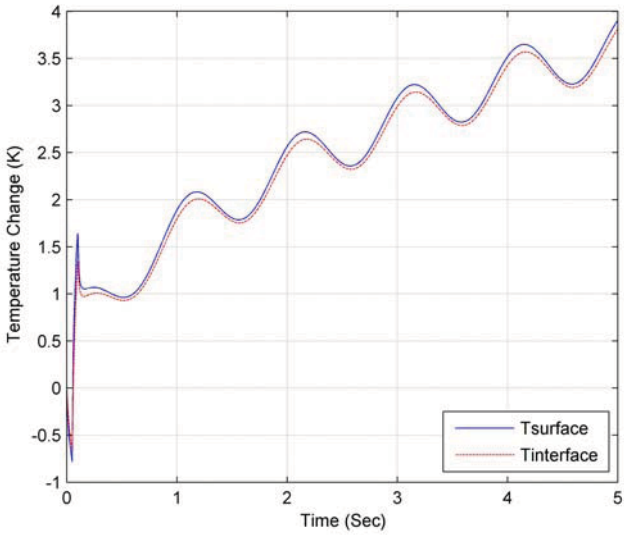

Figure 2.5. The temperature histories at the Mylar surface and interface between the 0.01 mm thick PVC sheet and a semi-infinite Nylon 6 base, responding to the simulated heat flux

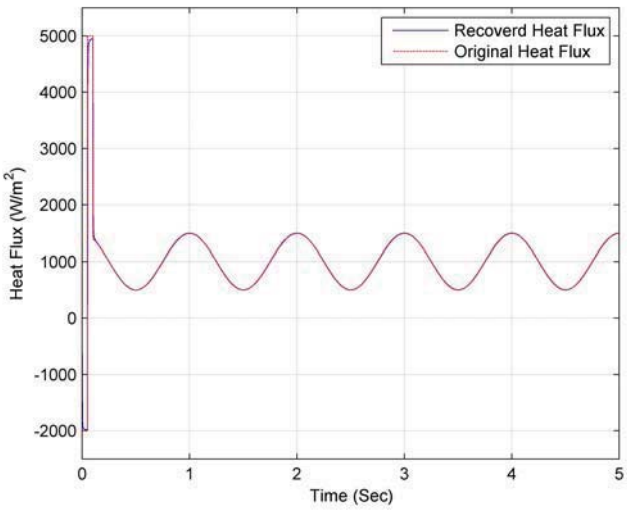

Figure 2.6. Comparison of the recovered heat flux using the general method with the given one for a 0.01 mm PVC layer on a semi-infinite Nylon 6 base

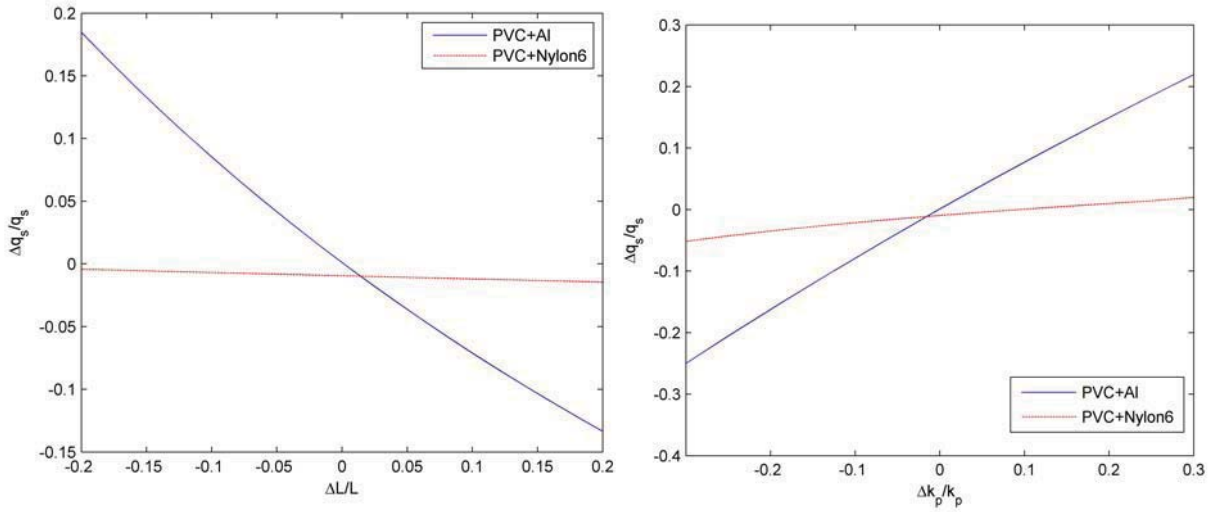

(a) (b)

Figure 2.7 (continued)

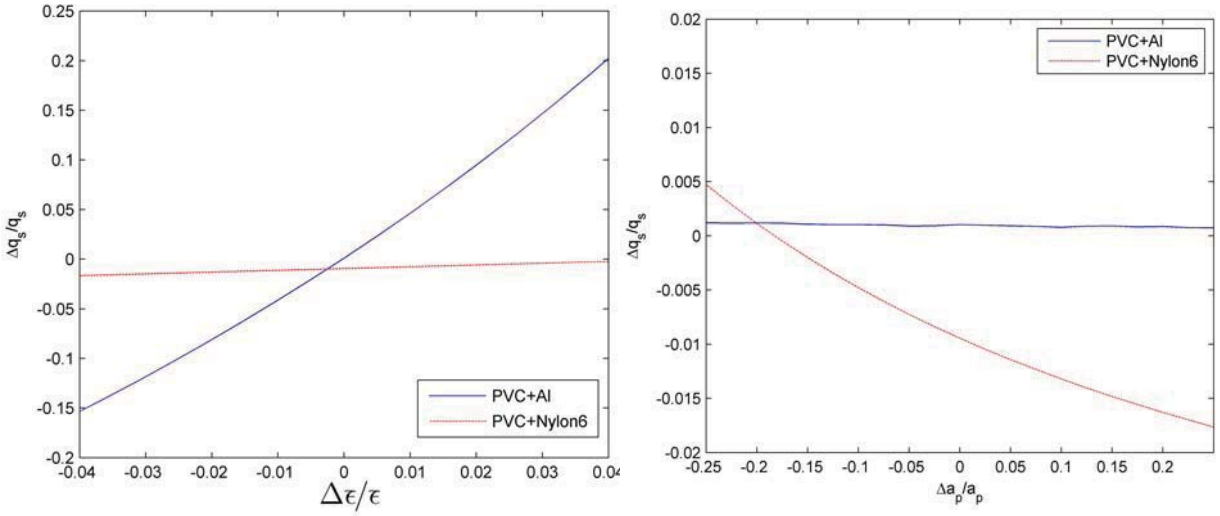

(c) (d)

Figure 2.7. The uncertainty of heat flux calculated by using the general method for a 0.05 mm PVC layer on a semi-infinite aluminum and Nylon 6 bases responding to a step change of heat flux, that results from the elemental errors of (a) polymer thickness, (b) thermal conductivity, (c) $\bar{\varepsilon}$, and (d) thermal diffusivity

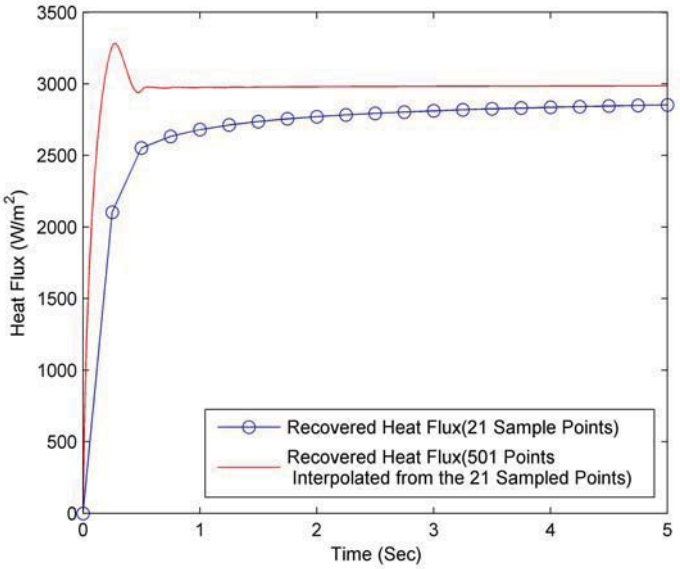

Figure 2.8. The improved results based on 501 points obtained from interpolation of 21 sample points in temperature for a 0.1 mm thick PVC layer on a semi-infinite Nylon 6

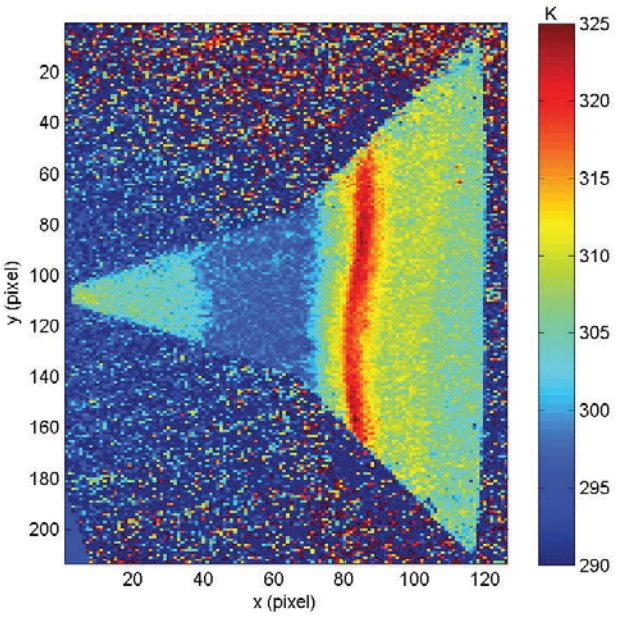

(a)

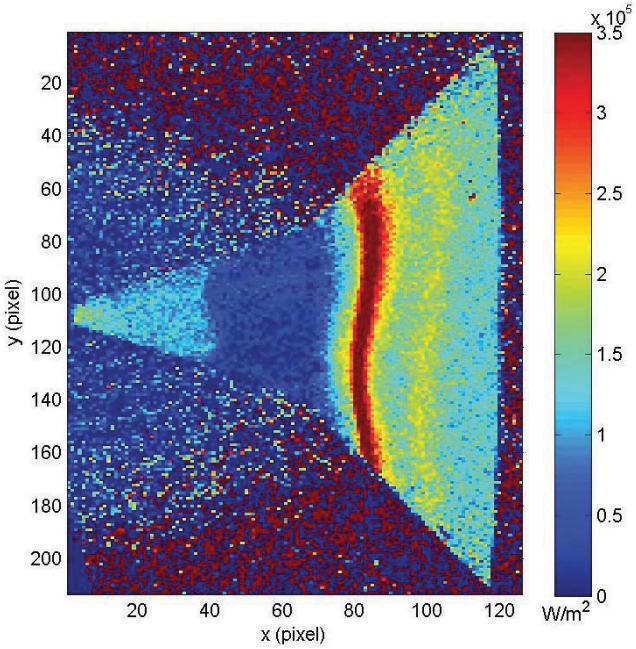

(b)

Figure 2.9. (a) Temperature image and (b) averaged heat flux image of the sharp $25^{o}/45^{o}$ indented cone model at Mach 11 (flow from left to right) [the original TSP images from Hubner et al. (2002)]

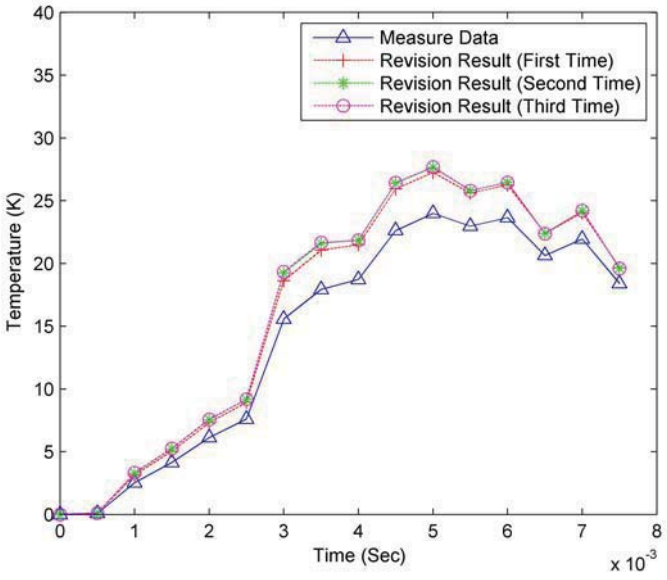

Figure 2.10. Three iterations for correction of the surface temperature at the maximum heat flux location

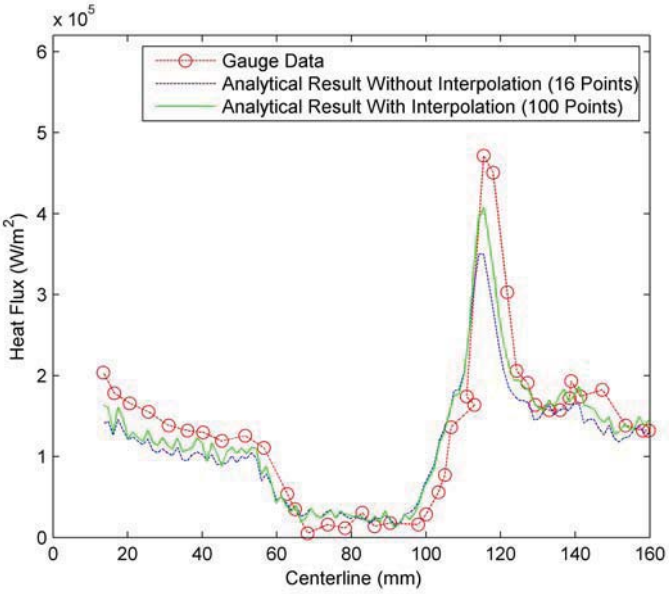

Figure 2.11. Heat flux distributions from TSP data along a ray on the sharp 25°/45° indented cone model at Mach 11 in comparison with the data from an array of thin-film heat flux gauges (the gauge data from Hubner et al. (2002)]

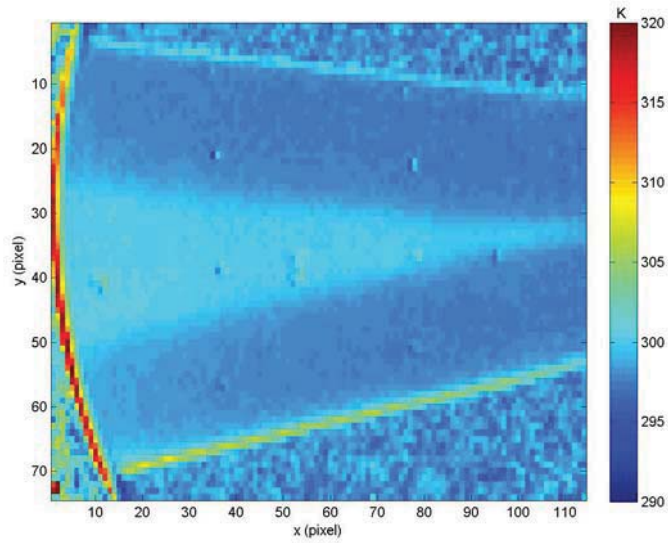

(a)

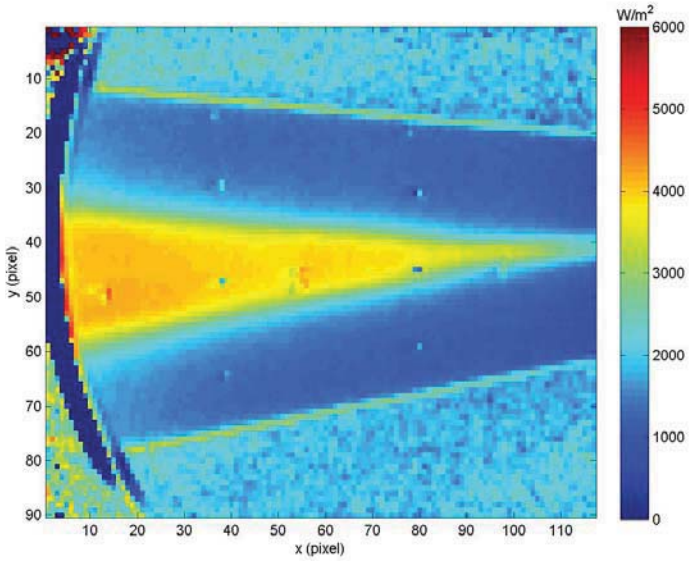

(b)

Figure 2.12. (a) Temperature image and (b) averaged heat flux image of a Nylon cone with a roughness element at Mach 6 (flow from right to left)

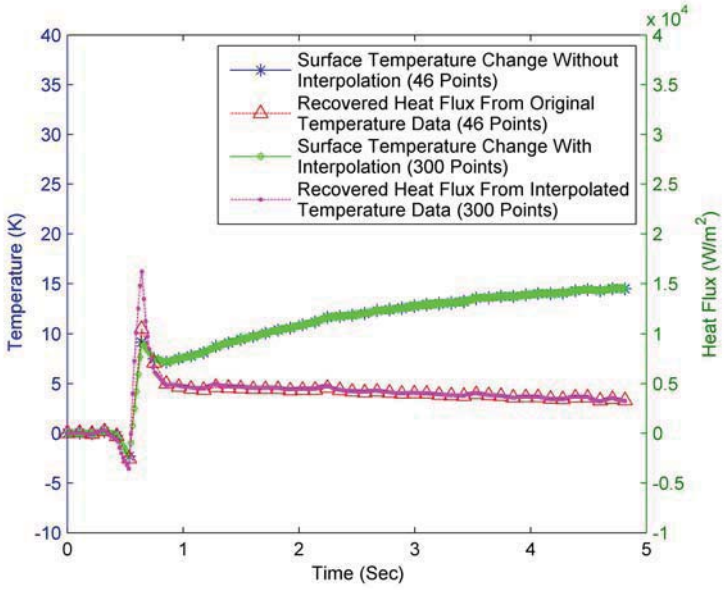

(a)

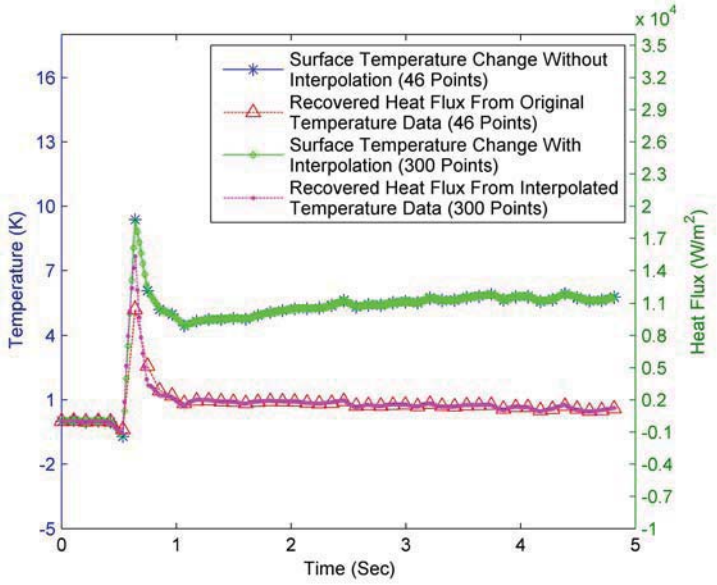

(b)

Figure 2.13. Typical time histories of the surface temperature and heat flux at (a) a point in the turbulent wedge triggered by a roughness element, and (b) a point in the laminar boundary layer

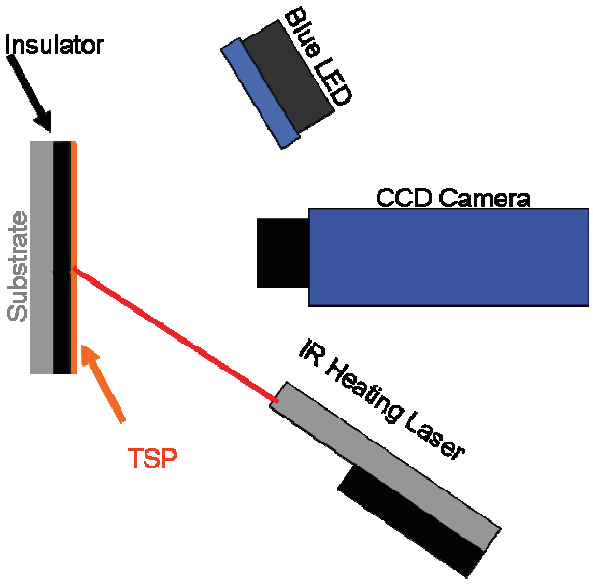

Figure 2.14. Infrared laser heating setup

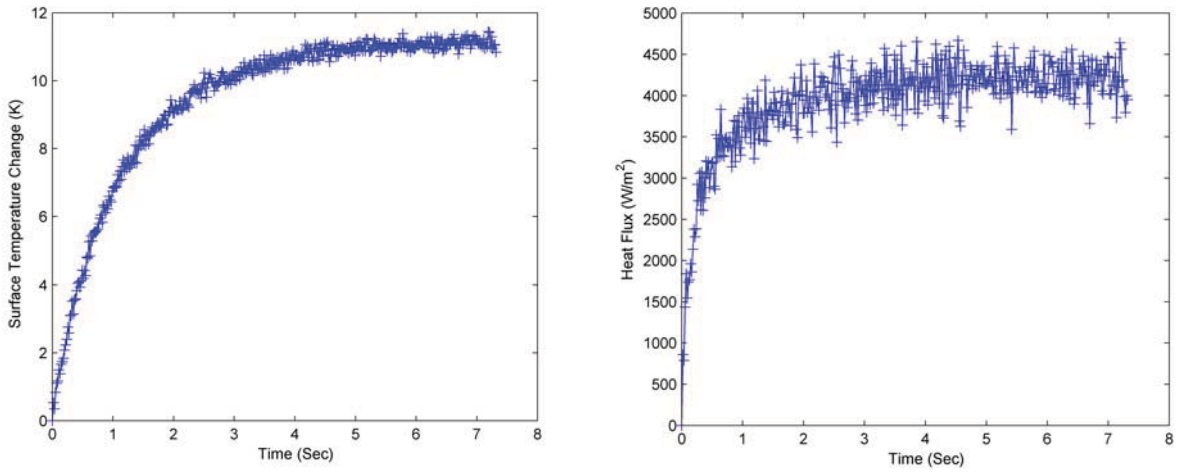

(a) (b)

Figure 2.15. Step laser heating: (a) the surface temperature and (b) the recovered surface heat flux as a function time at the center of the heated spot

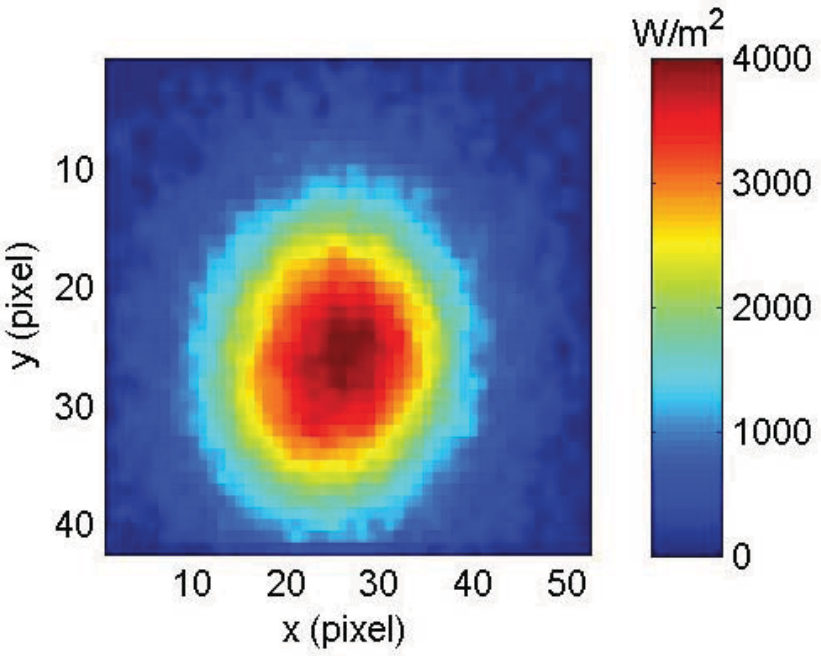

Figure 2.16. Time-averaged heat flux distribution in the step laser heating

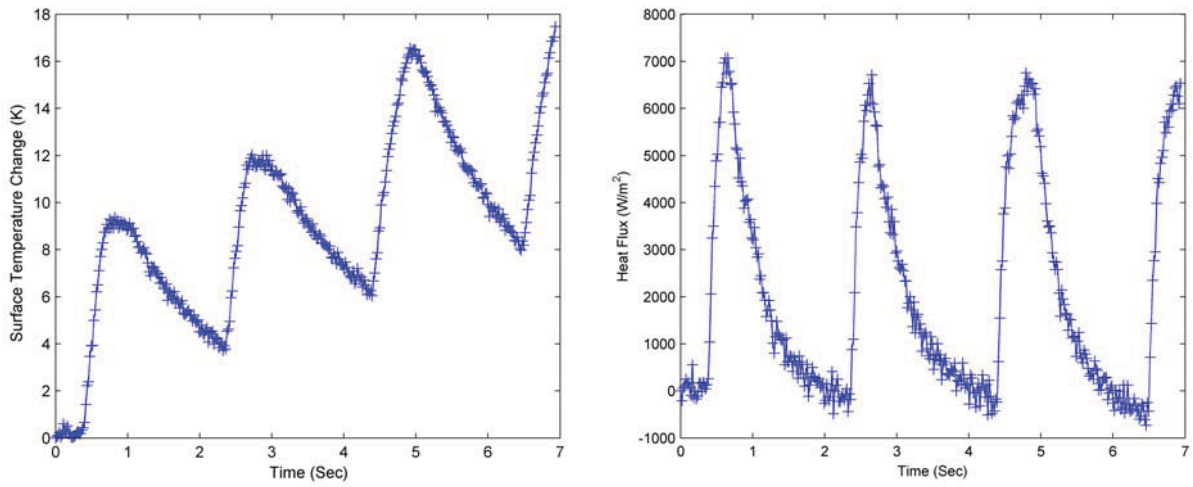

(a) (b)

Figure 2.17. Oscillating laser heating: (a) the surface temperature and (b) the recovered surface heat flux as a function time at the center of the heated spot

3. 1D Numerical Inverse Heat Transfer Method

This chapter describes a numerical inverse method used in temperature-sensitive-paint (TSP) measurements for quantitative global heat flux diagnostics in hypersonic tunnels. An iterative algorithm is developed to solve the one-dimensional inverse heat transfer problem for unsteady heat flux into a polymer layer (TSP) on a semi-infinite base, where the temperature dependencies of the thermal properties of materials are taken into account. Surface heat flux distributions on cone models are calculated by using this algorithm from TSP images acquired in hypersonic wind tunnel testing.

3.1. Introduction

Recently, Liu et al. (2010) (also in Chapter 2) have given a 1D analytical inverse solution for calculating heat flux from TSP surface temperature measurements (including other temperature-sensitive coatings). Here, the solution is briefly recapitulated for convenience of reading. Figure 2.1 shows a thin polymer layer on a semi-infinite base and a coordinate system used in this study. The transient solution of the 1D time-dependent heat conduction equation is sought by inverting the Laplace transform for a thin polymer on a semi-infinite base. The heat flux given by the 1D solution at the polymer surface is

$$q_{s(1D)}(t) = \frac{k_p(1-\bar{\varepsilon}^2)}{\sqrt{\pi\, a_p}} \int_0^t \frac{\overline{W}(t-\tau, \bar{\varepsilon})}{\sqrt{t-\tau}} \frac{d\theta_{ps}(\tau)}{d\tau} d\tau \ , \tag{3.1}$$

where $\theta_{ps}(t) = T(t,L) - T_{in}$ is the temperature change at the polymer surface from the initial temperature T_{in}, L is the polymer layer thickness, and a modified Gaussian integral for the effect of the polymer layer is

$$\overline{W}(t, \bar{\varepsilon}) = \frac{2}{\sqrt{\pi}} \int_0^\infty \frac{exp(-\xi^2)\, d\xi}{1+\bar{\varepsilon}^2 - 2\bar{\varepsilon}\, cos(2L\xi / \sqrt{a_p\, t})} . \tag{3.2}$$

The parameter $\bar{\varepsilon}$ is defined as $\bar{\varepsilon} = (1-\varepsilon)/(1+\varepsilon)$, where $\varepsilon = \sqrt{k_p \rho_p c_p / k_b \rho_b c_b}$, k_p, c_p and ρ_p are the thermal conductivity, specific heat and density of the polymer, respectively, k_b, c_b and ρ_b are the thermal conductivity, specific heat and density of the base material, respectively, and $a_p = k_p / c_p \rho_p$ is the thermal diffusivity of the polymer. For $\bar{\varepsilon} = 0$, Eq. (3.1) recovers the classical solution for a semi-infinite base since $\overline{W}(t, 0) = 1$. This means that the function $\overline{W}(t, \bar{\varepsilon})$ represents the effect of the polymer layer (or TSP itself) on the determination of heat flux, which depends on $\bar{\varepsilon}$, a_p and L. The discrete form of Eq. (3.1) for actual calculation of heat flux can be considered as a generalization of the Cook-Felderman method for a combination of a polymer layer and a semi-infinite base of any material.

Generally, Eq. (3.1) is able to give reasonable results when it is applied to a 3D model in tests in a short-duration wind tunnel. However, in a general 3D case, heat conduction in the lateral direction may be significant in certain locations where the spatial gradient in heat flux is large. This situation occurs near shocks, shock/shock interaction, shock/boundary-layer interaction, boundary-layer transition, flow separation, and strong vortex/wall interaction. Further improvement should be made by correcting the lateral heat conduction effect. According to Liu et al. (2011) (also in Chapter 4), the heat flux field $q_{s(1D)}(t,x,z)$ obtained by using the 1D

inverse method (either the analytical or numerical method) on a surface in a general 3D case is related the true heat flux $q_s(t,x,z)$ in the 3D case by the following equation

$$(1+\Delta\lambda)\, q_{s(1D)}(t,x,z) = \int_{-\infty}^{\infty}\int_{-\infty}^{\infty} g\left[x-x', z-z'; \sigma_r(t)\right]\, q_s\left(t,x',z'\right)dx'\,dz' \ . \tag{3.3}$$

The filter in Eq. (3.3) is the Gaussian distribution

$$g\left(x,z;\sigma\right) = \frac{1}{2\pi\sigma^2} exp\left(-\frac{x^2+z^2}{2\sigma^2}\right) \tag{3.4}$$

where $\sigma_r(t)$ is a standard deviation that represents the extent of the lateral heat conduction effect, $\Delta\lambda$ is a relative surface temperature change due to the lateral heat conduction, and t is the time elapsing from the start-up of a wind tunnel. In most applications where $\Delta\lambda << 1$ except at certain isolated region, $\Delta\lambda$ can be set at zero in the first-order approximation.

According to Eq. (3.3), due to the lateral heat conduction effect, $q_{s(1D)}(t,x,z)$ is a blurred (filtered or diffused) representation of a true heat flux field $q_s(t,x,z)$. Eq. (3.3) can be used as an approximate model for correcting the lateral heat conduction effect as long as $\sigma_r(t)$ is appropriately modeled. The linear relation $\sigma_r(t) = r_1 L_{diffu} + r_0$ is proposed as a model, where $L_{diffu} = \sqrt{2 a_p t}$ is the thermal diffusion length scale, and r_1 and r_0 are empirical coefficients to be determined. Given $q_{s(1D)}(t,x,z)$, $q_s(t,x,z)$ can be recovered by solving the convolution-type integral equation Eq. (3.3) as an image deconvolution problem (Liu et al. 2011). Although a 3D inverse heat conduction problem could be generally solved by coupling a positive solution with an optimization scheme (Lin et al. 2002, Wang et al. 2005), the aforementioned alternative is a two-step method that is a direct combination of the 1D inverse method and the 2D (image) deconvolution method based on the connection between the 1D and 3D solutions of the heat conduction equation.

Most analytical methods are based on an assumption that the thermal properties (thermal conductivity, specific heat and density) of a TSP (a polymer layer) are independent of temperature. In fact, the thermal properties are sensitive to temperature (Bryce 2001). When a change of surface temperature is significantly large in high-enthalpy hypersonic tunnels, the assumption of constant thermal properties may produce a considerable error in heat flux calculation if the temperature effects on the thermal properties are not taken into account. In this case, since no exact analytical solution can be obtained, a numerical inverse method has to be sought.

The objective of this work is to present a numerical development parallel to the analytical inverse analysis given by Liu et al. (2010) to calculate heat flux from TSP measurements. In TSP measurements, a white insulating layer (a thermally resistant base coating) is usually used for enhancing the luminescent light from TSP detected by a camera. In addition, this layer with a suitable thickness can be used to control the magnitude of the surface temperature change during a test. In this analysis, since both a TSP layer and an insulating layer are polymers with similar thermal properties, a combination of a TSP layer and an insulating layer is treated as a single polymer layer. Therefore, a polymer layer with a thickness on a semi-infinite substrate (in practice a sufficient thick base with 100 thermal diffusion length scales) is studied. The first step is to solve the direct heat transfer problem for the two-layer system, which is required not only for simulations but also for the development of the numerical inverse heat flux estimation

algorithm. The inverse heat transfer method starts from initial determination of heat flux by using a simple and fast approximation calculation. As the second step, an iterative algorithm refines the estimation through optimization. The inverse heat transfer algorithm is examined through simulations. Given a simulated heat transfer history and the temperature-dependent thermal properties, the surface temperature change on a polymer layer on a semi-infinite base (aluminum and Nylon-6) is obtained accurately by numerically solving the heat conduction equation (the direct heat transfer problem). Then, from the surface temperature change, the inverse heat transfer algorithm is used to recover heat flux for a direct comparison with the known heat flux history and the result given by the analytical inverse method. Applications of the numerical inverse heat transfer method in TSP measurements in hypersonic wind tunnels are described.

3.2. Finite Difference Method for Direct Heat Transfer Problem

Figure 2.1 shows a polymer layer with a thickness L on a semi-infinite base and the coordinate system. There are two regions in our problem: polymer layer and semi-infinite base. In the direct problem, the heat flux $q_s(t)$ into the polymer surface is known as a function of time t. We want to obtain the distribution of the temperature change $\theta(y,t) = T - T_{in}$ in the polymer and base by numerically solving the 1D time-dependent heat conduction equation. For the polymer layer, the heat conduction equation is

$$\left(\frac{\partial}{\partial t} - a_p \frac{\partial^2}{\partial y^2} \right) \theta_p(y,t) = 0 , \tag{3.5}$$

where $\theta_p(y,t) = T_p - T_{in}$ is the temperature change of the polymer layer from a constant initial temperature T_{in}, and $a_p = k_p / c_p \rho_p$ is the thermal diffusivity of the polymer in which k_p, c_p and ρ_p are the thermal conductivity, specific heat and density of the polymer, respectively. The boundary condition at the polymer surface ($y = L$) is $q_s - k_p \partial\theta_p / \partial y = 0$, where $q_s(t)$ is the heat flux into the polymer surface and L is the polymer layer thickness. The origin of coordinates is set at the interface between polymer layer and base, as shown in Fig. 2.1. The initial condition for the polymer layer is $\theta_p(y,0) = 0$.

Similarly, the equation for the base is

$$\left(\frac{\partial}{\partial t} - a_b \frac{\partial^2}{\partial y^2} \right) \theta_b(y,t) = 0 , \tag{3.6}$$

where $\theta_b(y,t) = T_b - T_{in}$ is the temperature change of the base layer from a constant initial temperature, and $a_b = k_b / c_b \rho_b$ is the thermal diffusivity of the base. The initial condition for the base is $\theta_b(y,0) = 0$. The boundary condition at infinity in the base is $\theta_b(-\infty, t) = 0$. The matching conditions at the interface between the two layers ($y = 0$) are $\theta_p = \theta_b$ and $k_p \partial\theta_p / \partial y = k_b \partial\theta_b / \partial y$.

Combination of the above equations and the boundary conditions gives a system of the two-region heat conduction equations with the known initial and boundary conditions. Here the direct (forward) heat conduction problem is to find the temperature fields $\theta_p(y,t)$ and $\theta_b(y,t)$ by using the standard finite difference method. Finite difference solution of the general heat

conduction equation is discussed by Morton and Mayer (1994), Fletcher (1980) and Hoffman (1992).

3.3. Inverse Algorithm for Determination of Heat Flux from TSP Data

Given a history of the polymer surface temperature θ_{ps} obtained from TSP measurements, the surface heat flux q_s is computed. This is an inverse heat transfer problem for the system of equations. Some methods for the conventional inverse heat conduction problem have been previously developed, such as sequential function specification methods and regularization methods (Stolz 1960, Beck et al. 1985, Alifanov 1994). In this paper, an iterative algorithm is proposed to solve this two-region inverse heat conduction problem. The initial step is based on the direct numerical method introduced in the above section, which is called initial determination of surface heat flux.

3.3.1 Initial Determination

For initial estimation, a linear matrix equation relating the surface heat flux and surface temperature data is proposed, i.e., $\theta_{ps} = \Phi q_s$, where θ_{ps} and q_s denote a measured polymer surface temperature vector and a surface heat flux vector, respectively, and Φ is the relation matrix. If Φ is defined and nonsingular, then $q_s = \Phi^{-1}\theta_{ps}$. However, the actual functional relation between the temperature data θ_{ps} and heat flux q_s is complicated, which is related to the thermal properties of the polymer and base layers. As an initial step of the iterative algorithm, we try to find the approximate relation matrix Φ' based on the two assumptions.

First, it is assumed that the inverse heat conduction problem to be linear, i.e., $\theta_{ps} = \sum_{j=1}^{M} P^j q_s^j$, where the vector P^j is the surface temperature response to a unite step heat flux at time j, q_s^j is the heat flux magnitude at time j. Another assumption is that the effect of heat flux at time j on the surface temperature change is instantaneous. If the history of surface temperature response to the unite step heat flux is $(T^1, T^2, \cdots, T^M)^T$, then $P^j = (0, \cdots, 0, T^j, 0, \cdots, 0)^T \ (j = 1,2,\cdots,M)$ and a diagonal matrix Φ' has the non-zero elements $(T^1, T^2, \cdots, T^M)$ only in the diagonal line.

To obtain Φ', a unit step heat flux is applied to the system of equations and the surface temperature is determined by using the numerical method for the direct problem for a step function of heat flux. From the initial condition for the polymer, we know $T^1 = 0$, and hence the first row and first column of Φ' are zero vectors. The first row and first column of Φ' are therefore discarded. Because of discarding the data, the first heat flux estimate q_s^1 cannot be determined. Fortunately, we can set q_s^1 to be zero in most time. For the nonsingular matrix Φ'_{2-M}, the history of heat flux can be estimated by $q_s^{2-M} = \Phi'^{-1}_{2-M}\,\theta_{ps}^{2-M}$. Since Φ'_{2-M} is a diagonal matrix, it is easy to compute the inverse matrix. The initial (coarse) determination of heat flux is simple and fast. For some simple simulated histories of heat flux, the recovered results are good enough as the initial approximation for the subsequent optimization. Hereafter, we use Φ to denote the nonsingular matrix Φ'_{2-M} by neglecting the influence of the initial condition.

3.3.2 Optimization

The determination of heat flux can be mathematically described as the following optimization problem

$$\min_{q_s} \left\| \theta_{ps} - \theta'_{ps}(q_s) \right\|_2^2 \tag{3.7}$$

where q_s is the heat flux to be found, and θ'_{ps} is the estimated surface temperature response to q_s that is calculated by solving the system of equations for the positive problem. The difference between the estimated temperature and TSP-measured temperature is minimized, and an iterative algorithm to solve the optimization problem is described in Table 3.1. The error bound ε in calculations of heat flux from TSP data is set at 10^{-5}.

3.4. Simulations

3.4.1. Constant Thermal Properties

To examine the algorithm, we consider a polyvinyl chloride (PVC) layer on a semi-infinite aluminum base and a Nylon-6 base. The initial step change followed by a sinusoidal change in heat flux is used to simulate the transient starting process in the Boeing/AFOSR Mach-6 Quiet Tunnel at Purdue University, as shown in Fig. 3.1. The time histories of temperature on a 0.01mm thick PVC surface on a semi-infinite aluminum base and a Nylon-6 base are generated by solving the system of equations. Figure 3.2 shows the resulting temperature histories responding to the simulated heat flux change, where $T_{surface}$ and $T_{interface}$ are the temperatures at the polymer surface ($y = L$) and interface between the polymer and base ($y = 0$), respectively. A comparison is made between the numerical and analytical inverse methods. As indicated in Fig. 3.3, the numerical and analytical inverse methods are in good agreement for the constant thermal properties, and the numerical algorithm gives satisfactory recovery of heat flux after five iterations. For a PVC layer on a semi-infinite Nylon-6 base is also considered, the iterative algorithm converges to the original heat flux history after 20 iterations.

3.4.2. Temperature-Dependent Thermal Properties

The analytical inverse method is based on an assumption that the thermal properties of the polymer and base layers are constant. This assumption is reasonably good for many applications. However, when the surface temperature change is sufficiently large in hypersonic testing, the effects of the temperature dependencies of the thermal properties should be considered for more accurate determination of heat flux. The thermal properties may change with increasing the surface temperature during a run. To take the temperature dependencies of the thermal properties into account, the coefficient matrix in the linear system of equations is updated after each time step, depending on the thermal properties that are given as the specified functions of temperature.

To illustrate the effects of temperature dependencies of the thermal properties, we consider the simulated heat flux with a starting step change followed by a sinusoidal change into a 0.01 mm PVC layer covered on an aluminum base and a Nylon-6 base. According to the data provided by Bryce (2001), the specific heat and thermal conductivity of PVC are fitted by the empirical formula $c(T) = 1540 + 4(T - 293)$ and $k(T) = 0.16 - 0.0004(T - 293)$, respectively, where T is temperature in Kelvin, c is in J/kg-K, and k is in W/m-K. It is assumed that the

density of PVC is independent of temperature, i.e., ρ = 1300 kg/m^3. Therefore, the thermal diffusivity of PVC is

$$a(T) = \frac{k}{c\,\rho} = \frac{0.16 - 0.0004(T - 293)}{[1540 + 4(T - 293)] \cdot 1300}. \tag{3.8}$$

For simplicity, it is assumed that the thermal properties of the base (aluminum or Nylon-6) are constant, as shown in Table 2.1.

In principle, the numerical inverse method can recover heat flux by taking the temperature dependencies of the thermal properties into account. The simulated heat flux history shown in Fig. 3.1 is used again. Based on the surface temperature history simulated by using the temperature-dependent thermal properties, heat flux is calculated by using the numerical inverse method, and good convergence to the original heat flux is achieved after 6 iterations for a 0.01 mm PVC layer on a semi-infinite aluminum base. Figure 3.4 shows a comparison with the analytical inverse method that is valid only for the constant thermal properties. As expected, in this case, the numerical inverse method can recover the correct heat flux history, while the analytical inverse method has a considerable error.

The simulated surface temperature for a PVC layer on a semi-infinite Nylon-6 base is also considered. A comparison of the recovered results between the numerical inverse method and the analytical inverse method is shown in Fig. 3.5. In this case, the analytical inverse method still can achieve as good recovery of heat flux as the numerical inverse method. Interestingly, the temperature dependencies of the thermal properties do not significantly affect on the calculation of the surface heat flux in the case of a low-conductive base. The insensitivity of heat flux calculation on the thermal properties for a low-conductive base like Nylon-6 has been found in an error analysis given by Liu et al. (2010).

3.5. Experiments

3.5.1. 48-inch Shock Tunnel

To examine the accuracy of the numerical inverse method, raw TSP images on the sharp 25^o/45^o indented cone model are re-processed, which were obtained by Hubner et al. (2002) in Run # 46 at Mach 11 in the 48-inch Shock Tunnel at Calspan-University of Buffalo Research Center. The analytical inverse method has been used previously to obtain the heat flux distributions for this case without considering the temperature dependencies of the thermal properties of the materials (Liu et al. 2010, also in Chapter 2). Here, it is assumed in the numerical inverse heat flux calculation that the polymer layer (TSP plus the base coating) has the same temperature dependencies as PVC in the thermal properties, which are described in Section 4.2. The thermal properties of the stainless steel base are assumed to be constant. Figure 2.9 shows a typical surface temperature image selected from a total of 16 temperature images in the run and the averaged heat flux image in an interval of 4-6 ms in which the flow was stabilized. The heat flux distributions along the centerline are shown in Fig. 3.6, where the numerical inverse method incorporates the temperature dependencies of the thermal properties in contrast to the analytical inverse method. The numerical inverse method gives the improved result that is closer to the data given by an array of thin-film heat flux gauges. The effect of the temperature dependencies of the thermal properties is pronounced in this case because the increase of the polymer temperature on the metal base is relatively large (about 20 K) in this tunnel.

3.5.2. Boeing/AFOSR Mach-6 Quiet Tunnel

TSP measurements on a 7°-half-angle Nylon-6 cone were conducted at zero angle of attack in the Boeing/AFOSR Mach-6 Quiet Tunnel at Purdue University. The stagnation temperature and pressure were 433 K and 255 psi, respectively. The 7°-half-angle nylon cone is 0.4 m (16 inches) long, including a 0.15 m long stainless steel nosetip that has a 1.52 mm (0.06 inch) nose radius. The TSP, Ru(bpy) in Chromaclear auto paint, was directly coated on the nylon surface. The coating thickness was about 50 microns. The temperature calibration for this TSP is given by (Swanson 2008)

$$T / T_{ref} = \sum_{n=0}^{4} C_n (I / I_{ref})^n , \tag{3.9}$$

where $C_0 = 1.2342$, $C_1 = -0.3804$, $C_2 = 0.3443$, $C_3 = -0.2543$, and $C_4 = 0.0542$ in a range of $0.9 < T / T_{ref} < 1.1$. For temperature conversion from the luminescent intensity of TSP in this test, the reference temperature in Eq. (3.9) is $T_{ref} = 298\ K$.

Figure 3.7 shows a generic setup of a CCD camera with a band-pass optical filter for detecting the luminescent emission from the TSP and a blue LED array (460 nm) for illuminating the TSP on a model in a dark environment in the Mach-6 tunnel. The camera (PCO 1600) and blue LED array are purchased from Innovative Scientific Solutions Incorporated (http://www.innssi.com). The time step in a sequence of 45 images acquired by the camera was 0.107 s. In our experiments where the total pressure was relatively high, a smaller circular window was used. A viewed region near the middle section of the cone is illustrated in Fig. 3.8. A square roughness element with a 1.27×1.27 mm^2 cross-section and a height of 0.28 mm was placed at 0.13 m from the nosetip to trigger the boundary-layer transition to turbulence. The basic testing procedures of TSP in wind tunnels are described by Liu and Sullivan (2004).

Surface temperature images were obtained by using Eq. (3.9) from a sequence of TSP images, and then heat flux images are calculated at every pixel by using the numerical inverse method and analytical inverse method. It is again assumed that the TSP has the same thermal properties as PVC described in Section 3.4.2. Table 2.1 lists the thermal properties of PVC and Nylon-6. Figure 3.9(a) shows a heat flux image obtained by using the 1D numerical inverse method on a 7°-half-angle circular cone at Mach 6 at t = 3 s from starting the tunnel. In this case, the effect of the temperature dependencies of the thermal properties of the polymer is negligible for a small change of temperature on the Nylon-6 base (see the simulation in Section 3.4.2). The significant spike noise found in these images is typical in TSP measurements particularly when the measured temperature change is small (less than a few degrees). Figure 3.9(b) shows the corresponding heat flux image improved by applying the image deconvolution method to Fig. 3.9(a) to correct the lateral heat conduction effect and remove the random noise (Liu et al. 2011). These images clearly indicate the formation and development of a turbulent wedge triggered by a roughness element in the boundary layer, which is evidenced by the difference in heat flux between the turbulent and laminar flow regimes.

Figure 3.10 shows the heat flux distributions in the vertical direction in images across the cone at the streamwise locations x = 0.16 m, 0.18 m, 0.21 m, 0.23 m and 0.26 m at t = 3 s from starting the tunnel along with the local values of heat flux given by the laminar boundary layer solution. For illustration, these locations are marked in Fig. 3.8. In fact, these distributions are the projected ones of those on a circular arc of a local cross-section of the cone. Then, the improved distributions of heat flux are obtained by applying the image deconvolution method to

correct the lateral heat conduction effect and reduce the random spike noise. This approach is called the two-step method (the 1D inverse method coupled with the image deconvolution method). This improvement is particularly appealing for the result at x = 0.16 m where the random noise is very large relative to the signal. At x = 0.16 m and 0.18 m where the turbulent wedge is narrow in its width and weak in its magnitude of heat flux, the TSP-measured values of heat flux outside of the wedge are consistent with the prediction by the laminar boundary layer solution on the cone. However, when the turbulent wedge considerably diffuses (expands) in the lateral direction as it develops downstream, the TSP-measured value of heat flux outside of the turbulent wedge deviates gradually from the prediction by the laminar boundary layer solution. This deviation is more evident at x = 0.23 m and 0.26 m, indicating that there is increasing influence of the turbulent wedge diffused along the lateral direction.

3.6. Conclusions

The numerical inverse method is developed to determine heat flux from temperature sensitive paint (TSP) images obtained in short-duration hypersonic tunnels. This method is an iterative algorithm based on a numerical solution for the positive heat transfer problem and an optimization scheme to minimize the error between the calculated and measured surface temperatures. Simulations indicate that the numerical and analytical inverse methods give the same result of heat flux for a simulated tunnel run when the thermal properties of the TSP and base materials are constant. Nevertheless, the numerical inverse method has the major advantage that it can take the effect of the temperature dependencies of the thermal properties into account in computations. The numerical inverse method is applied to TSP measurements on a sharp stainless steel $25^o/45^o$ indented model at Mach 10 and a sharp 7^o-half-angle Nylon-6 cone model with a roughness element at Mach 6. The extracted heat flux distributions are compared favorably with those given by thin-film heat transfer gauges and the laminar boundary-layer solution.

Table 3.1. Iterative Algorithm

Input: measured surface temperature θ_{ps} (TSP data)

Initialization:

- initialize error tolerance ε and construct matrix Φ
- compute coarse determination of heat flux q_{s_1} using $\theta_{ps} = \Phi q_s$
- from the direct heat conduction equations, compute θ'_{ps_1}
- calculate the temperature error $T_{err} = \left\| \theta_{ps} - \theta'_{ps_1} \right\|_2^2$
- $k = 1$

While $T_{err} > \varepsilon$**, repeat**

Step 1. from the matrix form $\Phi q_{err} = T_{err}$, compute q_{err}

Step 2. $q_{s_{k+1}} = q_{s_k} + q_{err}$

Step 3. compute surface temperature $\theta'_{ps_{k+1}}$ using the direct heat conduction equations

Step 4. update $T_{err} = \left\| \theta_{ps} - \theta'_{ps_{k+1}} \right\|_2^2$

Step 5. $k = k + 1$

End

Output: heat flux estimate $q_{s_{k-1}}$

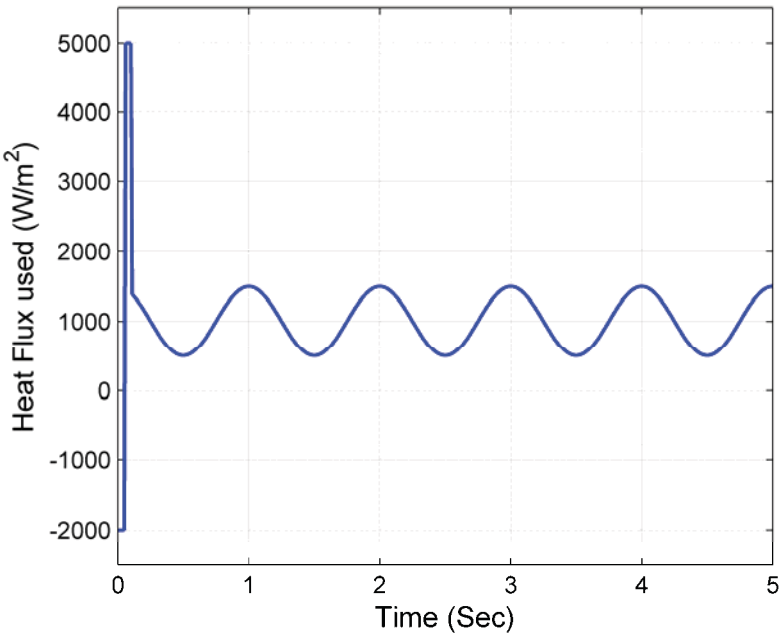

Figure 3.1. The simulated heat flux with starting step changes followed by a sinusoidal change

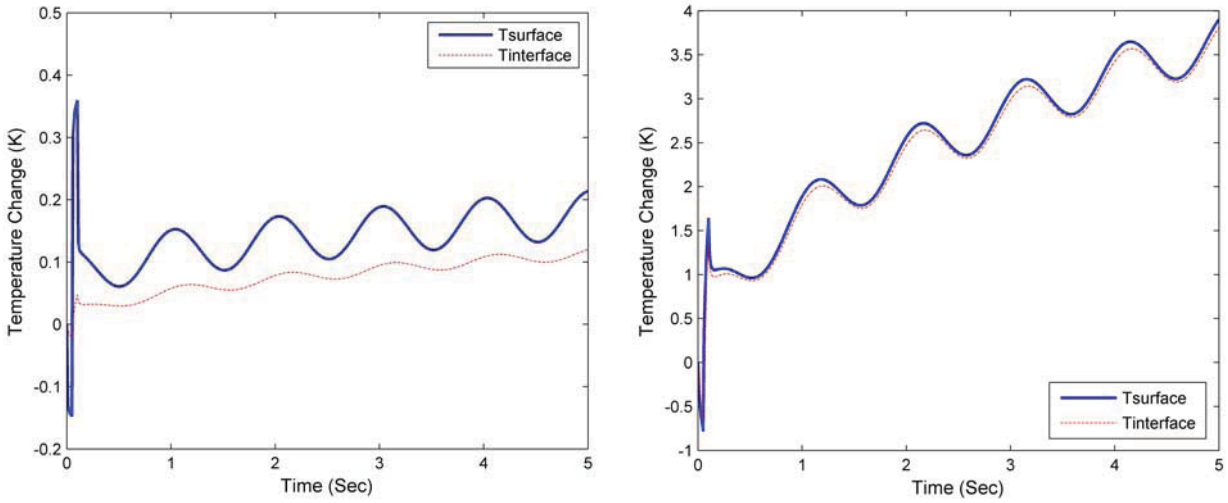

(a) (b)

Figure 3.2. The temperature history at the surface and interface between the 0.01 mm thick PVC sheet and a semi-infinite base responding to the simulated heat flux, (a) aluminum, and (b) Nylon-6 base

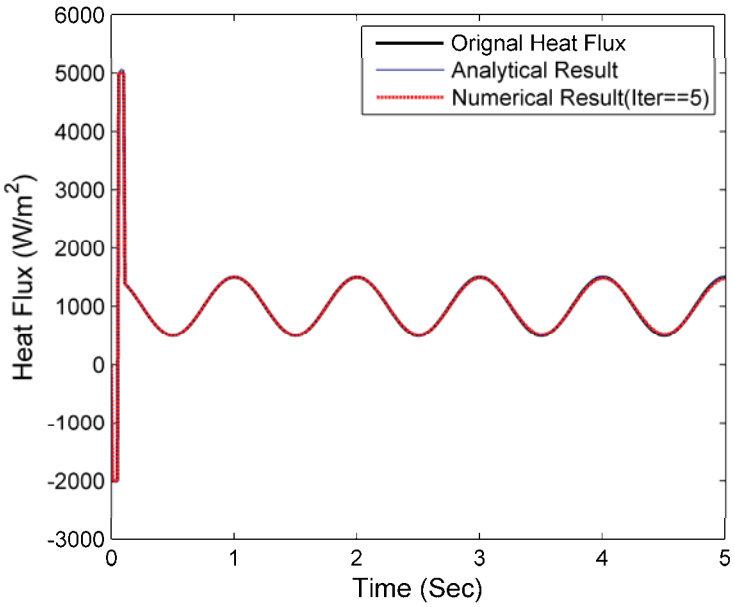

Figure 3.3. Comparison of the recovered heat flux by using the inverse numerical method and analytical inverse method for a 0.01mm PVC layer on a semi-infinite aluminum base

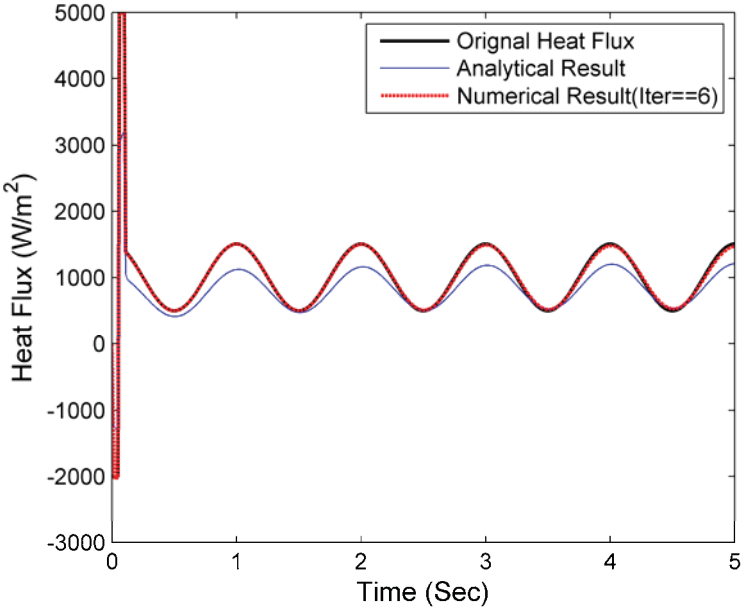

Figure 3.4. Comparison of the recovered heat flux by using the numerical inverse method and analytical method for a 0.01 mm PVC layer on a semi-infinite aluminum base, where the thermal properties of PVC are temperature-dependent

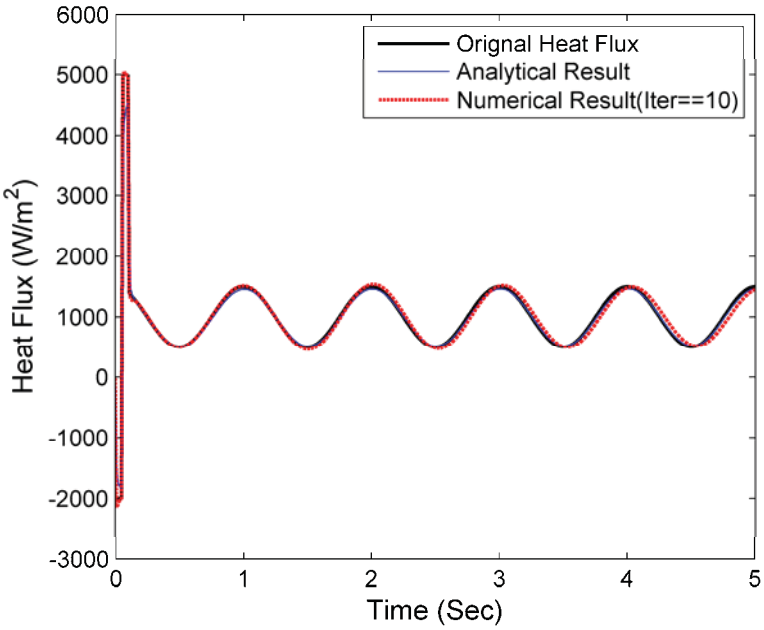

Figure 3.5. Comparison of the recovered heat flux by using the numerical inverse method and analytical method for a 0.01mm PVC layer on a semi-infinite Nylon-6 base, where the thermal properties of PVC are temperature-dependent

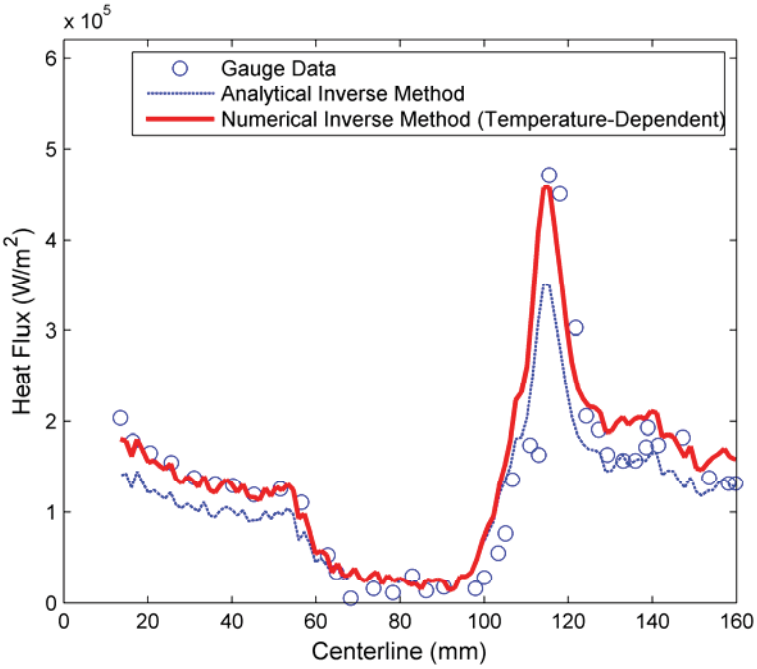

Figure 3.6. The averaged heat distributions along the centerline on the sharp $25^{o}/45^{o}$ indented cone model at Mach 11

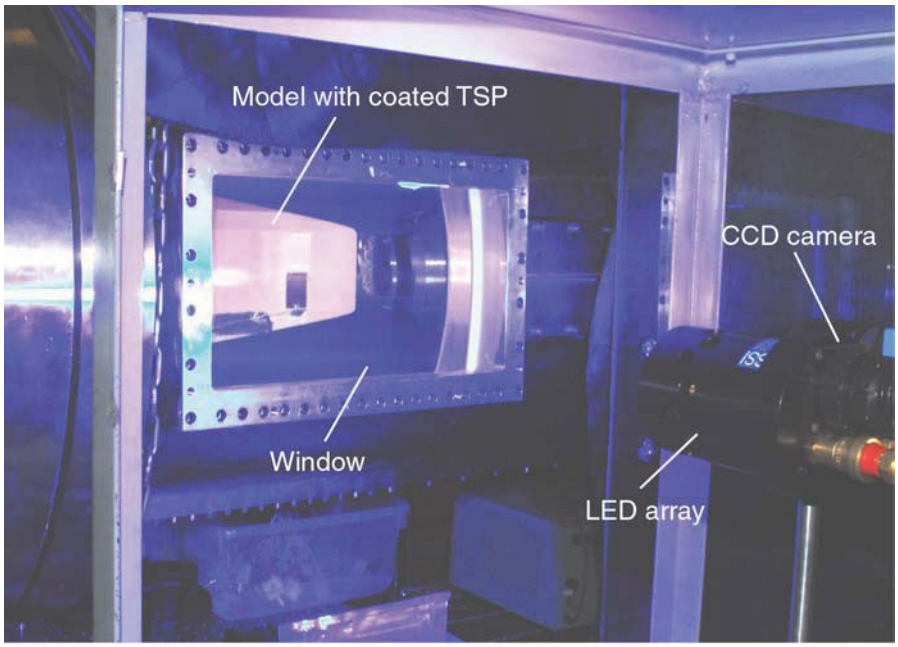

Figure 3.7. A generic setup of a CCD camera and a UV LED array for illuminating the TSP on a model at the Purdue Mach-6 tunnel

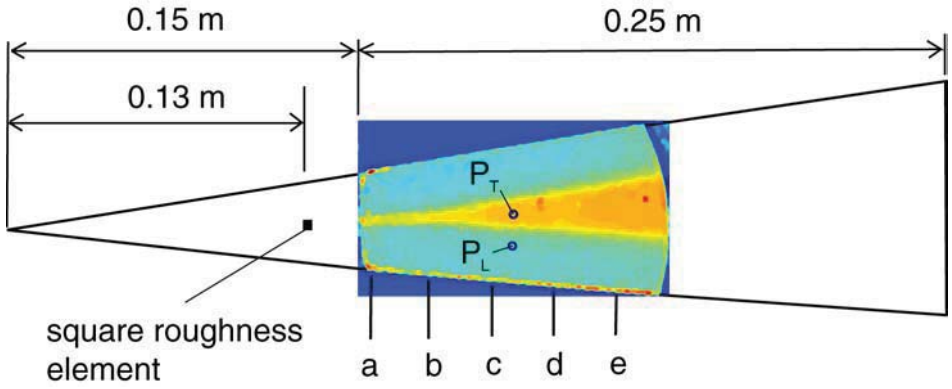

Figure 3.8. Region of TSP measurements on a 7°-half-angle circular cone

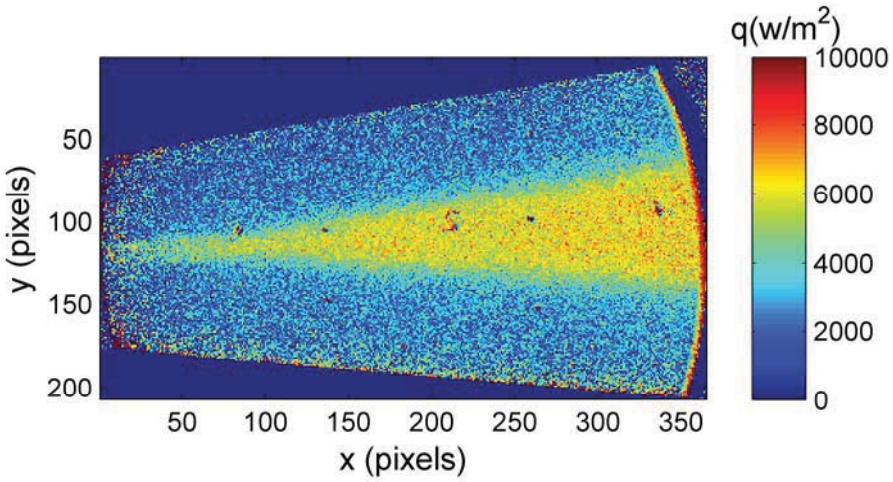

(a)

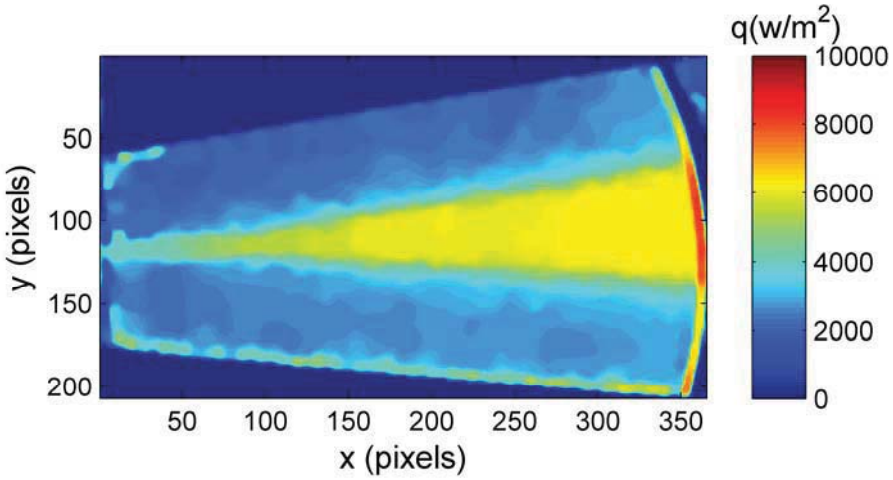

(b)

Figure 3.9. Heat flux images on a 7°-half-angle circular cone at Mach 6 at t =3 s, (a) image obtained by using the numerical inverse method, and (b) image improved by using the image deconvolution method

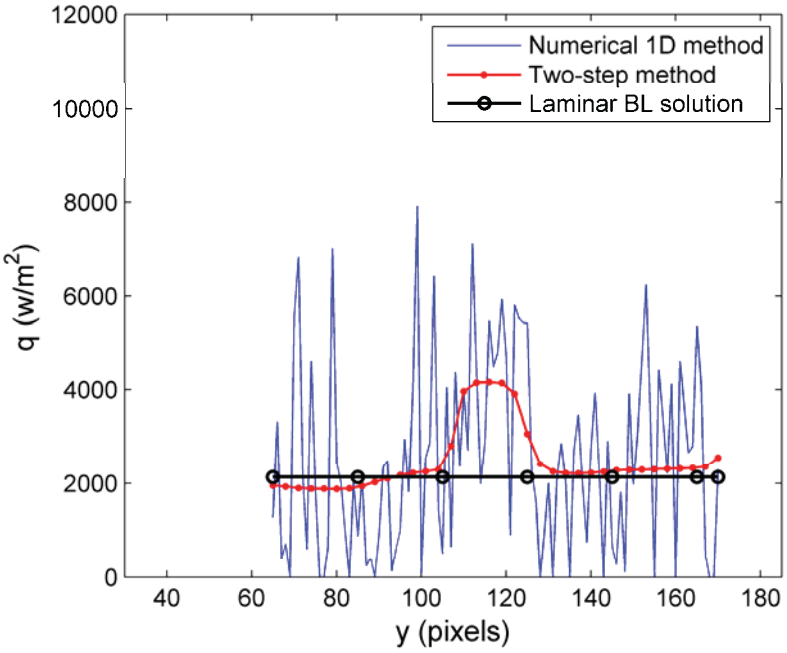

(a)

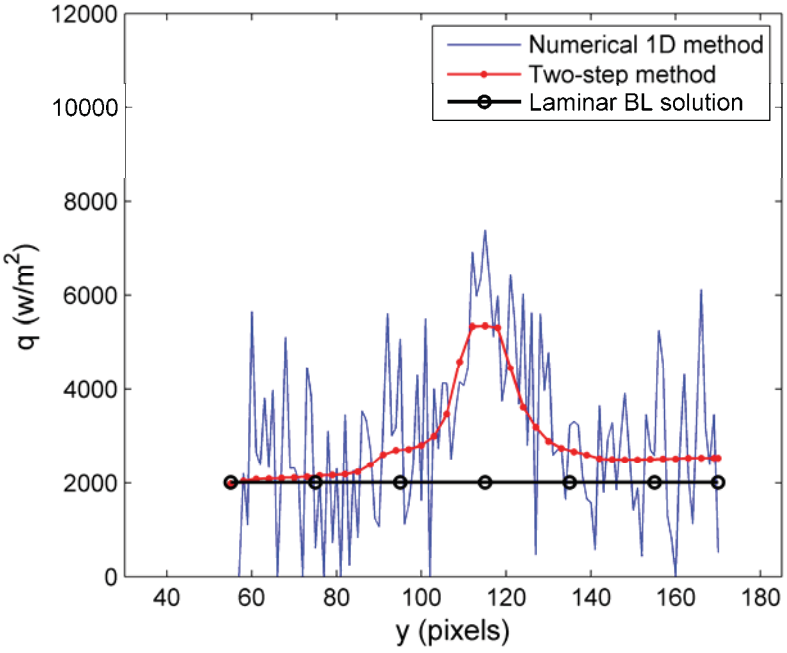

(b)

Figure 3.10. (continued)

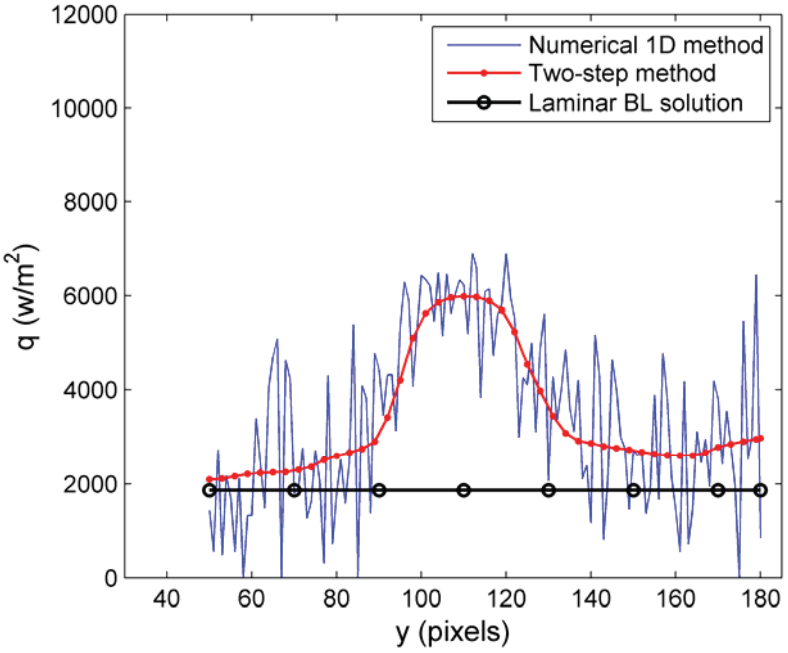

(c)

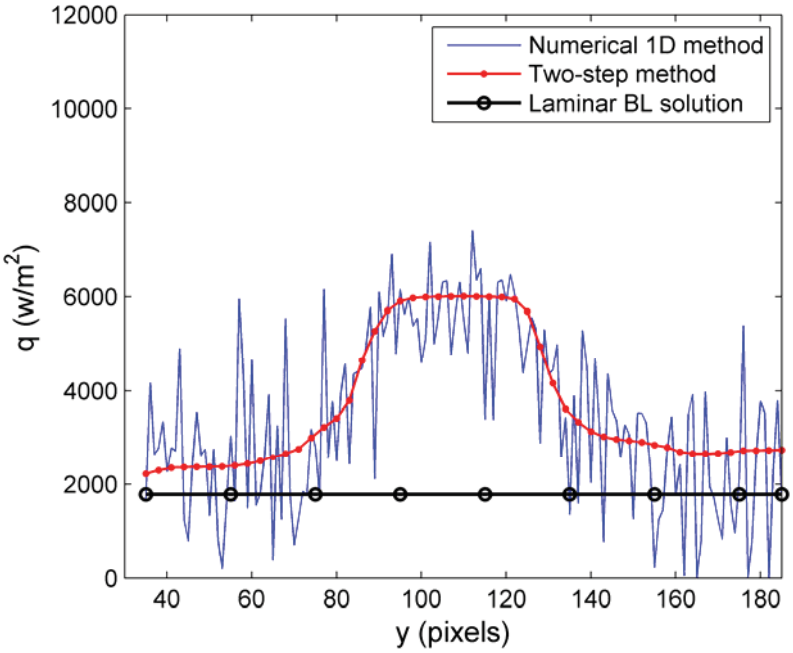

(d)

Figure 3.10. (continued)

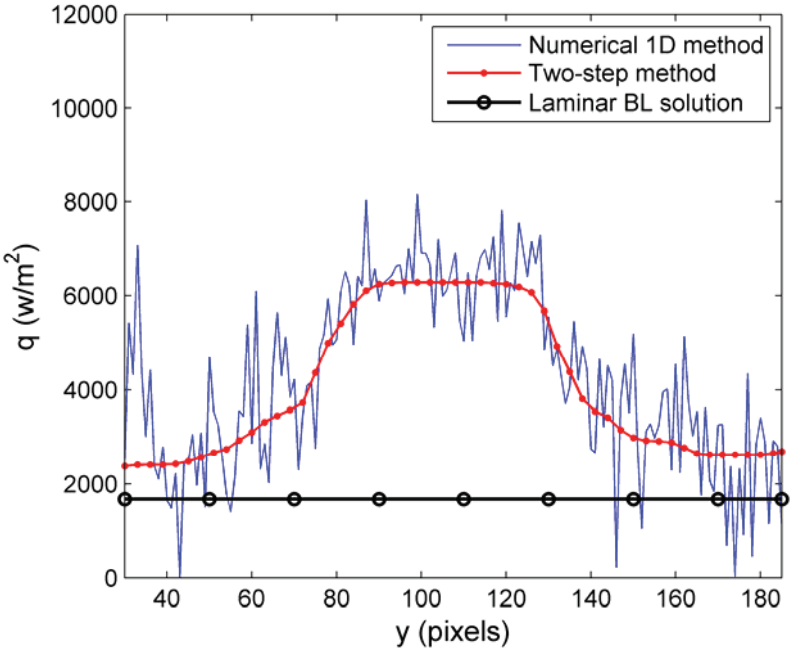

(e)

Figure 3.10. Heat flux distributions across the cone at (a) x = 0.16 m, (b) 0.18 m, (c) 0.21 m, (d) 0.23 m and (e) 0.26 m at t = 3 s from starting the tunnel. The results are obtained by the numerical inverse method with the temperature-dependent thermal properties in comparison with the laminar boundary layer solution. Further, the results are improved by using the image deconvolution method.

4. Correcting Lateral Heat Conduction Effect

The image deconvolution method is developed, which is coupled with the one-dimensional (1D) analytical inverse method to calculate more accurate heat flux fields by correcting the lateral heat conduction effect in image-based surface temperature measurements. The theoretical foundation is a convolution-type integral equation with a Gaussian filter (kernel) that relates a heat flux field obtained by using the 1D inverse method on a surface to the true heat flux field. The accuracy of this method is evaluated and the standard deviation in the Gaussian filter is determined for different materials through simulations. This method is used to calculate heat flux fields in temperature-sensitive-paint measurements on a 7^{o}-half-angle circular cone at Mach 6 in a short-duration hypersonic wind tunnel. In addition, a simple method is proposed to solve a projection problem associated with image deconvolution for a highly curved developable surface.

4.1. Introduction

The transient solutions of the one-dimensional (1D) time-dependent heat conduction equation have been used in heat flux calculations from data given by conventional local gauges like thin-film thermocouples in aerothermodynamic measurements hypersonic wind tunnels (Schultz and Jones 1973). The Cook-Felderman method, which is based on the classical 1D transient solution for a semi-infinite body, has been widely used to calculate heat flux from a time history of the surface temperature (Cook and Felderman 1970). This 1D method has been further adapted by Merski (1998, 1999) to process thermographic phosphor data obtained on a model injected to a hypersonic wind tunnel. The performance of several 1D methods has been evaluated by Walker and Scott (1998). In principle, the 1D heat conduction equation can be directly solved using a finite difference or finite element method to calculate heat flux when measured temperature fields are imposed as a boundary condition. However, due to the ill-posed nature of the problem, this forward numerical calculation of the temperature gradient is sensitive to the uncertainty of surface temperature measurements. In fact, the determination of heat flux from measured temperature fields is generally considered as an inverse or quasi-inverse heat transfer problem. Experiments in short-duration hypersonic wind tunnels have shown that the 1D method is able to give reasonably good results when it is applied to a 3D body. Even the discrete Fourier law, the simplest 1D method, is applicable to calculation of heat flux in TSP measurements in hypersonic wind tunnels for high-conductive metal bodies.

However, the 1D method ignores the lateral heat conduction effect on a 3D body that could be significant at certain locations where the spatial gradient in heat flux is large. The large gradient in heat flux is often found near shocks, shock/shock interaction, shock/boundary-layer interaction, boundary-layer transition, flow separation, and strong vortex/wall interaction. The application of the 1D method to a complex 3D body in complex flows may have some errors in some regions with high curvature. In general, to take the lateral heat conduction effect into account in heat flux calculation, an inverse solution for the 3D time-dependent heat conduction equation can be sought by using a finite-difference method or finite-element method coupled with an optimization method when suitable boundary conditions on the given geometry are imposed. However, the computational cost of this full numerical approach is high. To deal with the lateral heat conduction in heat flux calculation, Estorf (2005) obtained a formal analytical solution of the 3D time-dependent heat conduction equation by using the Fourier transform for a semi-infinite body, and then solved an inverse problem by using the regularization method for the transformed heat flux in the Fourier space. Further, the solution for heat flux in the physical space is given by inverting the Fourier transform. The Estorf's method, which combines the

analytical solution and the numerical regularization method, is advantageous in its simplicity and efficiency of computation relative to full numerical methods. However, the Estorf's method is not applicable to two-layer and multi-layer systems in temperature-sensitive coating techniques. The sensor coating itself could significantly alter a time history of surface temperature and as a result affect calculation of heat flux.

The objective of this work is to develop a simple and efficient method for calculating heat flux from image-based surface temperature measurements by temperature-sensitive coating techniques and IR camera. The coating techniques include temperature sensitive paint, thermographic phosphors and thermochromic liquid crystals. First, from a time sequence of measured surface temperature fields, heat flux fields on a surface are calculated by using the 1D analytical inverse method developed by Liu et al. (2010) for a polymer layer on a semi-infinite body. Note that a sensor polymer layer itself in the coating techniques also influences a time history of heat flux, and therefore its effect must be taken into account in heat flux calculations. Here, a TSP (TSP/insulator) layer, thermographic phosphor layer, or thermochromic liquid crystal layer is loosely referred to as a polymer layer. The results given by the 1D method are reasonably good in many cases. For further improvement, however, the lateral heat conduction effect should be corrected as the second step.

Based on an analogy between the 1D and 3D solutions of the heat conduction equation, a convolution-type integral equation with a Gaussian filter (kernel) is given as a model for correcting the lateral heat conduction effect. In this equation, a heat flux field obtained by using the 1D method is actually a Gaussian-filtered (spatially-averaged) heat flux field in a 3D case. This physical meaning is clear and intuitive. To extract the true heat flux field by solving this integral equation, this problem is mathematically equivalent to the classical image deconvolution problem or the image restoration problem, and the adaptive total variation regularization method can be used directly. Therefore, a two-step method is proposed to calculate heat flux fields from a time sequence of surface temperature images. The 1D inverse method is first used to calculate heat flux one point by one point on a surface, and then the image deconvolution method is applied to heat flux images obtained by using the 1D inverse method as a field approach to correct the lateral heat conduction effect and remove the random noise. To assess the accuracy of the two-step method and determine the empirical standard deviation in the Gaussian filter in the integral equation, simulations are conducted for a uniformly distributed heat flux source suddenly applied onto a surface in a square region. The two-step method is used in TSP measurements on a 7^{o}-half-angle circular cone in a Mach-6 hypersonic wind tunnel. Furthermore, a simple method is proposed to solve a projection problem associated with image deconvolution for a highly curved developable surface like the conical surface. Although the applications in aerothermodynamics are emphasized in this paper, the two-step method is applicable to image-based heat flux measurements in various applications.

4.2. 1D Inverse Solution

Recently, Liu et al. (2010) have given a 1D analytical inverse solution for calculating heat flux from TSP surface temperature measurements. Here, the solution is briefly recapitulated for convenience of reading. Figure 4.1 shows a thin polymer layer on a semi-infinite base and a coordinate system used in this study. The transient solution of the 1D time-dependent heat conduction equation is sought by inverting the Laplace transform for a thin polymer on a semi-infinite base. The heat flux $q_{s(1D)}(t)$ at the polymer surface is given by the 1D solution Eq. (2.1) or Eq. (2.3). The corresponding numerical inverse method to the analytical inverse solution

is given by Cai et al. (2011) to deal with the temperature-dependent thermal properties of materials.

4.3. Inverse Problem for Correcting Lateral Heat Conduction Effect

Generally, Eq. (2.1) is able to give reasonable results when it is applied to a 3D model in tests in a short-duration wind tunnel, and the recovered heat flux at a point on a surface can be intuitively considered as a certain averaged value in the neighborhood of that point. However, in a general 3D case, heat conduction in the lateral direction may be significant in certain locations where the spatial gradient in heat flux is large. This situation occurs near shocks, shock/shock interaction, shock/boundary-layer interaction, boundary-layer transition, flow separation, and strong vortex/wall interaction. Further improvement should be made by correcting the lateral heat conduction effect. As shown in Appendix B, based on the connection between the 1D and 3D solutions of the heat conduction equation, a heat flux field $q_{s(1D)}(t,x,z)$ obtained by using the 1D inverse method on a surface in a general 3D case is a spatially-averaged heat flux, i.e.,

$$(1+\Delta\lambda)\, q_{s(1D)}(t,x,z) = \int_{-\infty}^{\infty}\int_{-\infty}^{\infty} g\left[x-x', z-z'; \sigma_r(t)\right] q_s(t,x',z')\,dx'\,dz' \ . \tag{4.1}$$

The filter in Eq. (4.1) is the Gaussian distribution

$$g(x,z;\sigma) = \frac{1}{2\pi\sigma^2} exp\left(-\frac{x^2+z^2}{2\sigma^2}\right) \tag{4.2}$$

where $\sigma_r(t)$ is a standard deviation that represents the extent of the lateral heat conduction effect, $\Delta\lambda$ is a relative surface temperature change due to the lateral heat conduction (see Appendix), and t is the time elapsing from the start-up of a wind tunnel. In most applications where $\Delta\lambda << 1$ except at certain isolated region, $\Delta\lambda$ can be set at zero in the first-order approximation. In a sense, Eq. (4.1) is an approximate model since $\sigma_r(t)$ should be modeled. The linear relation $\sigma_r(t) = r_1 L_{diffu} + r_0$ is proposed as a model, where $L_{diffu} = \sqrt{2 a_p t}$ is the thermal diffusion length scale, and r_1 and r_0 are empirical coefficients to be determined. Furthermore, since the analysis of heat conduction in Appendix is made for a flat surface, Eq. (4.1) is a reasonable model for a surface whose curvature radius is much larger than $L_{diffu} = \sqrt{2 a_p t}$. Therefore, given $q_{s(1D)}(t,x,z)$, $q_s(t,x,z)$ can be recovered by solving the convolution-type integral equation Eq. (4.1) as an inverse problem.

Interestingly, this problem to solve Eq. (4.1) for $q_s(t,x,z)$ is the exactly same as the classical image deconvolution problem or the image restoration problem (Helstram 1967, Banham and Katsaggelos 1997). This coincidence is not surprising since image blurring is generally modeled by a diffusion process. In image-based surface temperature measurements, $q_{s(1D)}(t,x,z)$ and $q_s(t,x,z)$ are usually given in the image plane, and therefore they are conveniently treated as images in processing. Therefore, the existing image deconvolution algorithms can be directly applied to our problem. The total variation regularization method developed by Oliveria et al. (2009) is used in this paper. Based on the above discussions, the two-step method is proposed to calculate heat flux fields from a time sequence of surface temperature images, where the 1D inverse method is used in tandem with the image deconvolution method. Figure 4.2 is a flowchart of the two-step processing. The 1D inverse method is applied to a time sequence of temperature images one pixel by one pixel (one point by

one point on a surface) to obtain heat flux images at different times. Then, the resulting heat flux images are further processed one image by one image by using the image deconvolution method to reconstruct a time sequence of more accurate heat flux images. The key idea of the two-step method is that heat flux calculation in the normal direction to a surface is carried out without considering the lateral heat conduction effect as the first-order approximation, and then correcting the lateral heat conduction effect is treated separately as the image deconvolution problem.

4.4. Simulations

To facilitate image processing, Eq. (4.1) is projected onto the image plane. A special case is considered, where the image plane of a camera is parallel to the measured plane. In this case, the projection transform between the surface coordinates (x,z) in meters and the image coordinates (x_{pix}, z_{pix}) in pixels is particularly simple, i.e., $(x,z) = \lambda^{-1}(s_x x_{pix}, s_z z_{pix})$, where λ is a non-dimensional scaling constant, and (s_x, s_z) are the factors converting pixel to meter (meter/pixel) in the x and z coordinates. Therefore, Eq. (4.1) is written in the image coordinates as

$$(1+\Delta\lambda)\, q_{s(1D)}(t, x_{pix}, z_{pix}) = \int_{-\infty}^{\infty}\int_{-\infty}^{\infty} g\left[x_{pix} - x'_{pix}, z - z'_{pix}; \sigma_{r,pix}(t)\right] q_s\left(t, x'_{pix}, z'_{pix}\right) dx'_{pix}\, dz'_{pix} \quad , \tag{4.3}$$

where the filter function is

$$g\left(x_{pix}, z_{pix}; \sigma_{r,pix}\right) = \frac{1}{2\pi\sigma_{r,pix}^2} exp\left(-\frac{(s_x/s_z)^2 x_{pix}^2 + z_{pix}^2}{2\sigma_{r,pix}^2}\right). \tag{4.4}$$

The standard deviation $\sigma_{r,pix}(t)$ in pixels will be determined by optimization in simulations. A suitable model is $\sigma_{r,pix}(t) = (r_1 L_{diffu} + r_0)(\lambda / s_z)$, where $L_{diffu} = \sqrt{2 a_p t}$ is the thermal diffusion length scale, and r_1 and r_0 are empirical coefficients to be determined in simulations for different materials.

Simulations are conducted to examine the capability of the two-step method for correcting the lateral heat conduction effect. A CCD camera/lens system with a principal distance $c = 70\,mm$ (approximately the focal length) is located $990\ mm$ away from the measured plane that is parallel to the image plane. Therefore, the scaling constant is $\lambda = 0.0707$. If the size of a CCD sensor is $10\,mm \times 10\,mm$ and the numbers of both the horizontal and vertical pixels are 1000, the converting factors are $s_x = s_z = 10^{-5}$ m/pixel, and the factor λ / s_z is 0.707×10^4 pixel/m. A uniformly distributed heat flux source of $1000\ W/m^2$ is suddenly applied onto a surface in a square region of $9.1\,mm \times 9.1\,mm$ that corresponds to $64\,pixels \times 64\,pixels$ in the image plane, while the heat flux source is zero outside the square region. The time history of the surface heat flux is given by $q_s(t,x,z) = q_0(x,z)H(t)$, where $H(t)$ is a Heaviside function ($H(t) = 0$, if $t = 0$ and $H(t) = 1$, if $t > 0$), and $q_0(x,z) = 1000$ if $(x,z) \in D$ and $q_0(x,z) = 0$ if $(x,z) \notin D$ where D denotes the square region. As a typical case, we consider a 0.25 mm thick Mylar layer on a semi-infinite base of Nylon whose thermal properties are given in Table 2.1.

A time sequence of temperature images at the polymer surface is calculated by using Eq. (B24) in Appendix over a time span of 3 s in a time step of 0.1s after switching on the heat flux source. Figure 4.3 shows typical surface temperature distributions at t = 1.5, 2 and 2.5 s, which clearly indicating the effect of the lateral heat conduction near the edges of the square region. Then, a zero-mean white noise with a signal-to-noise ratio of 10 dB is added on the surface temperature images, and heat flux images are calculated pixel by pixel by using the 1D inverse method from a time sequence of the corresponding noisy surface temperature images. Figure 4.4 shows typical surface heat flux distributions at t = 1.5, 2 and 2.5 s obtained by using the 1D inverse method. The random noise patterns in these images mimics those in typical image-based heat flux measurements. The resulting random noise in heat flux in Fig. 4.4 is contributed by the random error sources in both the time and space domains. The random error source in the time domain mainly affects the calculation of heat flux through the time derivative of the surface temperature in Eq. (4.1) or (4.3). The cubic spline smoothing technique in the time domain has been used to minimize the random error in surface temperature and obtain smooth results (Taler 1996, Taler and Duda 2006). Similarly, a spatial filer could be used to remove the spatial random noise in surface temperature images at a cost of smearing sharp spatial features. In this work, such preprocessing is not applied to surface temperature images before calculation of heat flux, and it will be demonstrated that the image deconvolution method can not only remove the random noise, but also recover the sharp spatial features from diffused (blurred) heat flux images. More importantly, Eq. (4.1) as a model for image deconvolution has a physical foundation.

The deconvoluted heat flux images from the blurred noisy images in Fig. 4.4 are obtained by using the algorithm developed by Oliveria et al. (2009) to solve Eq. (4/3). For a Mylar layer on Nylon, the optimal standard deviation $\sigma_{r,pix}(t) = (r_1 L_{diffu} + r_0)(\lambda / s_z)$ in pixels is used, where $r_1 = 0.505$ and $r_0 = 3.56 \times 10^{-5}\ m$ that are determined by optimization (it will be discussed later). Figure 4.5 shows the deconvoluted surface heat flux distributions at t = 1.5, 2 and 2.5 s. These results indicate that the sharp edges in the heat flux distributions are recovered and the random noise is removed by using the image deconvolution method. For direct comparison with the given heat flux distribution in simulations, Figure 4.6 shows the surface heat flux distributions along the symmetrical axis across the square region calculated by using the 1D inverse method and the two-step method at t = 1.5, 2 and 2.5 s. Improvement by using the image deconvolution method is evident to remove the effect of the lateral heat conduction effect. For quantitative comparison, a relative error is defined as

$$error = \frac{\sum \left| q_{cal}(i,j) - q_{given}(i,j) \right|}{\sum \left| q_{given}(i,j) \right|}, \tag{4.5}$$

where q_{cal} and q_{given} are the calculated and given heat flux images, respectively. Figure 4.7 shows the relative errors in the heat flux fields calculated by using the 1D inverse method and the two-step method. A significant decrease in the relative error is achieved by using the image deconvolution method. It is noted that simulations were also conducted for other time histories of $q_s(t,x,z)$ such as $q_s(t,x,z) \propto \sqrt{t}$ and $q_s(t,x,z) \propto sin(t)$, and similar improvements were achieved.

A practical problem is how to determine the optimal standard deviation $\sigma_{r,pix}(t)$ in Eq. (4.6) for image deconvolution. Clearly, the optimal standard deviation depends on the thermal pr3perties of a polymer layer and a base. For an initial guess of $\sigma_{r,pix}(t)$, the given heat flux

image is substituted to Eq. (4.3) for $q_s(t, x_{pix}, z_{pix})$ to obtain a true filtered heat flux image, and then a L^2-norm difference between this true filtered image and the heat flux image obtained by the 1D inverse method from noisy temperature images is evaluated. The optimal value of $\sigma_{r,pix}(t)$ is determined by minimizing the L^2-norm difference. To find the optimal values of $\sigma_{r,pix}(t)$, computations are conducted for two polymers (Mylar and PVC) and three base materials (Nylon, stainless steel and aluminum). Figure 4.8(a) shows the optimal standard deviation $\sigma_{r,pix}(t)$ in pixels as a function of the thermal diffusion length scale $L_{diff,pix} = L_{diffu} \times (\lambda / s_z)$ in pixels for 0.25 mm thick Mylar and PVC on Nylon and the semi-infinite bases of Mylar, PVC and Nylon, where $L_{diffu} = \sqrt{2 a_p t}$ is the thermal diffusion length scale. The data for these low-conductive polymer materials are close each other. Figure 4.8(b) shows the optimal standard deviation $\sigma_{r,pix}(t)$ for 0.25 mm thick Mylar and PVC on stainless steel and aluminum, where the slopes of the curves for the metal bases are much smaller than those for the polymers. Clearly, for all the cases, the linear relation $\sigma_{r,pix}(t) = (r_1 L_{diffu} + r_0)(\lambda / s_z)$ in pixels for the optimal value is validated over a considerable range of $L_{diff,pix} = L_{diffu} \times (\lambda / s_z)$. The empirical coefficients r_1 and r_0 for the optimal value of $\sigma_{r,pix}(t)$ depend on the thermal properties of the polymer and base materials. Table 4.1 lists the values of r_1 and r_0 obtained by a linear fit to the data in Fig. 4.8 for different materials. For specific measurements, such simulations are useful to determine the optimal values of the empirical standard deviation in Eq. (4.3) for image deconvolution. In addition, simulations indicate that 10-20% variation in the optimal value of $\sigma_r(t)$ may occur for different time histories of $q_s(t,x,z)$. Therefore, it is suggested that simulation would be conducted for a time history that is close to the actual one in a particular experiment.

4.5. Heat Flux Measurements on a 7°-Half-Angle Circular Cone at Mach 6

4.5.1. Experimental Set-Up

TSP measurements on a 7°-half-angle Nylon cone were conducted at zero angle of attack in the Boeing/AFOSR Mach-6 Quiet Tunnel at Purdue University. In our experiments, the total temperature and pressure were initially 433 K and 255 psi, and then they decreased at the rates of 5 K/s and 30 kPa/s over a run time of 4 s, respectively. The 7°-half-angle Nylon cone is 0.4 m (16 inches) long, including a 0.15 m long stainless steel nosetip that has a 0.06 inch nose radius. The TSP, Ru(bpy) in Chromaclear auto paint, was directly coated on the Nylon surface. The coating thickness was about 50 microns.

Figure 3.7 shows a generic setup of a CCD camera with a band-pass optical filter for detecting the luminescent emission from the TSP and a blue LED array for illuminating the TSP on a model in a dark environment in the Mach-6 tunnel. The camera (POC 1600) and blue LED array are produced by Innovative Scientific Solutions Incorporated (http://www.innssi.com). The time step in a sequence of 45 images acquired by the camera was 0.107 s. In our experiments where the total pressure was relatively high, a smaller circular window was used. A viewed region near the middle section of the cone is illustrated in Fig. 3.8. A square roughness element with a 1.27×1.27 mm^2 cross-section and a height of 0.28 mm was placed at 0.13 m from the nosetip to trigger the boundary-layer transition to turbulence.

4.5.2. Processing in Images of Cone Surface

Surface temperature images were obtained by using Eq. (3.9) from a sequence of TSP images, and then heat flux images are calculated at every pixel by using Eq. (2.3). In the use of Eq. (2.3), it is assumed that the TSP has the same thermal properties as Mylar. Table 2.1 lists the thermal properties of Mylar and Nylon. Figure 4.9 shows heat flux images obtained by using the 1D inverse method on a 7^o-half-angle circular cone at Mach 6 at t = 1, 2, and 3 s from starting the tunnel. These images clearly indicate the formation and evolution of a turbulent wedge triggered by a roughness element in the boundary layer, which is evidenced by the difference in heat flux between the turbulent and laminar flow regimes. The significant random spiky noise found in these images is typical in TSP measurements (as well as in other coating techniques and IR camera) particularly when a temperature change to be measured is small.

The next step is the application of the image deconvolution method to the heat flux images obtained by using the 1D inverse method to correct the lateral heat conduction effect. In our camera setting, one pixel in the image plane corresponds to 0.32 mm on the cone surface in the object space. Based on the data for a Mylar layer on Nylon in Table 4.1, an estimate for the optimal standard deviation is $\sigma_{r,pix}(t) = 0.69\sqrt{t} + 0.11$ in pixels, where t is in seconds. For $t = 3\ s$, $\sigma_{r,pix}(t) = 1.3$ pixels, which indicates that the lateral heat conduction effect does not appear significant in the image plane in this case where the characteristic length scale across the edges of the turbulent wedge between the laminar and turbulent regions is about 10 pixels. Therefore, the application of the image deconvolution method mainly removes the random noise while the structures in the heat flux images are preserved.

In general, the inverse solution for Eq. (4.1) is sought in the surface orthogonal coordinate system in the object space. In the above simulations, image deconvolution based on Eq. (4.3) assumes that the planar surface is parallel to the image plane such that the simplest form of the perspective transformation can be used. However, the circular cone surface is not parallel to the image plane, and the image of the cone surface is formed through the general perspective projection transformation or the collinear transformation. As a result, the form of the integral equation Eq. (4.1) becomes complicated after the perspective projection transform is applied to it, and in particular the Gaussian filter is not homogenous and isotropic in the image coordinates. Computations for solving this problem become more difficult. Before this problem will be further discussed, the image deconvolution method is applied to the heat flux images in Fig. 4.9 under an assumption that the image plane is approximately parallel to the major portion of the cone. Figure 4.10 shows the deconvoluted heat flux images on the circular cone at Mach 6 at t = 1, 2, and 3 s from starting the tunnel. It can be seen that the sharp changes across the transition lines from the laminar to turbulent flow regions are retained in this case while the random spike noise are largely removed. Therefore, the more accurate heat flux fields are extracted from the very noisy images by using the image deconvolution method.

For more quantitative comparison, the heat flux distributions across the cone in the lateral direction have been examined at several streamwise locations marked in Fig. 3.8. Furthermore, for reference, the values of heat flux at these locations in the laminar boundary layer on the circular cone at Mach 6 under the testing conditions at t = 3 s (the total temperature and wall temperature are 418 K and 305 K, respectively, and the total pressure is 242 psi) are calculated by using the similarity solution and the reference temperature method. The similarity solution exists for a hypersonic laminar boundary layer on a circular cone (Marvin and Deiwert 1965, White 1974). The reference temperature method is originally based on the similarity solution for

a flat plate (White 1974), and for a circular cone, a factor of $\sqrt{3}$ is multiplied to the estimated heat flux according to the Mangler transformation. For both the similarity solution and the reference temperature method (see Appendices C and D), the Taylor-Maccoll solution for the conical flow is used for the outer flow conditions (Sims 1964, Anderson 1990). Computations of hypersonic flows and heat transfer are sensitive to the temperature dependencies of the viscosity and thermal conductivity of air. The relatively new models given by Lemmon and Jacobson (2004) for the thermodynamic properties are used in both the similarity solution and the reference temperature method. The heat flux distributions on the cone along the surface coordinate given by the two methods are consistent.

Figure 4.11 shows the heat flux distributions in the lateral direction (the vertical direction in images) across the cone at the streamwise locations x = 0.16, 0.18 and 0.21 m at t = 3 s from starting the tunnel along with the local values of heat flux given by the laminar boundary layer solution. These locations are marked as a, b and c in Fig. 3.8. In fact, these distributions are the projected ones of those on a circular arc of a local cross-section of the cone. Clearly, the more accurate distributions of heat flux are extracted from the images with a large random spike noise by using the image deconvolution method. This improvement is particularly appealing for the result at x = 0.16 m where the random noise is so large relative to the signal that the use of conventional filters cannot extract the signal satisfactorily. This indicates that the mathematical model for image deconvolution correctly describes the heat transfer physics. At x = 0.16 and 0.18 m where the turbulent wedge is narrow in its width and weak in its magnitude of heat flux, the TSP-measured values of heat flux outside the turbulent wedge (the laminar flow) are reasonably close to the prediction by the laminar boundary layer solution, but it is gradually increased and deviated from the solution downstream. This deviation is more evident after x = 0.21 m, indicating that the turbulent wedge increasingly influences the surrounding region along the lateral direction as it develops downstream.

Figure 4.12 shows the time histories of surface heat flux in the laminar flow (at the point P_L) and the turbulent wedge (at the point P_T), where the points P_L and P_T at x = 0.22 m are marked in Fig. 3.8. The results are obtained by using the 1D inverse method and the two-step method. There is a large oscillating change in heat flux in the start-up of the Purdue Mach-6 tunnel as indicated in Fig. 4.12, which is the result of the downstream valve which is unusual but necessary to achieve quiet hypersonic flow. The initial expansion wave during the start-up cools the test section and model, and this is followed by heating as the hot gas from upstream enters the test section. After the unusual transient start-up process, the heat flux decays slowly in the laminar flow, but it decreases much faster in the turbulent wedge with increasing time. This decaying behavior is caused by the decreases in the total temperature and pressure during a run in the tunnel. The finding that the decay of heat flux in the turbulent wedge is much faster than that in its surrounding laminar flow is interesting from a viewpoint of flow physics and worthwhile for further investigation.

4.5.3. Processing in Images of Plane Developed from Cone

As mentioned before, the Gaussian filter in Eq. (4.1) is homogenous and isotropic since the standard deviation $\sigma_r(t)$ is independent from the position and orientation on a surface in the object space. In image-based measurements, however, processing is often carried out in the image plane rather than on a surface in the object space. The integral equation Eq. (4.1) projected perspectively onto the image plane is complicated except in the simplest case demonstrated in the simulations (Liu 2004), and it does not have the homogenous isotropic

Gaussian filter. This makes computations more difficult and less efficient. An alternative is to map the heat flux data from the image plane onto the surface grid in the object space and then apply the deconvolution method to the data on the surface grid (Liu 2004). However, this approach requires data processing in the 3D space. Here, a simple method is proposed to solve this problem for a developable surface like a conical surface. Note that a general surface can be approximated by a number of pieces of developable surfaces.

A developable surface is considered, on which every point has a neighborhood that can be mapped isometrically into the Euclidean plane in the sense that arc lengths are preserved (Pottmann and Wallner 2000). A conical surface is a developable surface. The isometric mapping is a necessary condition for the application of the image deconvolution method with the homogenous isotropic Gaussian filter to a developable surface. The geometry of a circular cone surface is illustrated in Fig. 4.13(a), where $\theta_{1/2}$ is the half-angle of a circular cone, R is the base radius, and P denotes a point on the circular cone surface. Since a circular cone surface is developable, the heat flux field on the cone surface can be mapped isometrically onto the fan domain on the Euclidean plane as shown in Fig. 4.13(b), and the point P in the plane developed from the cone is given by the polar coordinates (r, β_r) originated at the tip of the fan domain. Thus, the image deconvolution method with the homogenous isotropic Gaussian filter can be applied to the fan domain (r, β_r) on the Euclidean plane. Figure 4.13(c) shows a triangular domain generated by the orthographically projection of the cone surface that is an approximation of the perspective projection when a camera is sufficiently far from the surface. The point P on the projected plane is given by the polar coordinates (s, θ_s). To map an image of the cone to the fan domain on the developed plane for image deconvolution, a relation between (r, β_r) and (s, θ_s) is needed. From Fig. 4.13, we have the transformations

$$r = s \frac{\cos \theta_s}{con\, \theta_{1/2}}, \quad \beta_r = \theta_s \frac{\pi \sin \theta_{1/2}}{2\, \theta_{1/2}}. \tag{4.6}$$

Further, by using Eq. (4.6), the deconvoluted heat flux image on (r, β_r) in the Euclidean plane can be mapped back to (s, θ_s) in the image plane.

To demonstrate the application of this method, an example is given for the heat flux image of the cone at t = 3 s [Fig. 4.9(c)] obtained by using the 1D inverse method. Figure 4.14(a) shows the heat flux image obtained by mapping the original image [Fig. 4.9(c)] onto the Euclidean plane developed from the circular cone surface via the transformations Eq. (4.6) where $\theta_{1/2} = 7^o$. The data interpretation is used in the mapping. Also, a clockwise rotational transformation of 2.4° is applied to the original image before the mapping since the horizontal axis in the image plane was not perfectly parallel to the axis of the cone in the experiments. The image deconvolution method with the homogenous isotropic Gaussian filter is applied to Fig. 4.14(a), and then the results on the developed plane are mapped back to the image plane as shown in Fig. 4.14(b). Figure 4.14(b) is the counterpart of Fig. 4.10(c) that is obtained by applying the image deconvolution method directly to the original images. Figure 4.15 shows quantitative comparison of the heat flux distributions across the cone at x = 0.26 m (the location e in Fig. 3.8) at t = 3 s between Fig. 4.14(b) and Fig. 4.10(c). In this case, the results given by the two approaches are almost the same. This is because the optimal value of the empirical standard deviation at t = 3 s is about $\sigma_{r,pix}(t) = 1.3$ pixels for a Mylar layer on Nylon, and the effect of the non-homogenous and non-isotropic property of the Gaussian filter in the image

plane is not significant. This example indicates that the image deconvolution method can be applied directly to heat flux images even for a highly curved surface like a circular cone surface when the estimated standard deviation in the Gaussian filter in Eq. (4.1) is sufficiently small.

4.6. Conclusions

The accuracy of image-based surface heat flux measurements by using temperature-sensitive coating techniques can be improved by correcting the lateral heat conduction effect. A convolution-type integral equation with a Gaussian filter (kernel) is given as a model, which physically interprets a heat flux field obtained by using the 1D inverse method as a Gaussian-filtered (spatially-averaged or spatially-diffused) heat flux field in a 3D case. Therefore, the problem for correcting the lateral heat conduction effect becomes the classical image deconvolution problem, and the total variation regularization method can be used for image deconvolution. The two-step method is developed to calculate a heat flux field from a time sequence of surface temperature images, where the 1D inverse method as a time-integral processing is used in tandem with the image deconvolution method as a field processing. In simulations, by utilizing a uniformly distributed heat flux source suddenly applied onto a surface in a square region, the accuracy of the two-step method for correcting the lateral heat conduction effect is evaluated. In particular, the linear relations between the empirical standard deviation in the Gaussian filter and the thermal diffusion length scale are determined by optimization for different materials. In temperature-sensitive-paint measurements on a 7^{o}-half-angle circular cone in the Purdue Mach-6 wind tunnel, improved heat flux images are obtained by using the two-step method to correct the lateral heat conduction effect and remove the random noise. The two-step method is not only computationally efficient and robust, but also easy to implement in applications. Furthermore, to deal with a projection problem related to the use of the image deconvolution method for a highly curved surface, a simple method is proposed and examined for a developable surface (e.g. the conical surface).

Table 4.1. Coefficients for Optimal Standard Deviation

Materials	r_1	r_0 (m)
Mylar+Nylon	0.5045	3.557×10^{-5}
PVC+Nylon	0.5603	2.208×10^{-5}
Mylar	0.5988	1.563×10^{-5}
PVC	0.6119	1.080×10^{-5}
Nylon	0.6255	3.132×10^{-6}
PVC+SS	0.0659	1.495×10^{-4}
PVC+Al	0.0287	1.572×10^{-4}
Mylar+SS	0.0575	1.515×10^{-4}
Mylar+Al	0.0245	1.586×10^{-4}

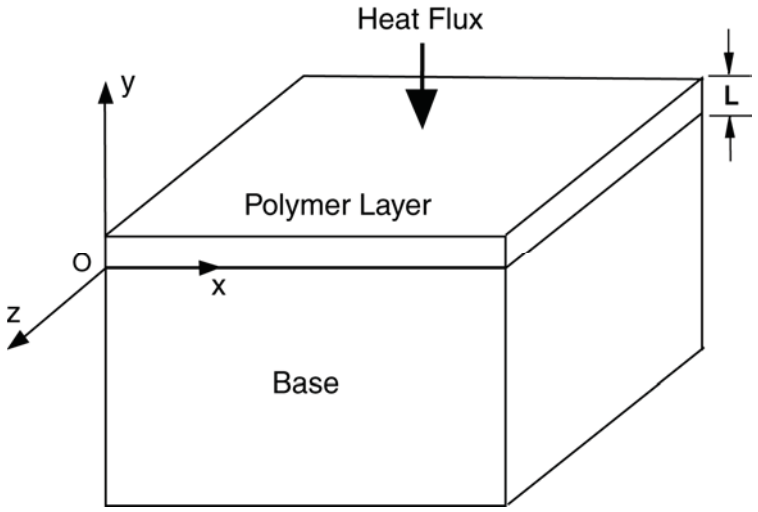

Figure 4.1. A thin polymer layer on a semi-infinite base and a coordinate system

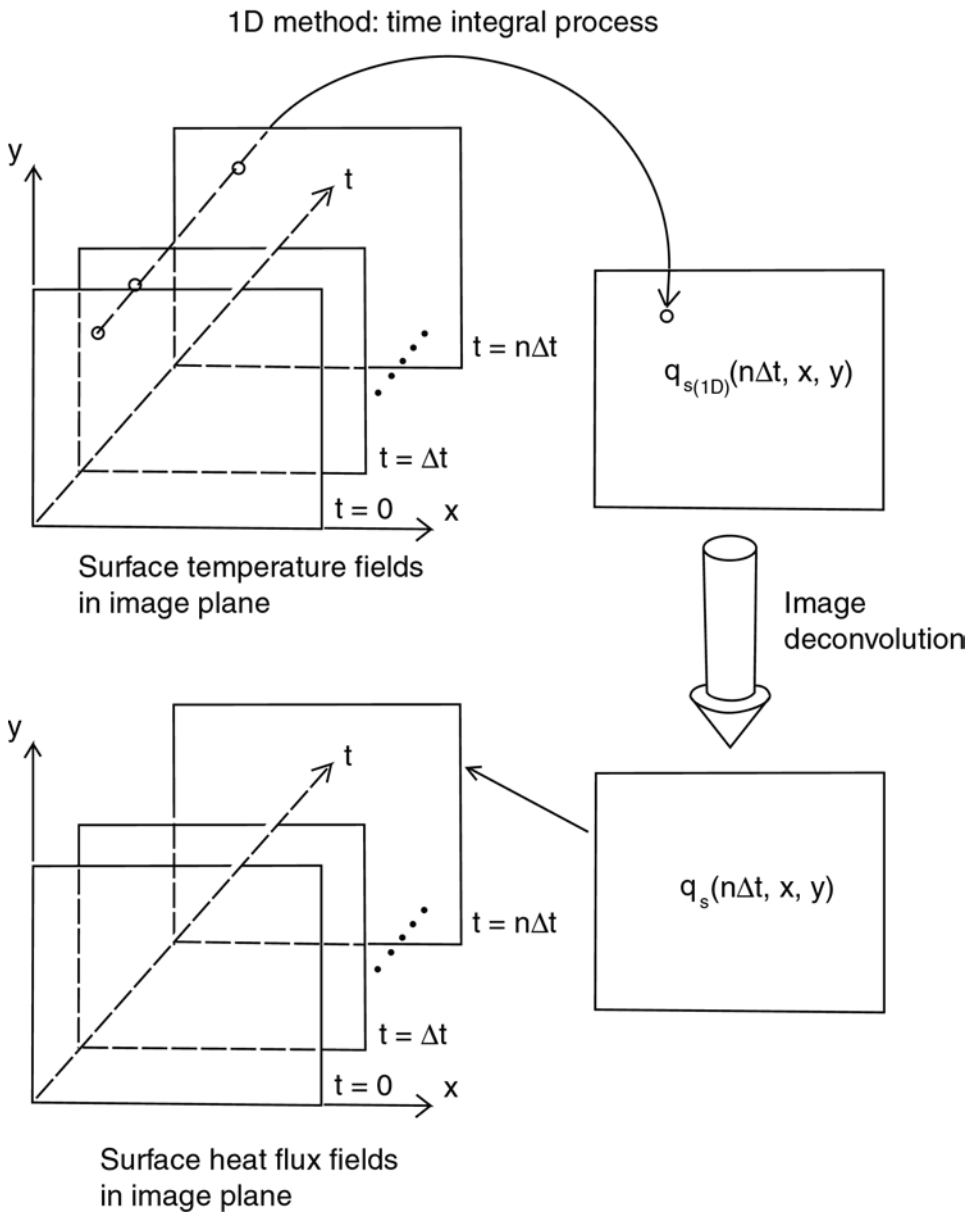

Figure 4.2. Two-step processing: the 1D inverse method coupled with the image deconvolution method

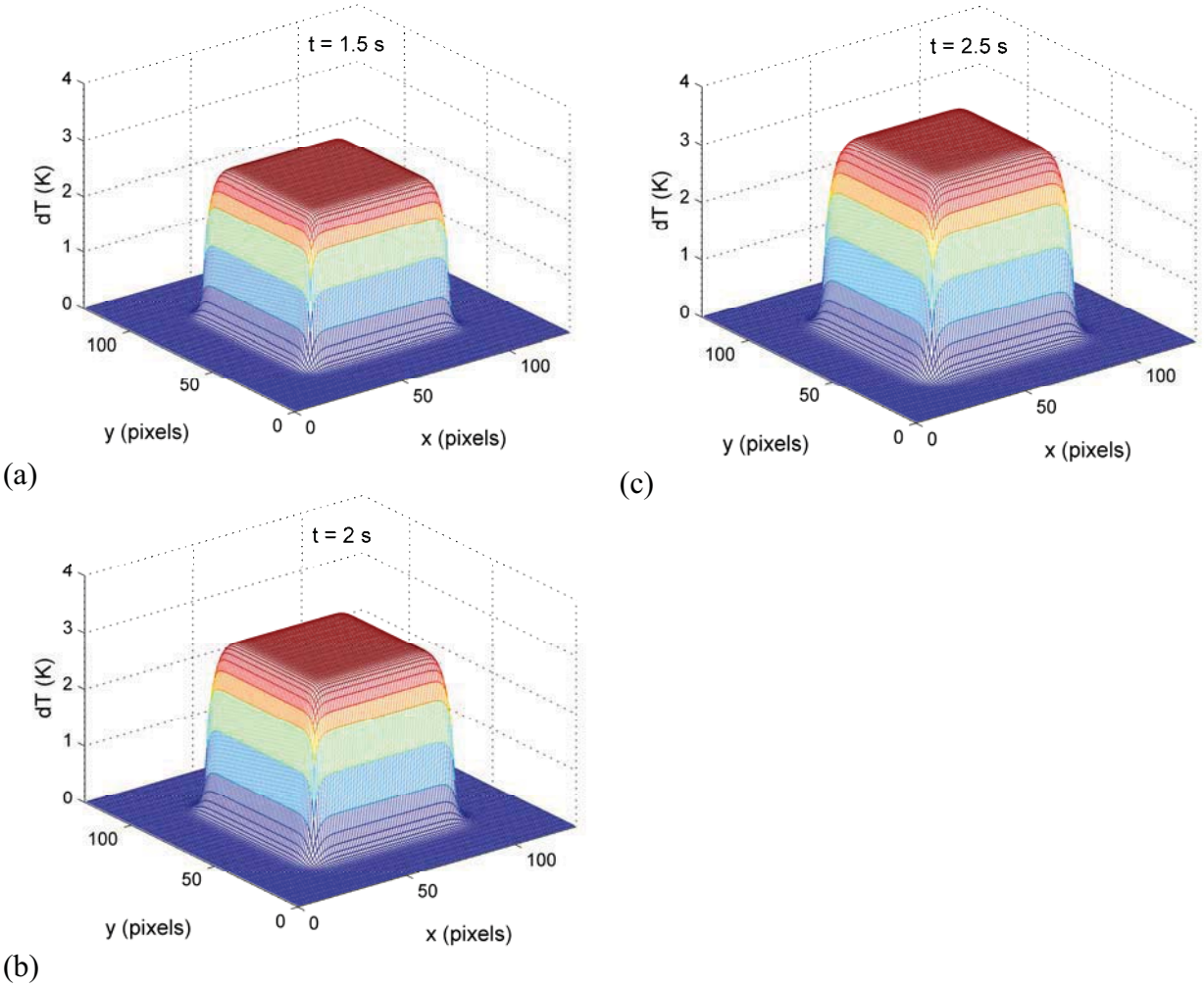

Figure 4.3. Surface temperature changes generated by a uniform heat flux of 1000 W/m^2 suddenly imposed on a square region on a Mylar layer on Nylon at (a) 1.5 s, (b) 2 s and (c) 2.5 s

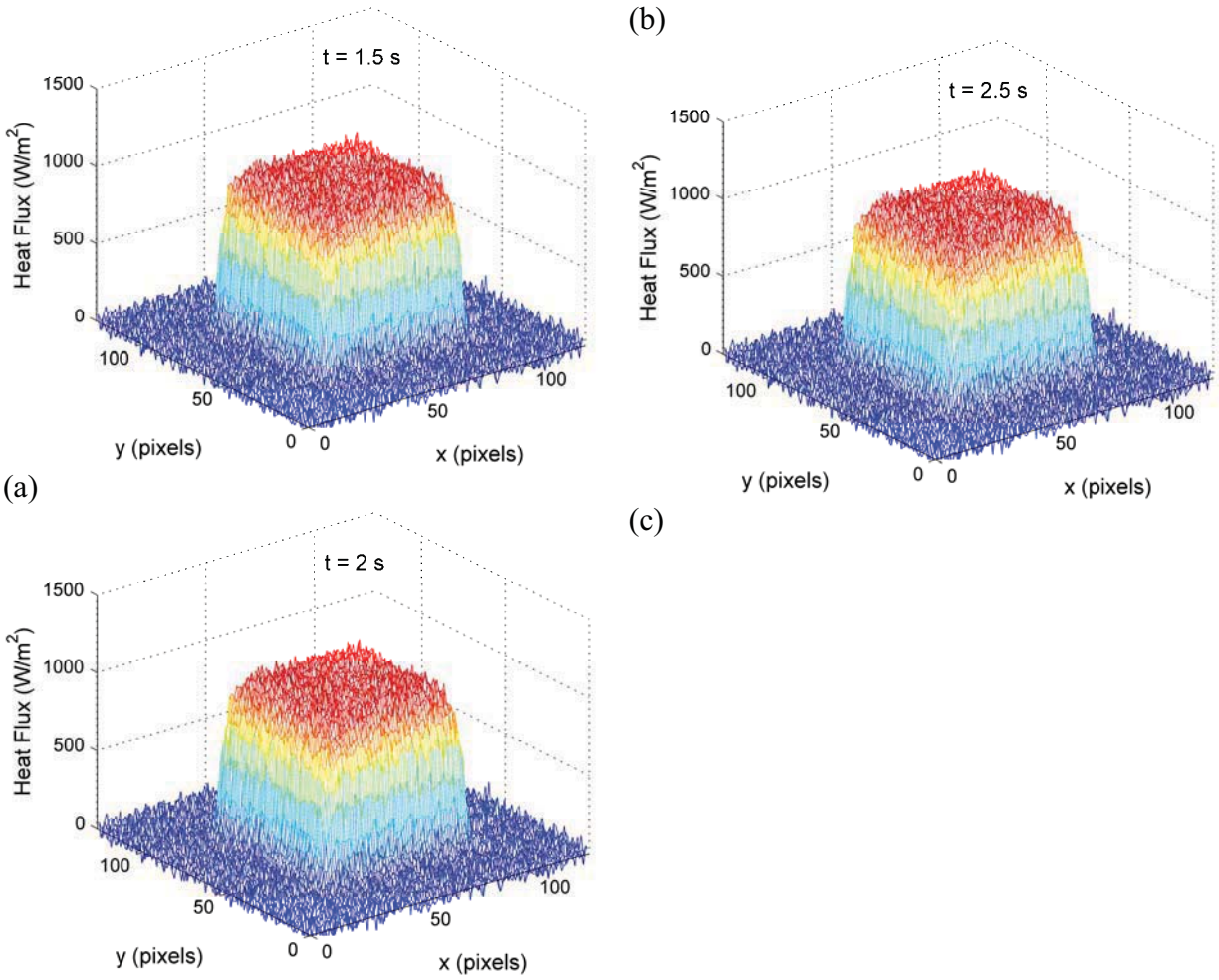

Figure 4.4. Surface heat flux distributions on a Mylar layer on Nylon calculated by using the 1D inverse method from a time sequence of noisy temperature images at (a) 1.5 s, (b) 2 s and (c) 2.5 s

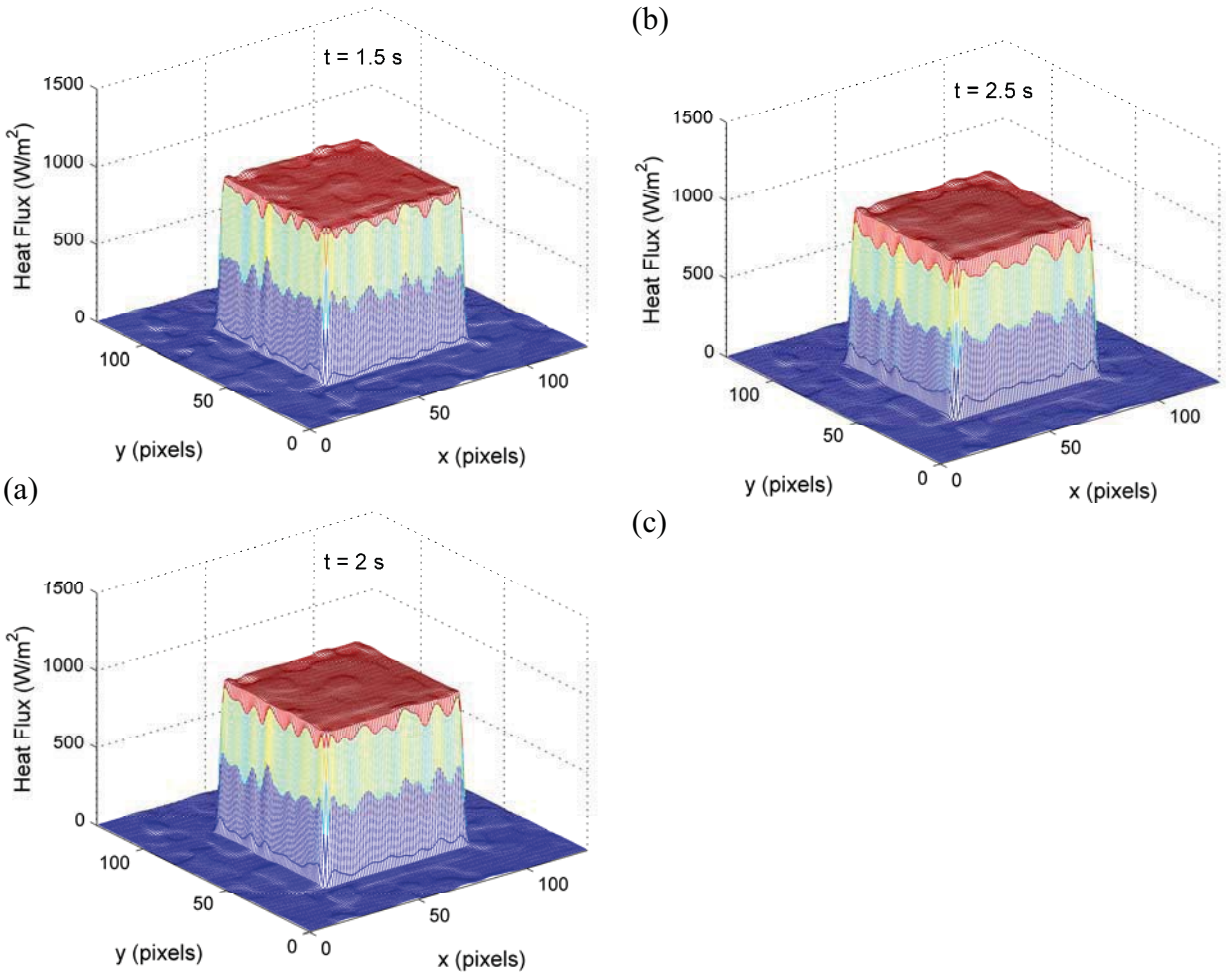

Figure 4.5. Surface heat flux distributions on a Mylar layer on Nylon calculated by using the two-step method from a time sequence of noisy temperature images at (a) 1.5 s, (b) 2 s and (c) 2.5 s

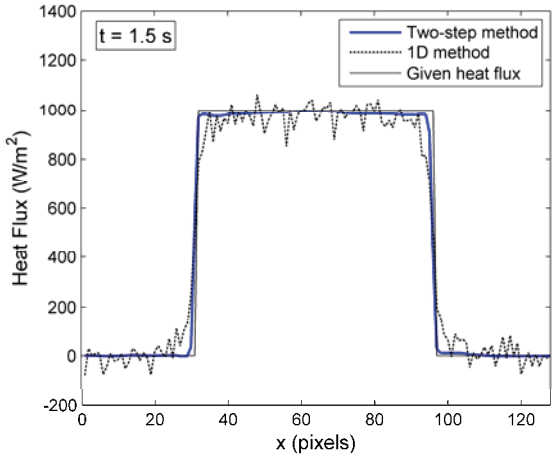

(a)

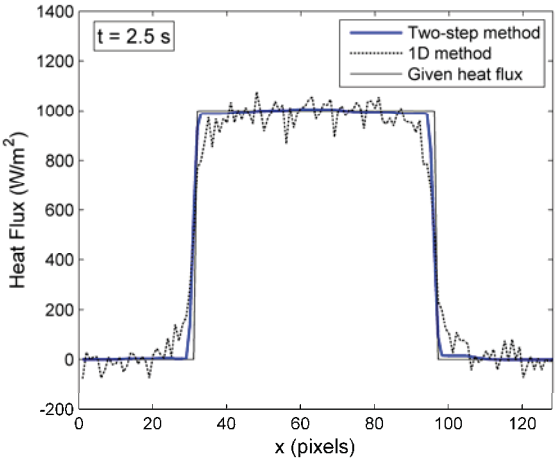

(c)

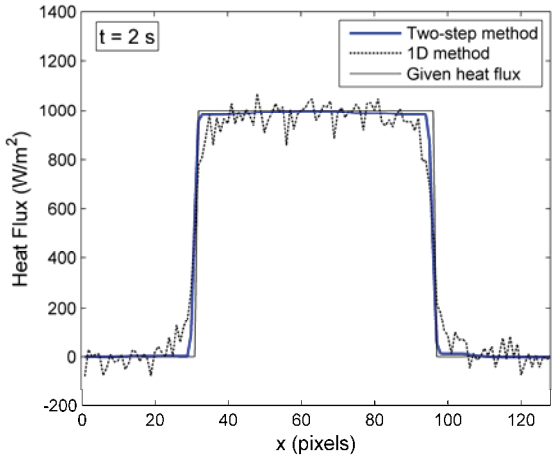

(b)

Figure 4.6. Surface heat flux distributions along the symmetrical axis across the square region on a Mylar layer on Nylon calculated by using the 1D inverse method and the two-step method at (a) 1.5 s, (b) 2 s and (c) 2.5 s

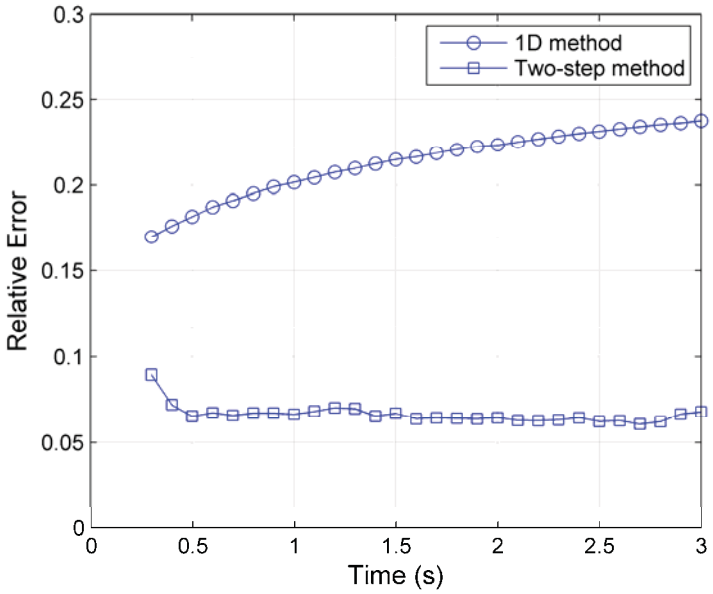

Figure 4.7. Relative errors in the heat flux fields calculated by using the 1D inverse method and the two-step method

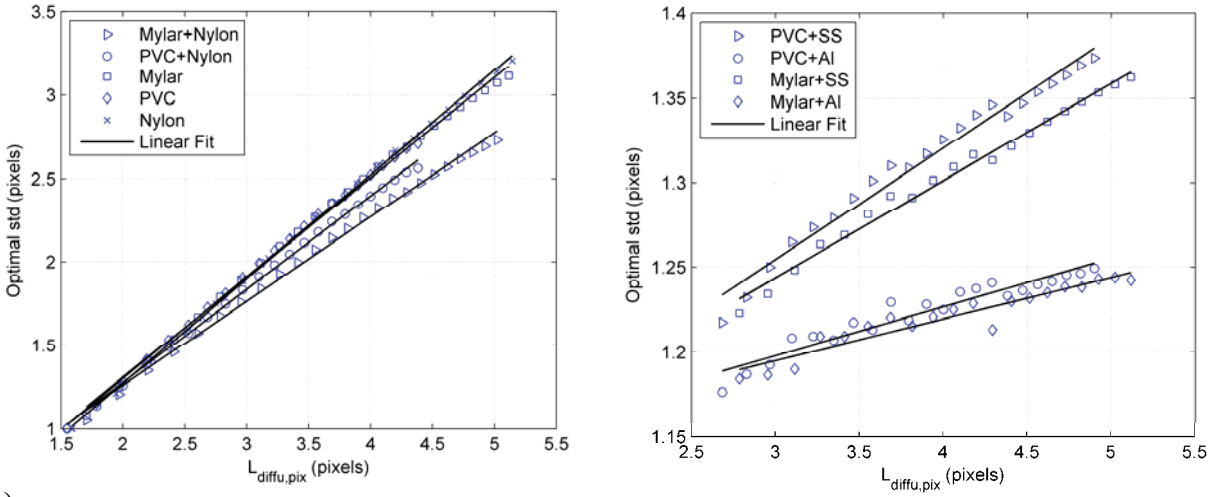

(a) (b)

Figure 4.8. Relations between the optimal standard deviation in the Gaussian filter and the diffusion length scale for (a) thin polymers on Nylon and polymer bases, and (b) thin polymers on stainless steel and aluminum

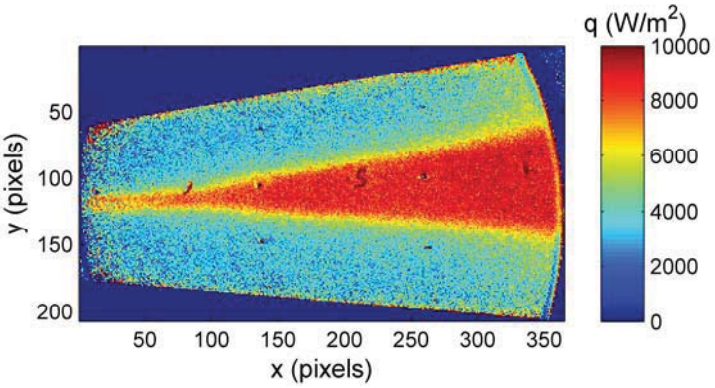

(a)

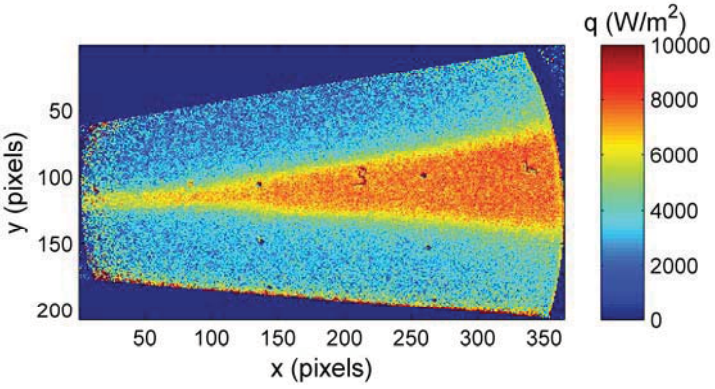

(b)

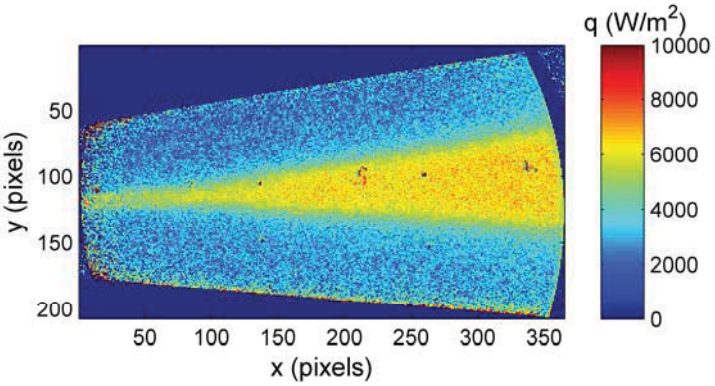

(c)

Figure 4.9. Heat flux images on a 7°-half-angle circular cone at Mach 6 at different times, which are obtained by the 1D inverse method, (a) 1 s, (b) 2 s, and (c) 3 s

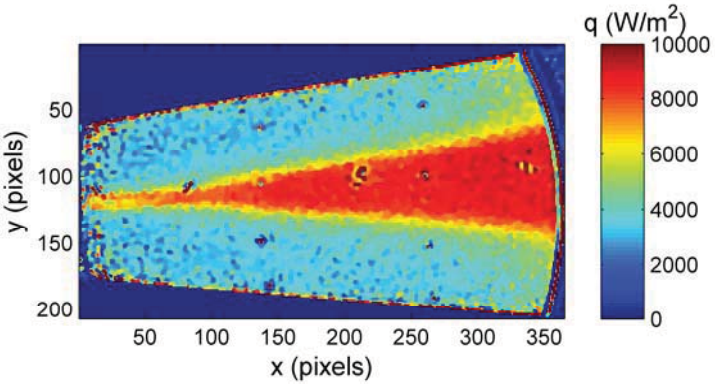

(a)

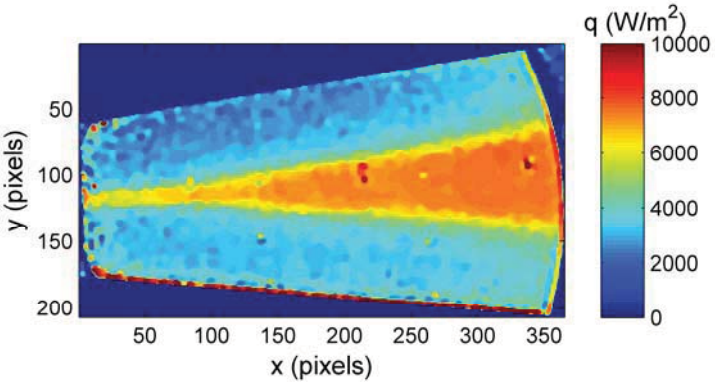

(b)

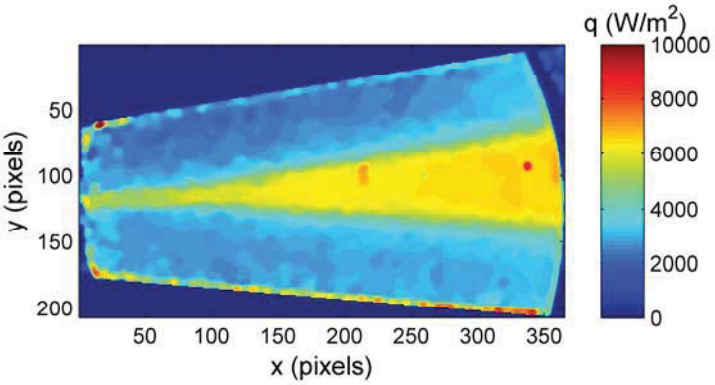

(c)

Figure 4.10. Heat flux images deconvoluted from the ones given by the 1D inverse method on a 7^{o}-half-angle circular cone at Mach 6 at different times, (a) 1 s, (b) 2 s, and (c) 3 s

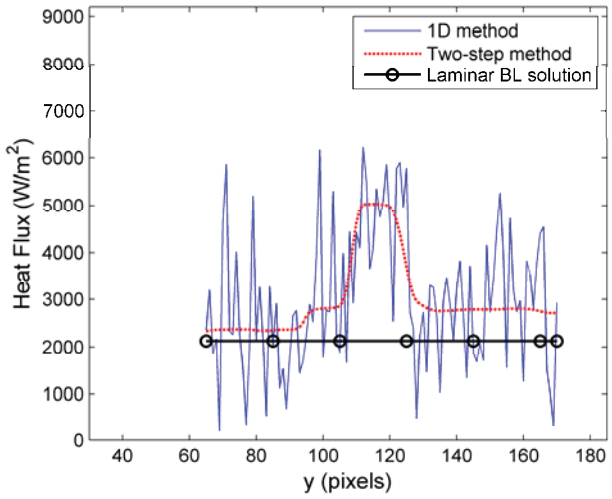

(a)

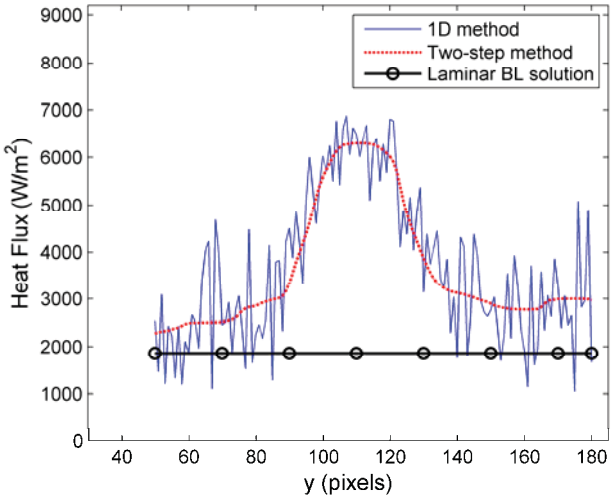

(c)

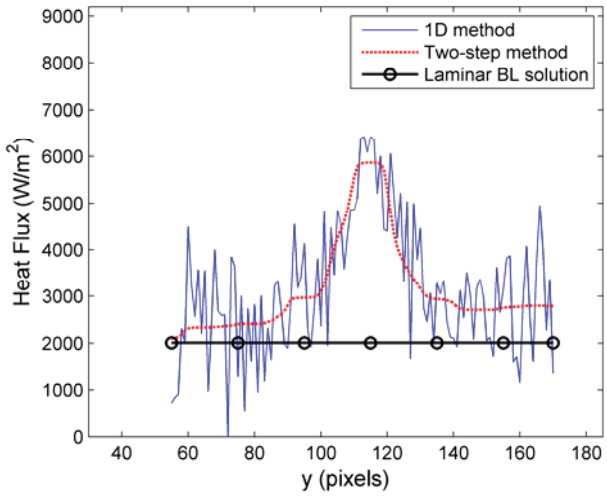

(b)

Figure 4.11. Heat flux distributions across the cone at x = 0.16 m, 0.18 m and 0.21 m at t = 3 s from starting the tunnel in comparison with the laminar boundary layer solution

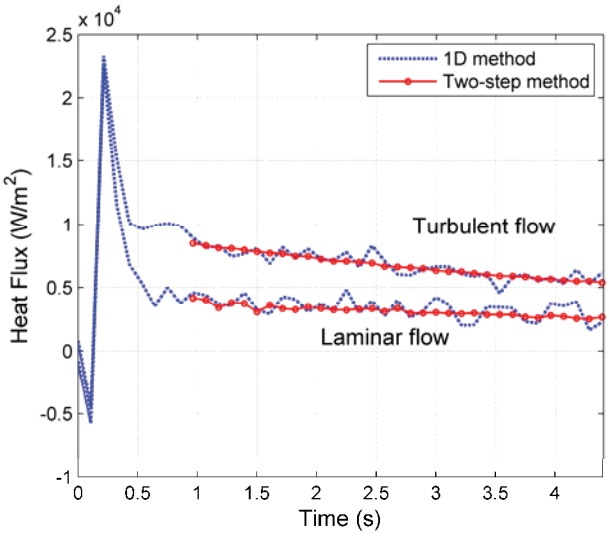

Figure 4.12. Time histories of surface heat flux at the point P_L in the laminar flow and the point P_T in the turbulent wedge in the Purdue Mach-6 tunnel, where the points P_L and P_T at x = 0.22 m are marked in Fig. 3.8

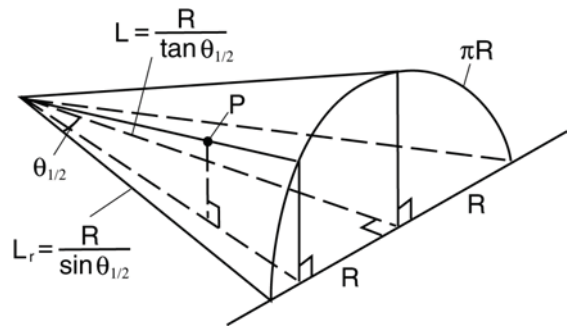

(a)

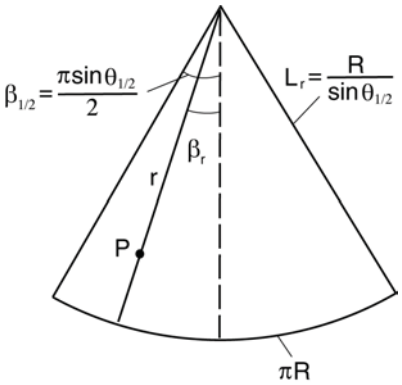

(b)

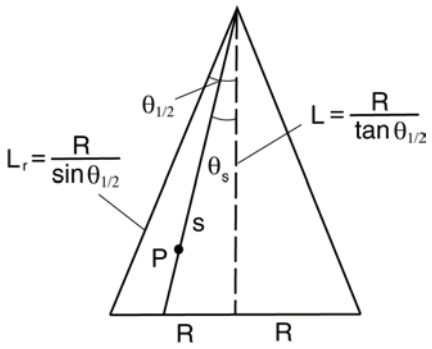

(c)

Figure 4.13. (a) Circular cone surface, (b) Euclidean plane developed from the circular cone surface, and (c) plane orthographically projected from the circular cone surface

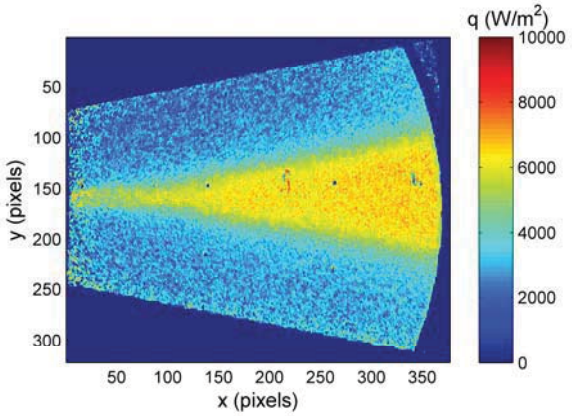

(a)

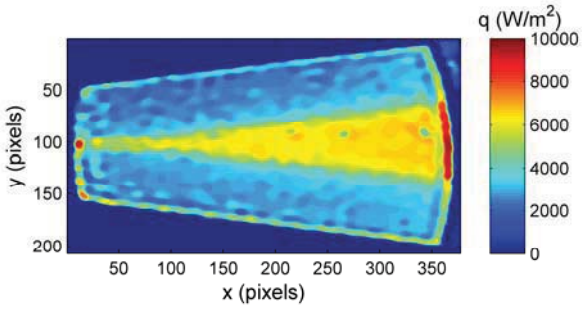

(b)

Figure 4.14. Heat flux images of the cone at t = 3 s, (a) image obtained by mapping the original image [Fig. 4.9(c)] on the Euclidean plane developed from the circular cone surface, and (b) image obtained by mapping back on the image plane from the developed plane

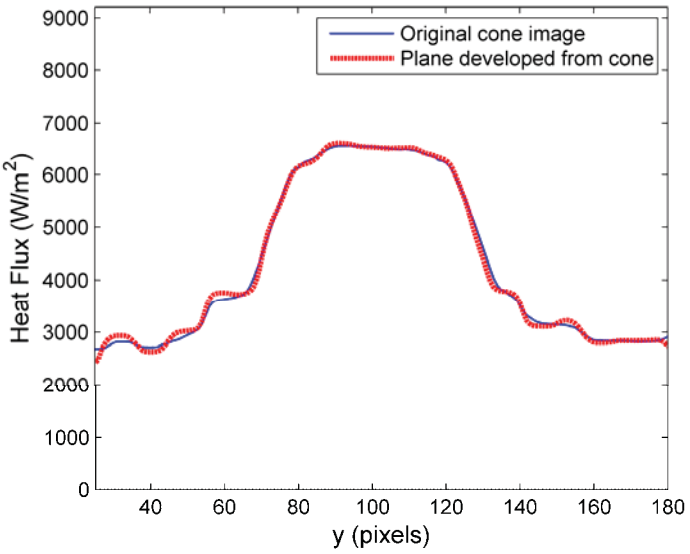

Figure 4.15. Heat flux distributions across the cone at x = 0.26 m at t = 3 s obtained by using the image deconvolution method on the original image and the Euclidean plane developed from the cone surface

5. Heat Flux Measurements on a Circular Cone

The data-processing procedure based on an analytical inverse method is developed to calculate heat flux distributions on a model from a time sequence of temperature sensitive paint (TSP) images acquired in the Purdue quiet Mach 6 Ludwieg tube. TSP measurements are conducted on a 7-deg-half-angle circular metal cone at Mach 6. It is found that the historical effect of the warming-up process of a model in sequential runs becomes significant and it must be corrected by in-situ calibration to obtain accurate heat flux distributions. After this historical effect and the effect of the non-uniform coating thickness are corrected, the TSP-derived heat flux distributions on the cone are in good agreement with those given by the similarity solution and the reference temperature method. The simple methods to determine the coating thickness distribution based on TSP measurements are developed. The error sources in TSP heat flux measurements in the Ludwieg tube are discussed.

5.1. Introduction

The Boeing/AFOSR Mach-6 Quiet Tunnel at Purdue University (simply referred to as the Ludwieg tube) is unusual compared to other hypersonic tunnels since the total pressure and temperature are much lower. This facility is the only operational hypersonic tunnel with low noise comparable to flight. TSP has been used as a main diagnostic tool in the studies of flow transition in the Ludwieg tube (Matsumura et al. 2003, 2005, Schneider et al. 2003, Swanson 2008, Casper et al. 2008). TSP is able to provide global high-resolution flow diagnostics with simple instrumentation and smooth surface coating. Compared to other optical methods, another advantage of TSP is that it works readily with thick conformal plexiglas windows. These are required to preserve low-noise flow and withstand the high stagnation pressures that are present prior to the bursting of the downstream valve. Qualitative information from TSP measurements has been very valuable in the past and continues to be very useful. However, quantitative global heat flux measurements using TSP in the Purdue Ludwieg tube have not been systematically achieved due to some unique problems associated with the unusual design that was necessary for the quiet Ludwieg tube.

Since the total pressure and total temperature in the Ludwieg tube is much smaller than those in conventional hypersonic tunnels, surface heat flux is in the order of 1000 W/m^2 in a laminar boundary layer on slender bodies (2-4 times higher for blunt bodies), and the corresponding surface temperature change is a few degrees even on a low-conductive model like a nylon model. This makes quantitative TSP heat flux measurements challenging in the Ludwieg tube. Some error sources that could be ignored in typical hypersonic tunnels become significant in measurements in the Ludwieg tube. In particular, the body warms up in sequential runs, and this historical effect will cause a systematic error if it is not corrected. The non-uniformity of the coating thickness also introduces a spatial variation of the measured heat flux distributions. Other potential error sources that may contribute to the heat flux measurement uncertainty include the start-up of the Ludwieg tube, unsteady model boundary and initial conditions, pressure sensitivity of TSP, inter-scattering between polished stainless steel surfaces of the test section, filter leakage, variation in material properties, paint preconditioning, and condensation. The objective of this work is to develop a data-processing procedure to improve the accuracy, sensitivity and spatial resolution of quantitative heat flux measurements using TSP in the Ludwieg tube.

5.2. Theoretical and Numerical Solutions

The purpose of this section is to assess the accuracy of the similarity solution and the reference temperature method for a hypersonic laminar boundary layer on a sharp circular cone for comparison with TSP data. A similarity solution exists for a hypersonic laminar boundary layer on a circular cone (White 1974, Marvin and Deiwert 1965). This similarity state seems to be quickly approached and sustained in the Ludwieg tube even though the total enthalpy and wall temperature fall moderately with time. In general, a similarity solution is sought under the constant wall temperature condition. The reference temperature method for a circular cone is also used (White 1974). For both the similarity solution and reference temperature method, the Taylor-Maccoll solution is used for the conical outer flow conditions (Sims 1964, Anderson 1990). Further, the similarity solution and the reference temperature method for hypersonic flows over circular cones are examined by comparing with numerical Navier-Stokes (NS) solutions for sharp cones (Wright et al. 1998).

Computations of hypersonic flows and heat transfer are sensitive to the temperature dependencies of the viscosity and thermal conductivity of air. The relatively new models of Lemmon and Jacobson (2004) for the thermodynamic properties are used in the similarity solutions and the reference temperature method. The viscosity of air as a function of temperature is given a two-piece power-law fit to the Lemmon and Jacobson's data. The temperature dependency of the thermal conductivity is given by a power-law fit. The specific heat is given by a quadratic function of temperature.

Kimmel's measurements at Mach 8 are used to evaluate the heat transfer computation methods (Kimmel 1993). The total pressure and temperature are p_0 = 443 psi and T_0 = 722 K, respectively, and the wall temperature is T_w = 303 K. Figure 5.1(a) shows comparisons of the heat flux distributions given by the similarity solution, reference temperature method, numerical NS solutions (Roy and Blottner 2006, Johnson 2009), and Kimmel's data in the laminar boundary layer. The NS solutions, similarity solution, and reference temperature method are consistent. The relative differences of the similarity solution and the reference temperature method are less than 5% compared with the NS solutions.

Chien's tests at Mach 7.9 on a 5-deg cone provide another case for the evaluation of the heat transfer computation methods since data from thermocouples are available (Chien 1974). Figure 5.1(b) shows Stanton number distributions given by the similarity solution, the reference temperature method, and a numerical NS solution compared with the Chien's data. Here, the Stanton number is defined based on the outer flow conditions and the Reynolds number is based on the freestream conditions. The experimental data in Fig. 5.1(b) are collected from Runs 21, 23, 24, 26 and 29 (Chien 1974), where T_w/T_0 = 0.35. In Runs 21, 23, 24, p_0 = 2190 psi, T_0 = 1470^o R. In Runs 26 and 29, p_0 = 1481 psi, T_0 = 1450^o R. The above results indicate that the similarity solution and the reference temperature method are sufficiently accurate in predicting heat flux in hypersonic flows over a sharp cone at zero angle of attack.

5.3. TSP Measurements on 7-Deg-Half-Angle Aluminum Cone

A series of runs at Mach 6 were performed with a 7-deg-half-angle aluminum cone in the Ludwieg tube. The aluminum cone has a total length of 0.4 m and the stainless steel tip nose has about 1 mm nose radius. The interchangeable nose is 0.15 m long. The whole cone was coated with LustreKote paint (made by TF Top Flite) that is composed of white primer and glass MonoCote. The purpose of this coating is two-fold. The white coating will enhance the luminescence emission of TSP detected by a camera for achieving a high signal-to-noise ratio.

Furthermore, for a metal model, an insulating coating on the surface will increase a change of surface temperature for given heat flux to improve the accuracy in heat flux calculation. It is speculated that its thermal properties are similar to those of a typical polymer. Then, the TSP, Ru(bpy) in Chromaclear auto paint, was coated on the top of the LustreKote paint. The mean paint thickness from x/L_c = 0.2-1 is about 250 μm based on paint thickness measurements using an eddy current gauge. The temperature calibration relation for Ru(bpy) in Chromaclear auto paint is given by Eq. (3.9).

Table 5.1 lists the test conditions for four sequential runs: Runs 1, 2, 3 and 4, including the initial total pressure and temperature, the pre-run wall (surface) temperature measured using a thermocouple at x/L_c = 0.75, the Reynolds number based on the base diameter, and times at which the tunnel started. The pre-run surface temperature was 296 K in Run 1, and increased to 307 K in Run 4. Figure 5.2 shows the total pressure and temperature as a linearly decreasing function of time in Run 1, where the pressure was measured using a Kulite pressure transducer (XTEL-190-500A) and then the temperature was calculated using the isentropic relations. For other runs, the total pressure and temperature have similar behaviors. The decay rates of the total pressure for Runs 1, 2, 3 and 4 are about 25 kPa/s, 34 kPa/s, 21 kPa/s, and 57 kPa/s, respectively. The decay rates of the total temperature for Runs 1, 2, 3 and 4 are about 5 K/s, 5 K/s, 5 K/s, and 7 K/s, respectively. Figure 5.3 shows time histories of surface temperature measured using the thermocouple for Runs 1, 2, 3 and 4. In Run 1, the initial model surface temperature was equal to the ambient temperature $T_{in} = 298\,K$. Then, the model surface temperature $T(t_{run})$ before a specific run was increased in the sequential runs (Runs 2, 3 and 4), where $t = t_{run}$.is the time just before a diaphragm breaks in the run. The large temperature increase indicated in Fig. 5.3 occurred when a transonic flow with a high mass flow rate passed the model after a Mach 6 run.

Figure 3.7 shows a generic setup of a CCD camera with a band-pass optical filter for detecting the luminescent emission from the TSP and a blue LED array for illuminating the TSP on a model in a dark environment in the Ludwieg tube. The 16-bit camera (POC 1600) and blue LED array (LM2X-460) whose emission peak is at 460 nm were used. They are produced by Innovative Scientific Solutions Inc. (http://www.innssi.com). A time sequence of 100 images was acquired by the camera for each run at 32 f/s. The basic testing procedures of TSP in a wind tunnel are described by Liu and Sullivan (2004). A surface temperature image is obtained by using the calibration relation [Eq. (3.9)] from a ratio image between a wind-on TSP image and a wind-off TSP image (a TSP image at a constant reference temperature). Then, from a time sequence of the surface temperature images, the corresponding heat flux images are calculated at every pixel by applying Eq. (2.3) to the interested image domain.

For the purpose of comparison and in-situ correction, a thin-film heat-flux sensor (Omega HFS-4) was attached on the back surface of the model (relative to the camera) at x/L_c = 0.67 to measure local heat flux. To monitor the changes of local surface temperatures of the model during and between runs, a surface thermocouple at x/L_c = 0.67 was located on top of the TSP covered with a 0.3 mm acrylic adhesive layer, and a base thermocouple was in contact with the base of the cone and insulated from the air by 5 layers of adhesive Mylar with 25 microns thickness. The thermocouple signals were amplified 25X and recorded on a digital oscilloscope.

For a specific run (such as Run 4), the camera records a time sequence of TSP images from $t = t_{run}$ just before a diaphragm breaks in this run. Based on these images, we can only calculate the following integral

$$q_{s,run}(t) = \frac{k_p(1-\bar{\varepsilon}^2)}{\sqrt{\pi a_p}} \int_{t_{run}}^{t} \frac{\overline{W}(t-\tau,\bar{\varepsilon})}{\sqrt{t-\tau}} \frac{d\theta_{ps,run}(\tau)}{d\tau} d\tau \ , \tag{5.1}$$

where $\theta_{ps,run}(t) = H(t/t_{run} - 1)[T_{ps}(t) - T_{in}]$ is the change of the surface temperature during this run and $H(\xi)$ is the Heaviside function [$H(\xi) = 0, if\ \xi < 0$ and $H(\xi) = 1, if\ \xi \geq 0$]. Note that the value of T_{in} does not change the value of the integration. In general, Eq. (5.1) is not equivalent to Eq. (2.1) unless at $t = t_{run}$ the temperatures of the paint layer and the aluminum base are equal to the ambient temperature. This problem will be further discussed later.

Figure 5.4 shows typical images of the change in surface temperature and the heat flux at t = 1.6 s, where the heat flux images are calculated by using Eq. (5.1) from a time sequence of 100 TSP images. Note that the whole cone from the tip to the end is shown in Fig. 5.4. Figure 5.5 shows time histories of surface temperature change and estimated heat flux at x/L_c = 0.59 along the centerline of the cone in Fig. 5.4, where L_c is the cone length. After the transient start-up, the heat flux only slightly decreases with increasing time. This gradual decrease in the heat flux is corresponding to the decrease in the total pressure and temperature during a run (see Fig. 5.2). To compare the steady-state theoretical solutions, the time-averaged heat flux from t = 0.6-2.75 s is calculated at each location. Figure 5.6 shows the time-averaged heat flux distributions along the centerline of the cone for Runs 1, 2, 3 and 4 in comparison with those given by the similarity solution and the reference temperature method. Note that a blunt tip of a cone has some effect on heat flux near the tip. Numerical NS solution for a blunt cone (with a tip of 1 mm radius) predicts a lower heat flux than that for a sharp cone in the front portion of about 20% length.

In Run 1, the heat flux distribution calculated by using Eq. (5.1) is close to the theoretical solutions. In Run 1, as indicated in Fig. 5.3, the temperatures of the paint layer and the aluminum base are equal to the ambient temperature, i.e., $T(t_{run}) = T_{in}$ just before a diaphragm breaks at $t = t_{run}$. Physically, this means that the model is in a thermal equilibrium with the ambient conditions in Run 1. However, as also indicated in Fig. 8, the TSP-derived heat flux distributions obtained by using Eq. (5.1) are increasingly deviated from the theoretical solutions. For Run 4, the TSP-derived heat flux even becomes negative, which is physically unrealistic in this case. This non-physical shift in the estimated heat flux after the first run has not been noticed in previous measurements in hypersonic tunnels. In the following section, we argue that it is related to the historical effect of the warming-up process of the model in the Ludwieg tube (see Fig. 5.3). This effect on heat flux calculation may be significant when the heat flux to be measured is small. In addition, the fixed variation pattern in the heat flux distributions is observed in all the cases in Fig. 5.6, which is generated by a non-uniform coating.

5.4. Historical Effect of Warming-Up Process of Model

As indicated before, the condition for Eq. (2.1) or (2.3) is that at $t = 0$ both the polymer (paint) and base temperatures are equal to the ambient temperature. However, as indicated in Fig. 5.3, measurements by a thermocouple on the surface show that the pre-run model temperature arises from the ambient temperature from Run 1 to Run 4 in the Ludwieg tube. The calculation by using Eq. (5.1) underestimates heat flux for Runs 2, 3 and 4. Thus, the effect of the increased pre-run model temperature could produce a significant systematic error if it is not corrected in the heat flux calculation.

In order to give an estimate of the historical effect of the warming-up process of the model before a specific run, the evolution of the polymer surface temperature can be decomposed into a

pre-run process and a run process for a specific run. The virtual initial time ($t = 0$) is generally set when the temperatures of the polymer and base are equal to the ambient temperature T_{in} and t_{run} denotes the time at which a diaphragm breaks in a specific run. An expression for the time history of the surface temperature on the polymer from $t = 0$ to the current time in a specific run is

$$\begin{aligned}\theta_{ps}(t) &= \theta_{ps,run}(t) + \theta_{ps,pre-run}(t) \\ &= H(t/t_{run}-1)[T_{ps}(t)-T_{in}] + [1-H(t/t_{run}-1)][T_{ps}(t_{run})-T_{in}]f(t/t_{run})\end{aligned}, \quad (5.2)$$

where $f(t/t_{run}) = [T_{ps}(t)-T_{in}]/[T_{ps}(t_{run})-T_{in}]$ is a non-dimensional function describing the warming-up process of the model before this run. The first and second terms in Eq. (5.2) are the time histories in this run and before this run, respectively. This decomposition is exact mathematically, which serves as a reasonable model for a rapid start-up process of a hypersonic tunnel like the Ludwieg tube. The time history $f(t/t_{run})$ of the warming-up process of the model before a specific run is not known, which includes the histories in preceding runs and intervals between runs.

For $t > t_{run}$, substitution of Eq. (5.2) into Eq. (2.1) yields

$$\begin{aligned}q_s(t) = \frac{k_p(1-\bar{\varepsilon}^2)}{\sqrt{\pi a_p}}\Bigg[&\int_{t_{run}}^{t} \frac{\overline{W}(t-\tau,\bar{\varepsilon})}{\sqrt{t-\tau}}\frac{d\theta_{ps,run}(\tau)}{d\tau}d\tau \\ &+ \int_{0}^{t_{run}} \frac{\overline{W}(t-\tau,\bar{\varepsilon})}{\sqrt{t-\tau}}\frac{d\theta_{ps,pre-run}(\tau)}{d\tau}d\tau\Bigg]\end{aligned} \quad (5.3)$$

The first term in Eq. (5.3) is just Eq. (5.1). The second integral in Eq. (5.3) presents the historical effect of the pre-run warming-up process of a model on the heat flux calculation. Further, the second integral is written as a function of a non-dimensional time $\bar{\tau} = \tau / t_{run}$, i.e.,

$$\begin{aligned}\int_0^{t_{run}} \frac{\overline{W}(t-\tau,\bar{\varepsilon})}{\sqrt{t-\tau}}\frac{d\theta_{ps,pre-run}(\tau)}{d\tau}d\tau &= \frac{T_{ps}(t_{run})-T_{in}}{\sqrt{t_{run}}}\int_0^1 \frac{\overline{W}(t/t_{run}-\bar{\tau},\bar{\varepsilon})}{\sqrt{t/t_{run}-\bar{\tau}}}\frac{df(\bar{\tau})}{d\bar{\tau}}d\bar{\tau} \\ &= \frac{T_{ps}(t_{run})-T_{in}}{\sqrt{t_{run}}}\left[A_0 + A_1\left(\frac{t}{t_{run}}-1\right) + A_2\left(\frac{t}{t_{run}}-1\right)^2\cdots\right]\end{aligned} \quad (5.4)$$

In Eq. (5.4), a Taylor expansion near the start-up time $t = t_{run}$ is used. Since τ / t_{run} is close to one when t_{run} is much larger than the run duration (about 2-5 s), an approximation is that only the first term in the Taylor expansion is retained in Eq. (5.4). Note that the coefficients in the Taylor expansion depend on the coating thickness. Therefore, Eq. (5.3) becomes

$$q_s(t) = \frac{k_p(1-\bar{\varepsilon}^2)}{\sqrt{\pi a_p}}\left[\int_{t_{run}}^{t} \frac{\overline{W}(t-\tau,\bar{\varepsilon})}{\sqrt{t-\tau}}\frac{d\theta_{ps,run}(\tau)}{d\tau}d\tau + B_0(\bar{L}/L)[T_{ps}(t_{run})-T_{in}]\right], \quad (5.5)$$

where B_0 is a proportional coefficient to be determined, L is the local coating thickness, and $\bar{L}$ is the averaged coating thickness over a region. The ratio $L/\bar{L}$ is the normalized thickness distribution, which represents the effect of the coating non-uniformity. The second term in Eq. (5.5) is considered as a correction for the effect of the increased pre-run polymer surface

temperature $T_{ps}(t_{run})$ from the ambient temperature T_{in} and the effect of the non-uniform coating thickness

According to the above argument, the heat flux distribution given by TSP for Run 1 is consistent with the theoretical solutions since the pre-run surface temperature is equal to the ambient temperature (297 K). In heat flux calculations, the ratio ($k_p / \overline{L}$) between the thermal conductivity and thickness of the polymer (Mylar) is 600, where the averaged coating thickness is $\overline{L} = 250\ \mu m$ and $k_p = 0.15$ W/m-K. For $T_{ps}(t_{run}) = T_{in} = T_b$ in Run 1, this value is confirmed by using the discrete Fourier law $k_p / \overline{L} = q_s / (T_{ps} - T_b)$ in which q_s is given by a thin-film heat flux sensor (Omega HFS-4) located at x/L_c = 0.65 and T_{ps} is the temperature measured by TSP at the same location.

As indicated before, since the time history $f(t/t_{run})$ of the warming-up process is not known, the coefficient B_0 in the correction term has to be determined in situ by using the data given by the thin-film heat flux sensor amounted at x/L_c = 0.65 on the surface. Figure 5.7 shows the time histories of surface heat flux given by the heat flux sensor. The difference between the time-averaged heat flux values given by TSP using the first term in Eq. (5.5) and the heat flux sensor is shown in Fig. 5.8 as a function of $T_{ps}(t_{run}) - T_{in}$. The data for these runs are approximately on a straight line as indicated by Eq. (5.5). Overall, the correlation between the runs in Fig. 5.8 is reasonably high, and the estimated value of B_0 is 1.3.

As shown in Fig. 5.6, after the single value of $B_0 = 1.3$ is applied to all the runs and the measured thickness distribution L is used in Eq. (5.5), good correction is achieved, indicating that the systematical error due to the warming-up process is eliminated and the spatial variation due to the non-uniform thickness is reduced. As indicated in Fig. 5.6(b), boundary layer transition is observed at x = 0.32 m in Run 2. Figure 5.9 shows the distributions of the heat transfer parameter $St \times Re_D^{1/2}$ given by TSP compared with the theoretical solutions for Runs 1, 2, 3, and 4. Here, the Stanton number is defined as

$$St = \frac{q_s}{\rho_e u_e (h_{aw} - h_w)},$$

where u_e and ρ_e are the velocity and air density at the edge of the boundary layer, respectively, and h_{aw} and h_w are the enthalpies at the adiabatic wall and wall, respectively. The Reynolds number is defined as $Re_D = \rho_\infty U_\infty D / \mu_\infty$, where D is the base diameter of the cone, and U_∞ ρ_∞, and μ_∞ are the frestream velocity, density and dynamic viscosity, respectively. The heat transfer parameter $St \times Re_D^{1/2}$ takes the effect of the Reynolds number into account in aeroheating scaling.

For a thin polymer layer on a high-conductive metal base, the first term in Eq. (5.5) can be approximated by the discrete Fourier law (Liu et al. 2009). Therefore, Eq. (5.5) can be approximated by

$$q_s(t) = (k_p / \overline{L})\left[T_{ps}(t) - T_b(t_{run})\right] + \overline{B}_0(\overline{L}/L)\left[T_{ps}(t_{run}) - T_{in}\right] \quad (5.6)$$

where $\overline{B}_0 = k_p(1-\bar{\varepsilon}^2)B_0/\sqrt{\pi a_p}$. For $k_p/\overline{L} = 600$, Eq. (5.6) gives a consistent result to that given by Eq. (5.5). Similar to Fig. 5.8, the coefficient B_0 is determined by fitting the data and a linear fit gives $B_0 = 2$ for the use of the discrete Fourier law.

The above correction procedure is not purely empirical, and it has a rational foundation based on an estimate $B_0(\overline{L}/L)[T_{ps}(t_{run}) - T_{in}]$ in Eq. (5.5) for the historical effect of the warming-up process and the effect of the non-uniform thickness. The historical effect is evident in the Ludwieg tube because the aerodynamic heating flux on a model during a specific run is relatively small (1000-5000 W/m^2) and the heating between runs is not negligible partially due to the downstream valve that is necessary to achieve quiet flow. In previous TSP measurements in hypersonic tunnels [11-14], the effect has not been noticed since the aerodynamic heating is so dominant. In addition, this effect is gone when a model cools down to the ambient temperature if the interval between two sequential runs is sufficiently long. However, this is not practical for tests in the Ludwieg tube since the productivity of wind tunnel testing is reduced.

5.5. Non-Uniformity of Coating Thickness

The fixed variation pattern in the heat flux distributions is observed in all the cases in Fig. 5.6. This error is caused by a non-uniform coating thickness distribution. For a TSP on a metal model, the effect of the coating thickness on TSP heat flux measurement is more sensitive to the coating thickness. This variation is enlarged when the total pressure is higher, as indicated in Figs. 5.6(b) and 5.6(d). To correct the effect of non-uniform thickness of a coating, the thickness distribution of the coating should be known. It is noticed that the start-up process has sudden heating on a model when the hot gas enters the test section from upstream. Then, the model surface temperature decays due to heat conduction to a high-conductive aluminum model, which depends on the coating thickness. Figure 5.7 shows the time histories of heat flux given by the Omega thin-film heat flux sensor at x/L_c = 0.65 on the cone in Runs 1, 2, 3 and 4. A question is whether the coating thickness distribution can be determined based on TSP measurements in the start-up process. Here, this possibility is explored.

For a thin polymer on a high-conductive model, Liu et al. (2009) gave an approximate solution for the polymer surface temperature change $\theta_{ps}(t) = T(t,L) - T_{in}$ from the initial temperature

$$\theta_{ps}(t) \cong \frac{1}{\sqrt{\pi k_p \rho_p c_p}} \int_0^t \frac{q_s(\tau) S(t-\tau)}{\sqrt{t-\tau}} d\tau , \tag{5.7}$$

where

$$\begin{aligned} S(t-\tau) = 1.163 &+ 3.676\, exp\left[-\frac{(0.5434L)^2}{4a_p(t-\tau)}\right] - 1.3\, exp\left[-\frac{(0.2592L)^2}{4a_p(t-\tau)}\right] \\ &- 3.576\, exp\left[-\frac{(0.8421L)^2}{4a_p(t-\tau)}\right] + \varepsilon\, exp\left[-\frac{L^2}{4a_p(t-\tau)}\right] \end{aligned} . \tag{5.8}$$

Note that $S(t-\tau)$ represents the effect of the thin insulating layer. Here, $\varepsilon = \sqrt{k_p \rho_p c_p / k_b \rho_b c_b}$, and k_p, c_p and ρ_p are the thermal conductivity, specific heat and density of the polymer, respectively, k_b, c_b and ρ_b are the thermal conductivity, specific

heat and density of the base material, respectively, and $a_p = k_p / c_p \rho_p$ is the thermal diffusivity of the polymer. For impulse heating $q_s = q_{so}\delta(t)$ where $\delta(t)$ is the Dirac-delta function, Eq. (5.7) can be written as

$$\theta_{ps}(t) = \frac{q_{s0} L}{2\sqrt{\pi} k_p} (t/\tau_p)^{-1/2} S(t/\tau_p), \tag{5.9}$$

where $\tau_p = L^2 / 4a_p$ is the characteristic timescale of the polymer layer.

To determine the coating thickness conveniently in practice, Eq. (5.9) should be suitably approximated. In the first method, $S(t/\tau_p)$ is approximated by a power-law function $S(t/\tau_p) \approx 0.96\left(t/\tau_p\right)^{-0.8}$, where the effect of ε is neglected since it is small for a polymer layer on a high-conductive model. Thus, we have

$$\theta_{ps}(t) = \frac{0.48\, q_{s0} L^{3.6}}{\sqrt{\pi}(4\, a_p)^{1.3} k_p} t^{-1.3}. \tag{5.10}$$

Eq. (5.10) indicates that the surface temperature of a polymer layer decays in a "-1.3" power law after the impulse heating. For linear least-squares regression of data, Eq. (5.10) is conveniently written as

$$ln[\theta_{ps}(t)] = -1.3 ln(t) + ln\left(\frac{0.48\, q_{s0} L^{3.6}}{\sqrt{\pi}(4\, a_p)^{1.3} k_p}\right). \tag{5.11}$$

By fitting the TSP data in the decay using Eq. (5.11), the coating thickness L can be estimated from the intercept when q_{so}, a_p and k_p are given. As shown in Fig. 5.10, the decay of the surface temperature can be fitted using the -1.3 power law. Thus, the intercept can be determined and the coating thickness can be estimated. Based on the data given by the heat flux sensor in Fig. 5.7, an estimated the peak heat flux value is $q_{s0} = 10\ kW/m^2$. It is also assumed that the sudden heating due to the passing of the hot gas is uniform over the surface and the decay of the polymer surface temperature is mainly caused by heat conduction to the aluminum model. Aerodynamic skin friction heating is neglected in this initial stage of the decay compared to the heat conduction to the model. This method is called the intercept-based method.

In the second method, we use the following approximation

$$(t/\tau_p)^{-1/2} S(t/\tau_p) \approx 11.7 exp\left(-\gamma(t/\tau_p)^{\beta}\right)$$

where $\gamma = 2.54$ and $\beta = 0.384$. Similar to Eq. (5.11), we have

$$ln[\theta_{ps}(t)] = -\gamma(t/\tau_p)^{\beta} + ln\left(\frac{11.7\, q_{s0} L}{2\sqrt{\pi} k_p}\right) \tag{5.12}$$

By fitting the TSP data in the decay using Eq. (5.12), the slope $-\gamma(\tau_p)^{-\beta}$ can be determined in a plot of $ln[\theta_{ps}(t)]$ as a linear function of t^{β}, which is related to the coating thickness L. This method is called the slope-based method, which has an advantage that the determination of the thickness does not depend on the value of q_{so} unlike the intercept-based method.

Figure 5.11 shows the coating thickness distributions along the centerline of the cone in images obtained by using the intercept-based method (Method 1) and the slope-based method

(Method 2) based on the TSP data in Run 4. The averaged thickness distribution from the two measured ones and the data given by an eddy-current gauge on the aluminum section of the cone are also plotted for comparison. The slope-based method is more sensitive to the thickness variation as well as a random noise. In Fig. 5.11, the random noise is filtered in the averaged distribution. The pattern in the estimated thickness distribution corresponds to that in the heat flux distribution. The mean thickness on the aluminum section (x = 0.15-0.4 m) is 250-300 microns, which is consistent with that given by the eddy-current sensor. The coating thickness distribution has been used in heat flux calculation using the analytical inverse method. Figure 5.6 shows the heat flux distributions with the correction for the coating thickness variation for Runs 1, 2, 3 and 4. The spatial patterns in the heat flux distributions for these runs are considerably smoothed out.

5.6. Other Error Sources

The general uncertainty analysis of TSP measurement has been given by Liu and Sullivan (2004). At nominal zero AoA in the present tests, the cone and support are considered to be rigid such that the major error sources related to model deformation are small. For large model deformation, an image registration procedure should be applied to align the wind-on and wind-off images. The temporal intensity variation of the blue LED array for illuminating the TSP was not monitored during the tests. However, since the time-averaged heat flux is obtained, the random variation is removed by averaging. The minimum temperature resolution that is limited by the photon shot noise of a camera is about 0.2^{o} C. The possible error sources in our measurements are discussed below. These errors are not corrected in this work, and estimates of these errors are required in further investigation.

a. Inter-scattering between polished stainless steel surface in test section and filter leakage

The inside of the Ludwieg tube test section is polished stainless steel so that inter-reflections of the emitted luminescence from the TSP are detected by the CCD camera. In addition, reflections of the incident LED light leak through the CCD camera filter. It is clear from many tests that both of these effects are contributing to errors. But the extent is not exactly known yet and it is complicated to correct the effect of inter-scattering.

b. Paint preconditioning

Past calibration results have showed that a polymer in TSP undergoes a physical change when temperature exceeds to its glass transition temperature during the first time the TSP is heated, which changes the calibration (Liu and Sullivan 2004). Then, subsequent heating and cooling cycles are stable and give the same calibration curve. It may be necessary to heat the new TSP on a model beyond its glass transition temperature prior to the first Ludwieg tube run. In our experiments, paint preconditioning is not done particularly.

c. Pressure sensitivity of TSP

The pressure sensitivity of TSP is relatively unknown. Ruthenium-based luminophores are susceptible to the effects of pressure through the oxygen quenching process. This is highly undesirable for TSP since the pressure effects will introduce errors in temperature measurements if they are not corrected. This is particularly important in the Purdue Ludwieg tube, where the model sits at stagnation pressure for an extended time before the run begins. Therefore, a binder which is oxygen impermeable must be chosen for TSP. It had been noticed by Matsumura et al.

(2003) that the TSP [specifically Ru(bpy) in a polyurethane binder with titaniumdioxide powder] did show an effect due to an increase in pressure. The pressure effect is considered as a major source contributing to the large systematic error in their TSP heat flux measurements. It is speculated that a mixture of the binder with titanium dioxide powder could enhance the pressure sensitivity of the TSP. However, experiments have been performed to determine the oxygen sensitivity of the TSP that is Ru(bpy) in automotive Chromaclear coat. It is found that there is virtually no sensitivity of the TSP to oxygen.

5.7. Conclusions

Temperature sensitive paint (TSP) heat flux measurements have been conducted on a 7°-half-angle aluminum circular cone at Mach 6 in the Purdue Ludwieg tube to evaluate the accuracy of the analytical inverse method in calculating heat flux from a time sequence of TSP images. The low heat flux and small surface temperature change, along with the unsteady oscillating thermal start-up process in the Ludwieg tube, pose challenges to quantitative global heat flux measurements. The similarity solution and the reference temperature method for the hypersonic laminar boundary layers on sharp circular cones are examined by comparing them with the numerical NS solutions. It is proved that the theoretical solutions are accurate enough as a reference for comparison with the TSP-derived heat flux distributions on a circular cone. Four tests were conducted sequentially under different total pressures and temperatures in the Ludwieg tube. It is found that the TSP-derived heat flux distribution increasingly deviates from the theoretical solutions as the pre-run surface temperature of the cone increased during the sequential runs. This non-physical shift is caused by the historical effect of the warming-up process of the cone model. This historical effect on the time integration in the analytical inverse method is estimated as a linear term of the difference between the pre-run surface temperature and the ambient temperature where the effect of the non-uniformity of the coating thickness is included. The unknown coefficient in this term is determined in situ by using the data given by a heat flux sensor amounted on the cone surface. The analytical inverse method coupled with an in-situ correction scheme for this historical effect and the effect of the coating non-uniformity improves the accuracy of TSP heat flux measurements in the Ludwieg tube. In addition, the coating thickness distribution is determined by utilizing the decay of the coating surface temperature immediately after the rapid heating in the start-up process of the Ludwieg tube.

Table 5.1. Test Conditions for the Aluminum Cone (10/12/2009)

	Run 1	Run 2	Run 3	Run 4
p_0 (initial)	625 kPa	896 kPa	521 kPa	896 kPa
T_0 (initial)	432 K	432 K	435 K	430 K
T_w (pre-run)	298 K	301 K	305 K	307 K
Re_D	5.9×10^5	8.5×10^5	4.8×10^5	8.3×10^5
Time	12:59 pm	1:48 pm	2:30 pm	3:10 pm

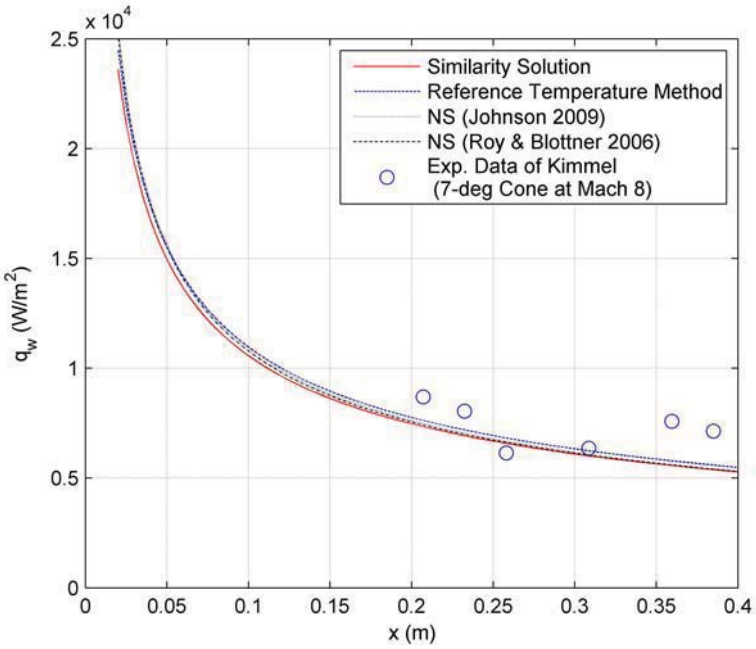

(a)

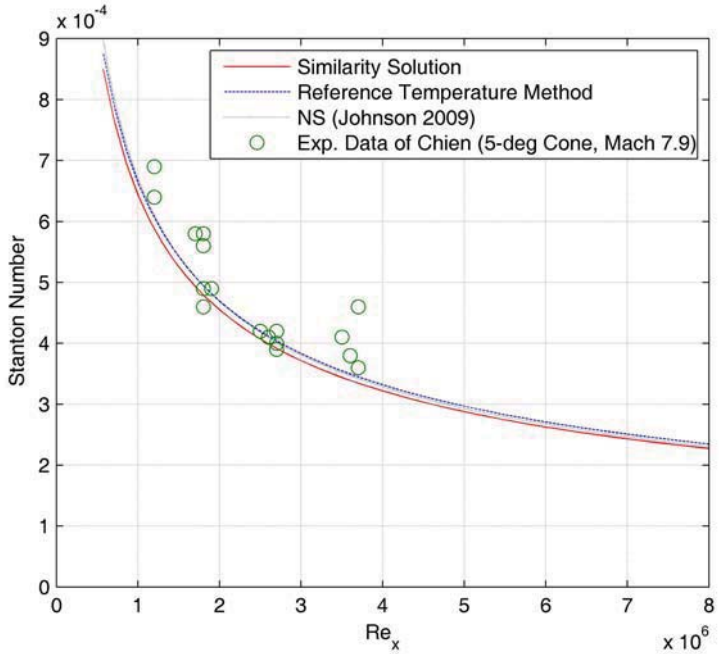

(b)

Figure 5.1. Comparisons of heat flux computations with (a) the Kimmel's data on the 7-deg cone at Mach 8 and (b) the Chien's data on the 5-deg cone at Mach 7.9

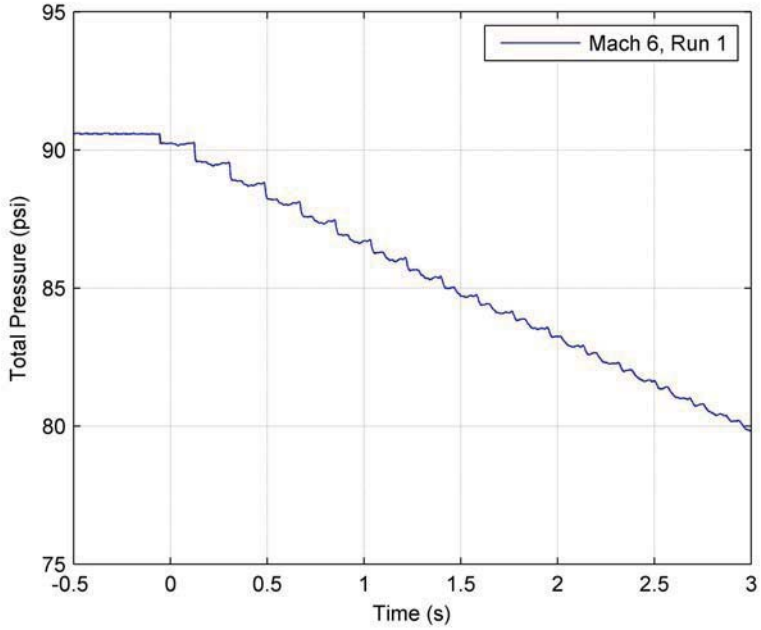

(a)

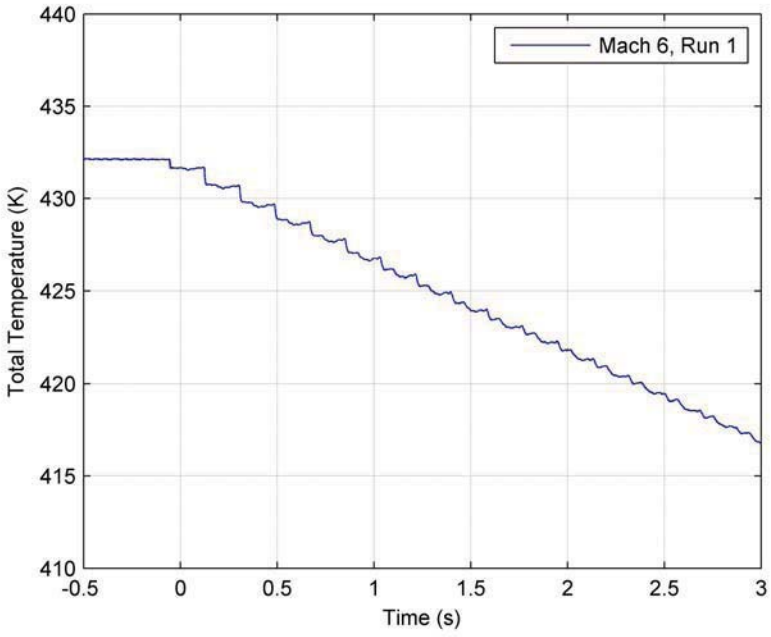

(b)

Figure 5.2. Total pressure and temperature as a function of time in Run 1

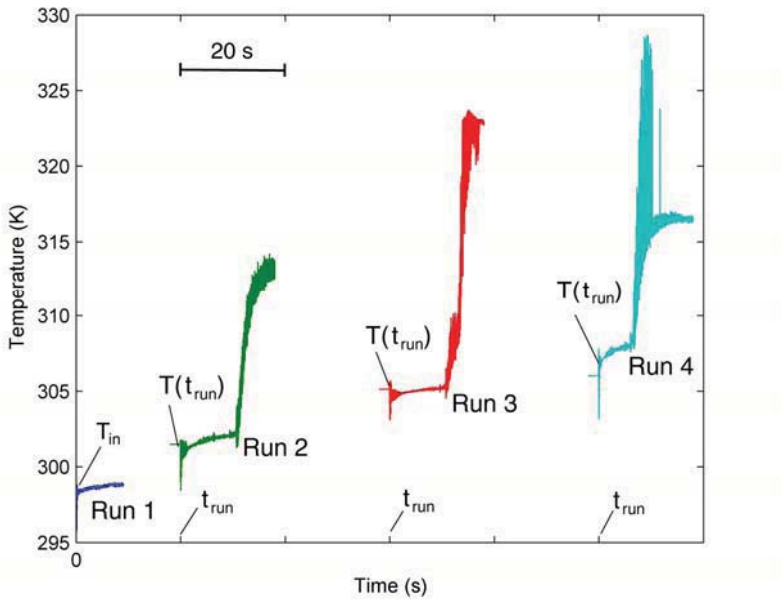

Figure 5.3. Time histories of surface temperature measured using a thermocouple for Runs 1, 2, 3 and 4

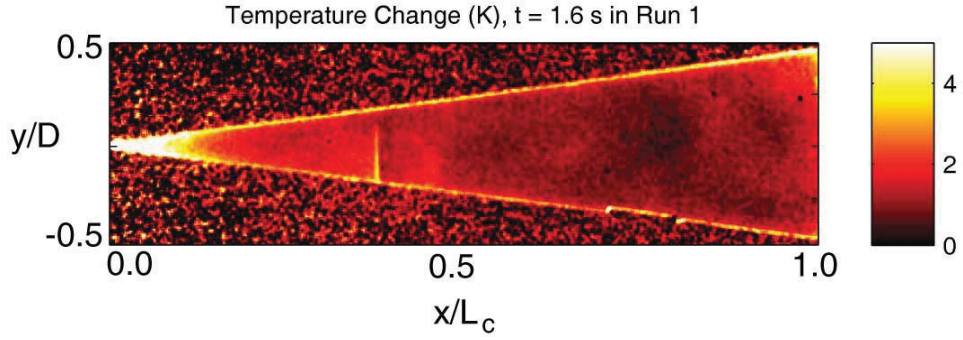

(a)

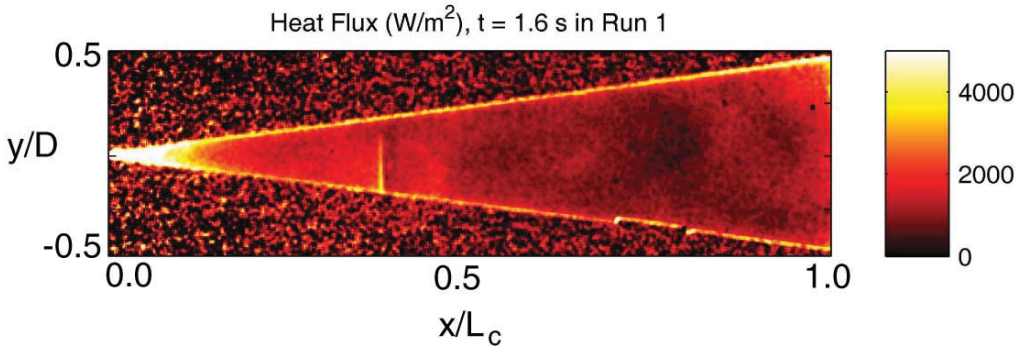

(b)

Figure 5.4. (a) Image of surface temperature change, and (b) heat flux image at t = 1.6 s in Run 1

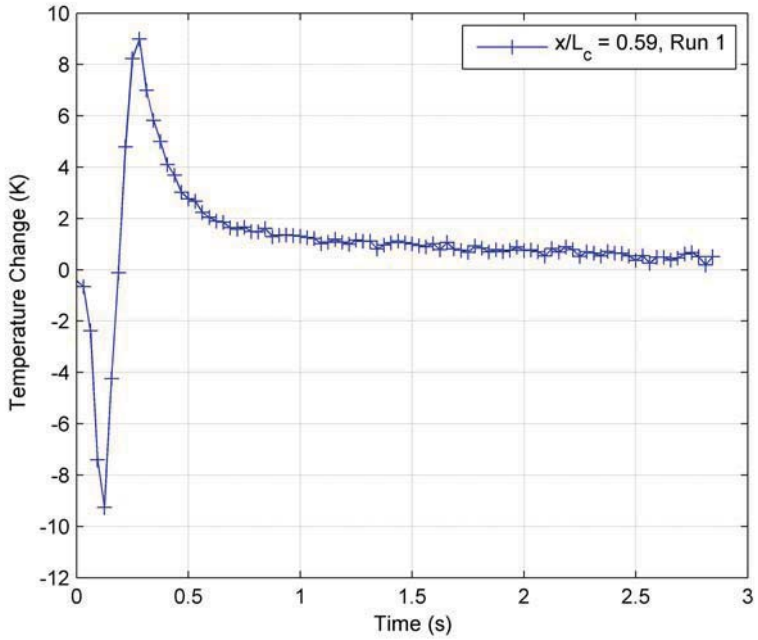

(a)

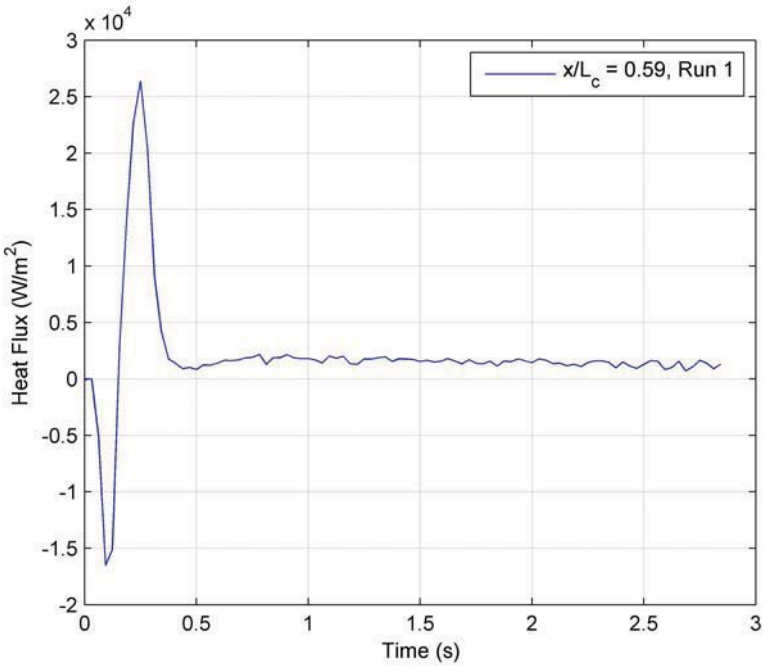

(b)

Figure 5.5. Time histories of (a) surface temperature change and (b) estimated surface heat flux at $x/L_c = 0.59$ in Run 1

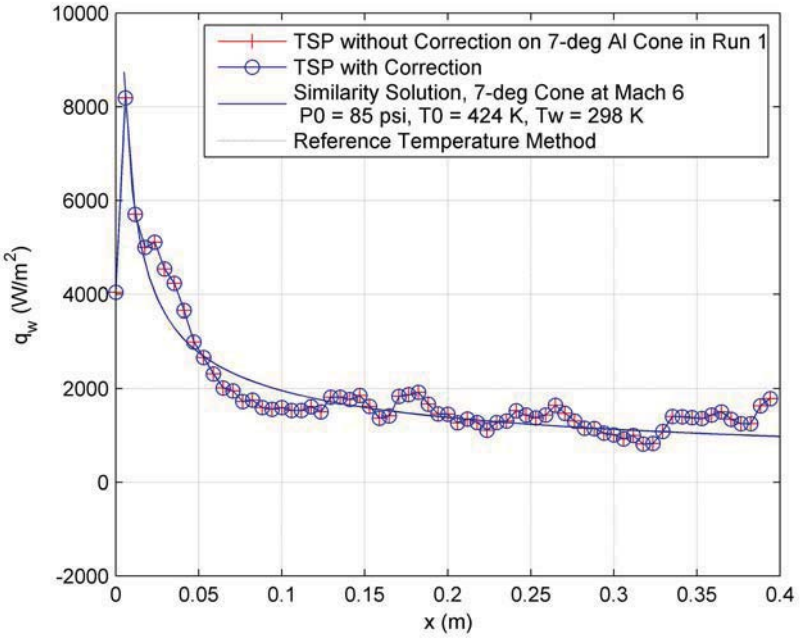

(a)

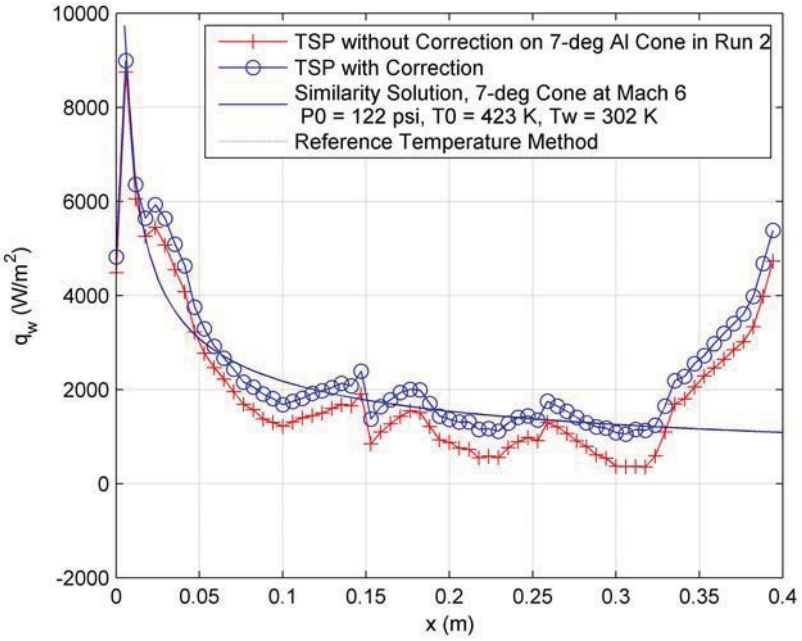

(b)

Figure 5.6. (continued)

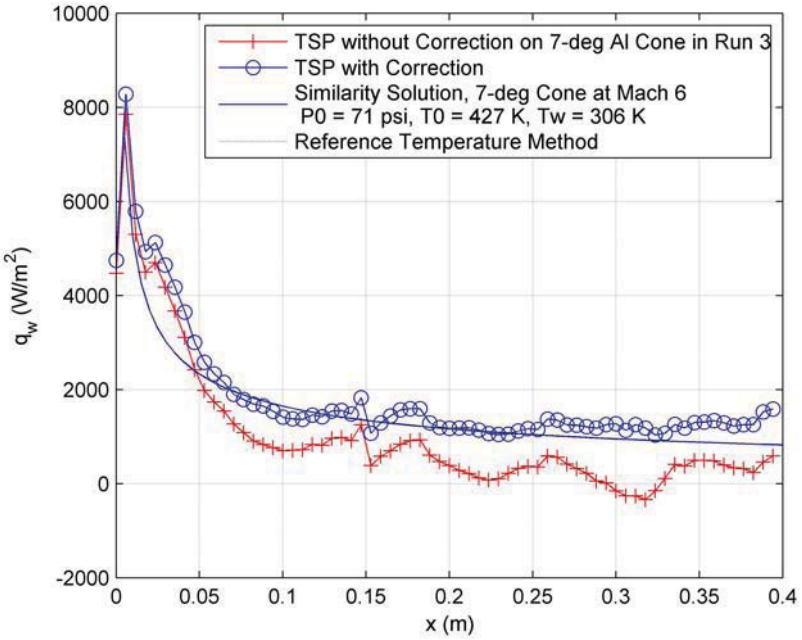

(c)

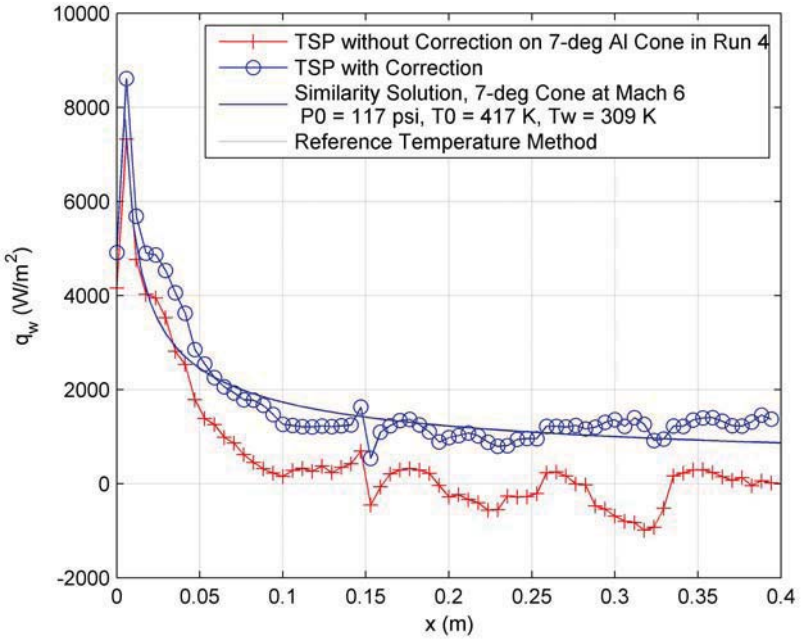

(d)

Figure 5.6. Heat flux distributions along a ray on the Al cone in (a) Run 1, (b) Run 2, (c) Run 3, and (d) Run 4

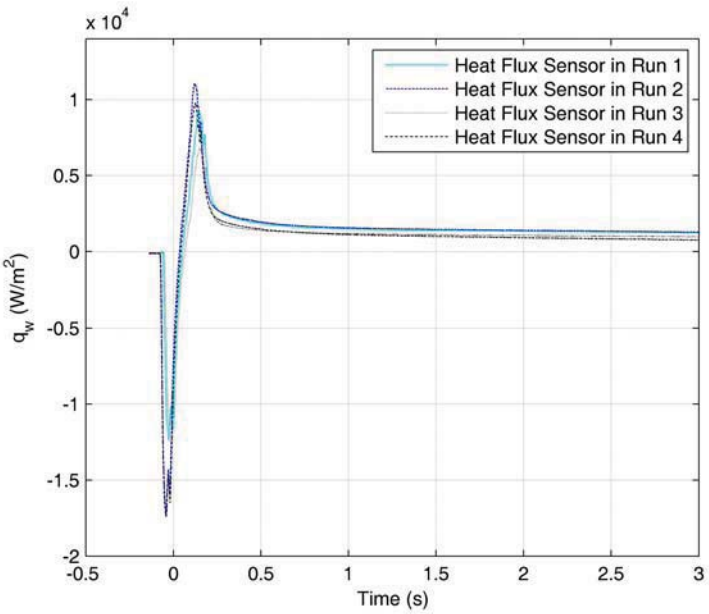

Figure 5.7. Histories of heat flux given by the heat flux sensor at $x/L_c = 0.65$ for the runs

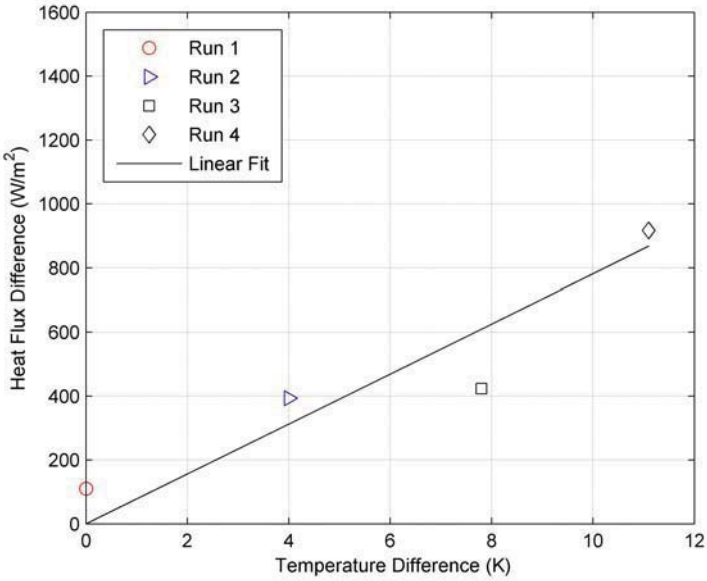

Figure 5.8. Difference between the time-averaged heat flux values given by TSP processed with the analytical method without correction and the heat flux sensor as a function of the difference between the pre-run wall temperature and ambient temperature. The linear fit gives $B_0 = 1.3$.

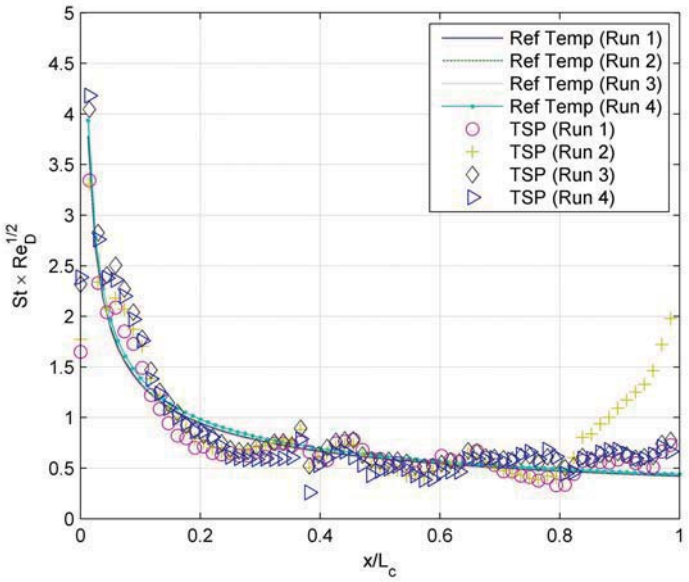

Figure 5.9. The distributions of the heat transfer parameter given by TSP processed with the analytical method with correction compared with the theoretical solutions for Runs 1, 2, 3, and 4

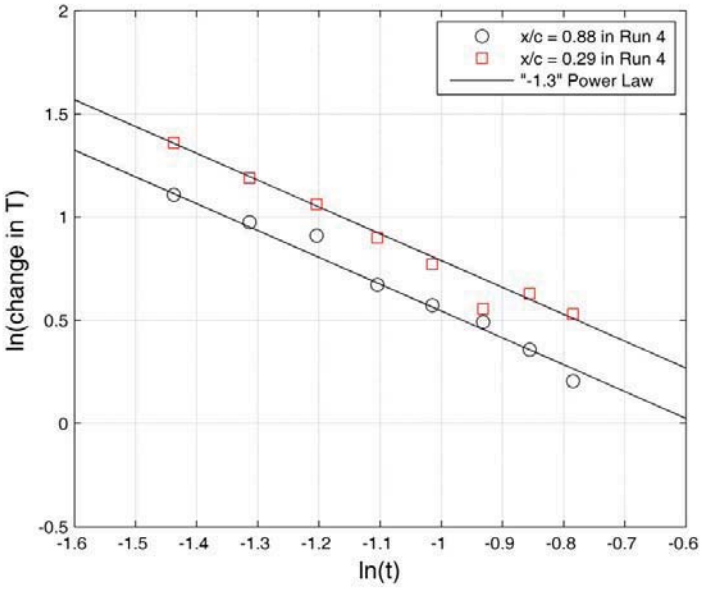

Figure 5.10. The surface temperature decays fitted by using the "-1.3" power law at two locations on a circular aluminum cone for Run 4

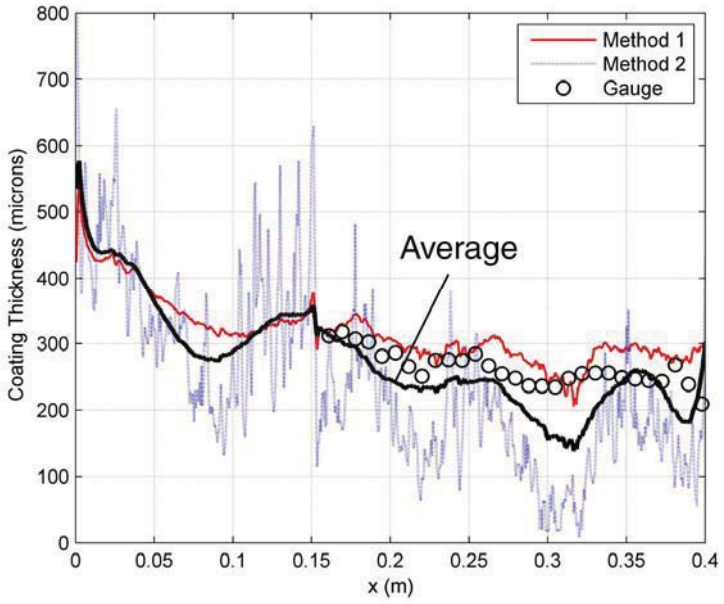

Figure 5.11. The coating thickness distributions along the centerline of the cone in images obtained by using the intercept-based method (Method 1) and the slope-based method (Method 2) in comparison with the data given by an eddy-current gauge

References:

Alifanov, O. M., "Inverse Heat Transfer Problems," Springer-Verlag, Berlin, 1994, Chapters 1 and 2

Anderson, J. D., Modern Compressible Flow (second Edition), McGraw-Hill Publishing Company, 1990, Chapter 10

Banham, M. and Katsaggelos, A., Digital Image Restoration, IEEE Signal Processing Magazine, March 1997, pp. 24-41

Beck, J. V., Blackwell, B. and St. Clair, "Inverse Heat Conduction: Ill-Posed Problem", Wiley-Interscience Publication, New York, 1985

Bryce D. M., "Troubleshooting: A Guide for Injection Molders", Techtrax, January 2001, Chapter 2

Cai, Z., Liu, T., Wang, B., Rubal, J. and Sullivan, J., "Numerical inverse heat transfer analysis for temperature sensitive paint measurements in hypersonic tunnels," Journal of Thermophysics and Heat Transfer, Vol. 25, No. 1, 2011, pp. 59-67

Campbell, B., Liu, T. and Sullivan, J. "Temperature sensitive fluorescent paint systems", AIAA Paper 94-2483, 1994

Carslaw, H. S. and Jaeger, J. C., "Conduction of Heat in Solids (Second Edition)", Oxford University Press, Oxford, 2000, Chapter I

Carslaw, H. S. and Jaeger, J. C., "Operational Methods in Applied Mathematics", Dover, New York, 1963, Chapter IV

Casper, K. M., Wheaton, B. M., Johnson, H. B. and Schneider, S. P., "Effects of Freestream Noise on Roughness-Induced Transition at Mach 8," AIAA Paper 2008-4291, Seattle, WA, 2008

Chien, K-Y, Hypersonic, Turbulent Skin-Friction and Heat-Transfer Measurements on a Sharp Cone, AIAA J., Vol. 12, No. 11, 1974, pp. 1522-1526

Cook, W. J. and Felderman, E. J., "Reduction of Data from Thin-Film Heat Transfer Gages: A Concise Technique," AIAA J., Vol. 8, No. 7, 1970, pp. 1366-1368

Estorf, M., "Image Based Heating Rate Calculation from Thermographic Data Considering Lateral Heat Conduction," International Journal of Heat and Mass Transfer, Vol. 49, 2005, pp. 2545-2556

Fletcher C. A. J., "Computational Techniques for Fluid Dynamics," Springer, Berlin, 1988

Helstram, C. W., Image Restoration by the Method of Least Squares, J. of the Optical Society of America, Vol. 57, Number 3, March 1967, pp. 297303

Hoffman J. D., "Numerical Methods for Engineers and Scientists," McGraw-Hill, New York, 1992

Hubner, J. P., Carroll, B. F., and Schanze, K. S., "Heat-Transfer Measurements in Hypersonic Flow Using Luminescent Coating Techniques," Journal of Thermophysics and Heat Transfer, Vol. 16, No. 4, 2002, pp. 516–522

Johnson, H. Private communication, 2009

Kimmel, R. L., Experimental Transition Zone Lengths in Pressure Gradient in Hypersonic Flow, In: Karal, L. D. & Zang, T. A., Eds., Transitianl and Turbulent Compressible Flows, 1993, FED-vol. 151, New York: ASME, 1993, pp. 117-127

Kojima, F., Fukuda, S. Asai, K., and Nakakita, K., "Identification of Time and Spatial Varying Heat Flux from Surface Measurements based on Temperature-Sensitive Paint Technology," SICE Annual Conference in Sapporo, Hokkaido Institute of Technology, Japan, August 44,2004

Kurits, I., Lewis, M., Hamner, M., and Norris, J. D., "Development of a Global Heat Transfer Measurement System at AEDC Hypervelocity Wind Tunnel 9," ICIASF, Pacific Grove, CA, 2007

Lin, M., Wang, T., 2002, "A Transient Liquid Crystal Method Using a 3-D Inverse Transient Conduction Scheme," International Journal of Heat and Mass Transfer, Vol.45, 2002, pp. 3491-3501

Liu, T., Campbell, B. and Sullivan, J., "Heat Transfer Measurement on a Waverider at Mach 10 Using Fluorescent Paint," Journal of Thermophysics and Heat Transfer, Vol. 9, No. 4, 1995, pp. 605-611

Liu, T., "Geometric and kinematic aspects of image-based measurements of deformable bodies," AIAA Journal, Vol. 42, No. 9, 2004, pp. 1910-1920

Liu, T. and Sullivan, J., "Pressure and Temperature Sensitive Paints," Springer, Berlin, 2004

Liu, T., Cai, Z., Lai, J., Rubal, J. & Sullivan, J. "Analytical methods for determination of heat transfer fields from temperature sensitive paint measurements in hypersonic tunnels," AIAA Paper 2009-0736, Orlando, FL 2009

Liu, T., Cai, Z., Lai, J., Rubal, J., and Sullivan, J., "Analytical Methods for Determining Heat Flux from Temperature-Sensitive-Paint Measurements in Hypersonic Tunnels," Journal of Thermophysics and Heat Transfer, Vol. 24, No. 1, 2010, pp. 85-94

Liu, T., Wang, B., Rubal, J., and Sullivan, J., "Correcting Lateral Heat Conduction Effect in Image-Based Heat Flux Measurements as an Inverse Problem," International Journal of Heat and Mass Transfer, Vol. 54, 2011, pp. 1244-1258

Marvin, J. G. and Deiwert, G. S., Convective Heat Transfer in Planetary Gases, NASA Technical Report, TR R-224, NASA, Washington DC, 1965

Matsumura, S., Berry, S. A., and Schneider, S. P., "Flow Visualization Measurement Techniques for High-Speed Transition Research in the Boeing/AFOSR Mach-6 Quiet Tunnel," AIAA Paper 2003-4583, July 2003

Matsumura, S., Schneider, S. P. and Berry, S. A., "Streamwise Vortex Instability and Transition on the Hyper-2000 Scramjet Forebody," Journal of Spacecraft and Rockets, Vol. 42, No. 1, 2005, pp. 78-88

Merski, N. R., "Reduction and Analysis of Phosphor Thermography data With the IHEAT Software Package," AIAA Paper 98-0712, 1998

Merski NR, "Global aeroheating wind-tunnel measurements using improved two-color phospher thermography method," Journal of Spacecraft and Rockets 36(2): 160-170, 1999

Morton K. W. and Mayers D. F., "Numerical Solution of Partial Differential Equations: An Introduction," Cambridge University Press, Cambridge, England, 1994

Norris, J. D., Hamner, M., Lafferty, J. F., Smith, N. T., and Lewis, M. J., "Adapting Temperature-Sensitive Paint Technology for use in AEDC Hypervelocity Wind Tunnel 9," AIAA 2004-2191, 2004, Portland, Oregon

Oliveira, J., Bioucas-Dias, J. and Figueiredo, M., "Adaptive total variation image deblurring: a majorization-minimization approach," Signal Processing Vol. 89, No. 9, 2009, pp. 1683-1693

Pottmann, H. and Wallner, J. "Computational Line Geometry," Springer, Berlin, 2000, Chapter 6

Roy, C. and Blottner, F. G., Review and Assessment of Turbulence Models for Hypersonic Flows, Progress in Aerospace Sciences, Vol. 42, 2006, pp. 469-530

Schlichting, H. and Gersten, K., "Boundary Layer Theory (8th Revisted)", Springer, 2000, Chapters 10 and 13

Schneider, S. P., Rufer, S., Skoch, C., and Swanson, E., “Hypersonic Transition Research in the Boeing/AFOSR Mach-6 Quiet Tunnel,” AIAA Paper 2003-3450, June 2003

Schultz D. L, Jones TV, “Heat transfer measurements in short-duration hypersonic facilities,” AGARDograph No. 165, 1973

Sims, J. Tables for Supersonic Flow around Right Circular Cones at Zero Angle of Attack, NASA SP-3004, 1964

Smith, M. G., “Laplace Transform Theory,” D. Van Nostrand Company LTD, London, 1966, Chapter 4

Smith, R. H., Scott, E. P., and Ligrani, P. H., “Experimental Validation of an Inverse Heat Conduction Problem Using Thermocouple and Infrared Data,” AIAA 2001-0507, Reno, NV, 2001

Stolz G. J., “Numerical Solutions to an Inverse Problem of Heat Conduction for Simple Shapes”, Journal of Heat Transfer, Vol. 82, 1960, pp. 20-26

Swanson, E., O., Boundary Layer Transition on Cones at Angle of Attack in a Mach-6 Quiet Tunnel, PhD Thesis, School of Aeronautics and Astronautics, Purdue University, 2008

Taler, J., Theory of transient experimental techniques for surface heat transfer, International Journal of Heat and Mass Transfer, Vol. 39, No. 17, 1996, pp. 3733-3748

Taler, J. and Duda, P., “Solving Direct and Inverse Heat Conduction Problems,” Springer, Berlin 2006, Chapters 7 and 18

Walker, D. G. and Scott, E. P., "Evaluation of Estimation Methods for High Unsteady Heat Fluxes from Surface Measurements," Journal of Thermophysics and Heat Transfer, Vol. 12, No. 4, 1998, pp. 543-551

Wang, T., Lin, M., and Bunker, R. S., “Flow and Heat Transfer of Confined Impingement Jets Cooling Using 3-D Transient Liquid Crystal Scheme”, International Journal of Heat and Mass Transfer, Vol.48, 2005, pp.4887-4903

White, F. M., Viscous Fluid Flow, McGraw-Hill, 1974, pp. 589-593

Wright, M. J.,. Candler, G. V and Bose, D., Data-Parallel Line Relaxation Method for the Navier-Stokes Equations, AIAA Journal, Vol. 36, No. 9, September 1998, pp. 1603-1609

Appendix A: 1D Heat Transfer Analysis

A.1. Heat Conduction Equation and Laplace Transform

A transient solution of the 1D time-dependent heat conduction equation is sought by using the Laplace transform. Since a polymer layer is usually thin, the 1D time-dependent heat conduction equation can be used, assuming that the lateral heat conduction can be neglected. The heat conduction equation for a polymer layer is

$$\left(\frac{\partial}{\partial t} - a_p \frac{\partial^2}{\partial y^2} \right) \theta_p(t,y) = 0, \tag{A1}$$

where $\theta_p(t,y) = T_p - T_{in}$ is a temperature change in the polymer layer from a constant initial temperature (T_{in}), and $a_p = k_p / c_p \rho_p$ is the thermal diffusivity of the polymer. Here k_p, c_p and ρ_p are the thermal conductivity, specific heat and density of the polymer. Similarly, the governing equation for the base is

$$\left(\frac{\partial}{\partial t} - a_b \frac{\partial^2}{\partial y^2} \right) \theta_b(t,y) = 0, \tag{A2}$$

where $\theta_b(t,y) = T_b - T_{in}$ is a temperature change of the base from a constant initial temperature, and $a_b = k_b / c_b \rho_b$ is the thermal diffusivity of the base, and k_b, c_b and ρ_b are the thermal conductivity, specific heat and density of the base, respectively. It is assumed that both the polymer layer and base have the same initial temperature. Here, the thermal properties are considered to be constant for both the polymer layer and base. When the thermal diffusivity *k* is temperature-dependent, the Kirchhoff's model temperature can be introduced such that the form of Eq. (A1) or (A2) remains unchanged (Carslaw 2000).

The boundary condition at the polymer surface is

$$q_s(t) - k_p \frac{\partial}{\partial y} \theta_p(t,L) = 0, \tag{A3}$$

where $q_s(t)$ is the heat flux into the polymer surface and L is the polymer layer thickness. The boundary condition at infinity in the base is

$$\theta_b(t,-\infty) = 0. \tag{A4}$$

The matching conditions at the interface between the polymer and base are

$$\theta_p(t,0) = \theta_b(t,0), \tag{A5}$$

and

$$k_p \frac{\partial}{\partial y} \theta_p(t,0) = k_b \frac{\partial}{\partial y} \theta_b(t,0). \tag{A6}$$

After applying the Laplace transform

$$\Theta_p(s,y) = \int_0^\infty \theta_p(t,y) exp(-st) dt, \tag{A7}$$

Eq. (A1) becomes

$$\frac{d^2 \Theta_p}{dy^2} = \frac{s}{a_p} \Theta_p(s,y). \tag{A8}$$

Similarly, the transformed form of Eq. (A2) is

$$\frac{d^2\Theta_b}{dy^2} = \frac{s}{a_b}\Theta_b(s,y)\,. \tag{A9}$$

The solutions for Eqs. (A8) and (A9) are obtained and the corresponding transformed boundary and matching conditions are applied to determine the unknown coefficients. Therefore, the transformed heat flux at the polymer surface is given by

$$Q_s(s) = k_p\sqrt{s/a_p}\,\Theta_{ps}(s)G(s)\,, \tag{A10}$$

where $\Theta_{ps}(s)=\Theta_p(s,L)$ is the transformed temperature change at the polymer surface. The function $G(s)$ is defined by

$$G(s) = \frac{1+\bar{\varepsilon}\,exp\left(-2L\sqrt{s/a_p}\right)}{1-\bar{\varepsilon}\,exp\left(-2L\sqrt{s/a_p}\right)}, \tag{A11}$$

where $\bar{\varepsilon} = (1-\varepsilon)/(1+\varepsilon)$ and $\varepsilon = \sqrt{k_p\rho_p c_p / k_b\rho_b c_b}$. Now, the main problem is how to obtain an inverse Laplace transform of Eq. (A10) for the heat flux into the polymer surface as a function of the polymer surface temperature change. The effect of the base is contained in Eq. (A11).

A.2. Inversion of Laplace Transform for General Case

The inversion of Eq. (A10) for a general case is sought. Eq. (A10) is written as

$$Q_s(s) = (k_p/\sqrt{a_p})\,s\Theta_{ps}(s)K(s)\,, \tag{A12}$$

where

$$K(s) = \frac{1}{\sqrt{s}}\frac{1+\bar{\varepsilon}\,exp\left(-2L\sqrt{s/a_p}\right)}{1-\bar{\varepsilon}\,exp\left(-2L\sqrt{s/a_p}\right)}. \tag{A13}$$

The inversion of $K(s)$ is

$$k(t) = \frac{1}{2\pi i}\int_{\gamma-i\infty}^{\gamma+i\infty} exp(st)K(s)ds\,. \tag{A14}$$

To calculate the inversion, following a standard procedure (Carslaw 1963, Smith 1966), we consider a contour integral

$$I = \int exp(st)K(s)ds\,. \tag{A15}$$

The function $K(s)$ has a branch point at $s=0$ and a pole at $s = i^4(a_p/4L^2)\left|ln\,\bar{\varepsilon}\right|^2$.

The integral Eq. (A15) alone a closed contour *C* illustrated in Fig. A1 is zero. The integral $I_{A'A}$ over the segment *A'A* approaches the integral in Eq. (A15) as the radius *R* of a large circle goes to infinity, where *A* and *A'* are at $\gamma+i\beta$ and $\gamma-i\beta$, respectively. For the segment *AB*, $s = R\,exp(i\theta)$ where $tan^{-1}(\beta/\gamma) \le \theta \le \pi/2$, and $\left|K(s)\right| < CR^{-1/2}$ as $R\to\infty$. Therefore, $I_{AB}\to 0$ as $R\to\infty$. Similarly, $I_{A'B'}\to 0$, $I_{BC}\to 0$ and $I_{C'B'}\to 0$ as $R\to\infty$. For the segments *CD* and *D'C'*, $s = r\,exp[i(\pi-\delta)]$ and $s = r\,exp[i(-\pi+\delta)]$ as $\delta\to 0$, respectively. After some arrangements, we have the integral

$$I_{CD} + I_{D'C'} = \frac{2(1-\bar{\varepsilon}^2)}{i} \int_{r_0}^{R} \frac{exp(-rt)}{\sqrt{r}} \frac{dr}{1+\bar{\varepsilon}^2 - 2\bar{\varepsilon}\, cos(2L\sqrt{r/a_p})}, \tag{A16}$$

where r_0 is the radius of a small circle around a branch point at $s = 0$. The limits $r_0 \to 0$ and $R \to \infty$ will be taken in Eq. (A16). For the segments *EF* [$s = r\, exp(i\delta)$ as $\delta \to 0$] and *F'E'* [$s = r\, exp(-i\delta)$ as $\delta \to 0$], $I_{EF} + I_{F'E'} = 0$. For a circular contour *DEE'D'* [$s = r_0\, exp(i\theta)$, where $\theta = \pi$ to $\theta = -\pi$], $I_{DEE'D'} \to 0$ as $r_0 \to 0$. Similarly, for a circular contour *FF'* [$s = r_0\, exp(i\theta)$, where $\theta = \pi$ to $\theta = -\pi$], $I_{FF'} \to 0$ as $r_0 \to 0$. Combining the integrals along all the segments of the contour *C*, we obtain

$$k(t) = (\sqrt{a_p}/L) W(t), \tag{A17}$$

where

$$W(t) = \frac{1-\bar{\varepsilon}^2}{\pi} \int_0^{\infty} \frac{exp\left[-(a_p t/4L^2)\eta^2\right] d\eta}{1+\bar{\varepsilon}^2 - 2\bar{\varepsilon}\cos\eta}. \tag{A18}$$

Therefore, the heat flux at the polymer surface is

$$q_s(t) = \frac{k_p(1-\bar{\varepsilon}^2)}{\sqrt{\pi a_p}} \int_0^t \frac{\overline{W}(t-\tau, \bar{\varepsilon})}{\sqrt{t-\tau}} \frac{d\theta_{ps}(\tau)}{d\tau} d\tau\ , \tag{A19}$$

where

$$\overline{W}(t, \bar{\varepsilon}) = \frac{2}{\sqrt{\pi}} \int_0^{\infty} \frac{exp(-\xi^2)\, d\xi}{1+\bar{\varepsilon}^2 - 2\bar{\varepsilon}\, cos(2L\xi/\sqrt{a_p t})}. \tag{A20}$$

A.3. Effect of Lateral Heat Conduction

We consider the 3D heat conduction equation for a polymer layer

$$\frac{\partial \theta_p}{\partial t} = a_p \left(\frac{\partial^2 \theta_p}{\partial x^2} + \frac{\partial^2 \theta_p}{\partial y^2} + \frac{\partial^2 \theta_p}{\partial z^2} \right), \tag{A21}$$

where *y* is the coordinate normal to the surface between the polymer layer and base, and *x* and *z* are the coordinates on the surface. Using the Fourier transform to Eq. (A21)

$$\hat{\theta}_p = \int_{-\infty}^{\infty} \int_{-\infty}^{\infty} \theta_p\, exp\left(-i[ux+vz]\right) dx dz, \tag{A22}$$

Eq. (A21) becomes

$$\frac{\partial \hat{\theta}_p}{\partial t} = a_p \left(\frac{\partial^2 \hat{\theta}_p}{\partial y^2} - \left(u^2 + v^2\right) \hat{\theta}_p \right), \tag{A23}$$

where $\hat{\theta}_p = \hat{\theta}_p(t, y, u, v)$. Further, applying the Laplace transform to Eq. (A23)

$$\hat{\Theta}_p(s, y) = \int_0^{\infty} \hat{\theta}_p(t, y)\, exp(-st)\, dt, \tag{A24}$$

Eq. (A23) becomes

$$\frac{d^2\hat{\Theta}_p}{dy^2} = \left[s/a_p + \left(u^2 + v^2\right)\right]\hat{\Theta}_p . \tag{A25}$$

In a similar way to the 1D analysis, considering the matching conditions at the interface, we have the transformed heat flux at the polymer surface

$$\hat{Q}_s(s,u,v) = \frac{k_p}{\sqrt{a_p}}\left[s + a_p(u^2 + v^2)\right]\hat{\Theta}_{ps}(s,u,v)K(s',u,v), \tag{A26}$$

where $\hat{\Theta}_p(s,L,u,v)$ is the transformed temperature change at the polymer surface. The function $K(s',u,v)$ is defined by

$$K(s',u,v) = \frac{1}{\sqrt{s'}}\frac{1 + \bar{\varepsilon}\, exp\left(-2L\sqrt{s'/a_p}\right)}{1 - \bar{\varepsilon}\, exp\left(-2L\sqrt{s'/a_p}\right)}, \tag{A27}$$

where $s' = s + a_p(u^2 + v^2)$, $\bar{\varepsilon} = (1-\varepsilon)/(1+\varepsilon)$ and $\varepsilon = \sqrt{k_p\rho_p c_p / k_b\rho_b c_b}$. The inverse Laplace transform of $K(s',u,v)$ is

$$\begin{aligned} k(t,u,v) &= \frac{1}{2\pi i}\int_{\gamma-i\infty}^{\gamma+i\infty} exp(st)K(s',u,v)ds \\ &= \frac{exp\left[-a_p(u^2+v^2)t\right]}{2\pi i}\int_{\gamma'-i\infty}^{\gamma'+i\infty} exp(s't)K(s',u,v)ds' \end{aligned} . \tag{A28}$$

Since the integral in Eq. (A28) is the same as Eq. (A14), the result of the contour integral of (A18) can be directly used, i.e,, $k(t,u,v) = \left(\sqrt{a_p}/L\right)exp\left[-a_p(u^2+v^2)\right]W(t)$. Therefore, the inverse Laplace transform of Eq. (A28) leads to

$$\begin{aligned} \hat{q}_s(t,u,v) = \frac{k_p}{L}\Bigg[&\int_0^t W(t-\tau)exp\left[-a_p(u^2+v^2)(t-\tau)\right]\frac{d\hat{\theta}_{ps}}{d\tau}d\tau \\ &+ a_p(u^2+v^2)\int_0^t W(t-\tau)exp\left[-a_p(u^2+v^2)(t-\tau)\right]\hat{\theta}_{ps}d\tau \Bigg] \end{aligned} . \tag{A29}$$

Further, the inverse Fourier transform of Eq. (A29) yields Eq. (2.4) for the heat flux at the polymer surface.

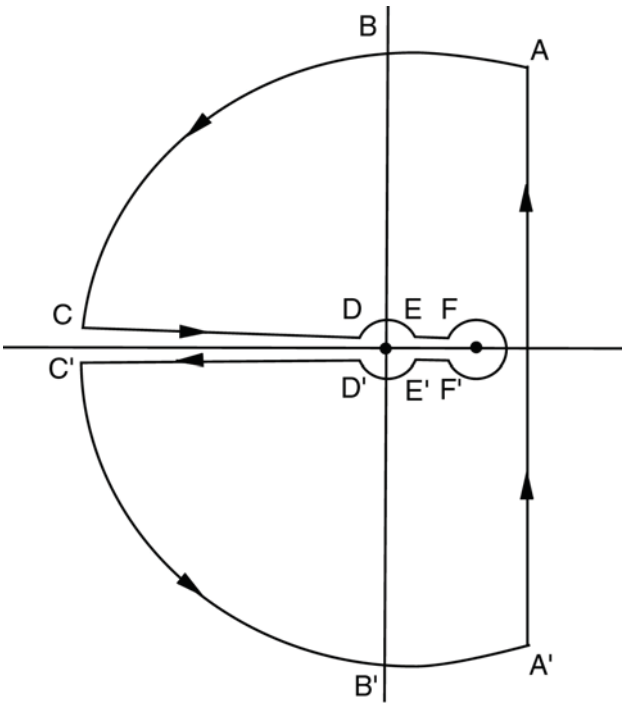

Figure A1. Contour for inversion of Laplace transform

Appendix B. Model for Correcting Lateral Heat Conduction Effect

B1. 1D and 3D Solutions for Direct Problems

Consider an element of a polymer layer and a semi-infinite base, as illustrated in Fig. 4.1, where y is the coordinate normal to the surface between the polymer layer and base, and x and z are the coordinates on the surface. The 3D unsteady heat conduction equation for a polymer layer is

$$\frac{\partial \theta_p}{\partial t} = a_p \left(\frac{\partial^2 \theta_p}{\partial x^2} + \frac{\partial^2 \theta_p}{\partial y^2} + \frac{\partial^2 \theta_p}{\partial z^2} \right), \tag{B1}$$

where $\theta_p(t,x,y,z) = T_p - T_{in}$ is a temperature change in the polymer layer from a constant initial temperature (T_{in}), and $a_p = k_p / c_p \rho_p$ is the thermal diffusivity of the polymer. Here, k_p, c_p and ρ_p are the thermal conductivity, specific heat and density of the polymer. The same equation is used for the temperature change $\theta_b(t,x,y,z)$ in the base. By applying the Fourier transform to Eq. (B1)

$$\hat{\theta}_p = \int_{-\infty}^{\infty} \int_{-\infty}^{\infty} \theta_p \, exp[-i(ux+vz)] \, dxdz, \tag{B2}$$

Eq. (B1) becomes

$$\frac{\partial \hat{\theta}_p}{\partial t} = a_p \left(\frac{\partial^2 \hat{\theta}_p}{\partial y^2} - \left(u^2 + v^2\right) \hat{\theta}_p \right), \tag{B3}$$

where $\hat{\theta}_p = \hat{\theta}_p(t,y,u,v)$. Further, applying the Laplace transform to Eq. (B3)

$$\hat{\Theta}_p(s,y) = \int_0^{\infty} \hat{\theta}_p(t,y) exp(-st) dt, \tag{B4}$$

Eq. (B3) becomes

$$\frac{d^2 \hat{\Theta}_p}{dy^2} = \left[s / a_p + \left(u^2 + v^2\right) \right] \hat{\Theta}_p. \tag{B5}$$

The boundary condition at the polymer surface is $q_s(t,x,z) - k_p \partial \theta_p(t,x,L,z) / \partial y = 0$, where q_s is the heat flux into the polymer surface and L is the polymer layer thickness. The boundary condition at infinity in the base is $\theta_b(t,x,-\infty,z) = 0$. The corresponding solution for the base has the same form as Eq. (B5) in the transformed domain. The matching conditions at the interface between the polymer and base are $\theta_p(t,x,0,z) = \theta_b(t,x,0,z)$, and $k_p \partial \theta_p(t,x,0,z) / \partial y = k_b \partial \theta_b(t,x,0,z) / \partial y$. After using the boundary conditions and matching conditions at the interface, we have the transformed temperature change at the polymer surface

$$\hat{\Theta}_{ps}(s,u,v) = \frac{\sqrt{a_p}}{k_p} H(s') \hat{Q}_s(s,u,v), \tag{B6}$$

where $\hat{Q}_s(s,u,v)$ is the transformed heat flux at the polymer surface. The function $H(s')$ is defined by

$$H(s') = \frac{1}{\sqrt{s'}} \frac{1 - \bar{\varepsilon}\, exp\left(-2L\sqrt{s'/a_p}\right)}{1 + \bar{\varepsilon}\, exp\left(-2L\sqrt{s'/a_p}\right)}, \tag{B7}$$

where $s' = s + a_p(u^2 + v^2)$, $\bar{\varepsilon} = (1-\varepsilon)/(1+\varepsilon)$ and $\varepsilon = \sqrt{k_p \rho_p c_p / k_b \rho_b c_b}$. The inverse Laplace transform of $H(s')$ is

$$h(t,u,v) = \frac{1}{2\pi i} \int_{\gamma - i\infty}^{\gamma + i\infty} exp(st) H(s') ds = exp\left[-a_p(u^2 + v^2)t\right] G(t). \tag{B8}$$

where a Green function is defined as

$$G(t) == \frac{1}{2\pi i} \int_{\gamma' - i\infty}^{\gamma' + i\infty} exp(s't) H(s') ds'. \tag{B9}$$

Therefore, the inverse Laplace transform of Eq. (B6) is

$$\hat{\theta}_{ps} = \frac{\sqrt{a_p}}{k_p} \int_0^t G(t-\tau) exp\left[-a_p(u^2 + v^2)(t-\tau)\right] \hat{q}_s(\tau,u,v) d\tau \ . \tag{B10}$$

Further, the inverse Fourier transform of Eq. (B10) leads to a relation between the surface temperature change and the heat flux into the surface of the polymer layer

$$\theta_{ps(3D)}(t,x,z) = \frac{\sqrt{a_p}}{k_p} \int_0^t G(t-\tau) \left\langle q_s \right\rangle_g (\tau,x,z;\sigma(t-\tau)) d\tau \ , \tag{B11}$$

where the spatially-averaged heat flux is

$$\left\langle q_s \right\rangle_g = \int_{-\infty}^{\infty} \int_{-\infty}^{\infty} g\left[x - x', z - z'; \sigma(t-\tau)\right] q_s(\tau, x', z') dx' dz' \ . \tag{B12}$$

The filter function in Eq. (B12) is the Gaussian distribution

$$g(x,z;\sigma) = \frac{1}{2\pi\sigma^2} exp\left(-\frac{x^2 + z^2}{2\sigma^2}\right), \tag{B13}$$

where $\sigma(t) = \sqrt{2 a_p t}$. The size of the filter functions characterizes the effect of the lateral heat conduction, and the standard deviation σ defines the affected region. Similarly, by using the Laplace transform, the direct solution for the 1D unsteady heat conduction equation is given by

$$\theta_{ps(1D)}(t) = \frac{\sqrt{a_p}}{k_p} \int_0^t G(t-\tau) q_{s(1D)}(\tau) d\tau \ . \tag{B14}$$

The inverse solution of Eq. (B14) for $q_{s(1D)}$ is actually given by Eq. (2.1) for the 1D case.

To explore the connection between the 1D and 3D solutions, $q_s(\tau, x', z')$ in Eq. (B12) is expanded as a Taylor series at a fixed point (x,z) on a surface,. Thus, we have

$$\left\langle q_s \right\rangle_g = q_s(\tau,x,z) + \frac{1}{2}\left\langle g, (x'-x)^2 \right\rangle \left.\frac{\partial^2 q_s}{\partial x^2}\right|_{(x,z)} + \frac{1}{2}\left\langle g, (z'-z)^2 \right\rangle \left.\frac{\partial^2 q_s}{\partial z^2}\right|_{(x,z)}, \tag{B15}$$

where the inner product is defined as

$$\left\langle g, f \right\rangle = \int_{-\infty}^{\infty} \int_{-\infty}^{\infty} g\left[x - x', z - z' : \sigma\right] f(x', z') dx' dz' \ . \tag{B16}$$

The derivation of Eq. (B15) utilizes the fact that the moments $\langle g, x'-x \rangle$, $\langle g, z'-z \rangle$ and $\langle g, (x'-x)(z'-z) \rangle$ vanish at the fixed point (x,z) because of the symmetry of the Gaussian function. Substitution of Eq. (B15) into Eq. (B11) yields

$$\theta_{ps(3D)}(t,x,z) = (1+\Delta\lambda)\frac{\sqrt{a_p}}{k_p}\int_0^t G(t-\tau)\, q_s(\tau,x,z)\, d\tau \ , \tag{B17}$$

where $\Delta\lambda$ is a relative surface temperature change due to the lateral heat conduction that is given by

$$\Delta\lambda = \frac{1}{2}\beta_{xx}\left.\frac{\partial^2 q_s}{\partial x^2}\right|_{(x,z)} + \frac{1}{2}\beta_{zz}\left.\frac{\partial^2 q_s}{\partial z^2}\right|_{(x,z)} \ , \tag{B18}$$

and the coefficients in Eq. (B18) are defined as

$$\beta_{xx} = \frac{\int_0^t G(t-\tau)\langle g, (x'-x)^2 \rangle d\tau}{\int_0^t G(t-\tau)\, q_s(\tau,x,z)\, d\tau} \ ,$$

$$\beta_{zz} = \frac{\int_0^t G(t-\tau)\langle g, (z'-z)^2 \rangle d\tau}{\int_0^t G(t-\tau)\, q_s(\tau,x,z)\, d\tau} \ .$$

Eq. (B17) gives the connection between the 3D solution and the 1D solution, which is simply written as $\theta_{ps(3D)} = (1+\Delta\lambda)\theta_{ps(1D)}$, since the integral in the right-hand side of Eq. (B17) is actually the 1D solution applied to the fixed point (x,z) on a surface. The factor $\Delta\lambda$ mainly depends on the second derivatives of q_s along the surface. The order estimates give $\partial^2 q_s / \partial x^2 \sim |\Delta q_s| / \sigma^2$, $\partial^2 q_s / \partial z^2 \sim |\Delta q_s| / \sigma^2$, $\beta_{xx} \sim \sigma^2 / |q_s|$ and $\beta_{zz} \sim \sigma^2 / |q_s|$. Therefore, $\Delta\lambda \sim |\Delta q_s| / |q_s|$, and when the relative change of q_s along a surface is small except in certain isolated region, $\Delta\lambda << 1$.

B2. Convolution-Type Integral Equation

When $\Delta\lambda$ is treated as a time-independent factor (it may weakly depend on time), $(1+\Delta\lambda)\theta_{ps(1D)} = \theta_{ps(3D)}$ gives

$$\int_0^t G(t-\tau)\Big[(1+\Delta\lambda) q_{s(1D)}(\tau,x,z) - \langle q_s \rangle_g (\tau,x,z;\sigma(t-\tau))\Big] d\tau = 0 \ . \tag{B19}$$

Since t is arbitrary, the integrand in Eq. (B19) must be zero. Further, for $G(t) > 0$, we obtain

$$(1+\Delta\lambda) q_{s(1D)}(t,x,z) = \int_{-\infty}^{\infty}\int_{-\infty}^{\infty} g\left[x-x', z-z'; \sigma(t''-t)\right] q_s(t,x',z') dx'\, dz' \ , \tag{B20}$$

where t is the time elapsing from the start-up of a wind tunnel, and $\sigma(t''-t)$ is the standard deviation over a time difference $t''-t$ in which t'' is free. Therefore, since $\sigma(t''-t)$ is

undetermined, it should be suitably modeled as an empirical standard deviation $\sigma_r(t)$ that describes the effect of the lateral heat conduction. According to Eq. (B20), the heat flux given by using the 1D method in a 3D case should be interpreted as a spatially-averaged heat flux.

It should be emphasized that $q_{s(1D)}(t,x,z)$ in Eq. (B20) is the heat flux given by applying the 1D method to a 3D case. In a general 3D case where the surface temperature at a point is influenced by its neighbor, $q_{s(1D)}(t,x,z)$ at that point is related to its neighbor by the convolution integral Eq. (B20). At this point, Eq. (B20) is an accurate formal representation of the physical situation when the 1D method is applied to a general 3D case. However, the standard deviation in Eq. (B20) is not known a priori, and $\sigma_r(t)$ should be suitably modeled and determined by optimization in simulations such that Eq. (B20) can serve as a useful model for correcting the lateral heat conduction effect. In this sense, Eq. (B20) is an approximate model with the empirical parameter $\sigma_r(t)$. By inspecting Eqs. (B11)-(B13), it is suggested that a linear relation $\sigma_r(t) = r_1\sqrt{2\,a_p\,t} + r_0$ could be a plausible model, where r_1 and r_0 are empirical coefficients to be determined. Therefore, when $q_{s(1D)}(t,x,z)$ is given and $\Delta\lambda$ is set at zero, improved calculation of the heat flux $q_s(t,x,z)$ can be made by solving the convolution-type integral equation Eq. (B20) as an inverse problem.

B3. Green Function

To calculate the Green function $G(t)$ in Eq. (B9), following a standard procedure of inversion of the Laplace transform, we consider a contour integral

$$I = \int exp(s't)H(s')ds' . \tag{B21}$$

The function $H(s')$ has a branch point at $s'=0$ and a pole at $s' = (a_p/4L^2)[ln^2(\bar{\varepsilon}^{-1}) - \pi^2 + 2\pi\, ln(\bar{\varepsilon}^{-1})\,i]$. The integral Eq. (B21) along a closed contour C illustrated in Fig. A1 is zero. The integral $I_{A'A}$ over the segment $A'A$ approaches the integral in the inverse Laplace transform as the radius R of a large circle goes to infinity, where A and A' are at $\gamma + i\beta$ and $\gamma - i\beta$, respectively. For the segment AB, $s' = R\,exp(i\theta)$ where $tan^{-1}(\beta/\gamma) \le \theta \le \pi/2$, and $|H(s')| < CR^{-1/2}$ as $R \to \infty$. Therefore, $I_{AB} \to 0$ as $R \to \infty$. Similarly, $I_{A'B'} \to 0$, $I_{BC} \to 0$ and $I_{C'B'} \to 0$ as $R \to \infty$. For the segments EF [$s' = r\,exp[i(\alpha + \delta)]$ as $\delta \to 0$] and $F'E'$ [$s' = r\,exp[-i(\alpha - \delta)]$ as $\delta \to 0$], $I_{EF} + I_{F'E'} = 0$, where α is an angular position of the pole. For a circular contour $DEE'D'$ [$s' = r_0\,exp(i\theta)$, where $\theta = \pi$ to $\theta = -\pi$], $I_{DEE'D'} \to 0$ as $r_0 \to 0$. Similarly, for a circular contour FF' [$s' = s'_0 + r_0\,exp(i\theta)$, where $\theta = \pi$ to $\theta = -\pi$ and s'_0 is the position of the pole], $I_{FF'} \to 0$ as $r_0 \to 0$. For the segments CD and $D'C'$, $s = r\,exp[i(\pi - \delta)]$ and $s = r\,exp[i(-\pi + \delta)]$ as $\delta \to 0$, respectively. After some arrangements, we have the integral

$$I_{CD} + I_{D'C'} = \frac{2(1-\bar{\varepsilon}^2)}{i} \int_{r_0}^{R} \frac{exp(-rt)}{\sqrt{r}} \frac{dr}{1 + \bar{\varepsilon}^2 + 2\bar{\varepsilon}\,cos(2L\sqrt{r/a_p})}, \tag{B22}$$

where r_0 is the radius of a small circle around a branch point at $s = 0$. The limits $r_0 \to 0$ and $R \to \infty$ will be taken in Eq. (B22). Combining the integrals along all the segments of the contour *C*, we obtain the Green function

$$G(t) = \frac{(1-\bar{\varepsilon}^2)\sqrt{a_p}}{\pi L} \int_0^\infty \frac{exp\left[-(a_p t / 4L^2)\eta^2\right] d\eta}{1+\bar{\varepsilon}^2 + 2\bar{\varepsilon}\cos\eta}. \tag{B23}$$

Substitution of Eq. (B23) into Eq. (B11) yields the temperature change at the polymer surface

$$\theta_{ps(3D)}(t,x,z) = \frac{\sqrt{a_p}(1-\bar{\varepsilon}^2)}{k_p\sqrt{\pi}} \int_0^t \frac{\overline{W_1}(t-\tau,\bar{\varepsilon})}{\sqrt{t-\tau}} \langle q_s \rangle_g (\tau,x,z;t-\tau) d\tau \ , \tag{B24}$$

where a modified Gaussian integral is

$$\overline{W_1}(t,\bar{\varepsilon}) = \frac{2}{\sqrt{\pi}} \int_0^\infty \frac{exp(-\xi^2)\, d\xi}{1+\bar{\varepsilon}^2 + 2\bar{\varepsilon}\cos(2L\xi / \sqrt{a_p t})}. \tag{B25}$$

When $\langle q_s \rangle_g$ in Eq. (B24) is replaced by $q_{s(1D)}(\tau)$, Eq. (B24) is reduced to the 1D solution for the polymer surface temperature.

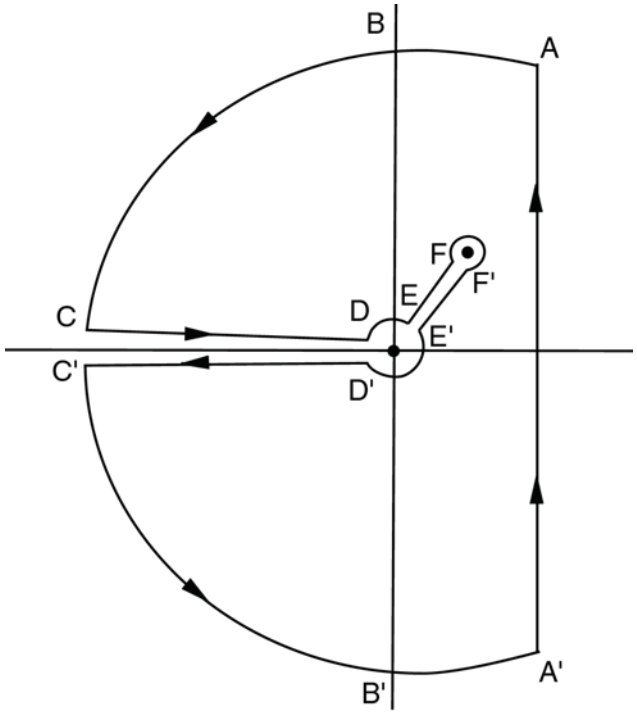

Figure B1. Contour for inversion of the Laplace transform

Appendix C: Similarity Solution

The continuity, momentum and energy equations for an unsteady compressible boundary layer on a slender sharp cone are

$$\frac{\partial(r^n\rho)}{\partial t}+\frac{\partial(r^n\rho u)}{\partial x}+\frac{\partial(r^n\rho v)}{\partial y}=0\,, \tag{C1}$$

$$\rho\frac{Du}{Dt}=-\frac{\partial p_e}{\partial x}+\frac{\partial}{\partial y}\left(\mu\frac{\partial u}{\partial y}\right), \tag{C2}$$

$$\rho\frac{DH}{Dt}=\frac{\partial p_e}{\partial x}+\frac{\partial}{\partial y}\left[\mu\left(\frac{\partial H}{\partial y}+\frac{1-Pr}{Pr}\frac{\partial h}{\partial y}\right)\right], \tag{C3}$$

where u and v are the velocity components in the x and y coordinates on the surface, $H=h+u^2/2$ is the enthalpy, h is the static enthalpy, $Pr=c_p\,\mu/k$ is the local Prandtl number, ρ is the air density, μ is the air viscosity, and p_e is the pressure at the edge of the boundary layer. Two-dimensional and axisymmetrical flows correspond to $n=0$ and $n=1$, respectively. The continuity equation, Eq. (C1), is approximately valid for $y\cos\delta \ll r$, where δ is the half-angle of a cone. When the stream function ψ is introduced such that

$$u=\frac{\rho_o}{r^n\rho}\frac{\partial\psi}{\partial y}\,,\; v=-\frac{\rho_o}{r^n\rho}\left(\frac{\partial\psi}{\partial x}+\frac{\partial\bar{y}}{\partial t}\right), \tag{C4}$$

Eq. (C1) is satisfied, where ρ_o is the convenient reference density that is a constant) and $\bar{y}=\int_0^y r^n\rho_o/\rho\,dy$ is interpreted as an equivalent incompressible distance from the wall (Schlichting 1972).

The similarity functions are defined as $f'=u/u_e$ and $g=H/H_s$, where u_e is the velocity at the edge of a boundary layer and H_s is the enthalpy at the stagnation point. The Illingworth-Stewartson transformation is introduced, i.e.,

$$\xi=\int_0^x\rho_w\mu_w u_e\,r^{2n}dx\,, \tag{C5}$$

$$\eta=\frac{r^n u_e}{\sqrt{2\xi}}\int_0^y\rho\,dy\,, \tag{C6}$$

where n = 1 for an axisymmetrical body and n = 0 for a flat plate. Since $f=\rho_o\psi/\sqrt{2\xi}$, v can be expressed as a function of f. The subscripts "w" and "e" denote the values at the wall and the edge of the boundary layer, respectively. Therefore, Eqs. (C2) and (C3) becomes

$$\frac{\partial}{\partial\eta}\left(\varphi\frac{\partial^2 f}{\partial\eta^2}\right)+f\frac{\partial^2 f}{\partial\eta^2}+\beta\left[\frac{\rho_e}{\rho}-\left(\frac{\partial f}{\partial\eta}\right)^2\right]=F(\xi,\eta)\,, \tag{C7}$$

$$\frac{\partial}{\partial\eta}\left(\frac{\varphi}{Pr}\frac{\partial g}{\partial\eta}\right)+f\frac{\partial g}{\partial\eta}+\frac{u_e^2}{H_s}\frac{\partial}{\partial\eta}\left[\left(1-\frac{1}{Pr}\right)\varphi\frac{\partial f}{\partial\eta}\frac{\partial^2 f}{\partial\eta^2}\right]=G(\xi,\eta)\,, \tag{C8}$$

where

$$F(\xi,\eta) = 2\xi\left(\frac{\partial f}{\partial \eta}\frac{\partial^2 f}{\partial \eta \partial \xi} - \frac{\partial f}{\partial \xi}\frac{\partial^2 f}{\partial \eta^2}\right) + 2\xi\left(u_e^3 \rho_w \mu_w r^{2n}\right)^{-1}\left[\left(\frac{\partial f}{\partial \eta} - \frac{\rho_e}{\rho}\right)\frac{\partial u_e}{\partial t} + u_e \frac{\partial^2 f}{\partial t \partial \eta}\right]$$
$$- \sqrt{2\xi}\frac{\rho_o}{u_e \rho_w \mu_w r^{2n}}\frac{\partial^2 f}{\partial \eta^2}\frac{\partial \bar{y}}{\partial t}, \qquad \text{(C9)}$$

$$G(\xi,\eta) = 2\xi\left(\frac{\partial f}{\partial \eta}\frac{\partial g}{\partial \xi} - \frac{\partial f}{\partial \xi}\frac{\partial g}{\partial \eta}\right) + 2\xi\left(u_e^2 \rho_w \mu_w r^{2n} H_s\right)^{-1}\left(H_s \frac{\partial g}{\partial t} + g\frac{\partial H_s}{\partial t}\right)$$
$$- 2\xi\frac{1}{\rho u_e^2 \rho_w \mu_w r^{2n} H_s}\frac{\partial p_e}{\partial t} - \sqrt{2\xi}\frac{\rho_o}{u_e \rho_w \mu_w r^{2n}}\frac{\partial g}{\partial \eta}\frac{\partial \bar{y}}{\partial t}. \qquad \text{(C10)}$$

In Eqs. (C7) and (C8), $\varphi = \rho\mu/(\rho_w \mu_w)$ is a density and viscosity ratio (the Chapman-Rubesin parameter), $Pr = c_p \mu / k$ is the local Prandtl number, and $\beta = 2\,d(\ln u_e)/d(\ln \xi)$ is the pressure gradient parameter. The first terms in Eqs. (C9) and (C10) are related to the dependence of the flow development along the streamwise direction. The second terms in Eqs. (C9) and (C10) represent the time dependence of the velocity and enthalpy, respectively. It will be pointed out that the third terms in Eqs. (C9) and (C10) are related to the time dependence of the wall temperature.

The main terms in Eqs. (C9) and (C10) are evaluated. For a circular cone (n = 1) with the half-angle of δ, $r = x\cos\delta\tan\delta$ and $\xi = \rho_w \mu_w u_e (\cos\delta\tan\delta)^2 x^3/3$. Therefore,

$$\frac{2\xi H_s}{u_e^2 \rho_w \mu_w r^{2n} H_s}\frac{\partial g}{\partial t} = \frac{2x}{3u_e}\frac{\partial g}{\partial t},$$
$$\frac{2\xi g}{u_e^2 \rho_w \mu_w r^{2n} H_s}\frac{\partial H_s}{\partial t} = \frac{2xg}{3u_e H_s}\frac{\partial H_s}{\partial t},$$
$$\frac{\sqrt{2\xi}\rho_o}{u_e \rho_w \mu_w r^2}\frac{\partial \bar{y}}{\partial t} = \frac{x(\lambda-1)\eta}{3u_e T_w}\frac{\partial T_w}{\partial t},$$

where the power law $\mu = BT^{\lambda}$ is used. It is assumed that after a transient start-up the flow rapidly approaches to a steady state ($\partial u_e/\partial t \to 0$, $\partial f/\partial t \to 0$, $\partial g/\partial t \to 0$) and an asymptotic state independent of the streamwise coordinate ($\partial f/\partial \xi \to 0$, $\partial g/\partial \xi \to 0$). Therefore, Eqs. (C7) and (C8) become the semi-similarity equations

$$\frac{\partial}{\partial \eta}\left(\varphi\frac{\partial^2 f}{\partial \eta^2}\right) + \left(f - \Gamma_{T_w}\eta\right)\frac{\partial^2 f}{\partial \eta^2} + \beta\left[\frac{\rho_e}{\rho} - \left(\frac{\partial f}{\partial \eta}\right)^2\right] = 0, \qquad \text{(C11)}$$

$$\frac{\partial}{\partial \eta}\left(\frac{\varphi}{Pr}\frac{\partial g}{\partial \eta}\right) + \left(f - \Gamma_{T_w}\eta\right)\frac{\partial g}{\partial \eta} + \frac{u_e^2}{H_s}\frac{\partial}{\partial \eta}\left[\left(1 - \frac{1}{Pr}\right)\varphi\frac{\partial f}{\partial \eta}\frac{\partial^2 f}{\partial \eta^2}\right] - \Gamma_{H_s} g = 0, \qquad \text{(C12)}$$

where

$$\Gamma_{H_s} = \frac{2x}{3u_e H_s}\frac{\partial H_s}{\partial t}, \quad \Gamma_{T_w} = \frac{x(\lambda-1)}{3u_e T_w}\frac{\partial T_w}{\partial t}. \qquad \text{(C13)}$$

In typical tests in the Boeing/AFOSR Mach-6 Quiet Tunnel, the estimated values of Γ_{H_s} and Γ_{T_w} are of the order of $10^{-6} - 10^{-7}$. Calculations indicate that the effects of of Γ_{H_s} and Γ_{T_w}

on the similarity solution are negligible. Therefore, the similarity equations for a compressible boundary layer on a cone are (Marvin and Deiwert 1965)

$$(\varphi f'')' + f f'' + \beta(\rho_e / \rho - f'^2) = 0, \tag{C14}$$

$$[(\varphi / Pr) g']' + f g' + \frac{u_e^2}{H_s}[(\varphi - \varphi / Pr) f' f'']' = 0. \tag{C15}$$

The power-law viscosity approximation $\mu = BT^{\lambda}$ (kg/m-s) for air is used, where T is in Kelvin, $B = 7.839 \times 10^{-8}$ and $\lambda = 0.9739$ for $0 < T < 200\ K$, and $B = 2.709 \times 10^{-7}$ and $\lambda = 0.7403$ for $200 \le T < 700\ K$. A model for the thermal conductivity of air is $k = CT^m$ (W/m-K) for air is used for $100 < T < 700\ K$, where T is in Kelvin, $C = 1.9554 \times 10^{-4}$ and $m = 0.8558$. These power-laws are obtained by fitting the model of Lemmon and Jacobson (2004). A model for the specific heat c_p is $c_p = 1004 + 0.0005(T - 293)^2$ (J/kg-K). An approximation $c_p \approx c_{pw}$ is used here. Thus, the relevant parameters in Eqs. (C14) and (C15) are further given by

$$\varphi = g_w^{1-\lambda}\left(g - \frac{u_e^2}{2H_s} f'^2\right)^{\lambda-1},$$

$$\varphi / Pr = \frac{g_w^{1-m}}{Pr_w}\left(g - \frac{u_e^2}{2H_s} f'^2\right)^{m-1},$$

$$\rho_e / \rho = \frac{H_s}{h_e}\left(g - \frac{u_e^2}{2H_s} f'^2\right).$$

The boundary conditions are $f(0) = 0$, $f'(0) = 0$, $g(0) = g_w$, $f'(\infty) = 1$ and $g(\infty) = 1$. The solution depends on the four parameters u_e^2 / H_s, g_w, Pr_w and h_e / H_s.

For a cone, $\beta = 0$ and $\xi = \rho_w \mu_w u_e (\cos\delta \tan\delta)^2 x^3 / 3$, where δ is the half-cone angle. The heat flux at the wall is

$$q_w = \frac{H_s (\mu_w \rho_w u_e)^{1/2} g'(0)}{\sqrt{2/3}\, Pr_w \sqrt{x}}, \tag{C16}$$

where q_w is in W/m^2 and other dimensional variables are in SI units. The fourth-order Runge-Kutta method with a shooting scheme is used to solve the similarity equations. The outer flow conditions are given by the Taylor-Maccoll solution (Anderson 1990).

Appendix D: Reference Temperature Method

In the reference temperature method (White 1974), the Stanton number on a flat plate

$$St = \frac{q_w}{\rho_e u_e (h_{aw} - h_w)} \tag{D1}$$

is given by

$$St = \frac{0.332\sqrt{\varphi^*}\,(Pr^*)^{-2/3}}{\sqrt{Re_{x,e}}}, \tag{D2}$$

where the relevant parameters are given by

$$Re_{x,e} = \frac{\rho_e u_e x}{\mu_e},\ Pr^* = \frac{\mu^* c_p^*}{k^*}, \text{ and } \varphi_e^* = \frac{\rho^* \mu^*}{\rho_e \mu_e}.$$

The reference temperature is given by $T^*/T_e = 0.5 + 0.039M_e^2 + 0.5T_w/T_e$. For the cone, a factor of $\sqrt{3}$ is multiplied to the estimated heat flux due to the Mangler transformation. The Chapman-Rubesin parameter φ_e^* is given by the Sutherland law (Eq. 7-44b in the White's book)

$$\varphi_e^* = \left(\frac{T^*}{T_e}\right)^{1/2} \frac{T_e + K_{air}}{T^* + K_{air}},$$

where $K_{air} = 200^o R = 111.1K$. The viscosity and thermal conductivity are calculated based on the model of Lemmon and Jacobson (2004).

Appendix E. Determination of Thermal Diffusivity of Material Using Laser Heating

Three solutions are given here that are useful for determination of the thermal diffusivity of material by using laser heating on a TSP-coated surface.

E1. Pulse Laser Heating on a Thin Film

The problem of pulse laser heating on a thin film is analyzed and the characteristic times scales are determined. The governing equation is

$$\frac{\partial \theta}{\partial t} = \alpha \nabla^2 \theta, \tag{E1}$$

where $\theta = T - T_{in}$ $\nabla^2 = \partial^2 / \partial r^2 + r^{-1} \partial / \partial r + \partial^2 / \partial y^2$, r is the radial distance from the center of the hot spot center, y is the coordinate normal to the surface, and α is the thermal diffusivity of the body material. The initial temperature T_{in} is assumed to be ambient temperature. If the surface temperature of the film decreases fast enough along the radial direction ($r\theta \to 0$ as $r \to \infty$), an area-average operator can be introduced

$$\langle \theta \rangle = \frac{2\pi}{A} \int_0^\infty r\theta dr, \tag{E2}$$

where A is the effective area of the heated spot. Hence, by spatially averaging, Eq. (E1) is reduced to the one-dimensional, unsteady heat conduction equation

$$\frac{\partial \langle \theta \rangle}{\partial t} = \alpha \frac{\partial^2 \langle \theta \rangle}{\partial y^2}. \tag{E3}$$

The initial and boundary conditions are

$$\begin{aligned} &\langle \theta \rangle (0, y) = 0, \\ &-k \frac{\partial \langle \theta \rangle (t,0)}{\partial y} = \langle P \rangle \delta(t) - h \langle \theta \rangle (t,0), \\ &-k \frac{\partial \langle \theta \rangle (t,\eta)}{\partial y} = h \langle \theta \rangle (t,\eta) \end{aligned} \tag{E4}$$

where h is the average heat transfer coefficient of natural convection, $\delta(t)$ is the delta function, and $\langle P \rangle$ is the area-averaged laser-heating flux magnitude at a surface, and η is the film thickness.

There are two physical processes: the rapid heating of the film by the laser pulse and the relatively slow cooling process due to natural convection. At the beginning, since the film is heated in a very short time, the natural convection terms in the boundary conditions can be neglected. Thus, for the rapid heating process, the mathematical problem can be simplified. Use of the Laplace transform $\Theta = L(\langle \theta \rangle)$ for the problem yields

$$\Theta_\delta(s,\eta) = \frac{2P\sqrt{\alpha}}{k\sqrt{s}} \frac{exp(-\sqrt{s/\alpha}\,\eta)}{1 - exp(-2\sqrt{s/\alpha}\,\eta)}, \tag{E5}$$

where s is the complex variable in the Laplace transform. An approximation of Eq. (E5) is

$$\Theta_\delta(s,\eta) \approx \frac{P\sqrt{\alpha}}{k} \left[\frac{exp(-\sqrt{s/\alpha}\,\eta)}{s\eta/\sqrt{\alpha}} + \frac{exp(-0.8\sqrt{s/\alpha}\,\eta)}{\sqrt{s}} \right]. \tag{E6}$$

Hence, the inverse transform leads to an approximate expression for the temperature at the back surface in pulse laser heating on a thin film

$$\langle\theta\rangle_{\delta}(t,\eta)=\frac{P\alpha}{k\eta}\left[erfc(\sqrt{\tau/t})+\frac{2}{\sqrt{\pi}}\left(\frac{\tau}{t}\right)^{1/2}exp\left(-\frac{0.64\tau}{t}\right)\right], \tag{E7}$$

where the characteristic timescale is $\tau=\eta^2/4\alpha$.

For the slow cooling process due to natural convection after the heat source ceases, an additional averaging operator is used, i.e.,

$$\langle\theta\rangle_2=\frac{1}{\eta}\int_0^{\eta}\langle\theta\rangle dy\,. \tag{E8}$$

Applying the operator Eq. (E8) to Eq. (E3) leads to a simple lumped model for the cooling process

$$\frac{d\langle\theta\rangle_2}{dt}=-\frac{2\alpha h}{\eta k}\langle\theta\rangle_2+\frac{\alpha P\delta(t)}{k\eta}\,. \tag{E9}$$

In the above model, an assumption is that $\langle\theta\rangle_2 \cong \langle\theta\rangle_3$. The solution of Eq. (E9) is

$$\langle\theta\rangle_2=\frac{P\alpha}{k\eta}exp(-2t/\tau_2)\,, \tag{E10}$$

where the characteristic timescale is $\tau_2=\rho c_p\eta/h$.

Clearly, Eq. (E7) can be used to determine the thermal diffusivity $\alpha=k/c_p\rho$ of a material. A schematic of a laser heating setup is shown in Fig. E1. One side of a thin film of the tested material is heated by a pulsed laser beam through a focusing lens. The other side of the film is coated with TSP. The heated spot on the painted side is illuminated using an appropriate light source. The luminescence response from TSP to the pulsed laser heating is detected by a CCD camera. The surface temperature is determined by using a calibration relation and then the area-averaged temperature change $\langle\theta\rangle$ is calculated as a function of time. Eq. (E7) is used to fit $\langle\theta\rangle$ in the heating process by adjusting $\tau=\eta^2/4\alpha$, and thus α is determined for a known film thickness η.

E2. Step Laser Heating on a Thin Film

For step laser heating on a thin film, the boundary condition at the heated side of the film is

$$-k\frac{\partial\langle\theta\rangle(t,0)}{\partial y}=\langle P\rangle H(t)-h\langle\theta\rangle(t,0)\,, \tag{E11}$$

where $H(t)$ is the Heaviside function. The Laplace-transformed temperature change for step heating is

$$\Theta_H(s,\eta)=\frac{2P\sqrt{\alpha}}{ks\sqrt{s}}\frac{exp(-\sqrt{s/\alpha}\,\eta)}{1-exp(-2\sqrt{s/\alpha}\,\eta)}\quad. \tag{E12}$$

The temperature change at the back surface in step laser heating on a thin film is

$$\langle\theta\rangle_H(t,\eta)=\int_0^t\langle\theta\rangle_{\delta}(t',\eta)dt'\,. \tag{E13}$$

Similar to pulse laser heating, Eq. (E13) can be used to determine the thermal diffusivity $\alpha = k / c_p \rho$ of a material based on step laser heating.

E3. Pulse Laser Heating on a Semi-Infinite Base

The problem of pulse laser heating on a semi-infinite base is considered, as shown in Fig. E2. The 3D heat conduction equation is

$$\frac{\partial \theta}{\partial t} = \alpha \left(\frac{\partial^2 \theta}{\partial x^2} + \frac{\partial^2 \theta}{\partial y^2} + \frac{\partial^2 \theta}{\partial z^2} \right), \tag{E14}$$

where y is the coordinate normal to the surface of a semi-infinite base, and x and z are the coordinates on the surface. The initial and boundary conditions are

$$\begin{aligned} &\theta(0,x,y,z) = 0, \\ &-k \frac{\partial \theta(t,x,0,z)}{\partial y} = P(x,z)\delta(t), \\ &\theta(t,x,\infty,z) = 0 \end{aligned} \tag{E15}$$

where $P(x,z)$ is the laser-heating flux distribution on a surface. Using the Fourier transform to Eq. (E14)

$$\hat{\theta}(t,y,u,v) = \int_{-\infty}^{\infty} \int_{-\infty}^{\infty} \theta(t,x,y,z) exp\left(-i\left[ux + vz\right]\right) dxdz, \tag{E16}$$

Eq. (E14) becomes

$$\frac{\partial \hat{\theta}}{\partial t} = \alpha \left(\frac{\partial^2 \hat{\theta}}{\partial y^2} - \left(u^2 + v^2\right)\hat{\theta} \right). \tag{E17}$$

Further, by applying the Laplace transform to Eq. (E16), i.e.,

$$\hat{\Theta}(s,y) = \int_0^{\infty} \hat{\theta}(t,y) exp(-st) dt, \tag{E18}$$

Eq. (E17) becomes

$$\frac{d^2 \hat{\Theta}}{dy^2} = \left[s/\alpha + \left(u^2 + v^2\right) \right] \hat{\Theta}. \tag{E19}$$

The boundary conditions are $-k \partial \hat{\Theta} / \partial y = \hat{P}$ at $y = 0$ and $\hat{\Theta} = 0$ as $y \to \infty$. The solution for $\hat{\Theta}$ at the surface ($y = 0$) is

$$\hat{\Theta}_w = \frac{\hat{P}\sqrt{\alpha}}{k} \frac{1}{\sqrt{s + \alpha(u^2 + v^2)}}. \tag{E20}$$

Inverse Laplace transform of Eq. (E20) leads to

$$\hat{\theta}_w = \frac{\hat{P}\sqrt{\alpha}}{k\sqrt{\pi t}} exp[-\alpha t(u^2 + v^2)]. \tag{E21}$$

Since the inverse Fourier transform

$$F^{-1}\left\{ exp[-\alpha t(u^2 + v^2)] \right\} = \frac{1}{4\pi\alpha t} exp\left(-\frac{x^2 + z^2}{4\alpha t} \right), \tag{E22}$$

the convolution theorem gives a solution for the surface temperature change in laser heating on a semi-infinite base

$$\theta_w(x,z) = \frac{1}{4k\sqrt{\alpha}(\pi t)^{3/2}} \int_{-\infty}^{\infty}\int_{-\infty}^{\infty} G(x-x', z-z', 2\alpha t) P(x', z')\, dx'\, dz', \tag{E23}$$

where $G(x,z,\sigma^2) = exp[-(x^2+z^2)/2\sigma^2]$ acts as a Gaussian filter. The variance $\sigma^2 = 2\alpha t$ represents the thermal diffusion process on the surface. Therefore, the thermal diffusivity $\alpha = k/c_p\rho$ can be determined by using Eq. (E23) to fit the measured surface temperature field generated by pulse laser heating.

E4. Step Heating Tests

These solutions are given that are useful for determination of the thermal diffusivity of material by using laser heating on a TSP-coated surface. Step infrared laser heating on a Nylon sheet was used to determine the thermal diffusivity of Nylon. A very thin dark coating was applied to the Nylon surface to increases absorption of the IR laser. As illustrated in Fig. E1, the backside of a Nylon sheet with 0.25 mm thickness was coated with TSP. After the laser with a 0.5 OD filter of 0.2 cm thickness to reduce the power of the laser was turned on, a time sequence of TSP images was captured by a camera at 22 frames per second. The laser heating is approximately considered as step heating. Figure E3 shows the area-average temperature change $\langle\theta\rangle$ calculated from TSP images and fitting by using Eq. (E13). The characteristic timescale $\tau = \eta^2/4\alpha$ for the Nylon sheet is determined, which is 0.0189 s. Thus, the estimated thermal diffusivity is 8.51×10^{-7} m^2/s.

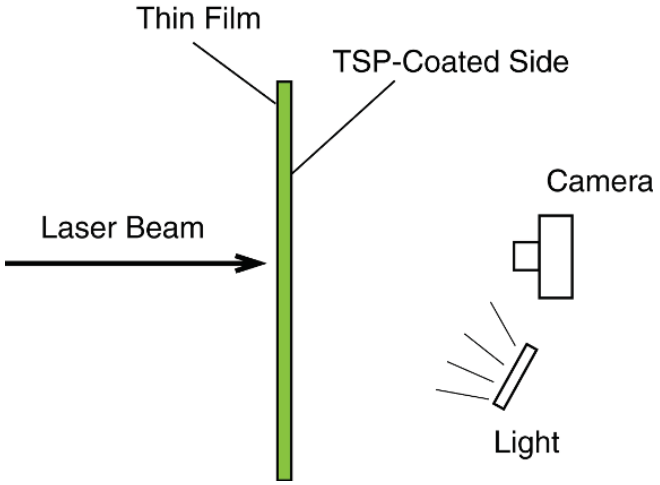

Figure E1. Laser heating setup for a thin film

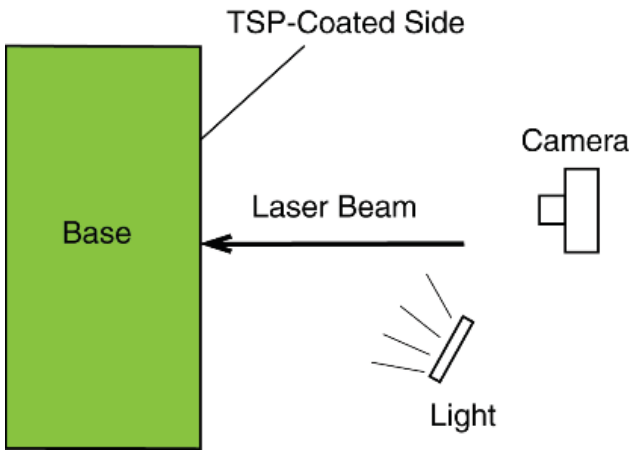

Figure E2. Laser heating setup for a semi-infinite base

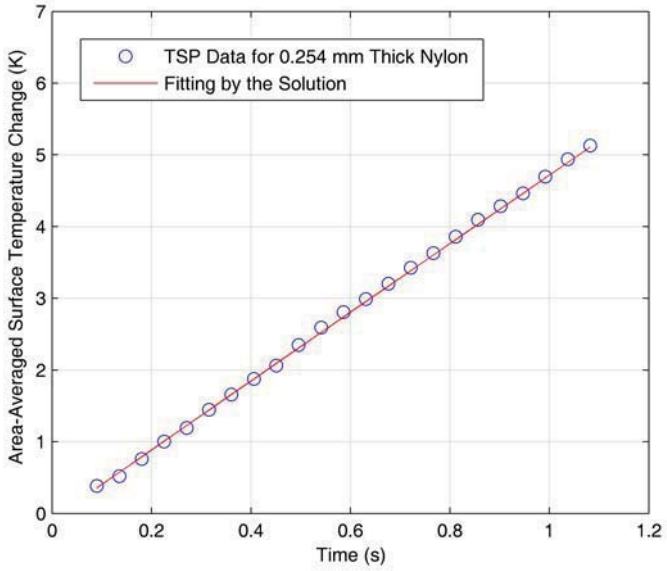

Figure E3. Area-averaged surface temperature as a function of time

Appendix F: Matlab Toolbox Manual for TSP Heat Flux Measurement

A Matlab toolbox is developed for TSP heat flux measurements, which includes 33 Matlab functions. The source codes (.m files) are available for users. There are several main functions for use while most functions are subroutines called by the main functions.

"HFComputation_GeneralCase" is the main function for calculating heat using the 1D analytical inverse heat transfer method from a time sequence of surface temperature at a point.

"HFComputation_Numerical" is the main functions for calculating heat flux using the 1D numerical inverse heat transfer method.

"HFComputation_Numerical_VariableParam" is basically the same function as "HFComputation_Numerical", but allowing inputs of the temperature-dependent thermal properties of materials.

"Heat_Flux_Cut_Al_Cone_Chris_Run 15" is an example on how to call the above function to calculate heat flux from a time sequence of TSP images. Users can change it for their applications.

REPORT DOCUMENTATION PAGE

Form Approved
OMB No. 0704-0188

1. REPORT DATE *(DD-MM-YYYY)*	2. REPORT TYPE	3. DATES COVERED *(From - To)*
01- 02 - 2012	Contractor Report	

4. TITLE AND SUBTITLE

Quantitative Global Heat Transfer in a Mach-6 Quiet Tunnel

5a. CONTRACT NUMBER

5b. GRANT NUMBER

NNX08AC97A

5c. PROGRAM ELEMENT NUMBER

6. AUTHOR(S)

Sullivan, John P.; Schneider, Steven P.; Liu, Tianshu; Rubal, Justin; Ward, Chris; Dussling, Joseph; Rice, Cody; Foley, Ryan; Cai, Zeimin; Wang, Bo; Woodiga, Sudesh

5d. PROJECT NUMBER

5e. TASK NUMBER

5f. WORK UNIT NUMBER

599489.02.07.07.04.11.01

7. PERFORMING ORGANIZATION NAME(S) AND ADDRESS(ES)

NASA Langley Research Center
Hampton, Virginia 23681-2199

8. PERFORMING ORGANIZATION REPORT NUMBER

9. SPONSORING/MONITORING AGENCY NAME(S) AND ADDRESS(ES)

National Aeronautics and Space Administration
Washington, DC 20546-0001

10. SPONSOR/MONITOR'S ACRONYM(S)

NASA

11. SPONSOR/MONITOR'S REPORT NUMBER(S)

NASA/CR-2012-217331

12. DISTRIBUTION/AVAILABILITY STATEMENT

Unclassified - Unlimited
Subject Category 02
Availability: NASA CASI (443) 757-5802

13. SUPPLEMENTARY NOTES

Langley Technical Monitor: Stephen P. Wilkinson

14. ABSTRACT

This project developed quantitative methods for obtaining heat transfer from temperature sensitive paint (TSP) measurements in the Mach-6 quiet tunnel at Purdue, which is a Ludwieg tube with a downstream valve, moderately-short flow duration and low levels of heat transfer. Previous difficulties with inferring heat transfer from TSP in the Mach-6 quiet tunnel were traced to (1) the large transient heat transfer that occurs during the unusually long tunnel startup and shutdown, (2) the non-uniform thickness of the insulating coating, (3) inconsistencies and imperfections in the painting process and (4) the low levels of heat transfer observed on slender models at typical stagnation temperatures near 430K. Repeated measurements were conducted on 7 degree-half-angle sharp circular cones at zero angle of attack in order to evaluate the techniques, isolate the problems and identify solutions. An attempt at developing a two-color TSP method is also summarized.

15. SUBJECT TERMS

Boundary layer transition; Cones; Heat transfer; TSP; Temperature sensitive paint

16. SECURITY CLASSIFICATION OF:			17. LIMITATION OF ABSTRACT	18. NUMBER OF PAGES	19a. NAME OF RESPONSIBLE PERSON
a. REPORT	b. ABSTRACT	c. THIS PAGE			STI Help Desk (email: help@sti.nasa.gov)
					19b. TELEPHONE NUMBER *(Include area code)*
U	U	U	UU	153	(443) 757-5802